Study of All-Optical FSO Relay based Systems under the Influence of the Atmospheric Turbulence Channel

Norhanis Aida Mohd Nor

PhD

2018

Study of All-Optical FSO Relay based Systems under the Influence of the Atmospheric Turbulence Channel

Norhanis Aida Mohd Nor

A thesis submitted in partial fulfilment of the requirements of the University of Northumbria at Newcastle for the degree of Doctor of Philosophy

Research undertaken in
the Faculty of Engineering and Environment

September 2018

Abstract

Free space optical (FSO) communications is an emerging high-speed data rate, high-bandwidth, and license-free access solution for a number of applications including the “last mile” access networks. However, the reliability and availability of FSO systems are affected by a number of atmospheric phenomena such as fog, rain, haze, smoke, and turbulence. Interestingly, the severity of such random degradations is highly related to the transmission distance, thus resulting in link deterioration and ultimately complete link failure. In this thesis, an all-optical FSO relay-assisted system technique is adopted to mitigate the destructive effects due to distance dependent atmospheric turbulence-induced fading. In this scheme, relays are incorporated to the direct link between the transmitter and the receiver nodes in order to reduce the turbulence induced path loss per link, thus extending the link span and ensuring higher link availability (i.e., 99.999%) as well as improving the overall system performance. Two all-optical relaying schemes are proposed and investigated, namely all-optical amplify-and-forward (AOAF) FSO relay and all-optical regenerate-and-forward (AORF) FSO relay assisted systems. In the AOAF FSO system, the performance analysis of triple-hop AOAF FSO communications system is investigated under the impact of non-homogeneous atmospheric turbulence condition. We present novel experimental results for the single, dual, and triple-hop AOAF FSO systems under several turbulence configurations and regimes. We also provide a mathematical framework for the end-to-end signal-to-noise ratio (SNR) and the bit error rate (BER) performance and confirm that the derived analytical results reasonably match with the experimental results especially at relatively high SNR. The evaluated BER performances under different turbulence regimes, modelled by the Gamma-Gamma distribution model show that the considered relay-assisted FSO system offers a significant

performance improvement for weak to strong turbulence regimes, even without the knowledge of the channel state information. For instance, at a target BER of 10^{-5} the proposed triple-hop FSO scheme offers ~5 dB and ~4 dB of SNR gains compared to direct transmission for turbulence strengths C_n^2 of $3.8 \times 10^{-10}\ m^{-2/3}$ and $5.4 \times 10^{-12}\ m^{-2/3}$, respectively. For the latter scheme, the AORF FSO relaying scheme is proposed to overcome the limitation imposed by AOAF system, where the signal and noise is accumulated at each relay, thus limiting the number of relay that can be used. Using AORF, the background noise is eliminated and the signal is regenerated at each relay, which significantly increase the total transmission distance as well as the system performance. We provide novel experimental results for AORF dual-hop FSO relaying system under several turbulence regimes. The measured BER and the *Q*-factor performances show that AORF outperforms AOAF for all tested turbulence regimes, thus demonstrating the capability of the AORF system in removing the undesired noise prior to re-transmission of the signal to the next relay or destination. For example, at a target BER of 10^{-3}, the AORF system offers ~3.5 dB, ~1.8 dB, ~3.7 dB, ~3.0 dB of SNR gains compared to AOAF system for no turbulence, C_n^2 of $1.6 \times 10^{-11}\ \mathrm{m}^{-2/3}$, $6.8 \times 10^{-10}\ \mathrm{m}^{-2/3}$, and $1.9 \times 10^{-9}\ \mathrm{m}^{-2/3}$, respectively. Findings from this work suggest that the all-optical FSO relay-assisted system can be adopted as an alternative mitigation technique to mitigate the turbulence-induced fading effect especially for Metrozones deployment, due to the easy deployment, less complexity (compared to electrical relaying), and can resolve the current wireless bandwidth bottleneck problem.

Table of Contents

List of Figures

List of Tables

Glossary of Abbreviations

1R	Re-amplification
2R	Re-amplification and re-shaping
3G	Third generation
3R	Re-amplification, re-shaping, and re-timing
4G	Fourth generation
AF	Amplify-and-forward
AGC	Automatic gain controller
ASE	Amplified spontaneous emission
AOAF	All-optical amplify-and-forward
AORF	All-optical regenerate-and-forward
APD	Avalanche photodiode
ARDO	Asymptotic relative diversity order
AWGN	Additive white Gaussian noise
BER	Bit error rate
BERT	BER tester
BPF	Bandpass filter
CDF	Cumulative density function
CSI	Channel-state-information
DF	Decode-and-forward
DFB	Distributed feedback
DoF	Degree-of-freedom
DWDM	Dense wavelength division multiplexing
EDFA	Erbium-doped fiber amplifier
EO	Electrical-to-optical
ERC	Equal ratio combiner
FCC	Federal Communications Commission
FRC	Fixed ratio combiner
FSO	Free space optics
FWHM	Full-width at half-maximum
FWM	Four-wave mixing

GRIN	Gradient-index
GPS	Global positioning system
HNLF	Highly nonlinear fibers
HON	Heterogeneous optical networking
IID	Identical distributed
IM	Intensity modulation
IM-DD	Intensity modulation with direct detection
IR	Infrared
LAN	Local area-network
LED	Light emitting diode
LD	Laser diode
LDPC	Low-density parity codes
LN	Log-normal
LoS	Line-of-sight
MISO	Multiple-input single-output
MIMO	Multiple-input multiple-output
MMF	Multimode fiber
MRC	Maximum ratio combiner
NRZ	Non-return-to-zero
NRZ-OOK	Non-return-to-zero on-off keying
OA	Optical amplifier
OE	Optical-to-electrical
OBPF	Optical bandpass filter
OHL	Optical hard-limiter
OOK	On-off-keying
OSA	Optical spectrum analyzer
OSNR	Optical signal-to-noise-ratio
PAM	Pulse amplitude modulation
PD	Photo-detector
PDF	Probability density function
POF	Plastic optical fiber
PPM	Pulse position modulation
PRBS	Pseudo-random binary sequence
PSK	Phase-shift keying
PtP	Point-to-point

RF	Radio frequency
RF ID	RF identification
RoF	Radio-over-fiber
RV	Random variable
Rx	Receiver
RZ	Return-to-zero
RZ-OOK	Return-to-zero on-off keying
SIM	Subcarrier intensity modulation
SIMO	Single-input multiple-output
SMF	Single mode fiber
SNR	Signal-to-noise
SOA	Semiconductor optical amplifier
SONET	Synchronous optical network
SPM	Self-phase modulation
Tbps	Terabits per second
TIA	Trans-impedance amplifier
Tx	Transmitter
UUVs	Unmanned underwater vehicles
UWB	Ultra-wideband
VCSEL	Vertical-cavity surface-emitting laser
WDM	Wavelength division multiplexing
WLAN	Wireless local area network
WSN	Wireless sensor networks
XGM	Cross gain modulation
XPM	Cross-phase modulation

Glossary of Symbols

A	Signal amplitude
AF	Aperture averaging factor
a	ASE noise of OA
a_1	ASE noise of OA at $R1$
a_2	ASE noise of OA at $R2$
a_3	ASE noise of OA after $R3$
A_{eff}	Effective mode area
α	Effective number of large-scale turbulence eddies
α_{att}	Fiber losses
B	Bandwidth of the detector filter
BER_0	BER in absence of turbulence
β	Effective number of small-scale turbulence eddies
β_2	Fibre dispersion coefficient
β_v	Total attenuation/extinction coefficient of the atmosphere
C_n^2	Refractive index structure parameter
C_T^2	Temperature structure constant
CH_4	Methane
CO_2	Carbon dioxide
D	Destination
D_{RX}	Rx aperture size
D_P	Diversity gain of the parallel relaying
D_S	Diversity gain of the serial relaying
$\mathfrak{D}$	Chromatic dispersion
δ	Duty cycle
$E[\cdot]$	Statistical expectation operator
e	Electronic charge
$erfc(\cdot)$	Error function
F	Noise figure
$F(\cdot)$	CDF expression
$f(\cdot)$	PDF expressions

$f(h_{SR_1})$	PDF for the channel gains from *S* to *R*1
$f(h_{R_1R_2})$	PDF for the channel gains from *R*1 to *R*2
$f(h_{R_2D})$	PDF for the channel gains from *R*2 to *D*
$f(z)$	PDF of random variables *x* and *y*
$\mathscr{g}$	Optical amplifier gain
$\mathfrak{H}$	Planck's constant
h	Channel gain
h_{SR_1}	Channel gain from *S* to *R*1
$h_{R_1R_2}$	Channel gain from *R*1 to *R*2
h_{R_2D}	Channel gain from *R*2 to *D*
h_c	Channel state
H_2O	Water vapour
I	Irradiance of the optical laser beam
I_c	Constant output pulse intensity
I_{cr}	Critical pulse intensity
I_{log}	Log-intensity
I_o	Intensity in no turbulence medium
I_{out}	Output pulse intensity
I_p	Pulse intensity
I_t	Intensity in the turbulence medium
i_s	Instantaneous signal current
K	Boltzmann constant
k	Wave number
k_{nl}	Nonlinear propagation coefficient
κ	Linear loss coefficient
L	Link distance
L_D	Fibre dispersion length
L_{eff}	Effective fibre length
L_f	Total fibre length
L_{NL}	Nonlinear fibre length
L_0	Outer scale of turbulence
L_p	Propagation distance at two points
l_0	Inner scale of turbulence

λ	Wavelength
λ_{ZD}	Zero dispersion wavelength
N_0	Power spectral density
N_2	Nitrogen
n_1	Background noise at *R*1
n_2	Background noise at *R*2
n_3	Background noise at *D*
n_2	Nonlinear refractive index
η	Detector quantum efficiency
O_2	Oxygen
O_3	Ozone
P	Atmospheric pressure
P_{avg}	Average optical power
P_e	BER expression for *N*-hop link
P_{e2}	BER of the dual-hop system
P_{e3}	BER of the triple-hop system
P_{in}	Input power
P_{ro}	Received optical power
P_0	Peak power of the incident pulse
P_{out}	Output power
P_{peak}	Peak optical power
P_R	Received power at Rx
P_r	Average electrical power
P_S	Transmit power at Tx
P_{sat}	Saturation point
P_{S0}	Signal power in the absence of atmospheric effects
$p(t)_{\text{RZ–OOK}}$	Transmitted pulse of RZ-OOK
$p(I)$	Gamma-Gamma irradiance distribution function
$p_{LN}(I)$	Log-normal PDF of the received irradiance
$p_I(s)$	Probability distribution of irradiance
$\langle P_S \rangle$	Mean of instantaneous input signal power
ρ_o	Coherence length
Q	*Q*-factor
$Q(\cdot)$	Gaussian-*Q* function

q	Particle size distribution coefficient
$\mathcal{R}$	Response of the Rx
R	Relay
$R1$	Relay 1
$R2$	Relay 2
R_b	Bit rate
r	Radius of atmospheric particle
S	Source
SNR_0	SNR in absence of turbulence
$s_0(t)$	Transmitted signal from the source
$\langle SNR \rangle$	Mean SNR
$\mathbb{T}$	Transmittance
T	Absolute temperature
T_b	Bit duration/ bit interval
T_N	Effective noise temperature
$\mathcal{T}_0$	Pulse width.
τ	Normalized time scale
U	Normalized amplitude
V	Visibility range
V_H	Mean received voltage of 'high' level signal
V_L	Mean received voltage of 'low' level signal
v	Optical frequency
v_g	Group velocity
w_f	Center frequency
Δw_0	Initial spectral bandwidth of the pulse
$\overline{\Delta w_{SPM}}$	Average spectrum broadening for a Gaussian pulse
x_o	Atmospheric particle size parameter
χ	Gaussian distributed field log-amplitude fluctuation
$y_D(t)$	Received signal at destination prior to amplification
$y_D'(t)$	Received signal at destination after amplification
$y_{R_1}(t)$	Received signal at relay 1
$y_{R_2}(t)$	Received signal at relay 2
γ	Nonlinearity coefficient
γ_{e2e}	End-to-end SNR

σ_H	Standard deviation for the 'high' level signal
σ_L	Standard deviation for the 'low' level signal
σ^2	Variance
$\sigma_{a_1}^2$	Variance of ASE noise of OA at *R*1
$\sigma_{a_2}^2$	Variance of ASE noise of OA at *R*2
$\sigma_{a_3}^2$	Variance of ASE noise of OA at *R*3
$\sigma_{n_1}^2$	Variance of background noise at *R*1
$\sigma_{n_2}^2$	Variance of background noise at *R*2
$\sigma_{n_3}^2$	Variance of background noise at *R*3
σ_I^2	Scintillation index
σ_N^2	Variance for *N*-hop
σ_R^2	Rytov variance
σ_χ^2	Log-normal amplitude variance
$\sigma_i^2(\varnothing)$	Scintillation index for a Rx lens of diameter $\varnothing$
$\varnothing$	Rx lens diamater
$\emptyset_{NL}$	Nonlinear phase shift
$\emptyset_{SPM}$	Nonlinear phase shift induced by SPM

Dedication

This thesis is dedicated

To my husband, Danial,

my sons: Farish, Farhan, and Fateh,

and

to my dear parents.

Acknowledgement

The journey through my PhD studies, which bears enlightening life and research experiences, fruitful technical achievements and timely completion of this thesis, is impossible without the wonderful people who have walked with me and uplifted me through numerous good and difficult moments.

My thanks are wholly devoted to Almighty ALLAH for upholding me with perseverance, wisdom, and strength throughout this journey, and allowing everything to happen miraculously such that I could success and have smooth accomplishment of this research project.

First and foremost, I would like to express my heartfelt gratitude to my supervisor Prof. Zabih Ghassemlooy for giving us his most sincere and thoughtful advice, guidance, valuable suggestions, and constant support and encouragement particularly in justifying proper research direction of the project and ensuring that the research aims and objectives are fulfilled. It is an honour for me to study and do research under his supervision. I would also like to thank my co-supervisor, Prof. Stanislav Zvanovec from Czech Technical University (CTU) in Prague for the insightful guidance and support, especially in practical skills to carry out the experimental work in the laboratory, thereby generating some interesting results and notable findings. Not to forget, many thanks to the members of Electromagnetic Laboratory at CTU, John, Mathew, Petr, who sincerely helped me in the practical setup. In addition, I would like to thank Dr. Muhammad-Ali Khalighi, Dr. Manav Bhatnagar, and Prakriti Saxena for the insightful discussions, which have helped me to solve the analytical problems and improve my research work.

Moreover, I would like to express my utmost appreciation to my sponsor and employer, Ministry of Higher Education Malaysia and International Islamic University

Malaysia for providing the much-needed financial support during my study. Next, I would like to convey my sincere acknowledgement to my parents and my siblings for their inspiration, prayer, and moral support, especially during the most challenging moments of my research. In addition, I am deeply thankful to my beloved husband and children who have persistently accompanied me in completing this journey, consistently give me courage and support, as well as sharing my tears and showering upon me with love, joy, and laughter. I would also like to express my heartfelt gratitude to my colleagues and acquaintances for sharing the knowledge, experiences, and opinions, which have inspired me with more feasible ideas and solutions to overcome any barrier encountered in my research studies. Not forgetting, my fellow Malaysian's friends at Newcastle who support and cheer me up when needed. Thank you everyone.

Declaration

I declare that the work contained in this thesis has not been submitted for any other award and that it is all my own work. I also confirm that this work fully acknowledges opinions, ideas, and contributions from the work of others.

I declare that the word count of this thesis is 34538 words.

Name: Norhanis Aida Mohd Nor

Signature:

Chapter 1

INTRODUCTION

1.1 Overview

The evolution of wireless communication applications over the past decades is enormous, driven by the ever increasing number of wireless broadband internet, mobile phones, smart devices, social web, gaming, and videocentric applications. Statistics show that, the number of users has exponentially grown from 16 million in 1995 to 3.6 billion in 2016, approximately 30-40% per annum [1], [2], which become the quest for the network hardware vendors and operators to replenish and upgrade the current available systems for higher wireless access data rate and better quality of service. Until now, the radio frequency (RF) based systems have been the prominent and mature wireless technology as a result of the rapid deployment and utilization of wireless RF devices and systems in various fields such as wireless local area network (WLAN), global positioning system (GPS), cellular network, RF identification (RF ID) systems, and home satellite network [3]. However, the volume of mobile and wireless users are predicted to increase a thousand-fold over the next decade [4], thus resulting in the mobile spectrum crunch (i.e., wireless bandwidth bottleneck) [5].

Fiber optical communications evince the most reliable transmissions means to ensure the bandwidth requirements and high data rates transmission. However, it is significantly more costly and impractical to lay fiber in some particular areas such as urban and hilly areas [6]. Therefore, free space optics (FSO) is the viable solution that

offers high bandwidth and data rates, free spectrum licensing, no RF based electromagnetic interference, inherent security, and low-cost implementation and maintenance [7]. With the emergence of powerful and efficient optoelectronic component and advanced communication techniques, current states-of-the-art FSO prototypes have demonstrated data transmission at high speeds up to terabits per second (Tbps) [8]–[10].

The growing bandwidth demand of reliable FSO communications in various applications require the FSO terminals to offer variable link capacity in order to maximize the system availability and throughput. Hence, FSO communication systems should therefore be properly designed to dynamically optimize the system performance under varying atmospheric conditions. The proposed works unfold new insight on the FSO system design and performance characteristics under adverse atmospheric conditions in implementing a reliable FSO communications system for used particularly in the rural urban areas, where the deployment of optical-fibre links are not feasible (cost, complex and time).

1.2 Problem Statements

1.2.1 Atmospheric channel effects on the FSO communication systems

Since FSO is using a wireless channel as a transmission medium, the system performance fundamentally dependent on the characteristics of the atmospheric channel. The atmospheric channel effects can be classified into absorption, scattering (caused by fog, snow, smoke, haze, aerosols, and dust particles), and turbulence-induced fading or scintillation [7], and are highly variable and unpredictable. This can cause a significant power penalty at the receiver, thus resulting increased bit error rate (BER) performance, reduced link range, temporary signal degradation and eventually lead to complete link

outage under the influence of deep signal fades, making it very difficult to attain the requirement of 99.999% link availability [5][9]. Unlike fog, snow, and cloud, which induce attenuation, the atmospheric turbulence, also known as scintillation, is the main source of random fluctuations of received optical radiation irradiance both in terms of intensity and phase even under the clear weather condition [11]. Atmospheric turbulence-induced signal losses will increase as the distance between the transmitter and receiver is increased. Thus, the characteristics of the atmospheric turbulence are very critical factor in determining the FSO system performance.

Through an in-depth survey of the relevant literatures, it is evident that a substantial number of studies have portray the contributing effects of turbulence induced fading on FSO performance analytically [12]–[15] and experimentally [16]–[19]. Moreover, various models exist to describe the stochastic behaviour of atmospheric turbulence, which can be approximately modelled by the log-normal and Gamma-Gamma distributions, valid for the weak-to-moderate and moderate-to-strong turbulence regimes, respectively. Thus, this research work will appropriately address and taken into account the effect of turbulence-induced fading the proposed FSO system design. The atmospheric effects discussed in details in Chapter 2.

1.2.2 Mitigation techniques in FSO systems

Various mitigation techniques have been proposed and implemented so far to combat the deterioration of signal quality due to the adverse atmospheric conditions such as hybrid RF/FSO systems [20]–[22], complex modulation and coding [23]–[25], adaptive optics [26], [27], spatial diversity [28]–[30], and aperture averaging [31]–[33]. Among them, the simplest technique that can be adopted is the aperture averaging, where by using a receiver aperture larger than the fading correlation length, the intensity fluctuation can be averaged out over the aperture area. However, this technique has been

found to be effective mostly for the weak-to-moderate turbulence regime, but not for the strong turbulence regime even using very large aperture receivers. In addition, the aperture averaging of a fixed size receiver may not sufficiently reduce the fading for a particular link since the type of platform on which the receiver is located may limit the practical size of the receiver aperture [5]. Besides that, spatial diversity has been proved to provide substantial performance improvement in spatially uncorrelated channels, for instance, by employing multiple receiver apertures that are sufficiently spaced [34]. Nevertheless, employing space diversity results in increased size, cost, and hardware complexity of the transmitter and/or receiver modules.

While majority of these mitigation techniques have been proposed at the expenses of increased circuit complexity and massive signal processing requirements, more competent methods may be introduced in FSO systems in order to improve link reliable and availability in delivering high data rates. Relay-assisted or also known as multi-hop FSO communications is one of the alternative solutions, which offers diversity within the networks that can be adopted to combat link failure, thus substantially improving the link availability. However, the existing relay nodes are based on optical-to-electrical (OE) and electrical -to- optical (EO) conversion routing, which requires high-speed electronics and electro-optics devices, analog gain units, and digital control, which significantly increase the link latency, complexity, and excessive cost of the system [35]. Hence, with the aims of avoiding complex optoelectonic and electronic processing at each relay and simultaneously increases the transmission link span, this research investigates an alternative approach based on the path routing using the all-optical FSO relay-based system. With this method, a virtual antenna array is created to extract the spatial diversity advantages in a distributed manner. Furthermore, the abundance of research results of all-optical relay-assisted techniques are mostly theoretical with not much experimental work in the last few years, thus leaving the practical implementation, characterization and

evaluation of an all-optical FSO relay system an open research problem, which needs addressing. Majority of the research works reported so far also consider highly-idealized relay-assisted communication systems with assumptions such each relay node has an exact knowledge of channel and thus signal transmission.

In this research the investigation of all-optical FSO relay is extended and enhanced by carrying out a substantial and in-depth experimental investigation by developing a state of the art laboratory test-bed. The test bed is used for comprehensive test and measurements and measured results are compared with the predicted data.

1.3 Research Aims and Objectives

The aim of this research project is to carry out extensive theoretical investigation, and experimental demonstration pertaining to the system design and performance analysis of all-optical relay-assisted FSO communications systems. The desired system should be adequate to mitigate the turbulence-induced fading effect by providing an improved performance compared to the traditional terrestrial FSO links.

Based on the research aims, the objectives of this research work are defined as follows:

1. To carry out in-depth literature review and preliminary studies to the key areas related to FSO communications particularly the relay-assisted FSO system under the turbulence channel.
2. To carry detailed theoretical investigation and simulation on the all-optical relay-assisted FSO system over an atmospheric turbulence channel using Gamma-Gamma distribution model.
3. To evaluate the system performance using the standard metrics of the BER, signal-to-noise ratio (SNR), *Q*-factor, and eye-diagrams.

4. To conduct analytical and simulation studies of the all-optical amplify-and-forward (AOAF) FSO relaying system.
5. To carry out experimental investigation and performance evaluation of the AOAF FSO relaying system under a laboratory-controlled atmospheric environment and compare the results with the predicted data.
6. To perform experimental campaign of an all-optical regenerate-and-forward (AORF) FSO relaying system under a laboratory-controlled atmospheric environment.
7. To compare the measured BER and *Q*-factor performances of AORF and AOAF FSO relaying systems.

1.4 Thesis Contributions

This thesis investigates the performance of relaying technique for FSO communication systems in which the relaying processes have been performed in all-optical domain. Two AOAF and AORF based-FSO relay-based systems are investigated, and novel experimental works are successfully executed for both techniques.

The contributions of this research work are outlined below:

1. In Chapter 4, the performance analysis of the AOAF FSO relay-assisted system particularly triple-hop systems is investigated theoretically and experimentally under the turbulence condition. A mathematical framework for the end-to-end SNR and BER performance for the proposed scheme is outlined, governed by Gamma-Gamma distribution model. Different turbulence configurations are tested to ascertain the capability of the systems in combating the turbulence induced fading. The results show that the predicted data match well with the experimental results.

2. In Chapter 5, the performance analysis of a dual-hop AORF FSO relay-assisted system is investigated experimentally using a dedicated indoor-laboratory testbed. The proposed novel technique is introduced in order to overcome the limitation imposed by the AOAF relaying system, which will limit the transmission span. The purpose of this new relaying scheme is to assess the effectiveness of an optical regenerator in combating the scintillation effect (i.e., turbulence) compared to the AOAF relaying scheme. The link performance is demonstrated in terms of the measured BER, SNR, *Q*-factor, and eye-diagrams.

1.5 Research Outcomes (Publications)

The research work led to a number of publications as outlined below:

Journals:

[J1] N. A. M. Nor, Z. Ghassemlooy, J. Bohata, P. Saxena, M. Komanec, S. Zvanovec, M. Bhatnagar, and M.-A. Khalighi, "Experimental investigation of all-optical relay-assisted 10 Gb/s FSO link over the atmospheric turbulence channel," *Journal of Lightwave Technology*, vol. 35, no. 1, pp. 45–53, 2017.

[J2] N. A. M. Nor, Z. Ghassemlooy, S. Zvanovec, M.-A. Khalighi, R. Bhatnagar, J. Bohata, and M. Komanec, "Experimental analysis of a triple-hop relay-assisted FSO system with turbulence," *Elsevier Journal of Optical Switching and Networking*, 2017, [online] Available: 10.1016/j.osn.2017.11.002.

[J3] N.A.M. Nor, M. Komanec, J. Bohata, Z. Ghassemlooy, M. R. Bhatnagar, S. Zvanovec, "An experimental all-optical relay-assisted FSO link with reconstruct and forward scheme transmitting ultra-short pulses", submitted to IEEE Journal of Lightwave (JLT) on 13th April 2018.

Conferences:

[C1] N. A. M. Nor, Z. Ghassemlooy, S. Zvanovec, M. -A. Khalighi, and M. R. Bhatnagar, "Comparison of optical and electrical based amplify-and-forward relay-assisted FSO links over gamma-gamma channels," in *10th International Symposium on Communication Systems, Networks and Digital (CSNDSP16)*, 2016, no. 1, pp. 1–6.

[C2] N. A. M. Nor, Z. Ghassemlooy, S. Zvanovec, and M. -A. Khalighi, "Performance analysis of all-optical amplify-and-forward FSO relaying over atmospheric turbulence," in *IEEE Student Conference on Research and Development*, 2015, no. 1, pp. 1–5.

[C3] N. A. M. Nor, J. Bohata, Z. Ghassemlooy, S. Zvanovec, P. Pesek, M. Komanec, and M. -A. Khalighi, "10 Gbps all-optical relay-assisted FSO system over a turbulence channel," in *International Workshop on Optical Wireless Communication*, 2015, pp. 1–4.

[C4] N.A.M. Nor, Z. Ghassemlooy, S. Zvanovec, and M. -A. Khalighi, "Performance analysis of tri-hop all-optical free space optical communications under the atmospheric turbulence channel", Northumbria Research Conference, Northumbria University, 2015

[C5] N. A. M. Nor, E. Fabiyi, M. M. Abadi, X. Tang, and Z. Ghassemlooy, "Investigation of moderate-to-strong turbulence effects on free space optics - A laboratory demonstration," in *International Conference on Telecommunications*, 2015, pp. 1–5.

1.6 Organization of the Thesis

This thesis is organised in six chapters as follows:

Chapter 1 – Introduction: An introduction of the FSO technology and its challenges are presented. Taking into account the main challenges and open research issues pertaining to the system addressed in Section 1.2, and the aims and objectives of the proposed research study are highlighted in Section 1.3. Correspondingly, the original contributions and outcomes of this research are presented in Section 1.4 and Section 1.5, respectively.

Chapter 2 – An overview of free space optical communication networks: This chapter presents a brief review and discussion on the key aspects of the FSO technology in order to optimize the FSO systems for long-distance terrestrial application as well as to solve the last-mile access network issue using optical topology networks. Beforehand, the fundamental aspects regarding FSO communication systems, the advantages, and the area of applications are highlighted. Following that, the important characteristics and modelling of the atmospheric channel effects encompassing the atmospheric attenuation and turbulence-induced effect are presented. Also, this chapter discuss the relevant performance metrics to quantify the FSO communication systems, which include SNR, BER and eye diagrams.

Chapter 3 –Fading mitigation techniques in FSO systems: In this chapter, in-depth review of the relevant literatures pertaining to the investigation studies of all-optical FSO relaying systems are presented. This includes the principle of traditional and all-optical relay-assisted FSO communication systems, which are comprehensively discussed. Following this, two of the all-optical relaying techniques that are proposed in this research

are deliberated, which are AOAF and AORF FSO relaying schemes. The fundamental theory of optical amplifier and the regenerator are presented accordingly.

Chapter 4 –All-optical AF FSO relay-assisted system under turbulence effects: This chapter present the main finding of this research work regarding to the AOAF FSO relay-assisted system. The first part of the chapter introduces the relevant literature regarding to the relay-assisted FSO communication and the basic AOAF configuration that is used throughout the analysis. Following this, numerical simulation results using the MATLAB and Optisystem are presented and the mathematical framework for the end-to-end SNR and BER performances of the AOAF FSO triple-hop system performance, considering Gamma-Gamma distribution model are derived. Subsequently, the experimental setup of single, dual, and triple-hop AOAF FSO systems are explained. The notable findings are discussed here where the results are divided in two parts. In first part the performances of single, dual-hop, and triple-hop AOAF FSO system are investigated through identical turbulence channel (i.e., all links experiencing the same turbulence induced fading). Further analysis is carried out for the triple-hop AOAF FSO system, considering seven different turbulence configurations and the results are explicitly discussed here.

Chapter 5 – All-optical regenerate-and-forward FSO relay-based system: This chapter presents the novel experimental works and findings of AORF FSO relay-assisted FSO communication system, which is done under laboratory controlled atmospheric turbulence conditions. This chapter begins with some discussion pertaining to the relevant literatures of optical regeneration in optical communication systems as well as the mathematical concepts of self-phase-modulation (SPM) based AORF FSO system. Experimental setup, data acquisition, and post-analysis processes are explained in details here. The analyses include the comparison of BER performance of the dual-hop AORF

FSO systems with the dual-hop AOAF FSO system under several turbulence regimes, as well as the evaluation of the captured eye-diagram and *Q*-factor.

Chapter 6 – Conclusions and Future Works: Last but not least, the conclusion of the thesis is presented in this chapter along with the possible direction for further research related to all-optical FSO relay-assisted based systems.

Chapter 2

AN OVERVIEW OF FREE SPACE OPTICAL COMMUNICATION NETWORKS

2.1 Introduction

As third and fourth generations (3G/4G) of mobile networks have experienced a tremendous increase in data traffic, the service providers must address the bandwidth bottleneck issues at both the backhaul and last mile access networks to increase the network capacity. Both microwave and optical fiber based technologies will continue to retain their importance as a backhaul bearer. However, operators may also consider alternative technologies to overcome the spectrum congestion in certain applications, thus ensuring the most efficient use of the RF spectrum in dense-traffic areas. This could include point-to-multipoint links in areas where spectrum for the conventional point-to-point links is becoming scarce and costly. To increase the bandwidth and capacity, service providers are considering moving to higher frequencies (i.e., 40 and 80 GHz bands), but at the expense of reduced transmission coverage, which has adverse effects on the cost (i.e., deployment, site rental, maintenance, equipment, etc.). Alternatively, FSO

communications-based technology could be adopted to address the aforementioned problems particularly in the last mile access networks at much reduced cost compared to RF based schemes. FSO systems are mostly used for line-of-sight applications, thus offering similar capabilities as optical fiber communications with attractive features including a huge bandwidth, no licensing fee, inherent security, low cost of installation and maintenance, and immunity to electromagnetic interference [7], [36]. Data rates up to 10 Gbps are readily available in commercial FSO systems operating over a link span of few kilometers [37] and up to 1.6 Tbps over a 80 m single outdoor link based on the dense wavelength division multiplexing technique was reported in [8].

Despite of the advantages offered by the FSO, this technology is hampered by the atmospheric channel which is highly variable, unpredictable, and vulnerable to different weather conditions such as scattering, absorption, and turbulence, thus resulting in optical attenuation, waveform distortion, and phase wandering [13], [38]–[40]. Therefore, with these channel imposed constraints, it is very challenging to attain up to 99.999% link availability. Hence, another easy way to increase the link availability is by structuring the optical link into optical networks topologies such as mesh and ring networks.

To substantiate the design, analysis, and optimization of FSO communication systems for long-distance terrestrial applications as well as to solve the last-mile access network issue, this chapter presents an extensive review and discussion on the key aspects of the FSO technology, which include the introduction of optical networks and their topology to become massive wireless access network, which are point-to-point (PtP), ring, and mesh topology, discuss in Section 2.2. Next, the FSO communications systems is explained with an insightful literature survey is provided about the FSO transmitter (Tx) and receiver (Rx), on-off-keying (OOK) modulation, and the choice of wavelength in Section 2.3. Following this, Section 2.4 enumerates the advantages of FSO and the area of applications that is suitable to be implemented. Section 2.5 describes the important

characteristics and modelling of the atmospheric channel effects encompassing the atmospheric attenuation (i.e. scattering and absorption), and turbulence-induced effect. The relevant performance metrics to quantify the FSO communication systems, which include SNR, and BER, and eye diagrams are highlighted in Section 2.6. Last but not least, the summary of the chapter is drawn in Section 2.7.

2.2 Optical Networks

The capacity bottleneck issue is become the crucial problem to the current wireless communication systems. One of the alternative to solve this bottleneck issue is to combine the transmission of ultra-wideband (UWB), which operates in 60 GHz radio operating over fiber optical links, or so called radio-over-fiber (RoF). However, this approach requires frequent EO and OE conversion and also requires expensive optical components. It is also inefficient in terms of optical bandwidth utilization, as it transmits low-speed wireless signals over high-bandwidth optical channel [6]. Therefore, another approach to deliver high-speed signal to the end-user is proposed by using heterogeneous optical networking (HON), where FSO, plastic optical fiber (POF)/ multimode fiber (MMF) and indoor optical wireless communications link are simultaneously used. This HON can deliver a high speed optical signal i.e., 40 Gbps and beyond to the end-user, provide high-bandwidth, and solve interoperability problem of future optical networks [6].

Currently, incredible developments in circuit integration, optical transceivers, and optical systems and networks capable of transmitting huge amount of data in a second, which now up to few Terabit in one second. This huge achievement is the result of evolutions in laser devices, ultra-fast modulators, high-sensitive photodetectors, low attenuation fiber, and etc. As the consequences, optical communications is become the

dominant technology especially in the backbone network, as nowadays the fiber optic technology has fulfil all the expectations and has replaced copper almost 100% [41]. However, there are certain issues regarding to the optical fiber where it does not reach to some of the applications that require high-data rate services because of there are insufficient fiber infrastructure and no fiber deployment due to geographical areas. As the result, the high-speed amount of data cannot be delivered to the end users, thus creating the so-called the "last mile access bottleneck" issue.

In this situation, another optical communications technology that can be as an alternative solution to this problem is FSO. This FSO is a PtP outdoor wireless communications technology that transmits high data rates, which currently is up to 1.6 Tbps [8] as illustrated in Fig. 2.1. FSO transmits an intensity modulated laser beams to a photodetector over a line-of-sight (LoS) free space path with a typical link span of a few kilometres [42]. The wavelengths used are typically 850 nm, 930 nm, 1550 nm, and 10 μm [43], therefore no need for Federal Communications Commission (FCC) license approvals. In most cases, the link is installed on the tall buildings, connected from rooftop-to-rooftop, window-to-rooftop or window-to-window. FSO also comes in compact sizes, which is easy to setup, deploy, maintain, and also flexible to change the locations in a matter of only few days. FSO is more effective compared to fiber in terms of labor intensive fiber planning and deployment, and to get permits approval. Other advantages include, inherent security and reliable data transmission due to the use of narrow and directional beam, and robustness against electromagnetic interference as compared to radio frequency [7]. Among popular applications of FSO are last/first mile connectivity to the access network, local-area-network (LAN)-to-LAN inter-connectivity especially for campus and metropolitan applications, short term communication needs such as for disaster and emergency relief network applications, inter-satellite

communication, ground to/from satellite communication, and deep space communications [44].

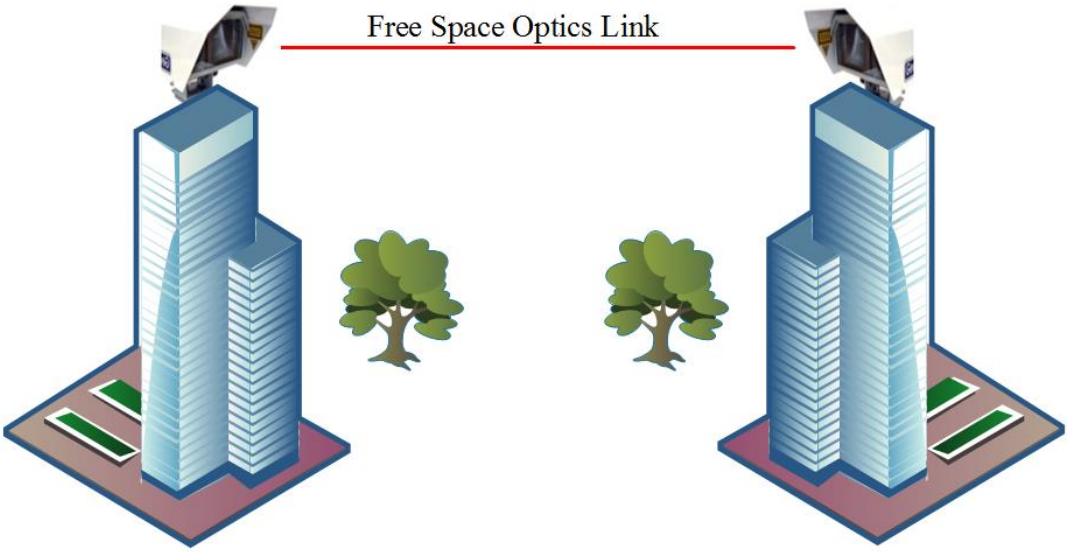

Fig. 2.1: Point-to-point FSO concept.

2.2.1 FSO network topologies

The FSO network topology can be classified into three categories which are PtP, ring, and mesh networks as shown in Fig. 2.2. This topology can be combined to become a massive wireless access network. The basic approach is just having two LoS points connected together, which is also called the traditional FSO link.

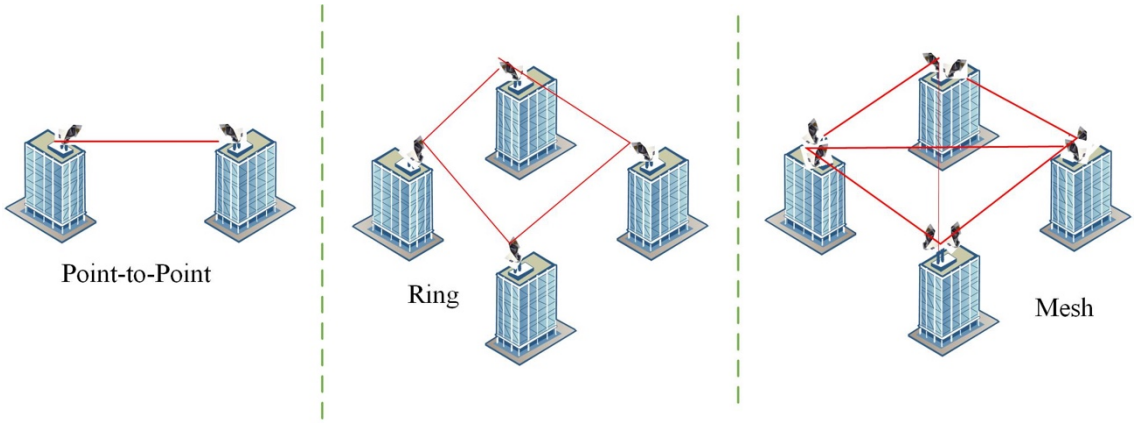

Fig. 2.2: Point-to-point, ring, and mesh topologies.

The FSO PtP topology is the simplest and commonly used for quick link establishment. It only requires two LoS FSO transceivers at two separated locations, typically between few hundred meters up to few kilometers (usually ≤ 4 km). It does not require intermediate nodes. Even though the protocol is inexpensive and straightforward, PtP is the abominable network and low traffic protection, as well as has limited link propagation span, especially for unidirectional FSO link. This is because the link is vulnerable to failure either due to the equipment failure or vast atmospheric conditions, which the system cannot tolerate.

The ring topology consists of more than two nodes. This protocol has better network and traffic protection. The ring topology is also vulnerable to failure. However, it can be fixed using traffic loop back mechanism, considering the system are having monitoring mechanism to detect the fault and also the protocols to activate the loop-back mechanism, which usually been placed at the physical layer near to the transceiver head or at the MAC layer [41].

The ring network will be extended with another ring network so that the communication link is established for longer distance as shown in Fig. 2.3.

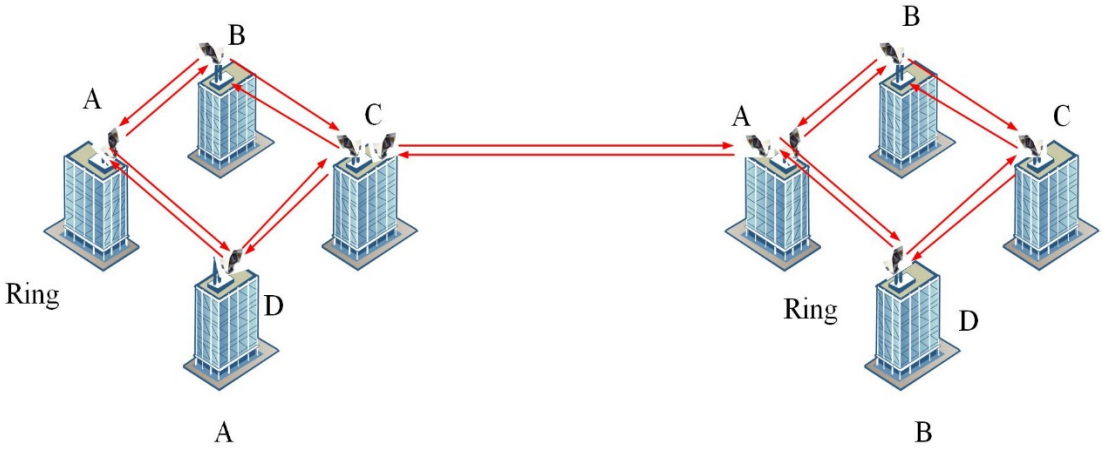

Fig. 2.3: Ring topology extension networks.

The mesh topology is capable to interconnect multi-nodes and the communication links is scalable and expandable up to several kilometers-square. The mesh topology is

the best solution to interconnect the FSO node at different terrain, either uneven or mountainous terrain or with buildings with different heights as illustrated in Fig. 2.4. This protocol also allow flexibility in mounting the individual FSO head at different environmental conditions (i.e., temperature, humidity, pressure, wind sway, and etc.). This protocol is the best network and service protection, which suitable to be applied as ad-hoc network applications as long as the LoS is sustained due to high availability, connectivity, increased capacity, and network utilization [45]. When the faulty node is detected, the traffic is rerouted over another path according to the routing algorithms. However, the drawbacks are complexity and increase the maintenance cost. It requires traffic capacity, traffic routing, and traffic balancing. The same condition as ring topology network, mesh network needs thorough monitoring for fault detection, require traffic balancing so that all nodes deliver the acceptable performances, and also maintain the traffic priorities.

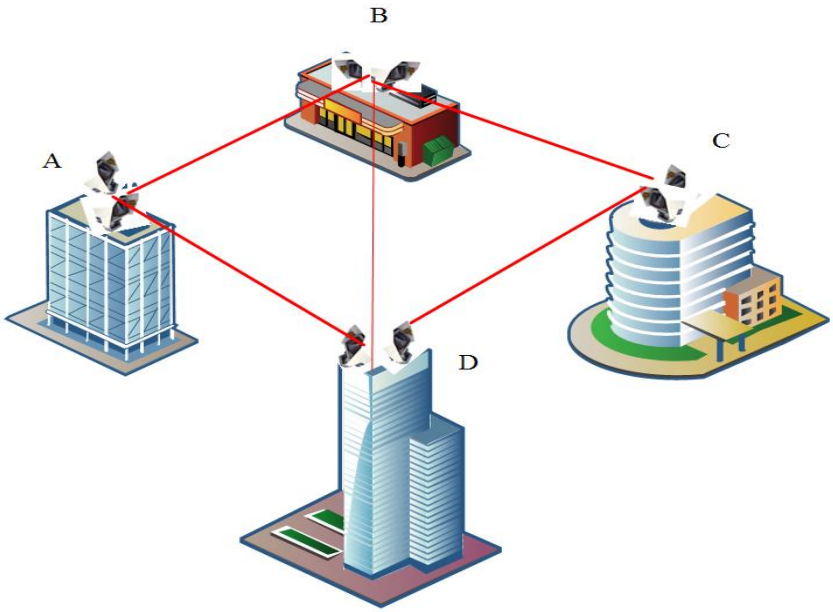

Fig. 2.4: Mesh FSO topology network at different heights.

The following criteria should be followed to ensure that the best topology is adopted for a specific terrain in order to meet the service and performance requirements, as well as to provide a robust and fault-tolerant network. It includes area surveying where

FSO is to be deployed, area localization, measuring the latitude of each node, spots the problem in that area such as LoS and angles, estimation of both the peak and average data traffic per node, and determination of the traffic volume [41]. Another crucial aspect to be considered is the scalability of the network, which means the possibility to add more nodes in the network when necessary[46].

2.3 Fundamental of FSO

An FSO link is fundamentally based on LoS. Thus, both the Tx and the Rx must directly point to each other without having any obstruction in their path to ensure the communication link is always established. The fundamental system of an FSO system is depicted in Fig. 2.5. The unguided channel could be either space, sea-water, or the atmosphere.

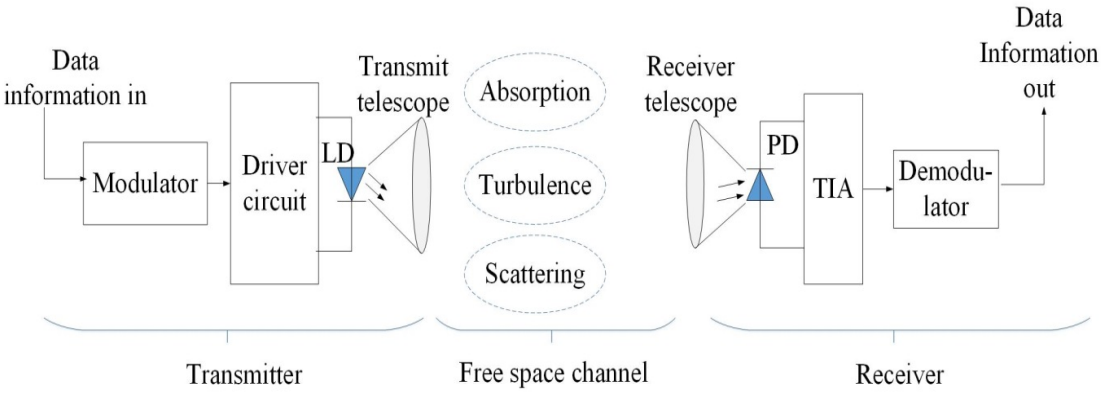

Fig. 2.5: The block diagram of an FSO communication system.

The following subsection present further discussion of the main block diagram of optical Tx and Rx, the main modulation technique in optical communications, which is OOK, and the FSO wavelength. The atmospheric channel effect will be discussed in details in Section 2.5.

2.3.1 FSO Tx

The Tx composed of four main components which include laser modulator, driver, optical source, and transmit telescope. This main functional system has a responsibility to modulate the electrical input signal onto the optical carrier using light emitting diode (LED) or laser diode (LD). Both LED and LD are the most commonly used because of the compact size, low forward voltage and drive current, excellent brightness in the visible wavelength, and have the option of emission at a single wavelength or range of wavelengths [7]. Then, the very narrow beam will be transmitted by the transmit telescope, which collimates and directs the optical radiation towards the Rx telescope at the other end through free space channel. For an optical wave, modulation scheme named as intensity modulation (IM) is often used, in which the data information is modulated onto the irradiance of the optical radiation. This can be achieved by varying the driving current of the optical source directly in line with the transmitted data, resulting in the modulates source output. Such a scheme simplifies the Tx design and generally more cost–effective. This step can also be accomplished but often it requires high bit rates [47]. The functionality of the driver is to regulate current flowing through the LD and stabilizes its performances as well as neutralizes temperatures and aging effects on the performance of the laser.

2.3.2 OOK modulation formats

While there are many modulation possibilities, the most common modulation formats considered for FSO links is the binary amplitude-shift-keying or widely-known as OOK modulation format due to its high bandwidth efficiency. OOK has become a dominant form of signalling because of the Tx and Rx hardware are relatively simple and fiber optics networks generally operate a high SNR with a lower dynamic range requirement and well controlled signal levels at the Rxs [48]. The implementation of

OOK in an optical Tx requires the intensity of the optical carrier is turned on and off in response to an electrical bit stream. Typically, the laser is biased slightly below a threshold, so that it emits no light during bit 0. During each bit 1, the laser goes beyond its threshold and emits a pulse whose duration is nearly equal to that of the electrical pulse. OOK can use either non-return-to-zero (NRZ) or return-to-zero (RZ) pulse formats, see Fig. 2.6.

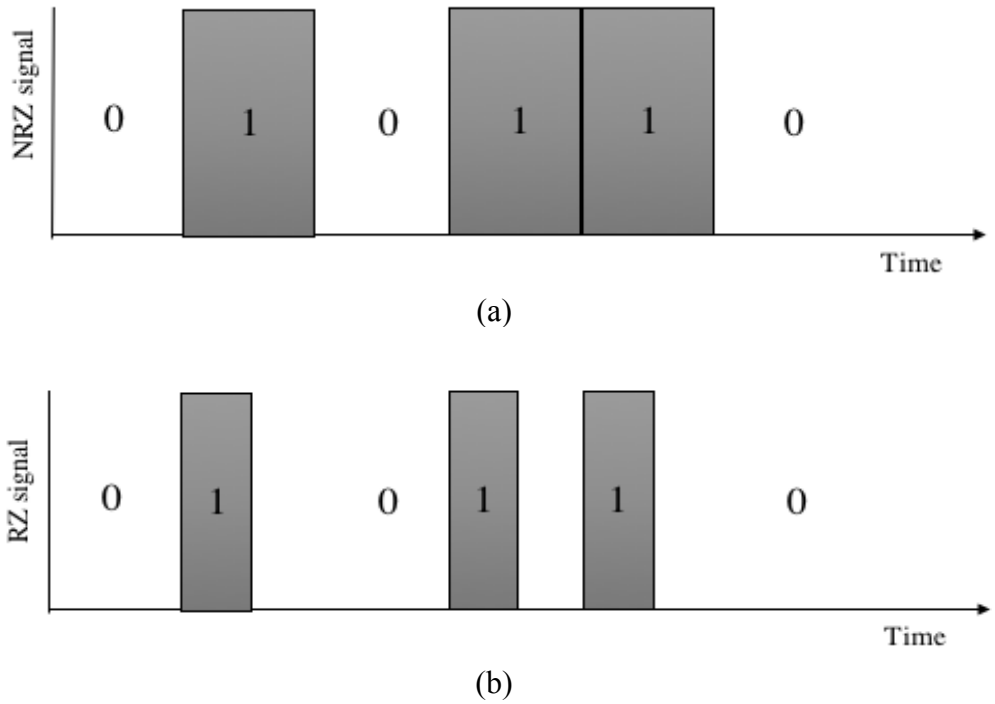

Fig. 2.6: Optical bit stream 010110.. . coded using (a) non-return-to-zero (NRZ) and (b) return- to-zero (RZ) formats.

The bit rate $R_b = \frac{1}{T_b}$, where T_b is the bit duration. The normalized transmit pulse shape for NRZ-OOK is given by [49]:

$$p(t) = \begin{cases} 1 & \text{for } t \in [0, T_b] \\ 0 & \text{elsewhere.} \end{cases} \tag{2.1}$$

The waveform of an NRZ-OOK modulation scheme can be represented as:

$$X(t) = \sum_k a_k P_{peak} P_{Tb}(t - kT_b), \tag{2.2}$$

where $P_{Tb}(t) = 1$ for $0 \leq t \leq T_b$ and $P_{Tb}(t) = 0$ elsewhere, and $a \in \{0,1\}$. The peak optical power P_{peak} is related to the average optical power P_{avg} as $P_{peak} = 2P_{avg}$.

In the demodulator, the received pulse is integrated over one bit period, then sampled and compared to a threshold to decide a '1' or '0' bit, which is called the maximum likelihood Rx that can also minimizes the BER [50]. The electrical power density for NRZ-OOK assuming the independently and identical distributed (IID) input is given by [50]:

$$S_{OOK-NRZ}(f) = (P_r\mathcal{R})^2 T_b \left(\frac{\sin \pi f T_b}{\pi f T_b}\right)^2 \left[1 + \frac{1}{T_b}\delta(f)\right], \tag{2.3}$$

where δ represents the duty cycle, which the pulse shape is high for only a fraction of bit duration δT_b with $0 < \delta < 1$, P_r is the average electrical power and $\mathcal{R}$ is the response of the Rx.

The transmitted pulse of RZ–OOK (with 50 percent duty cycle) is given as:

$$p(t)_{\text{RZ-OOK}} = \begin{cases} 1 & \text{for } t \in [0, T_b/2] \\ 0 & \text{elsewhere.} \end{cases} \tag{2.4}$$

The spectra of this form of signalling do contain discrete components at the bit rate which simplifies clock recovery. Unfortunately, the bandwidth efficiency of RZ signalling with 50 percent duty cycle is also reduced by 50 percent [49]. This makes it necessary to find compromise between the complexity of the clock recovery and the bandwidth efficiency. In this case, the waveform of the RZ-OOK modulation scheme can be expressed as [49]:

$$X(t) = \sum_k a_k P_{peak} P_{\delta Tb}(t - kT_b), \tag{2.5}$$

where $P_{\delta Tb}(t) = 1$ for $0 \leq t \leq \delta T_b$ and $P_{\delta Tb}(t) = 0$ elsewhere, and $a \in \{0,1\}$. Here, the relationship between the P_{peak} and the P_{avg} is given as:

$$P_{peak} = \frac{2P_{avg}}{\delta}. \tag{2.6}$$

Here, the power requirement is reduced to half compared to regular NRZ-OOK, with the expense of doubling the bandwidth. The expression for electrical power density for RZ-OOK assuming random input bits is given as [50]:

$$S_{OOK-RZ}(f) = (P_r\mathcal{R})^2 T_b \left(\frac{\sin \pi f T_b/2}{\pi f T_b/2}\right)^2 \left[1 + \frac{1}{T_b}\sum_{-\infty}^{\infty} \delta\left(f - \frac{n}{T_b}\right)\right], \quad (2.7)$$

Based on the explanation above, there are trade-off between NRZ-OOK and RZ-OOK signalling formats. The main advantage of the NRZ-OOK format is that the bandwidth requirement is smaller than the RZ-OOK by about a factor of 2.

2.3.3 FSO wavelength

Current available commercial FSO system can be classified into two transmission windows of 780-850 nm and 1520-1600 nm [51]. The wavelength 780-850 nm are preferable for FSO operation due to low cost, reliable, and high performance Tx and detector components are readily available and commonly used in network and transmission equipment. Moreover, avalanche photodiode (APD) and vertical-cavity surface-emitting laser (VCSEL) can be used in this range of wavelengths, which VCSEL is cheaper than many of its alternative and can produce direct modulation speeds beyond 3 Gbps [52]. On the other hand, the 1550 nm wavelength is well suited for free space transmission due to low attenuation due to Rayleigh scattering, as well as the proliferation of high-quality Tx and detector components. It is also allowed more transmit power level, 50 times greater than 800 nm wavelength [52], thus the system to propagate over longer distance through heavier attenuation. According to [51], laser beams at 1550 nm wavelength are more eye safety since the laser beam at wavelength above 1400 nm is absorbed by the lens and the cornea, and thus there is no destructive focal point to create

damage on the retina [41]. On the other hand, at 800 nm the retina could be permanently damaged as the collimated light beam entering the eye is concentrated by a factor of 100 000 times when it strikes the retina. Most of the optical devices are also compatible with the 1550 nm. However, the trade-off are less Rx sensitivity and higher component cost.

2.3.4 FSO Rx

The Rx side of the FSO link, which converts the optical signal received into the original electrical signal, basically comprises of Rx telescope, photo-detector (PD), a trans-impedance amplifier (TIA), and demodulator as illustrated in Fig. 2.5. Optical beam arrived from the free space channel is collected and focused by the Rx telescope to the PD that converts the optical signal into an electrical form before being amplified by TIA. Semiconductor photodiodes (i.e., p-i-n and avalanche photodiode) are usually preferable as PDs because of their compact size, relatively high spectral sensitivity, and very fast response time (rise and fall time) [7], [47]. Normally, optical band filter is placed before the PD to minimize the effects of background radiation [53]. Following amplification by the TIA, the original electrical signal is reconstructed by the demodulator from the time-varying current in spite of the channel-induced degradation and the noise added at the Rx. The design of demodulator is depends on the nature of the signal (i.e., analog or digital) and the modulation format by the lightwave system. Most widely and practical systems employ a digital binary scheme referred to as intensity modulation with direct detection (IM-DD) [54][43], see Fig. 2.7. Prior to the information is recovered, post detection processor is used where the necessary filtering and signal processing is done to guarantee a high-fidelity data are carried out.

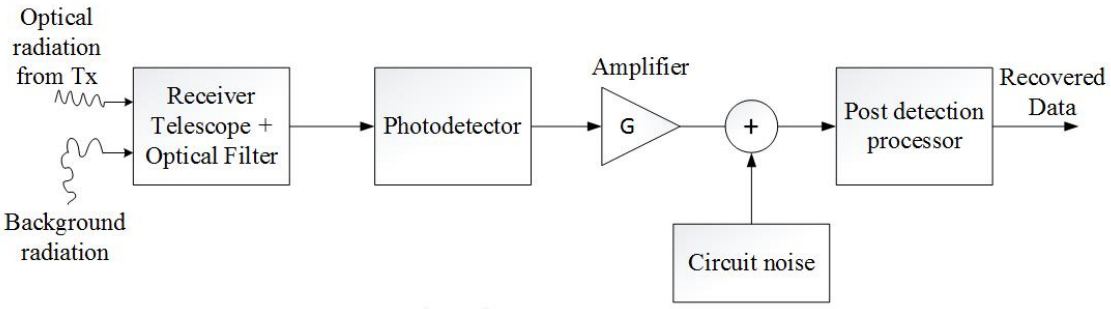

Fig. 2.7: Block diagram of direct detection optical Rx.

2.4 FSO Advantages and Applications

Complementing the existing wireless RF solutions, FSO has been considered a viable, affordable, and attractive high data rates technology and is poised to become a promising candidate for the next generation broadband communications to resolve the existing 'last mile' and 'last-leg' access network problem [55], [56]. This is mainly due to the vastly attractive features of FSO technology including virtually unlimited bandwidth to support high speed applications, better energy efficiency with low power consumption, no electromagnetic interference and fading immunity, no licensing requirement, high scalability and re-configurability, high degree of security against eavesdropping, and cost-effective in terms of price per bit [9], [55], [57]. Furthermore, the fact that FSO is transparent to traffic type and data protocol makes its integration into the existing access network far more rapid, reliable, and profitable way in comparison the traditional fiber communications. With these advantages, together with rapid development and maturity in the optoelectronics devices, FSO has now witnessed a restore in many major applications which include:

i) Metro Access Networks/ Last Mile Connectivity - FSO can be extended to the existing metropolitan area fiber rings with FSO access to the customers to complete synchronous optical network (SONET) rings in the

carrier core infrastructure and to bypass local loop systems to provide environment with high speed connections.

ii) Enterprise/ LAN connectivity - In this application, state-of-the-art FSO system support 10 Gbps Ethernet, which equals the bandwidth provided by metro fiber optics systems and significantly higher than the 1.25 Gbps Ethernet provided by competing RF wireless systems that operate in the 60 GHz frequency range, which is suitable for offices, financial institution networks, healthcare campus networks, and government agencies [58]

iii) Ultra-long-haul systems - Numerous ultra-long-haul outdoor optical wireless systems have been deployed in a wide range of applications including earth-to-satellite and satellite-to-earth, earth-to-high altitude platform, intersatellite, and interplanetary communication links [59]–[62]. Major technical advances in the field of adaptive optics and beam acquisition/tracking, which are the critical and importance functions in ultra-long-haul outdoor FSO links have enabled the deployment of tractable broadband outdoor optical wireless communications systems. FSO satellite network can provide a high-bandwidth optical wireless network access to the end users since the satellites can cover large areas on the earth.

iv) Underwater FSO communication networks - Is suitable for various applications like undersea explorations, environmental monitoring, disaster prevention, distributed tactical surveillance (unmanned underwater vehicles (UUVs)), and underwater sensors to monitor the surveillance, targeting, and intrusion detection [5]. FSO can provide broadband communication for underwater wireless sensor networks (WSN) such as to transmit video streams or downloads a large burst of

stored data in a brief time slot. This is very crucial when the data is required from a specific location or within a short polling time slot.

v) Backup and disaster recovery - Disaster recovery is a specialized application used to provide backup systems for mission-critical connectivity. The reliability and adjustability of the equipment makes the FSO systems are easy to be mounted on rooftops, lampposts, billboards, bridges, and even inside office window. A tragic example of the deployment efficiency was witnessed following the September 11th attacks. Communication with the disaster area was operational within hours, aiding in the recovery work itself and regaining connectivity with many of the business and companies hit by devastation [63]. Other than that, the technology finds application where temporary link is needed, be it for a conference or ad-hoc connectivity in the event of a collapse of an existing communication network.

2.5 Factor Affecting FSO Communication Systems

The terrestrial FSO laser beam particularly operates in troposphere layer in which the medium is continuously changes in chemical composition, humidity, pressure, temperature, and air movements. Due to that, the FSO link performance is aggravated by the atmospheric phenomena, which are highly variable and unpredictable, such as fog, smoke, clouds, snow, turbulence, and smog, thus resulting in significant optical power attenuation, waveform distortion, beam spreading, phase wandering, and link distance reduction due to scattering and absorption [64]. With conditions of the earth's atmosphere, only a few atmospheric windows are suitable for FSO due to selective absorption by gases and water vapour [9]. The interaction with solid and liquid water

particles in adverse weather can also generates signal fades which can lead to link outage [65]. Moreover, even in clear sky conditions, the turbulence induced by temperature and pressure gradients results into random fluctuations and loss of wave-front coherence [11]. Thus, with these channel imposed constraints, it is very challenging to attain up to 99.999% link availability [7]. The following subsections will discuss laser beam attenuation due to absorption and scattering while the turbulence induced effects will be in-depth elaborated in next section.

2.5.1 Atmospheric attenuation

The degrading effects in wireless optical channel can be classified as large-scale (long term) impairments including path loss, shadowing and small-scale (long term) impairments which is commonly referred as fading [66]. The large-scale impairment is usually used to predict the transmission coverage area and average signal power at the Rx side. While the latter impairment is mainly due to atmospheric channel effects and multi-path propagation which can cause ransom fluctuations in the received signal level and affects the instantaneous SNR. The small-scale fading, known as atmospheric attenuation can be classified into molecular absorption and scattering. This occurs due to the interaction with aerosol particles of different type composition within the earth's atmosphere, which include carbon dioxide (CO_2), oxygen (O_2), nitrogen (N_2), water vapour (H_2O), methane (CH_4), ozone (O_3), and other small particles generated by combustion, dust, debris, and soil [67]. Scattering processes imply a deviation from the original propagation path, whereas absorption means annihilation [9].

2.5.1.1 Absorption

Absorption results from the interaction between the photons and atoms or molecules that leads to the extinction of the incident photons, elevation of the

temperature, and radiative emission [68]. In other words, absorption exterminated photons, resulting in decreased laser beam power. Some of the photons are extinguished and their energies converted into heat [53]. The absorption coefficient depends very much on the type of gas molecules and concentration [69]. Molecular absorption is a selective phenomenon which results in the spectral transmission of the atmosphere presenting transparent zones referred to atmospheric transmission windows (also called transmittance) [70]. Among the optical bands free from absorption are the visible window (0.400-0.700 μm), the first optical window (0.785-0.850 μm), the third optical window (centered at 1.55 μm), and a few mid-infrared (IR) windows up to the 10.6 μm window. Practically, gas absorption has little impact on terrestrial link in the near-IR windows, resulting in the attenuation coefficient being dominated by scattering [64].

2.5.1.2 Scattering

Scattering causes redirection of energy by particles along the propagation path with and without wavelength modification which results from the interaction of light with atmospheric particles [43]. The type of scattering is determined by the radius, *r* of the particular atmospheric particle with respect to the transmission laser wavelength. One way of describing this is by the characteristic size parameter, x_o given by:

$$x_o = \frac{2\pi r}{\lambda}, \tag{2.8}$$

where λ is the wavelength. If $x_o \ll 1$, where the atmospheric particles sizes are smaller than wavelength of incident light or 1, is classified as Rayleigh scattering, which is mainly contributed by air molecules and haze particles. If $x_o \approx 1$ or the particles comparable in size as wavelength of incident light, then it is Mie scattering [68]; in which this scattering effect is concentrated in the forward direction. Aerosols and microscopic water particles are predominant components of Mie scattering at λ=1550 nm and 850 nm such as mist,

fog, and haze. Aerosols can be defined as fine solids or liquids particles suspended in the atmosphere with very low fall speed. When the atmospheric particles are much larger than the laser wavelength, then it is non-selective or geometrical scattering or $x_o \gg 1$. Non-selective refers to the fact that scattering is independent of wavelength. The particles that are classified under geometrical scattering are rain drops, snow, hail, and cloud droplets. Table 2.1 presents the typical atmospheric scattering particles with their radii and their classification done by [71].

Table 2.1: Typical atmospheric scattering particles with their radii and scattering process at λ=850 nm [71].

Type	**Radius (μm)**	**Size parameter, x_o**	**Scattering process**
Air molecules	0.0001	0.00074	Rayleigh
Haze particles	0.01-1	0.074-7.4	Rayleigh-Mie
Fog droplet	1-20	7.4-147.8	Mie-Geometrical
Rain	100-10000	740-74000	Geometrical
Snow	1000-5000	7400-37000	Geometrical
Hail	5000-50000	37000-370000	Geometrical

A large number of theoretical and experiments research works have been carried out to investigate the atmospheric attenuation effects on FSO communications links. Based on the researches done, it can be concluded that fog droplets is the most destructive factor to FSO links where the attenuation can be over 300 dB/km in dense maritime fog condition and up to 130 dB/km in moderate continental fog conditions [72]. Furthermore, [73] reported that in foggy weather conditions where visibility is less than 500 m, the attenuation is independent of wavelength either using 785 nm, 850 nm, or 1550 nm where all attenuated equally. There is slight increase in attenuation in fog at 1550 nm compared to 785 nm, but the effect is small and negligible. For a terrestrial FSO link, the received irradiance at a link distance from the Tx is related to the transmitted irradiance by Beer-Lambert's law as [74]:

$$\mathbb{T} = \frac{P_{ro}}{P_t} = e^{-\beta_v s}, \tag{2.9}$$

where $\mathbb{T}$ is the transmittance, β_v represents the total attenuation/extinction coefficient of the atmosphere at wavelength λ and P_o is the received optical power. β_v comprises the aerosol scattering, aerosol absorption, molecular scattering, and molecular absorption. The molecular/Mie scattering will be described based on empirical formulae expressed in term of visibility range V in km. Visibility can be defined as maximum distance that the visible 550 nm can travel while distinguishing between the target object and its background at 2% contrast [75]. For clear and foggy weather conditions, the attenuation coefficient can be determined from the visibility data through Kim's model as [73]:

$$\delta = \frac{3.91}{V}\left(\frac{\lambda}{550}\right)^{-q}, \tag{2.10}$$

where q being the particle size distribution coefficient, which is defined as:

$$q = \begin{cases} 1.6 & V > 50 \text{ km} \\ 1.3 & 6 \text{ km} < V < 50 \text{ km} \\ 0.16V + 0.34 & 1 \text{ km} < V < 6 \text{ km} \\ V - 0.5 & 0.5 \text{ km} < V < 1 \text{ km} \\ 0 & V < 0.5 \text{ km}. \end{cases} \tag{2.11}$$

2.5.2 Atmospheric turbulence

The atmospheric turbulence fading is one of the main challenges in FSO systems, is the result of in-homogeneities in the temperature and pressure of the atmosphere, which leads to refractive index variations along the propagation path [7]. Turbulence can be considered to consists of eddies with different sizes and strengths. Each eddy has different characteristics in terms of size (diameters), velocity and timescale. The large eddies are unstable and will break up and transferring the energy to smaller eddies. This break-up process, which is known as turbulence energy cascade is continuously occurs until the smallest eddies is stable, and molecular viscosity is effective in dissipating the kinetic

energy into heat, illustrated in Fig. 2.8. The most widely accepted theory of turbulence is Kolmogorov's theory [76]. According to the first Kolmogorov's hypothesis, which is for statistically homogeneous and isotropic turbulence, the turbulence kinetic energy is the same everywhere and the turbulence eddies are also having the same behaviour in all directions. It means, energy is transferred from larger turbulence eddies (characterized by the outer scale parameter L_0) to smaller eddies (characterized by the inner scale l_0) without loss. However, the refractive index of each turbulence eddies are randomly varies from each other, which cause amplitude and phase variations to the wavefront [6]. Ultimately, this phenomenon induces intensity fluctuations of the received optical wave-front as a result of several numbers channel effects including scintillation, beam wandering, image dancing, beam spread, and spatial coherence degradation [5], that limit the performance of FSO communication link. Turbulence also can ultimately result in optical power dropping below the Rx threshold level, thus leading to performance deterioration or even a total link failure [18], [77], [78].

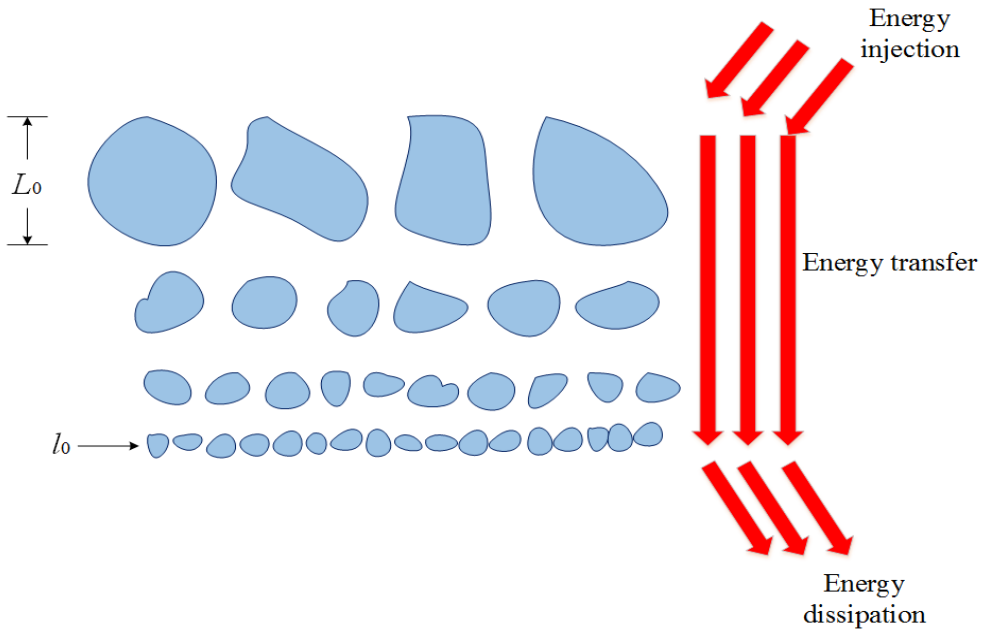

Fig. 2.8: Illustration of the Kolmogorov energy cascade theory of turbulence.

Considering the homogeneous and isotropy turbulence, the turbulence strength can be measured using the refractive index structure parameter C_n^2 (in unit $m^{-2/3}$) given as [11]:

$$C_n^2 = (86\times10^{-16}\frac{P}{T^2})^2 C_T^2, \tag{2.12}$$

where P is atmospheric pressure in millibar and T is the absolute temperature in Kelvin. C_n^2 values typically range from 10^{-17} $m^{-2/3}$ for weak turbulence scenarios and up to 10^{-13} $m^{-2/3}$ in the case of strong turbulence, and essentially C_n^2 is constant for horizontal paths over short time intervals [6]. The temperature structure constant C_T^2 is related to the universal 2/3 power law of temperature and can be calculated as [11]:

$$\begin{aligned} D_T &= \langle (T_1 - T_2)^2 \rangle \\ &= \begin{cases} C_T^2 l_0^{-\frac{4}{3}} L_p^2 & \text{for } 0 \ll L_p \ll l_0 \\ C_T^2 L_p^2 & \text{for } l_0 \ll L_p \ll L_0 \end{cases}, \end{aligned} \tag{2.13}$$

where T_1 and T_2 are the temperature at two points separated by the propagation distance L_p.

The scintillation index [79] presents a viable statistical quantitative measure of the magnitude of atmospheric turbulence-induced irradiance fluctuations (i.e., the level of scintillations) given by [76]:

$$\sigma_I^2 = \frac{\langle I^2 \rangle - \langle I \rangle^2}{\langle I \rangle^2} = \frac{\langle I^2 \rangle}{\langle I \rangle^2} - 1, \tag{2.14}$$

where I is the irradiance of the optical laser beam, and $\langle \cdot \rangle$ denotes the ensemble averaging, equivalent to long-time averaging with the assumption of an ergodic process. Another important parameter that is commonly used to characterize the turbulence induced irradiance fluctuations of over a path of length L is unitless Rytov variance σ_R^2 given by [11]:

$$\sigma_R^2 = 1.23 C_n^2 k^{7/6} L^{11/6}, \tag{2.15}$$

where $k = \frac{2\pi}{\lambda}$ is the wave number with λ being the laser wavelength. σ_R^2 distinguishes the classifications of the turbulence defined as:

$\sigma_R^2 < 1$ for weak turbulence

σ_R^2 ~1 for moderate turbulence

$\sigma_R^2 > 1$ for strong turbulence

$\sigma_R^2 \rightarrow \infty$ for saturation regime.

2.5.2.1 Log-normal distribution

Log-normal distribution has gained considerable attention in the literature to describe weak turbulence because of its mathematical convenient and simplicity. According to [52], the turbulence is considered weak when Rytov variance is less than 0.3. The turbulence effect can be characterized by the variance σ_χ^2, often referred as Rytov parameter. For horizontal propagation with uniform C_n^2 profile, σ_χ^2 can be calculated as [80]:

$$\sigma_\chi^2 = 0.30545\, C_n^2 (2\pi/\lambda)^{7/6} L^{11/6}. \tag{2.16}$$

In the weak turbulence regime, the normalized intensity variance [var/mean^2] or scintillation index is approximately four times the log-amplitude variance or [52]:

$$\sigma_I^2 = \exp(4\sigma_\chi^2) \cong 4\sigma_\chi^2, \tag{2.17}$$

where $A = \exp[\chi]$ is the amplitude, χ is the Gaussian distributed field log-amplitude fluctuation and $I_t = |A(r)|^2$ is the intensity (field irradiance) in the turbulence medium. Given the intensity in no turbulence medium as $I_o = |A_0(r)|^2$, the log-intensity is then expressed by [7]:

$$I_{log} = log_e \left| \frac{A\,(r)}{A_0(r)} \right|^2 = 2\chi. \tag{2.18}$$

Hence,

$$I_t = I_0 \exp(I_{log}). \tag{2.19}$$

As light propagates through a large number of elements within the atmosphere, each element induces independently random scattering and phase delay to the optical beam. Thus, the log-normal probability density function (PDF) of the received irradiance *I* due to the turbulence is derived by [76]:

$$p_{LN}(I) = \frac{1}{I\sqrt{2\pi\sigma_x^2}} exp\left[\frac{\left(\ln(I/I_o) - {\sigma_I^2}/{2}\right)^2}{2\sigma_I^2}\right], \tag{2.20}$$

where I_o is the irradiance at the Tx with no turbulence. After obtaining the pdf of the irradiance fluctuations, it is also necessary to derive an expression for the variance of the irradiance σ_I^2, which characterizes the strength of irradiance fluctuation, given as:

$$\sigma_I^2 = I_0^2[\exp(\sigma_l^2) - 1]. \tag{2.21}$$

Then, the normalized variance of intensity, which is often referred to as the scintillation index (S.I.) is thus:

$$S.I. = \sigma_N^2 = \frac{\sigma_I^2}{I_0^2} = \exp(\sigma_I^2) - 1. \tag{2.22}$$

Fig. 2.9 demonstrates the log-normal PDF for a range of log-irradiance variance σ_I^2 using (2.20). Note that, as the value of σ_I^2 increases, the distribution becomes more skewed with longer tails towards the infinity. This describes the extent of intensity fluctuations as the channel inhomogeneity increases due to the atmospheric turbulence.

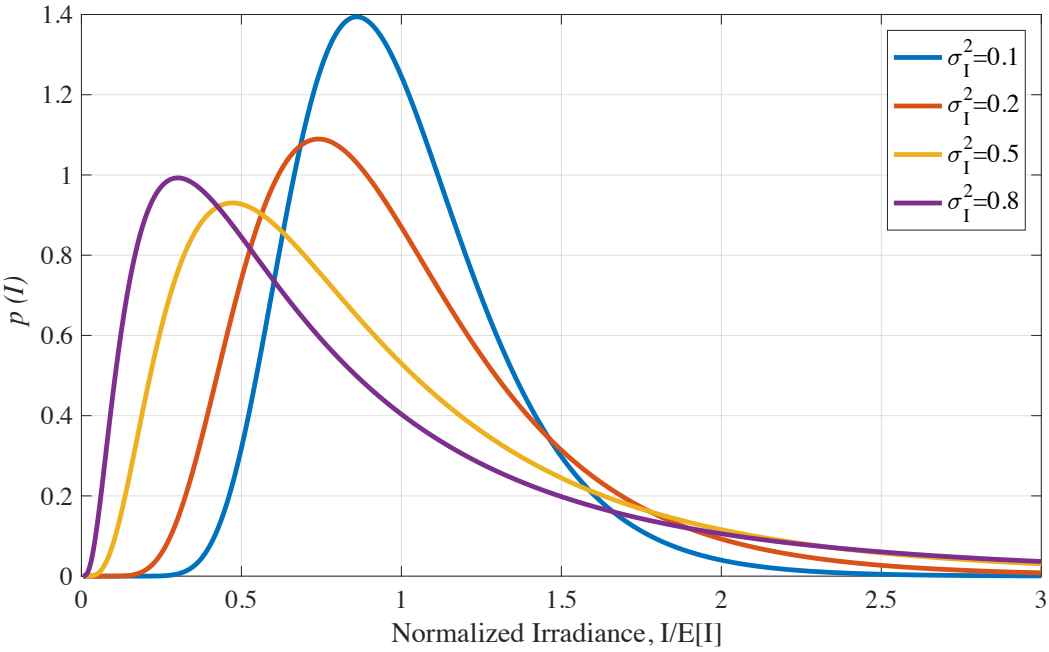

Fig. 2.9: Log-normal PDF against normalized irradiance for different values of log irradiance σ_I^2.

Nevertheless, log-normal underestimates the peak irradiance of the PDF and the behaviour in the distribution tails, particularly with increasing turbulence strength, which affect the accuracy of statistical analysis such as detection and fade probabilities arrived. Another shortcoming of log-normal distribution is that Rytov variance will not be able to account for multiple scattering caused by turbulence eddies for long distance transmission links [81]. Hence, this work will implement another distribution of turbulence which is called as Gamma-Gamma turbulence model. Gamma-Gamma distribution has been widely adopted to describe accurately the turbulence statistics for all atmospheric turbulence regimes (from weak to strong) [82], [83], discussed further in next section.

2.5.2.2 Gamma-Gamma distribution

The Gamma-Gamma distribution has evolved based on the modulation process where the fluctuation of light radiation traversing a turbulence atmosphere is comprised of small-scale (scattering) and large-scale (refraction) effects, proposed by Andrews et

al. [11], [84]. Gamma-Gamma has been shown to describe accurately the turbulence statistics within all conditions of turbulence, from weak to strong regimes. [85], [86] had accurately modelled weak turbulence using Gamma-Gamma distribution function and have showed a good agreement between simulation and experimental results, which has been done under a controlled indoor environment. Therefore, Gamma-Gamma model is more appropriate model to describe the turbulence irradiance covering weak to strong regimes.

Consequently, the heuristic model treats the irradiance *I* of the received optical wave as a product of statistically independent random processes I_x and I_y:

$$I = I_x I_y, \tag{2.23}$$

where I_x and I_y arise from the large-scale and small-scale turbulence eddies, respectively. Their pdfs are thus given as:

$$p(I_x) = \frac{\alpha(\alpha I_x)^{\alpha-1}}{\Gamma(\alpha)} \exp(-\alpha I_x) \qquad I_x > 0; \quad \alpha > 0, \tag{2.24}$$

$$p(I_y) = \frac{\beta(\beta I_y)^{\beta-1}}{\Gamma(\beta)} \exp(-\beta I_y) \qquad I_y > 0; \quad \beta > 0. \tag{2.25}$$

By fixing I_x and using the change of variable, $I_y = I/I_x$, the conditional pdf given by (2.27) is obtained in which I_x is the (conditional) mean value of *I* as:

$$p(I/I_x) = \frac{\beta(\beta I/I_x)^{\beta-1}}{I_x \Gamma(\beta)} \exp(\frac{-\beta I}{I_x}) \qquad I > 0. \tag{2.26}$$

To obtain the unconditional irradiance distribution, the conditional probability $p(I/I_x)$ is averaged over the statistical distribution of I_x given by (2.24) to obtain the following Gamma-Gamma irradiance distribution function, which can be expressed as:

$$p(I) = \int_0^{\infty} p\left(I/I_x\right) p(I_x)\, dI_x = \frac{2(\alpha\beta)^{\frac{\alpha+\beta}{2}}}{\Gamma(\alpha)\Gamma(\beta)} I^{\left(\frac{\alpha+\beta}{2}\right)-1} K_{\alpha-\beta}\left(2\sqrt{\alpha\beta I}\right). \tag{2.27}$$

where $\Gamma(.)$ and $K_{\alpha-\beta}(.)$ denote the Gamma function and the modified function of the 2nd kind of order (α-β), respectively. α and β represent the effective numbers of large-scale and small-scale eddies of the scattering process, respectively. For the case of plane wave propagation through homogeneous and isotropic atmopsheric turbulence, we have [11]:

$$\alpha = \left[\exp\left(\frac{(0.49\sigma_I^2)}{\left(1 + 1.11\sigma_I^{12/5}\right)^{7/6}}\right) - 1\right]^{-1}, \tag{2.28}$$

$$\beta = \left[\exp\left(\frac{(0.51\sigma_I^2)}{\left(1 + 0.69\sigma_I^{12/5}\right)^{5/6}}\right) - 1\right]^{-1}. \tag{2.29}$$

While the *S.I.* is given by:

$$\sigma_I^2 = \exp\left[\frac{0.49\sigma_I^2}{(1 + 1.11\sigma_I^{12/5})^{7/6}} + \frac{0.51\sigma_I^2}{(1 + 0.69\sigma_I^{12/5})^{5/6}}\right] - 1. \tag{2.30}$$

Fig. 2.10 presents σ_I^2, α, and β as a function of Rytov variance for weak, moderate and strong turbulence regimes and for L_p of 100 m and λ of 1550 nm, compatible for a short communication link for last mile access network. From the figure we can notice that, σ_I^2 increases with σ_R^2 reaching the saturation level at σ_R^2 of ~4.5, wheras α decreases in weak turbulence reaching a minimum level at σ_R^2 of ~2.5 and then increasing with $\sigma_R^2 > 2.5$. Whereas, β exponentially decreases with σ_R^2 reaching a minimum value determined by the transverse spatial coherence radius of the optical wave [7]. While using Eq. (2.27), we plotted Fig. 2.11 for three diferrent turbulence regimes with weak (α=20.8, β=18.36), moderate (α=11.6, β=10.1), and strong (α=4.84, β=3.13). The plots show that as the

turbulence increases from weak to strong regime, the distribution spread out, with an increase in the range of possible values of the irradiance.

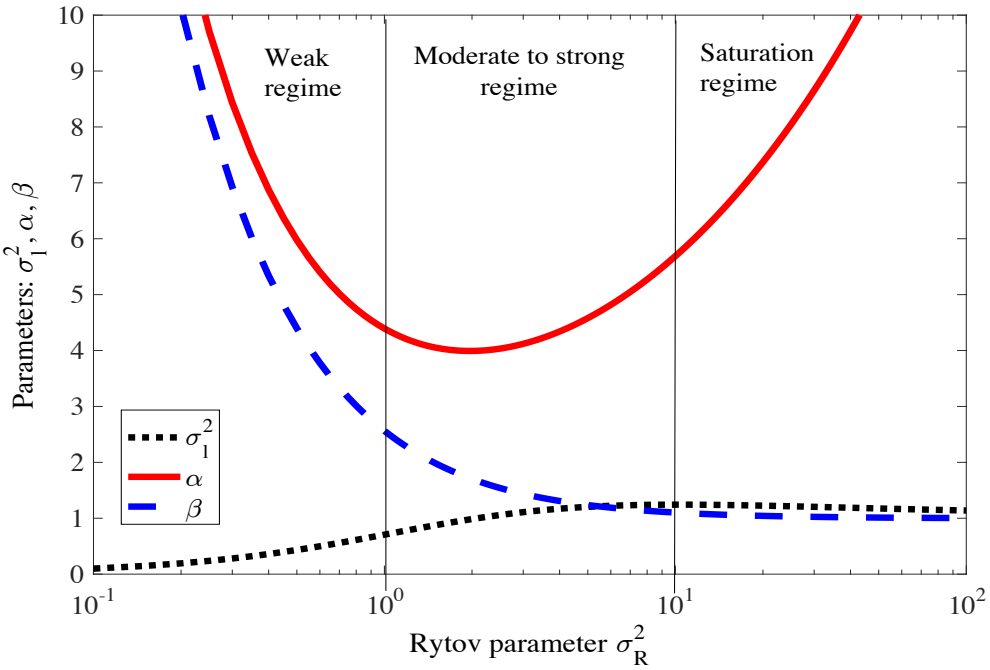

Fig. 2.10: Values of σ_I^2, α, and β under different turbulence regimes: weak, moderate to strong, and saturation.

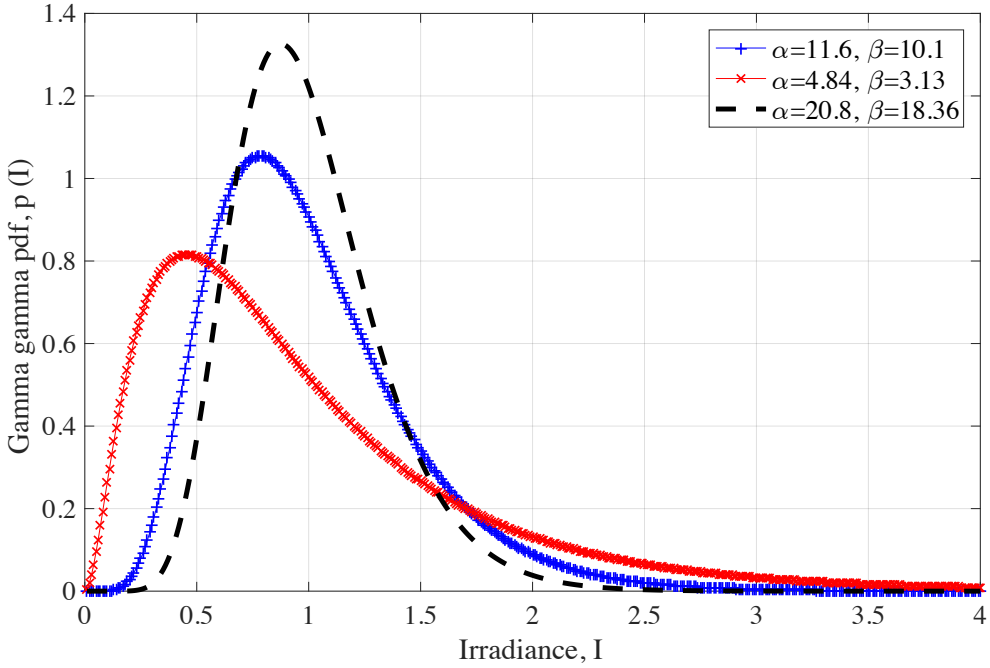

Fig. 2.11: Gamma-gamma PDF for three different turbulence regimes namely weak (α=20.8, β=18.36), moderate (α=11.6, β=10.1), and strong (α=4.84, β=3.13).

2.6 Performance Evaluation

In almost every area of measurements, the ultimate objective is to measure the performance of the signal at the Rx end in the presence of loss. The goal of laser communication systems is to transmit a maximum number per bit per second over the maximum possible range with the fewest errors. In this work, three key elements of performance indicators will be employed throughout the studies which are SNR, BER, and the eye diagrams in order to present a comprehensive performance evaluation of the FSO relaying systems.

2.6.1 Signal-to-noise ratio (SNR)

SNR is the most common and well-understood qualitative measurement performance. The variations in the received optical signal caused by the atmospheric turbulence determine the received fluctuating SNR. The system performance characterized by the BER is therefore affected by the random loss of SNR. SNR also depends on the noise contributed from all possible sources which include shot noise, dark current noise, thermal noise, and the background noise. Assuming Gaussian distribution of noise, SNR at the output of PD in the absence of turbulence is given by [48]:

$$SNR_0 = \frac{P_S}{\sqrt{\left(\frac{2\mathfrak{H}vB}{\eta}\right)(P_S + n) + \left(\frac{\mathfrak{H}v}{\eta e}\right)^2 \left(\frac{4KT_N B}{\mathcal{R}}\right)}}, \tag{2.31}$$

where P_S is the Tx output power (in watts), n is the background noise (in watts), η is the detector quantum efficiency, e is the electronic charge (in Coulombs), $\mathfrak{H}$ is the Planck's constant, v is the optical frequency (in Hertz), K is the Boltzmann constant, B is the bandwidth of the detector filter, T_N is the effective noise temperature, and

$\mathcal{R}$ is the effective input resistance to the amplifier of the detector. For shot noise limited operation, the background noise and the thermal nose can be ignored.

In the presence of turbulence, the SNR is a fluctuating term (i.e. instantaneous value) and usually the mean (average) value is taken. The mean SNR with *S.I.* of σ_I^2 can be expressed as [48]:

$$\langle SNR \rangle = \frac{SNR_0}{\frac{P_{S0}}{\langle P_S \rangle} + \sigma_I^2 SNR_0^2}, \tag{2.32}$$

where P_{S0} is the signal power in the absence of atmospheric effects and $\langle P_S \rangle$ is the mean of instantaneous input signal power P_S.

2.6.2 Bit error rate (BER)

Assuming the Gaussian distribution for the total noise contribution as well as signal plus noise, the BER in absence of turbulence, BER_0 is given by:

$$BER_0 = \frac{1}{2}\left(\frac{SNR_0}{2\sqrt{2}}\right). \tag{2.34}$$

In the presence of turbulence, the BER is given by [5], [87]:

$$BER = \frac{1}{2}\int_0^\infty p_I(s)\, erfc\left(\frac{\langle SNR \rangle s}{2\sqrt{2}\langle i_s \rangle}\right) ds, \tag{2.35}$$

where $erfc(\cdot)$ is complementary error function, $p_I(s)$ is the probability distribution of irradiance, i_s is the instantaneous signal current whose mean value is given by $\langle i_s \rangle = \eta e \langle P_s \rangle / h\nu$, $\langle P_s \rangle$ is the mean signal power, and $\langle SNR \rangle$ is the mean SNR in presence of turbulence defined earlier.

Another method calculating BER is using Gaussian-Q function, $Q(\cdot)$ in a function of channel state h_c, given by:

$$P(1|0, h_c) = P(0|1, h_c) = Q\left(\sqrt{SNR\ (h_c)}\right), \tag{2.36}$$

where $Q(\cdot)$ can be calculates as [88]:

$$Q(y) = \frac{1}{\sqrt{2\pi}} \int_{y}^{\infty} \exp\left(\frac{-t^2}{2}\right) dt. \tag{2.37}$$

Considering the symmetry of the problem defined earlier on with $P(0) = P(1) = 0.5$ and $P(1|0) = P(0|1)$, the average BER can be determined by averaging over the PDF of h as [88]:

$$P_e = \int_{0}^{\infty} f_h(h) Q\left(\sqrt{SNR(h)}\right) dh. \tag{2.38}$$

The various form of probability distribution can be modeled depending on the level of turbulence and the communications link scenario. In Chapter 4, we will derive end-to-end BER for triple-hop all-optical FSO relaying system under gamma-gamma probability distributions.

2.6.3 Eye diagram

An alternative approach used to evaluate the quality of high-speed digital signals is eye diagram. The eye diagram is a useful tool for accessing the distortion of a digital signal and allows key parameters of the signal to be visualized and determined. The eye diagram is captured using an oscilloscope, by overlaying sweeps of different segments of a long data stream to each individual bit into a single graph with signal amplitude on the vertical axis and time on horizontal axis [3]. By repeating this construction over many samples of the waveform, the resultant graph will represent the average statistics of the signal and will resemble an eye. Fig. 2.12 illustrates some of the typical measurements that can be performed on the eye diagram. The one level and zero level shows the mean value of logic one and logic zero respectively, while the eye amplitude is the difference between the one and zero levels. Eye height and eye width are the measure of the vertical and horizontal opening of an eye diagram correspondingly. The bit period is a measure of horizontal opening of an eye diagram at the crossing points of the eye is usually

measured in picoseconds for a high speed digital signal. The data rate is the inverse of bit period (1/bit period). Eye crossing percentage gives an indication of duty cycle distortion of pulse symmetry problems in the high-speed data signal. Rise time and fall time are the measure of the mean transition time of the data on the upward and downward slope of an eye diagram respectively. Last but not least, jitter is the time deviation from the ideal timing of a data-bit event [89].

In addition, the Q-factor is one of the alternative indicator to quantify the performance of the system using [77]:

$$Q = \frac{V_H - V_L}{\sigma_H - \sigma_L}. \tag{2.39}$$

where V_H and V_L are the mean received voltages and σ_H and σ_L are the standard deviations for the 'high' and 'low' level signal, respectively.

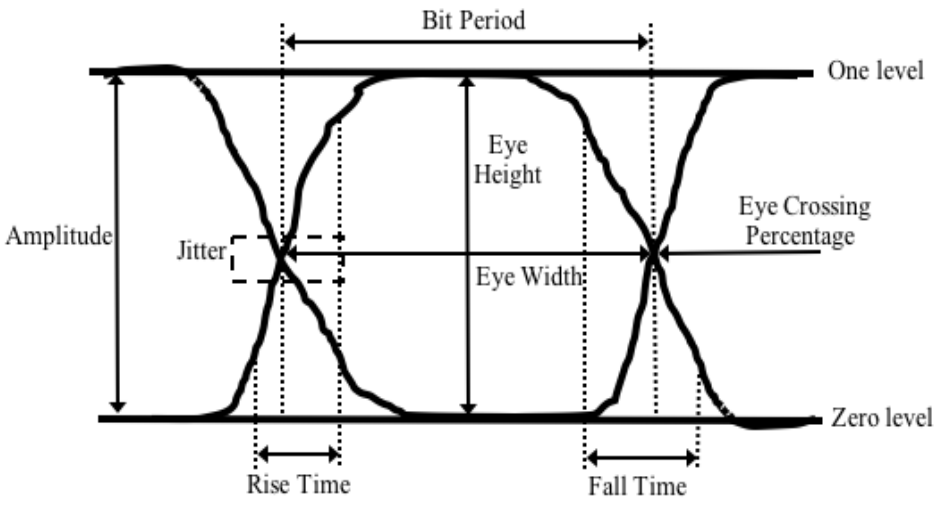

Fig. 2.12: Typical eye diagram measurements.

2.7 Summary

This chapter outlined the literature review on FSO communication systems. The optical networks and FSO networks topology has been presented to extend the capability of the traditional PtP FSO technology, which also necessary to realize the main potential of FSO systems to solve the capacity bottleneck issue. The fundamentals of FSO communication systems is discussed, which encompasses the optical Tx and Rx, the simplest and widely used OOK modulation signalling scheme, and the suitable FSO wavelength that can be selected based on the application and equipment suitability. Next, the features of FSO technology that makes it more viable compared with other existing RF and its potential areas of application were also explained. Also, the main challenges and deteriorate effects of FSO communication link have been discussed in-depth, which include molecular scattering, molecular absorption, and turbulence-induced effects. The log-normal and Gamma-Gamma probability distribution functions characteristics and analytical approach were explained in details here. Nonetheless, Gamma-Gamma distribution is used in the subsequent analyses since it describes all turbulence regimes from weak to strong. In addition, using log-normal distribution, Rytov variance is not able to account for multiple scattering caused by turbulence eddies for long distance transmission links. Finally, the FSO performance metrics of SNR, BER, and eye diagrams were highlighted in quantify the link efficiency.

Chapter 3

FADING MITIGATION TECHNIQUES IN FSO SYSTEMS

3.1 Introduction

In order to design a reliable FSO system with maximum link availability and data throughput over the adverse atmospheric conditions, a number of channel enhancement approaches including aperture averaging [30], [33], [90], adaptive optics [26], [27], [91], error control coding [25], [92], complex modulation technique [23], [93]–[95], spatial diversity [28], [34], [96], and hybrid RF-FSO [20], [97] have been reported. Error control coding techniques such as convolution coding with hard Viterbi coding [98], turbo coding [24], [99], and low-density parity codes (LDPC) [100] are the most widely adopted, which offer good resistance to burst errors in fading channels. However, error control coding often imposes long delay latencies, efficiency degradation (due to the number of redundant bits required) and necessitates the use of large memories for storing long data frames [30]. Aperture averaging is the simplest technique to implement, where by using a Rx aperture larger than the fading correlation length, intensity fluctuations can be averaged out over the aperture area. The spatial diversity scheme is a more efficient method in reducing the fading effects by employing sufficiently spaced multiple Txs/Rxs especially under strong turbulence conditions and over a long transmission span [30]. Recently, relay-assisted or multi-hop transmission systems have been introduced as a

powerful fading mitigation tool as an alternate option in realizing the spatial diversity scheme advantages [101].

In this chapter, a thorough review of the relevant literatures pertaining to the investigation studies of all-optical FSO relaying techniques are presented. The basic concepts of aperture averaging and spatial diversity are explained in Sections 3.2 and 3.3, respectively. Subsequently, the main concept of this research work is highlighted in Section 3.4, where the principle of relay-assisted FSO communication systems, the configurations of relaying systems, and the concept of all-optical FSO relay-based systems are discussed. Two approaches of all-optical FSO relaying systems are chosen to be investigated in this research and the associated devices and principles are discussed in Sections 3.5 and Section 3.6. In Section 3.5, the AOAF model is explained, which enlighten the fundamental theory of optical amplifiers specifically erbium-doped fiber amplifier (EDFA) and semiconductor optical amplifier (SOA). Section 3.6 explores another approach of an all-optical FSO system named AORF. The comprehensive theory of the system is discussed, which involves the nonlinear effects in optical fibers (Sections 3.6.1) and the concept of SPM based regenerator (Sections 3.6.2). Also highlighted are the fundamental concepts behind highly nonlinear fibers (HNLF) (Sections 3.6.3) and tunable mode-locked lasers (Sections 3.6.4), both of which will be used in the SPM-based regenerator. Finally, concluding remarks are underlined in Section 3.7.

3.2 Aperture Averaging

After an optical beam propagates a sufficiently long path over an atmospheric turbulence channel, the received beams at the Rx tend to break up into regions of high and low intensity, which leads to significant signal fades. In order to improve the signal quality, the size of the Rx can be correspondingly increased to cover the area of the high

and low intensities, which acts to average these signal fluctuations over the aperture area [33]. This phenomenon is known as the aperture averaging effect and is intentionally utilized in direct detection systems [5]. The coherence length ρ_o is a particularly useful parameter in determining the size of the Rx aperture needed to collect the bulk of the propagating field and to determine the separation distance of detectors in multiple Rx based systems [90]. The fading effect can be reduced significantly if the Rx aperture $A_{rx} > \rho_o$. This technique is one of the simplest techniques to enhance the system performance through the reduction of scintillation [33], whereby the fast fluctuations caused by the small-scale eddies (i.e., the adverse effects of scintillation) are averaged out and thus the frequency content of the irradiance spectrum is shifted towards lower frequencies [11], [102]. Hence, the remaining scintillation measured at the Rx is produced by the eddies whose size is larger than the aperture. The parameter that is usually used to quantify the fading reduction by aperture averaging is the aperture averaging factor, which is defined as [11]:

$$AF = \frac{\sigma_I^2(\varnothing)}{\sigma_I^2(0)}, \tag{3.1}$$

where $\sigma_i^2(\varnothing)$ and $\sigma_I^2(0)$ denote the scintillation index for a Rx lens of diameter $\varnothing$ and a "point Rx" ($\varnothing \approx 0$), respectively.

For the case of a plane wave propagation with zero inner scale of turbulence ($l_0 = 0$) and infinite outer scale of turbulence ($L_0 = \infty$), the aperture averaged scintillation index is given by [11]:

$$\sigma_{i,\mathrm{pl}}^2(\varnothing) = \exp\left[\left(\frac{(0.49\sigma_R^2)}{\left(1+0.65d^2+1.11\sigma_R^{\frac{12}{5}}\right)^{\frac{7}{6}}}\right)+\left(\frac{0.51\sigma_R^2(1+0.69\,\sigma_R^{\frac{12}{5}})^{-\frac{5}{6}}}{1+0.90d^2+0.62d^2\sigma_R^{\frac{12}{5}}}\right)\right]^{-1} - 1, \tag{3.2}$$

where $d = \sqrt{k\varnothing^2/4L}$ is the scaled aperture size and the subscript pl denotes the assumption of plane-wave propagation.

Although the aperture averaging mechanism is a simple and reliable to be practically implemented, the Rx aperture needs to be far greater than the spatial coherence distance of the atmospheric turbulence in order to receive several uncorrelated signals. This condition is not always achievable in FSO as the spatial coherence distance is in the order of centimetres. In addition, a wide aperture also leads to more background radiation and, as such, more noise will be captured. Hence, an alternative way needs to be adopted to enhance the overall system performance and mitigate the aforementioned limitations.

3.3 Spatial Diversity

Spatial diversity, also known as the diversity technique in the RF technology, is an alternative and efficient method to reduce the turbulence-induced fading effects. This technique has been demonstrated to provide substantial link performance improvement in spatially uncorrelated channels by employing multiple apertures at the Tx and/or the Rx that are sufficiently spaced as in single-input multiple-output (SIMO), multiple-input single-output (MISO) or multiple-input multiple-output (MIMO) systems [96]. The Rx collects the received optical beams from different spatial angles, so that the effective level of scintillation and probability of fade can be reduced [34]. Ultimately, the inherent redundancy of spatial diversity has the potential to significantly enhance the system performances [103]. Apart from mitigating scintillation, this technique can also reduce the potential temporary blockage of the laser beam due to obstructions by small objects flying across the link path such as birds and drones, thus longer transmission spans can be covered under harsh weather conditions. In addition, it is much easier to provide independent aperture averaging with multiple apertures than a single aperture where the aperture size has to be far greater than the irradiance spatial coherence distance [7].

Despite the capabilities of this technique to combat fading, uncorrelated turbulence channels require the distances between Tx/Rx to exceed the fading correlation length. This implies that the Tx/Rx should be placed as far apart as possible from each other to maximize the spatial diversity performance, which is not always possible to implement practically [29]. In addition, these diversity techniques also require complex electronic and processing overheads in order to accommodate the synchronization, buffering, retiming processes, and logical combining of the replicated transmission [58]. The encoding/decoding protocols increase the hardware and signal processing complexity, and the cost of the system. Therefore, a better technique that virtually utilize the concept of the spatial diversity scheme, named relay-assisted communication system, has been proposed and is introduced below.

3.4 Relay-Assisted FSO Communications

Cooperative diversity is a paradigm shift in wireless technologies, which solves many shortcomings in the conventional point-to-point communications, mainly to combat fading and extend the coverage area. This technique has been introduced as an alternative way of realizing spatial diversity advantages without the need for using physical antenna arrays [104]–[107]. It is based on the broadcast nature of the RF wireless medium and enables single-antenna users to take advantage of space diversity by sharing their physical resources through a virtual transmit and/or receive antenna array. This technique has been proposed in the FSO context point of view and is known as relay-assisted or multi-hop transmission. It offers an efficient and low-cost solution compared to the MIMO systems as it does not need an additional Tx and Rx aperture. The basic relay channel model is comprised of three main elements, a source (*S*)/Tx, a destination (*D*)/ Rx, and a relay (*R*).

3.4.1 The concept of relay-assisted communications

In a relay-assisted transmission link, the total communication distance is divided into several hops, known as relays or hops between *S* and *D*. Note that, either a single or multiple relays can be placed between the *S* and the *D* as illustrated in Fig. 3.1. In RF wireless systems, relay-assisted communications take advantage of the broadcasting nature of RF transmission, where a message transmitted from the *S* to the *D* can be overheard by neighbouring nodes, thus enabling the retransmission of the same message to the *D*. As a result, the repetition messages received by the *D* will enhance the quality of signal reception since the *D* essentially averages out the channel variations resulting from fading, shadowing, and other forms of interference. The *S* nodes along with the neighbouring nodes that are willing to share their resources, creates a virtual antenna array. An advantage of this virtual multiple-aperture system is that multiple paths are spatially separated from one another, thus ensuring the independence of the corresponding fading channels. However, the broadcasting nature of RF leads to higher possibility of eavesdropping. Thus, the relay-assisted concept has been considered in the context of FSO system, which circumvents this issue while simultaneously offering higher data rates communications. To the best of our knowledge, the cooperative FSO transmission was first proposed by Acampora and Krishnamurthy in [108] and this technology has been adopted as a widely accepted solution for combating turbulence-induced fading in FSO systems [109]–[111].

A few relay-assisted techniques offer diversity, which can significantly improve the link availability in network based FSO systems where there is no direct link or a line of sight (LOS) path available between the *S* and the *D*. Unlike wireless RF systems, the severity of the small-scale fading in the FSO channel is distance dependent. This inherent characteristic allows the relay-assisted FSO based systems to smartly exploit the shorter distance by improving the small-scale fading statistics of the channel and simultaneously

reducing the path loss [112]. Besides widening the coverage area, multi-hop transmissions also offer a number of advantages including higher capacity, lower deployment cost, and extended connectivity, while minimizing the need for a fixed infrastructure, and as such can be adopted in wireless local area networks and hybrid networks [113]. Such relaying systems also allow lower launch power levels but with no diversity gain [114]. The diversity gain is offered by adopting parallel relaying schemes, which can effectively combat the atmospheric turbulence induced fading (due to near independent fading coefficients) [115] [66].

The relaying technique (parallel or serial) is quite efficient for increasing the link span and improving link availability. Due to the stringent pointing requirement and operational implementation complexity of parallel relaying, serial relaying has been extensively studied in the literature, despite the fact that parallel relaying was shown to outperform serial relaying for higher SNR levels by providing a high diversity gain [101]. The serial scheme is typically used to broaden the signal coverage for limited transmission power with no increased diversity order [36]. In such a scheme, AF or decode-and-forward (DF) transmission protocols in the relay nodes are among the most famous.

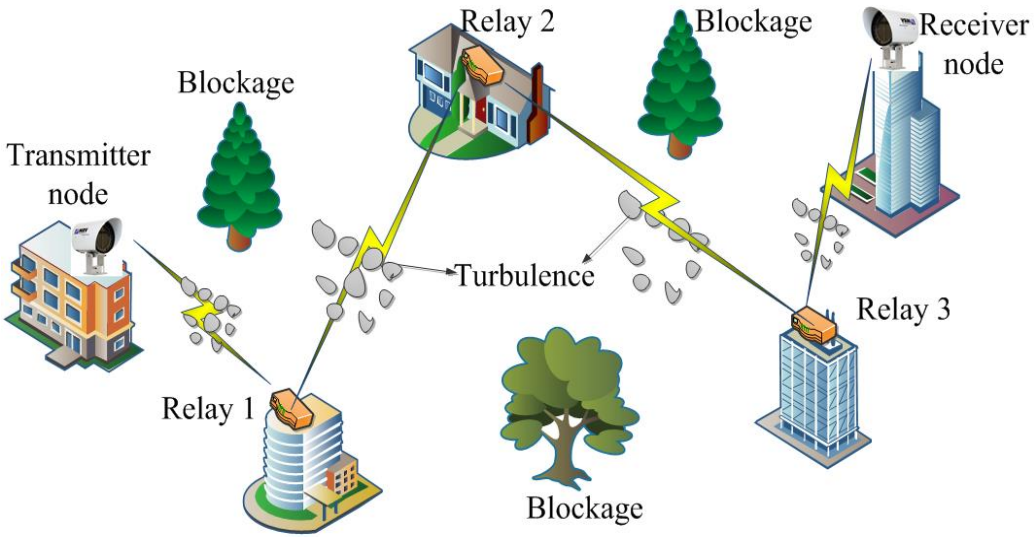

Fig. 3.1: Illustration of relay-assisted FSO communications.

3.4.1.1 Serial relaying

In the serial relaying scheme, an intensity modulated signal at the *S* is transmitted to the first *R* and is processed and forwarded to the subsequent *Rs* and ultimately to the *D*, as shown in Fig. 3.2. Using this approach, a longer transmission span with higher link availability under turbulence conditions can be realized in both urban and rural areas. The asymptotic relative diversity order (ARDO) of the serial relaying scheme with N^{th} relay can be expressed as [116]:

$$D_S = (N+1)^{11/6}. \tag{3.3}$$

In [117] it was demonstrated that the minimum outage probability for serial relaying is achieved when the relay nodes are equidistantly placed along the direct line from the *S* to the *D*. Furthermore, an outage occurs when any of the intermediate link fails. Therefore, the outage occurrences can be minimized by reducing the length of each *R*. This scheme takes advantage of shorter individual intermediate hops and bring substantial improvement against the degrading effects of turbulence induced fading. However, the trade-off is an increase in the path loss gain as a result of increasing the number of serial relaying nodes [118].

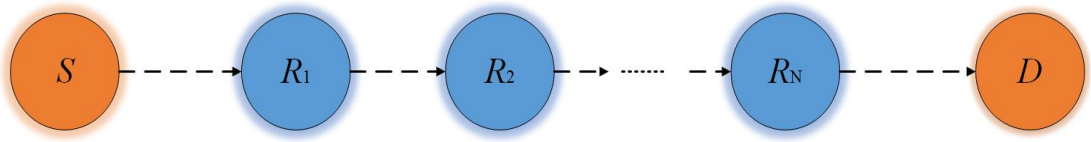

Fig. 3.2: Serial relay transmission.

3.4.1.2 Parallel relaying

In parallel relay transmission, the signal propagates from the *S* to the *D* through parallel *R*s in the same hop, as shown in Fig. 3.3. In this scheme, the *S* is equipped with

a multi-Tx laser, with each Tx pointing out in the direction of the corresponding *R* node. Based on the AF or DF relaying method, the *R*s either amplify or decode the received signal, and retransmit it to the *D*. At the *D,* the signals received with the help of various combining schemes such as equal ratio combiner (ERC), fixed ratio combiner (FRC), and maximum ratio combiner (MRC). This topology is commonly used when the serial-relay transmission suffers from multipath fading effects. For this scheme, the ARDOcan be expressed as [116]:

$$D_P = 2^{11/6}N. \tag{3.4}$$

Based on Eqs. (3.3) and (3.4), it is clear that the number of hops (raised to the power 11/ 6 ≈ 2) has more impact than the number of diversity paths. Note that, in parallel relaying, if an outage occurs in one of the *R*s, it does not necessarily lead to an outage in the whole relaying scheme. However, as the number of *R*s increases, the parallel relaying scheme takes less advantage of the distance-dependence of fading variance than serial relaying, which makes serial relaying better than the parallel relaying in such a case.

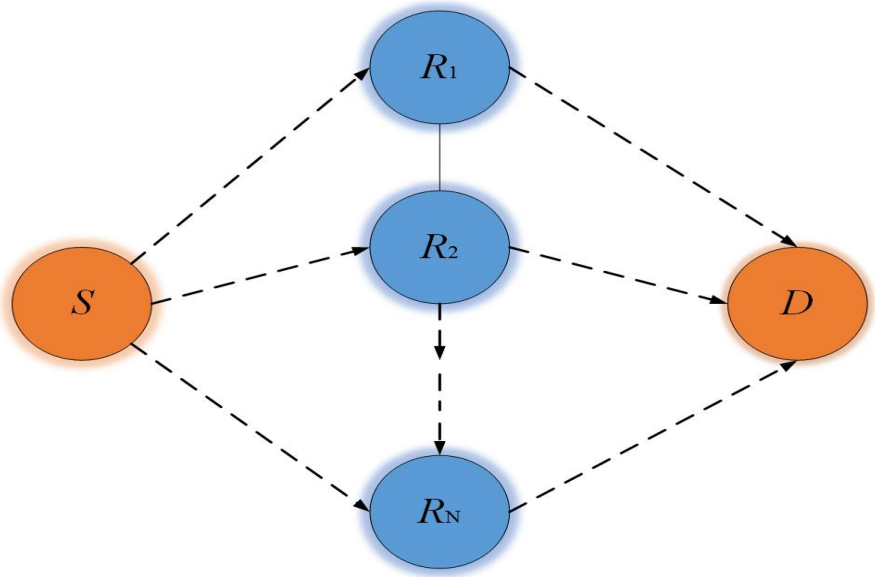

Fig. 3.3: Parallel relay transmission.

3.4.2 All-optical relay-assisted FSO communications

As a means to further boost the growth in network capacity, an all-optical network structure is currently being envisaged as a result of higher bandwidth requirements and new technological progress to avoid electrical termination of all connections in each network. The reason for all-optical systems' deployment is the fact that it is the only available technology today that can handle the enormous amount of capacity in a cost-effective and efficient way. As previously mentioned, two processing techniques have been proposed for multi-hop FSO systems namely AF and DF. In traditional AF systems, relaying is accomplished by means of OE conversion, amplification in the electrical domain, and EO conversion [101], [119], [120]. On the other hand, in DF, further electrical processing is implemented following OE conversion, which involves decoding and re-encoding of the electrical signal to combat the background noise prior to re-transmission [82], [121]–[123]. Although DF greatly improves the system performance, it suffers from the noise floor at the Rx due to erroneous relaying of the data [124] and requires synchronization and clock recovery at each relay [35], thus increasing system complexity.

The existing relay-assisted FSO systems are based on using relay nodes with OE and EO conversion modules with high-speed electronics and electro-optics devices, analog gain units, and digital control, which result in an increased link latency, complexity and cost [35]. Therefore, there is the need for alternative schemes that can be used to improve the system performances and achieve higher data rates. In [8], a 1.6 Tbps FSO system was introduced and shown to efficiently solve the network bottleneck issue. Therefore, an alternative solution would to be to have an all-optical system where all signal transmission, routing, switching, and signal processing are kept in the optical domain. This approach requires only low-speed electronic circuits to control and adjust the gain of amplifiers as well as avoids the use of complex optoelectronics devices and

electronic processing at the relay nodes. Consequently, cost savings are envisaged as a result of keeping the information in the optical domain.

In this work, the all-optical FSO relay based systems are investigated in terms of two protocols named AOAF and AORF. Although the AOAF relaying technique has been widely used in fiber optic communications systems [125], its application in FSO systems is still in its infancy stage where the concept was tested for the first time in 2002, implementing a cascaded point-to-point located 250 m apart and using dense wavelength division multiplexing (DWDM) with bit rates up to 10 Gbps [126]. However, this work only considered cascaded relay at the Rx (i.e., there was no separation between the relay and the destination) and it neglected the effect of atmospheric channel. Following this test field, most researches have since only focused on the theoretical aspects, as the practical implementation seemed to pose an open problem. Since the AOAF scheme accumulates the noise at each relay, the performance deteriorates as the number of hops increases. Consequently, AORF has been proposed for the first time in [35], where a 2R regeneration scheme was implemented in FSO communications system to suppress the impact of background and ASE noise at each relay before re-transmission to the next relay/destination. However, their work only demonstrated the superior capability of AORF compared to AOAF for relaying system (up to N=3) by estimating the BER performances in mitigating the accumulation of background noise, while neglecting the impact of atmospheric turbulence and path loss. Although it was proven that the AORF outperforms AOAF by 73% for dual-hop FSO system at a BER of 10^{-5} compared to direct transmission link, there has been no continuity to this work since then. Therefore, inspired by the high capability of AORF in mitigating noise, we continue the work by experimentally investigating the performance of AOAF FSO dual-hop system over various turbulence regimes. The theoretical aspects of AOAF and AORF will be

discussed in Sections 3.5 and 3.6, respectively while an in-depth discussion of the experiments will be presented in Chapters 4 and 5, consequently.

3.5 All-Optical Amplify-and-Forward (AOAF)

Optical amplifiers are critical components in the development of transparent all-optical networks, particularly AOAF based networks. Such networks rely on optical amplification to avoid optoelectronic conversion. Furthermore, the use of optical amplifiers overcome the limitation of direct-detection Rxs, which are limited by the thermal noise, without the use of more complex coherent (heterodyne or homodyne) systems.

AF protocol is the simplest relaying protocol, as its concept simply relies on amplifying the received signal and forwarding it to the next destination. The basic configuration of the AOAF relaying technique is illustrated in Fig. 3.4. Each relay is composed of all-optical elements, which are optical lens, optical fiber, and optical amplifier (OA). Two optical lenses (normally convex lenses) are placed before and after the OA, acting as the Rx and Tx, receiving and forwarding the beams to the next relay or towards the destination, respectively. The fundamental concepts of OAs will be presented in next sub-sections, while the details of the setup will be discussed in Chapter 4.

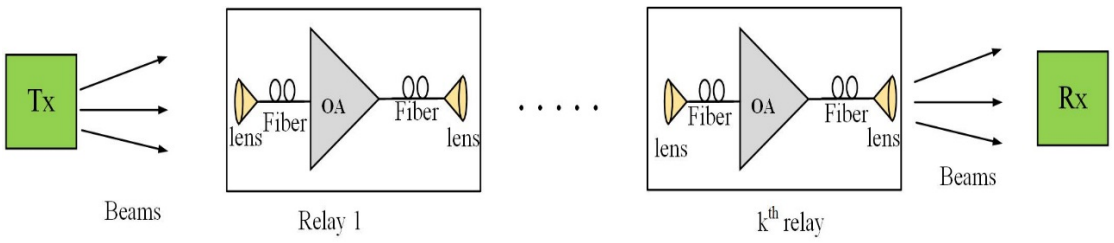

Fig. 3.4: Basic configuration of AOAF relay-based system; OA: optical amplifier.

3.5.1 Optical amplification

Over the last two decades, OAs have become integral components in optical communication systems and have successfully replaced electrical repeaters by means of compensating the optical signal loss and extending the communications link span. In previous electrical repeaters, also known as O-E-O amplifiers, a multistep process at the relay was carried out where, at the beginning, the optical signal is converted to electric signal. Subsequently, the signal is retimed, reshaped and amplified in the electric domain before it is converted back to an optical signal prior to further transmission [41]. This conversion has slowed down the signal data rates and also proved to be costly. Alternatively, OAs, which are purely optical in nature, have been widely used in optical communication systems to simplify the process as well as to maintain the speed of the signal transmission. This is because OAs offer large gain bandwidth, which has been practically utilized in optical wireless networks, including wavelength division multiplexing (WDM), whereby a single amplifier can amplify multiple signals on different wavelength simultaneously [127]. Additionally, OAs are easily adaptable for various bit rates and signal modulation formats while repeaters are designed to operate at specific bit rates and modulation schemes.

There are four important parameters to describe the performance of any OA, which are the signal gain, frequency bandwidth, saturation output power, and the noise figure [128]. The signal gain g of an OA is given, in decibels, by [129]:

$$g = 10log\left(\frac{P_{out}}{P_{in}}\right), \tag{3.5}$$

where P_{out} is the output power and P_{in} is the input power of the OA, which is given by:

$$P_{out} = gP_{in} + a \tag{3.6}$$

where a is the amplified spontaneous emission (ASE) noise, which relates to both the signal-spontaneous beat noise and spontaneous-spontaneous beat noise [130]. The

frequency bandwidth of an OA is determined by the optical gain spectrum of the amplifier, and is typically defined by the -3 dB point in the spectrum. This value affects the performance of an optical communication systems when OAs are used as repeaters or preamplifiers [129]. P_{sat} is a saturation point, where the output power is at the -3dB. The amplifier will be saturated if total optical input power exceeds the P_{sat}. Similar to an electronic amplifier, the OAs are not free from noise and the noise performance can be measured by a noise figure *F*, which describes the degradation of SNR due to addition of amplifier noise and is given as [129]:

$$F = \frac{SNR_{in}}{SNR_{out}} \tag{3.7}$$

where SNR_{in} and SNR_{out} are the SNR levels of the signal at the amplifier input and output, respectively. Since ASE noise is unavoidable in any OA, the minimum *F* of an ordinary OA is 3 dB [129]. The noise in an OA is an important parameter as it imposes a few limitations on various applications in optical communication systems. This intensity noise can lead to poor signal reception in analog communications or high-bit error rates. Furthermore, this noise accumulates as the signal passes through multiple amplifiers along the propagation path.

Based on principles of operations, OAs are typically classified into a few categories, which are SOAs, EDFAs, stimulated Raman amplifiers and stimulated Brillouin amplifiers. However, only SOA and EDFA are commonly used in FSO applications and will be discussed in the next section.

3.5.2 Erbium-doped fiber amplifier (EDFA)

The emergence of lightwave communication systems is vastly owed to the relatively recent development of EDFAs and the advantages they offer in term of capacity and cost. The demand for fiber based amplifiers has triggered an enormous number of

research papers and a successful commercial development. The EDFA was invented in 1987 at the University of Southampton and AT&T Bell Laboratories for travelling wave amplification of 1.5 μm wavelength [131]. In 1996, AT&T and its European partners installed an EDFA across the Atlantic for long haul communication systems for the first time, replacing the expensive and intrinsically unreliable electronic regenerators [127].

The EDFA as shown in Fig. 3.5, is one of the most popular OAs in optical communication networks due to its wide spectral emission, which ranges from 1530 nm to 1565 nm and matches the C-band in DWDM networks. The gain material of an EDFA is made of single-mode optical fiber that has been heavily doped with erbium ion (Er^{3+}), which constitutes the optically active element [127]. The fiber is pumped using a pump signal from a laser, typically operating at a wavelength of 980 nm or 1480 nm. The doped fiber is preceded by a wavelength-selective coupler to combine the output of the pump laser with the input signal. At the output, an isolator is used to prevent reflections from propagating back into the amplifier [132]. In addition, an EDFA also consists of a power supply line, a pump driving circuit, a monitoring circuit, and an electrical monitoring line [133].

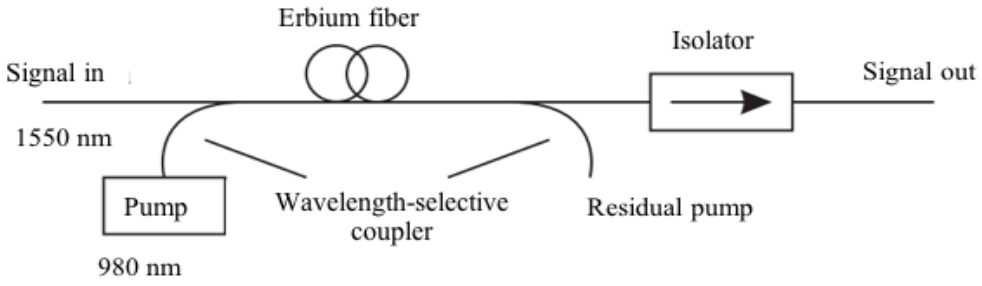

Fig. 3.5: An erbium-doped fiber amplifier.

A combination of several desirable characteristics has made the EDFAs the amplifier of choice in today's optical communication systems. It includes high gain (>40 dB), large output power (>10W), ultra-wide bandwidth (>10THz), high power transfer

efficiency from pump to signal (>50%), low noise figure, and suitability for long-haul applications [127], [134]–[136]. Since most of the FSO signals are not shared by many channels as fiber-optic communications, low gain and low noise EDFAs are suitable to use in relay stations, to simultaneously increase signal quality and decrease the cost. However, EDFAs are not small devices and cannot be integrated with other semiconductor devices. Moreover, EDFAs also exhibit ASE even when there is no incoming optical signal, crosstalk, and gain saturation.

3.5.3 Semiconductor optical amplifier (SOA)

Even though EDFAs are widely used for signal amplification, SOAs are intensively studied as an alternative option for system applications as preamplifiers, inline amplifiers and booster amplifiers. Furthermore, SOAs are also investigated for their applications as optical switching elements, optical modulators, frequency converters and frequency chippers for pulse compression [46]. SOAs are characterized by an extremely strong non-linearity, high operation speed, low power and energy consumption, and small size compared to EDFAs [137].

SOAs' most significant characteristics include high gain (25-30 dB), an output saturation power in the range of 5 to 13 dBm, a wide gain bandwidth of 30 nm-50 nm, an input power level that can be as low as -30 dBm (1μW), and a spectral response in the 0.8, 1.3, and 1.5 μm wavelength regions. Unfortunately, SOAs have some disadvantages when used merely as gain elements. SOAs have a higher noise figure than EDFAs since the gain coefficient of SOAs is very large, which is higher than 6 dB over 50 nm. Moreover, SOAs have higher cross-talk level than EDFAs when operating at 10 Gbit/s or above due to the conduction band lifetime becoming comparable to the bit period. This effect is known as the cross gain modulation (XGM) phenomena [137], [138].

3.5.4 Comparison between EDFAs and SOAs

Both EDFAs and SOAs can be used to amplify the optical signal in optical communication systems. They each have some fundamental differences, which provide both advantages and disadvantages as aforementioned. However, EDFAs are widely preferred to SOA mainly for the following reasons. Firstly, EDFAs can have high gains of up to 50 dB with a lower noise figure than SOAs where the maximum gain that can be achieved is 30 dB. In addition, in EDFAs, the spontaneous emission lifetime is within 5-10 ms [130], which is large enough compared to a bit period of interest for the electron transition (from higher to lower energy level) to respond to the optical signal fluctuations, and hence avoid any significant distortion to the amplified signal. Contrary to the EDFAs, the spontaneous emission lifetime of SOAs is usually within the range of 100-200 ps [130], which implies that the electron transition easily responds to the fluctuation of the optical signal at Gbps rates, thus resulting in potentially major signal impairments and significant crosstalk. Even though SOAs can operate at different wavelength regions, have compact size and weight, and possibly require lower pump power levels compared to EDFAs, EDFAs are still a competitive and more widely used technology. The reason lies behind the fact that EDFAs contain a couple of high power pump lasers, fibres, control electronics and other cheap optical components, all of which make them easy to integrate with planar waveguide optics and other devices.

3.6 All-Optical Regenerate-and-Forward (AORF)

Although AOAF relaying systems are an attractive option for practical implementation due to their simplicity, they accumulate the noise to the signal at each relay, thus limiting the maximum transmission distance. As such, the key component to enable large-scale transparent all-optical networks is utilising an all-optical regenerator

at the intermediate node/hop. This process is referred to as the AORF relaying technique. This field has witnessed a significant world-wide research activity recently, even though the field is far from realizing a practical solution yet [139]–[142], as there has been no implementation of this regenerator in FSO systems to date. When an optical signal propagates through a channel either in free space or a fibre, several signal impairments take place that degrade the optical signal-to-noise-ratio (OSNR) and which originate from the accumulating noise from the fading channel effect as well as the presence of ASE noise and nonlinearity of the fibre. In order to preserve the signal integrity and ensure it can be transmitted over long distances while routed across several optical nodes, signal restoration or regeneration can be used periodically along the transmission path. Signal regeneration designates from any combination of the three processes named re-amplification, re-shaping, and re-timing, which are conveniently referred to using the prefix 1R, 2R, or 3R. The implementation of signal regeneration is dependent on the network-case scenario and it is not always beneficial to systematically provide these three operations at each optical relay node. It should be mentioned that the regeneration effort is not only put into 3R regenerator but also on 2R regenerators, which involve only re-amplification and re-shaping. This is necessary for smaller networks or domains, where only 2R regeneration is adequate to maintain satisfactory signal quality, while achieving a lower cost. Furthermore, for a long-haul communication link, loss and amplitude fluctuations are usually considered to be the two major sources of signal impairment in most systems as compared to timing-jitter, and as such, the re-timing process is required less frequently. Therefore, in this work, we focus on the function of 2R regenerators and discuss the technique in-depth in the sub-sections below.

3.6.1 Nonlinear effects

Nonlinear effects are a commonly used term in fiber optics communication systems. Since we opted to investigate the AORF technique that involves the use of optical fibers and OAs, this section will describe the concepts of nonlinear effects that are relevant to this research work, which is SPM nonlinear effect. SPM leads to a change in the dispersion behaviour in high-bit-rate transmission systems, in which the phase of the signals get modulated such that a wavelength can spread out onto an adjacent wavelength [143]. SPM leads to pulse chirping and spectral broadening, which can be detrimental to the performance of optical systems. On the other hand, nonlinear effects can also offer a variety of useful applications such as ultrafast all-optical switching, amplification, optical phase conjugation, pulse compression, and regeneration [144]. Each of these applications require properly designed single mode fibers with high nonlinearity, right dispersion properties, and low attenuation.

This SPM effects results in the leading edge of the signal experiencing a positive refractive index gradient (dn/dt) and the trailing edge encountering a negative refractive index gradient $(-dn/dt)$ as depicted in Fig. 3.6.

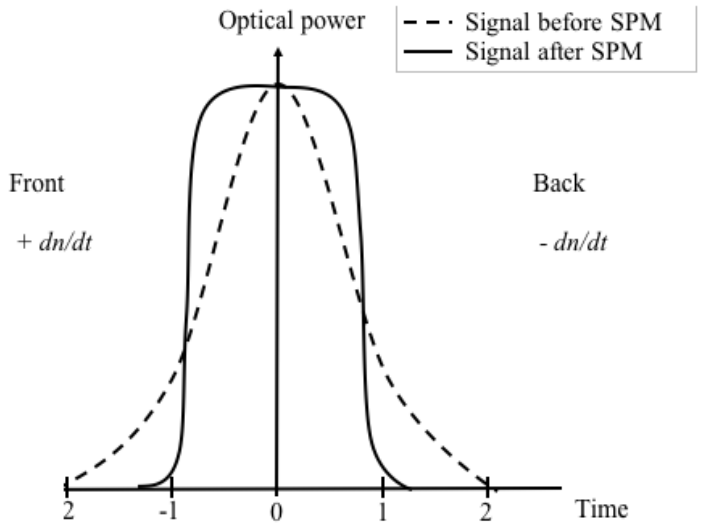

Fig. 3.6: Pulse broadening due to SPM-induced temporal variations.

The effective nonlinear propagation coefficient is given by [145]:

$$k_{nl} = \frac{(2\pi n_2)}{\lambda A_{eff}}, \tag{3.8}$$

where λ is the wavelength of the incident photons, n_2 is the nonlinear refractive index, and A_{eff} is the effective mode area. Then, the nonlinear phase shift induced by SPM can be expressed as [146]:

$$\emptyset_{SPM} = k_{nl} P_0 L_{eff}, \tag{3.9}$$

where P_0 is the optical peak power of input pulses and L_{eff} is the effective fibre length, which is related to the physical fibre length L_f given by [144]:

$$L_{eff} = \left[1 - exp\left(-\kappa L_f\right)\right]/\kappa \tag{3.10}$$

where κ is the linear loss coefficient. The equation shows that SPM gives rise to an intensity-dependent phase shift but the pulse shape remains unaffected. Typically, $\kappa = 0.2$ dB/km at $\lambda = 1550$ nm and $k_{nl} = 2.35 \times 10^{-3}$ 1/mW [145]. In the absence of fiber losses, $\kappa = 0$ and thus $L_{eff} = L_f$. Increasing the link span between the in-line OAs often necessitates the use of higher power levels to be launched into the fiber, which ultimately leads to pulse broadening due to SPM.

The next sub-section will present a detailed discussion of the concept behind optical regeneration based on SPM effects, as it will be used in building our all-optical regenerator, which will be explained in Chapter 5.

3.6.2 The concept of SPM-based optical regenerator

As aforementioned, optical regeneration can be divided into three categories, which are 1R, 2R, and 3R (see Fig. 3.7) based on the degenerative effects corrected at each stage. 1R regeneration is the simplest regeneration process and only involves re-amplification of the signal using OAs such as rare-earth doped optical amplifiers or Raman amplifiers, which are used to overcome power loss due to signal attenuation and

connection losses. In other words, 1R can also be referred to as the AOAF technique. 2R regeneration involves 2 processing types, which are the re-amplification and re-shaping of an optical signal. Reshaping is used to supress the noise accumulated and to improve the extinction ratio in an intensity modulation signal. Finally, a 3R regenerator performs the additional task of re-timing the signal by extracting the signal clock from the input data signal and transferring it to a newly generated pulse train [147].

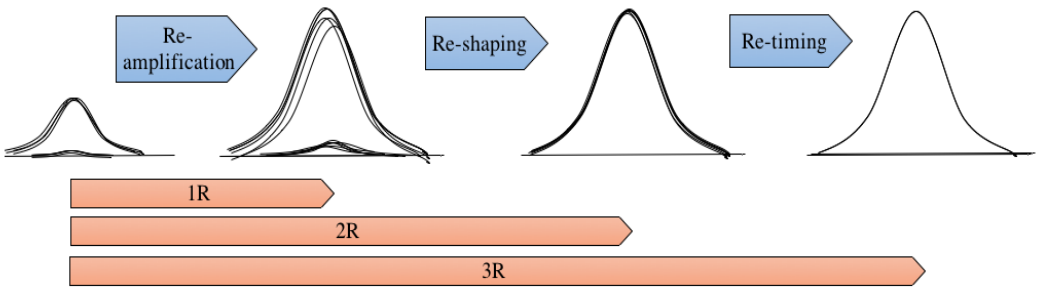

Fig. 3.7: A signal regeneration scheme illustrating the re-amplification, re-shaping, and re-timing operations.

Among various regenerator configurations, the 2R regenerator based on SPM-based spectral broadening, has received significant research attention owing to the ease of its implementation, scalability to high bit rates and multiple channels [148] and ease with which a retiming stage can be integrated with it to provide a 3R regenerator [149]. The structure of the regenerator is simpler because it has no pump or probe source inside the regenerator. This type of regenerator achieves their functionality via a nonlinear transfer function, governing the instantaneous output versus input power of the regenerator [150]. Although the basic idea of the SPM-regenerator, which is also known as the Mamyshev optical regenerator, was developed in 1998 [151], the devices were studied extensively only after 2003 [152]–[155].

Fig. 3.8 illustrates the schematic diagram of a 2R SPM-based all-optical regenerator. The regenerator normally consists of three main elements, which are EDFA,

HNLF, and optical bandpass filter (OBPF). At the beginning of regeneration, the degraded optical signal is fed into an EDFA to boost the peak power of the incoming noisy signal to a power level that is enough to cause spectral broadening through the SPM effect. The amplified signal is then passed through an ASE rejection module (filter) that rejects the out-of-band ASE noise added by the high-power EDFA. The bandwidth of the filter is chosen to be wider than the signal wavelength. Following that, the filtered signal is injected into the HNLF, where it experiences SPM induced spectral broadening. An OBPF is subsequently used after the output of the HNLF as a reshaping element, whose centre wavelength is slightly shifted from the input signal wavelength. The OBPF slices a portion of the broadened spectrum with which more power and width-stabilized output pulse is generated. The bandwidth of the output filter sets the output pulse width and needs to be optimized carefully.

Note that, the OBPF acts an optical decision gate to discriminate marks and spaces based on the difference in SPM-induced spectral broadening in an optical fiber with nearly zero normal dispersion [6]. If the centre wavelength of the band-pass filter is offset with respect to the carrier frequency of the signal, then only pulses with sufficient power to produce large enough spectral broadening can pass through the filter. This results in a nonlinear transfer function for the regenerator, and therefore, a suppression in the noise present in the signal. Clearly, this nonlinear transfer function depends strongly on the launch power, filter offset, fiber length, and fiber dispersion [152]. Ultimately, the performance of an SPM-based regenerator depends on three main parameters, which are the maximum nonlinear phase shift (see Eq. (3.9), the filter-passband offset, and the filter bandwidth, which must be large enough to accommodate the entire signal so that the width of the optical pulses remain intact [156]. This 2R all-optical regenerator improves the extinction ratio and the optical SNR of a degraded signal, and have been demonstrated

in highly nonlinear silica based fibers to achieve a million kilometres of error free transmission without electrical conversion [157].

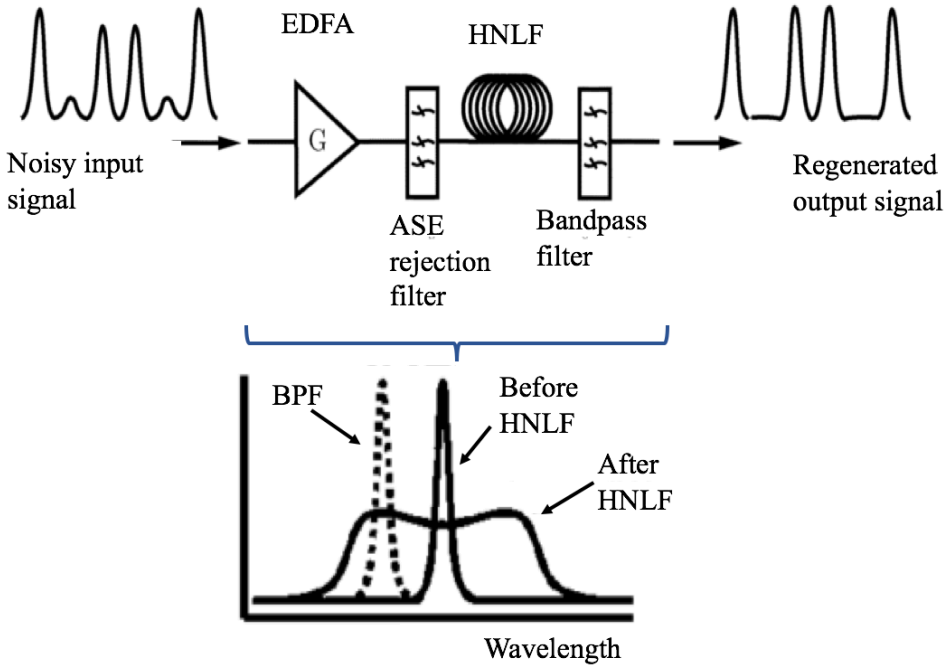

Fig. 3.8: Schematic diagram of an SPM-based 2R regenerator.

3.6.3 Highly nonlinear fibers

Nonlinear fiber optics play an important role in the design of high capacity lightwave communication systems. One of the relatively recent developments is a new type fibers known as HNLFs. HNLFs is one of the new types fibers that describe a family of different fibers including microstructured fibers, holey fibers, and photonic crystal fiber, all of which share the common property that a relatively narrow core is surrounded by a cladding containing a large number of air holes [156]. These HNLF fibers are designed to maximize fiber nonlinearity and minimize optical loss, which makes such fibers optimal for constructing highly efficient fiber amplifiers, dispersion compensators, and various other non-linear devices.

The nonlinear effects occurring inside optical fibers including SPM are governed by a single nonlinear parameter k_{nl} defined in Eq. (3.8). For most optical fibers, k_{nl} has a value of ~ 1 W^{-1}/km, which is too small for nonlinear applications. Thus, HNLFs were developed to overcome this issue by having k_{nl} > 10 W^{-1}/km [146]. As stated in Eq. (3.8), k_{nl} depends on wavelength of light λ, the effective mode area A_{eff}, and nonlinear index coefficient n_2. n_2 is a material parameter, which is fixed for each glass material. Hence, the only parameter that can be adjusted to enhance k_{nl} is A_{eff}, which can be reduced with a proper silica-based optical fiber design, which often involves controlling the refractive-index profile. The invention of these HNLFs led to various novel applications of nonlinear fiber optics such as the generation of extremely broad optical spectra (supercontinuum generation) and large Raman-induced frequency shifts allowing wavelength tuning of mode-locked lasers due to the ultrafast nature of the nonlinear response of the fiber.

3.6.4 Tunable mode-locked lasers

The ever-increasing demand for greater bandwidth requires optical communication systems that can process data and operate at ever higher speeds. Therefore, wavelength tunable optical sources capable of generating short pulses at high repetition rates have garnered an increasing amount of interest. Laser is a device that is capable of generating optical picosecond pulse widths by three different techniques: *Q*-switching, gain switching, and mode-locking [158]. Depending on the application, one technique can be preferred over the others. However, mode-locking is considered the most reliable and simplest way to achieve the generation of ultra-short pulses with picosecond and femtosecond pulse duration. In addition, the pulses produced with this technique exhibit low timing jitter. Mode-locking, or as sometimes referred to as self-mode-locking, is a technique whereby a laser produces a very fast sequence of regularly spaced separate pulses, called a pulse-stream. This generation of mode-locked pulse is

not akin to turning the laser on and off. In mode-locking, an intracavity gain, loss, or phase element is used to lock the longitudinal modes in the semiconductor laser structure and produce short optical pulses [159]. When a laser is mode-locked, one or sometimes several pulses circulate in the laser resonator. Each time the pulse hits the output coupler mirror, a part of its energy is emitted, so the laser output is a regular pulse train [160]. The gain medium replenishes the pulse energy in each round trip. The pulse repetition rate is determined by the resonator's round-trip time and the number of pulses, while the pulse duration is usually far shorter than the round-trip time. Typical pulse durations are between 30 fs and 30 ps [160].

3.7 Summary

This chapter has presented a brief description of a few mitigation techniques, particularly to combat turbulence-induced fading in FSO communication systems such as aperture averaging, spatial diversity, and relay-assisted systems. FSO relay-based systems have established a new paradigm shift in improving FSO link communications in terms of increasing the link span and reducing the error rate. Hence, the fundamental background of relay-assisted FSO communication systems was thoroughly discussed in this chapter in term of the features, configurations, and the associated devices. The concept of all-optical FSO relaying systems was also elaborated, and the promise and advantages of these systems in comparison to the conventional relaying schemes was also highlighted. Two techniques of all-optical FSO relay-based systems that are used in this research were explained in detail, which are AOAF and AORF. In AOAF FSO systems, the fundamental configurations, which mainly involve the use of OAs were outlined. Two options of OAs were considered, namely EDFAs and SOAs. The basic fundamentals of each amplification technology were covered and a comparison between them was

presented. Next, the concept of the AORF scheme was introduced, and a discussion of the configurations and the principle of the system was given. The foundation of nonlinear effects in fiber were explained with special focus on the SPM effect, which will be utilized in the modelling of the AORF system in this work. Last but not least, the theoretical background of HNLFs and tunable-mode-locked lasers was also highlighted, as these devices will play key roles in realizing the SPM-based AORF setup.

Chapter 4

ALL-OPTICAL AF FSO RELAY-ASSISTED SYSTEM UNDER TURBULENCE EFFECTS

4.1 Introduction

Relay-assisted FSO communication systems is one of the alternative solutions that offers diversity within the networks, which can be adopted to combat link failure. Thus, substantially extending the link span, and improving the link performance and system throughput under the influence of diverse atmospheric channel effects. Since the technique take advantage of independent underlying fading paths by replacing a single long range link with a chain of short-range links, this scheme not only reduces the path loss but also improves the small-scale fading statistic of the channel. Meanwhile, we can benefit from reduced launch power at the Tx and efficient fading reduction at the Rx in the case of employing parallel relays, due to almost independent fading coefficients [66]. Albeit its improved performances, the distance-dependent turbulence fading variance is still the main concern in overall system performance assessment. This is because the turbulence is the main source of random fluctuations of received optical irradiance in

terms of both intensity and phase variations even under a clear weather condition [11]. However, measuring the turbulence under a diverse weather condition practically is very challenging. This is mainly due to a long waiting time to observe and experience the reoccurrence of atmospheric turbulence events, which sometimes can take weeks or months, and the difficulty in controlling and characterising the atmospheric turbulence. Because of that, the practical investigations based on turbulence effects are very limited. Until now, almost all works reported on relaying system under turbulence effects are theoretical in nature with very little or no experimental verifications. Despite the limitation, we have built an indoor laboratory chamber, which can simulate the atmospheric turbulence channel under a controlled condition, thus mimicking the real turbulence scenarios as reported in [19], [77], [93], [161]. This chamber reduces the test and measurement time considerably compared with the outdoor FSO link.

In this chapter, an AOAF relaying technique is embraced for a relay-assisted FSO communication link for utilization of the FSO network capabilities. This is done, by using an OA at the relay, to boost the received signal and forward it to the next relay/destination. This intermediate node is essential particularly when there is no direct transmission path between the Tx and the Rx. Compared to the traditional relaying system, which requires the conversion of OE and EO, this new AOAF system avoids the need for OE to EO conversion, mainly to maintain the high transmission speed between the links. The contribution of this chapter is to study the performance analysis of triple-hop AOAF FSO system theoretically and experimentally under the effects of a turbulence channel. A mathematical framework for the end-to-end SNR and BER performance for the proposed scheme is outlined and show that the predicted data match well with experimental results.

The rest of chapter is organized as follow: A thorough review of the relevant literatures pertaining to the investigation studies and performance analysis of relay assisted in FSO communications is presented in Section 4.2. Section 4.3 introduces the

basic AOAF configuration that will be used throughout the analysis. Section 4.4 outlines the mathematical frameworks of AOAF FSO system performances, which include BER and SNR for triple-hop systems. Using the MATLAB and Optisystem software, Section 4.5 presents numerical simulation results, which quantify the comparison of optical and electrical AF and comparison of NRZ-OOK and RZ-OOK modulation formats for the AOAF FSO system in Sections 4.5.1 and 4.5.2, respectively. The main contributions are outlined in Sections 4.6 and 4.7 where experimental analysis of AOAF triple-hop FSO systems under different turbulence regimes are investigated. We show the experimental setup in Section 4.6.1 and the results for single, dual, and triple-hop AOAF systems are discussed in Section 4.6.2. In this section, we assume the turbulence are identical for all-hops, which means that all-hops have the same C_n^2. Using the same experimental setup as in Section 4.6.1, Section 4.7 investigates the performance analysis of the triple-hop AOAF system for different turbulence configurations, where seven turbulence scenarios are considered. Further explanation of experimental setup and results are discussed in Sections 4.7.1 and 4.7.2, respectively. Finally, concluding remarks are highlighted in Section 4.8.

4.2 Background and Motivation

A number of researchers have reported the reliability of relay-assisted FSO systems to broaden the coverage areas as well as to reduce the fading effects. To the best of our knowledge, the relay-assisted FSO system was first proposed by Acampora and Krishnamurthy in [108], where the performance of a mesh FSO network was investigated from a network capacity point of view. The authors emphasized on the effectiveness of relay-assisted transmission to extend the coverage area. The authors also focused on the networking perspective and did not address the physical layer aspects. In [162], Akella et al. studied the BER performance of decode-and-forward (DF) and AF FSO multi-hop

schemes compared to the single-hop FSO system under the atmospheric attenuation and geometric loss effects, with each hop length is fixed to 500 m. It was shown that the mean and variance of the error rate is smaller in multi-hop systems compared to the single hop for the same link range and the launched power. Since in [162] the turbulence effect was not considered, whereas in [163] the effect of turbulence in multi-hop FSO communication systems modelled by Gamma-Gamma distribution was outlined. The authors showed that the outage probability of AF and DF degraded with the increasing number of hop under the strong turbulence regime. The results also showed that the DF system slightly outperformed the AF based FSO link with the performance gap increased with the increase of number of hops. The capabilities of relay based system using subcarrier phase shift keying (PSK) to combat the Gamma-Gamma atmospheric turbulence fading was demonstrated in [114], by considering both the channel-state-information (CSI) and fixed-gain relays. The numerical results demonstrated that by increasing the number of hops while keeping the hop length fixed, the outage performance deteriorated accordingly. In [101], for the case of a Gamma-Gamma turbulence channel the authors showed through the simulation that the SNR gains of ~12 dB and ~19 dB at a target outage probability of 10^{-6} for AF and DF dual-hop serial relay based link, respectively, compared with the direct transmission link with strong turbulence (i.e., $C_n^2 = 1 \times 10^{-14}$ $m^{-2/3}$ and a link range of 5 km). Using a triple-hop transmission system, the SNR improvements were ~18 dB and ~25 dB. Note that, the advantage of DF over AF is at the cost of increased system complexity i.e., the need for decoding and encoding modules at the relay nodes.

Most of reported numerical studies have focused on the conventional electrical relaying scheme, where amplification is carried out in the electrical domain. However, most recently researches have focused on the provision of applying all-optical relaying system specifically for FSO communications. The concept of all-optical multi-hop FSO

system was proposed by [126] with the λ of 1548 nm, where a dual-hop test-field setup was developed for a total link distance of 500 m. In the experiment, an all-optical automatic gain controller (AGC) was used to adjust the OA gain to compensate for any distortion experienced by the propagating optical signal. The field test results showed that a BER of $2.1e^{-12}$ was achievable at a data rate of 2.5 Gbps, which reduced to a BER of 3.5e-^{11} for data rate of 10 Gbps. However, the experiment neglected the effect of turbulence-induced fading. Despite that, this works broadened the horizons on all-optical multihop FSO communication systems, which lead to a considerable amount of research works. After about a decade, the analytical investigation on the BER performance of all-optical multihop FSO systems for both AF and DF was presented in [35]. The author had performed Monte Carlo simulations under weak turbulence by assuming either a fixed-gain OA or an optical regenerator. The study showed that for the OOK based system at a BER of 10^{-5} under weak turbulence (i.e., $C_n^2 = 1 \times 10^{-14}$ m$^{-2/3}$) the SNR gain of 6.6 dB was achieved for the all-optical dual-hop AF relay, and total links span were increased by 0.9 km and 1.9 km for AF and DF two-hops systems, respectively compared to a 3 km long of the direct transmission. However, the authors underestimated the effect of ASE in their system.

Following [35], numerous studies have been reported to explain the significant of adopting all-optical FSO relay-based systems specifically using the EDFA based on the AF relay [112], [164]–[171]. In particular, in [112], the outage probability analysis for a dual-hop and multi-hop system using EDFA over the lognormal fading was investigated through numerical simulations. They showed that the all-optical relay based FSO link outperformed the electrical relay based links by reducing the outage probability from 10^{-2} to 10^{-5} at -130 dBJ of background radiation energy based on a a 1550 nm laser source, a 2 Gbps OOK data format and a 5 km link span with $C_n^2 = 1.7 \times 10^{-14}$ m$^{-2/3}$ and the atmospheric attenuation of 4.2 dB/km. The authors also considered all relevant noise

sources including thermal noise, background radiation, ASE, beat noise, and signal dependent noise. Also shown was the link performance for all-optical relaying, which improved with the increasing number of relays *m* until *m* = 8. For increasing *m* to up 10 resulted in the link's performance degradation. Further outage performance analyses of dual-hop all-optical AF relaying taking into account the effects of ASE and degree-of-freedom (DoF) was reported in [165]. The authors stated DoF (i.e., *M* = 1,10,100, and 1000) is an important parameter in quantify the ratio of optical filter bandwidth to the electrical bandwidth and should be in the order of 1000 unless a narrowband optical filter is employed (for an ideal case *M* = 1). The numerical results showed that SNR reduced from 14.7 dB (*M*=1) to 14.4 dB, 13.2 dB and 10.3 dB for *M* = 10,100, 1000, respectively at a target outage probability of 10^{-6}, compared to a direct transmission at 1550 nm wavelength is transmitted over a link span of 10 km with $C_n^2 = 10^{-14}$ $m^{-2/3}$ and visibility of 10 km.

In [169], an all-optical AF dual-hop FSO system employing a 4-pulse position modulation (4-PPM) operating at the wavelength of 1550 nm over the Gamma-Gamma turbulence channel was reported showing that the required transmit power was reduced in proportion to the amplifier gain. The authors theoretically showed the benefit of combining relaying and multiuser diversity. For example, for an amplifier gain of 10 dB, the transmit power per bit of 10 dBm was conserved at a target BER of 10^{-6} over a link span of 3 km. In [170] a novel cumulative density function (CDF) analysis for the end-to-end SNR for relay-assisted subcarrier intensity modulation (SIM) based all-optical FSO networks over the Gamma-Gamma fading channel was reported where both the variable AF gain and the pointing error effect were taken into consideration. The authors theoretically showed the benefit of combining relaying and multiuser diversity.

Recently, in [166], [167] a novel relaying technique based on combining EDFA with an optical hard-limiter (OHL) to improve the BER performance were reported. In

these approaches OHL was before EDFA to mitigate the accumulated background noise. The analyses carried out were based on Monte Carlo simulations for the multi-hop system with moderate turbulence using the Gamma-Gamma distribution. The results showed that the proposed setup improved the BER performance and extended the link distance by removing the accumulative background noise over multiple relays. For instance, for a 2.5 Gbps OOK based link of 5 km long and with $C_n^2 = 5 \times 10^{-14}$ $m^{-2/3}$ a transmit power gain of 5 dB was at a target BER of 10^{-6} compared to the system employing a conventional EDFA for the triple-hop relaying system with turbulence. Nevertheless, the drawback of the proposed technique was the BER performance was dependent on the threshold level of OHL, and the optimal threshold levels must be set based on the strength of turbulence and the background noise level, which are not straightforward.

Recently a hybrid RF-FSO scheme was considered to further enhance the system performance when adopted between source-to-relay and relay-to-destination [172], [173]. The authors derived analytical expressions for the probability density function (PDF) and CDF, and investigated the outage probability and the BER performance of a dual-hop relaying system. However, almost all works reported on this topic are theoretical in nature with very little or no experimental verifications. Therefore, this chapter will further investigate both theoretically and experimentally the performance of all-optical relaying system employing OA as the relaying technique.

4.3 AOAF Configuration

The basic relay communication networks contain of a three-element communication link, which are the Tx/source (*S*), the relay (*R*), and the destination (*D*). In a AOAF multi-hop relaying scheme at least a single OA is used prior to retransmission of the signal to the next relay/ destination as shown in Fig 4.1. This configuration is also

known as serial AOAF multihop, which is simple and can combat signal attenuation in a long range communications, making it the most popular structure implemented today. A distinguishing feature of this configuration is that each node communicates only with the next node, the one before and the one after. At each OA, the background light is added to the received data field in addition to the OA generates ASE noise. The structure of typical AOAF relay is depicted in Fig. 4.2, where convex lenses are used for capturing and launching the optical beam into and out of the optical fibre.

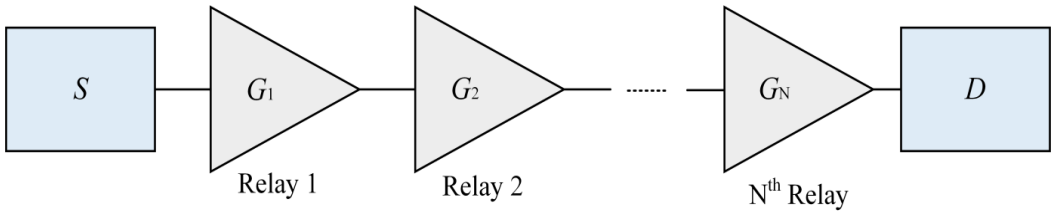

Fig. 4.1: Serial OAF Configuration.

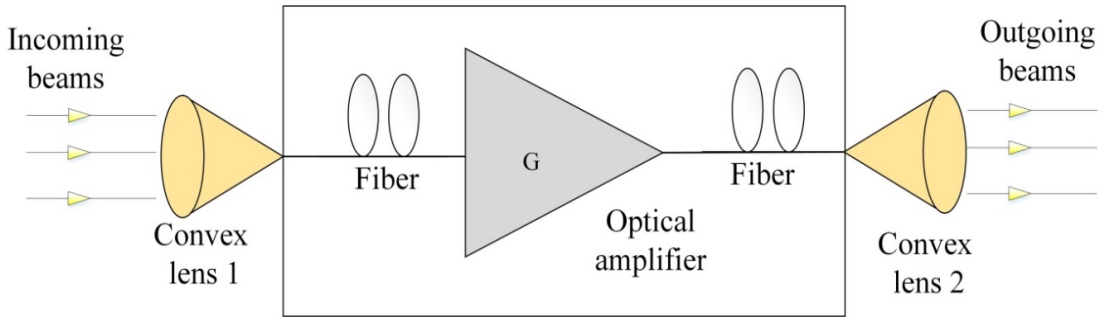

Fig. 4.2: Structure of an AOAF.

4.4 Performance Analysis of Triple-Hop AOAF FSO Signal Transmission

This section outline the end-to-end mathematical frameworks for the SNR and the BER for triple-hop AOAF based intensity modulation-direct detection (IM-DD) FSO link over the Gamma-Gamma turbulence channel. The simulation results are shown in the next section and validated by experimental results. We assumed that, there is no direct link between *S* and *D*. At each hop, the relay amplify the received signal and forward it to the next relay or to the destination. We assume that, channels are stationary, memoryless, and ergodic with independent but not necessarily identically distributed fading statistics. The schematic system block diagram is illustrated in Fig. 4.3. The *S* transmit the modulated signal of $s_0(t)$ to *R*1 through a disperse turbulence channel h_{SR_1}. At the *R*1, the signal is amplified using an OA with the gain of $\mathcal{G}_1$ prior to re-transmission to the next relay *R*2. The OA and the Rx of *R*1 impose the ASE noise ($a_1(t)$) and $n_1(t)$, respectively to the signal. The signal is then transmitted to *R*2 via turbulence channel $h_{R_1R_2}$. The same process at *R*1 are repeated in *R*2 and *D*, where the transmission of *R*2 to *D* is via the turbulence channel of h_{R_2D}.

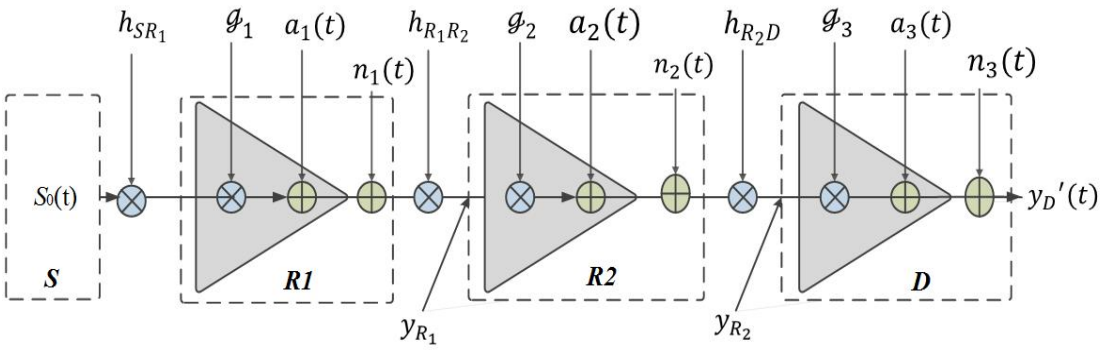

Fig. 4.3: Schematic block diagram of a triple-hop all-optical OAF relay-assisted FSO link.

The signal $s_0(t)$ is transmitted from *S* to *R*1, and the received signal at *R*1 is given by:

$$y_{R_1}(t) = h_{SR_1} s_0(t) + n_1(t), \quad (4.1)$$

where h_{SR_1} is the channel gain from *S* to *R*1, $n_1(t)$ is the noise at *R*1, which can be considered as a combination of the ambient light, thermal, dark, and shot noise, which is modeled as an additive white Gaussian noise (AWGN) with zero mean and a power spectral density of N_0 [7]. $y_{R_1}(t)$ is afterwards amplified using an OA and then retransmitted to *R*2 via the second free space turbulence channel. The received signal at *R*2 is given as:

$$y_{R_2}(t) = h_{R_1R_2}(g_1 y_{R_1}(t) + a_1(t)) + n_2(t), \quad (4.2)$$

where a_1 is the ASE noise of OA at *R*1 and $n_2(t)$ is the noise at *R*2. In most previous works reported on relay-assisted FSO networks, the OA gain g was assumed to be fixed [35], [101], [164], [165], [174]. However, in this work we define g for *j*th OA relay (*j* = 1, 2, 3) as [170]:

$$g_j = \sqrt{\frac{P_{R_j}}{h_{j-1,j}^2 P_S^2 + N_0}}, \quad (4.3)$$

where P_s and P_R are the transmit and received powers at *S* and *R*/*D* (i.e., either *R*1, *R*2, or *D*), respectively. Note that, we assume that the relay transmits the signal under a maximum total power constraint and g is self-adjusted in order to ensure a fixed output power with varying input powers, which is typical for real optical networks comparable to theoretical works based on assumptions from the RF domain. At *D*, the received signal prior to amplification is given as:

$$y_D(t) = h_{R_2D}\left(g_2 y_{R_2}(t) + a_2(t)\right) + n_3(t), \quad (4.4)$$

where a_2 is the ASE noise of OA at *R*2 and n_3 is the noise at *D*. Following pre-amplification at the *D* the signal is given as:

$$y_D{}'(t) = g_3 y_D(t) + a_3, \tag{4.5}$$

where a_3 is the ASE noise of OA at *R*3. Similarly, (4.5) can be written as:

$$\begin{aligned} y_D{}'(t) = g_1 g_2 g_3 h_{R_1R_2} h_{R_2D}[h_{SR_1} s_0(t) + n_1(t)] + g_2 g_3 h_{R_2D}[h_{R_1R_2} a_1(t) \\ + n_2(t)] + g_3[h_{R_2D} a_2(t) + n_3(t)] + a_3(t) \end{aligned} \tag{4.6}$$

Note that, (4.6) can be consider to be the same for a direct transmission system whose input-output relation is represented by:

$$y_D{}'(t) = h_{eq} s_0(t) + n_{eq}(t), \tag{4.7}$$

where $h_{eq} = g_1 g_2 g_3 h_{SR_1} h_{R_1R_2} h_{R_2D}$ and n_{eq} is the AWGN with zero mean and variance σ^2 given by:

$$\sigma^2 = \frac{g_1{}^2 g_2{}^2 g_3{}^2 \sigma_{n_1}^2 + g_2{}^2 g_3{}^2 \sigma_{a_1}^2 + g_2{}^2 g_3{}^2 \sigma_{n_2}^2 + g_3{}^2 \sigma_{a_2}^2 + g_3{}^2 \sigma_{n_3}^2 + \sigma_{a_3}^2}{g_1{}^2 g_2{}^2 g_3{}^2 + 2 g_2{}^2 g_3{}^2 + 2 g_3{}^2 + 1}, \tag{4.8}$$

where, $\sigma_{a_1}^2$, $\sigma_{a_2}^2$ and $\sigma_{a_3}^2$ are the variance of ASE noise of OA at *R*1, *R*2, and *R*3, respectively, while $\sigma_{n_1}^2$, $\sigma_{n_2}^2$, and $\sigma_{n_3}^2$ are the variance of the background noise at *R*1, *R*2, and *R*3, accordingly. In (4.8), we have used the fact that $E\left[h_{SR_1}^2\right]$, $E\left[h_{R_1R_2}^2\right]$, and $E\left[h_{R_2D}^2\right]$ of Gamma-Gamma distribution are equal to 1, where $E[\cdot]$ denotes the statistical expectation operator. Thus, the end-to-end SNR γ_{e2e} of the overall system can be written as:

$$\gamma_{e2e} = \frac{(g_1 g_2 g_3 h_{SR_1} h_{R_1R_2} h_{R_2D})^2}{\psi}, \tag{4.9}$$

where

$$\psi = g_2{}^2 g_3{}^2 h_{R_2D}{}^2 \left(g_1{}^2 h_{R_1R_2}\sigma_{n_1}^2 + \sigma_{a_1}^2\right) + g_3{}^2 h_{R_2D}{}^2 (g_2{}^2\sigma_{n_2}^2 + \sigma_{a_2}^2) + g_3{}^2\sigma_{n_3}^2 + \sigma_{a_3}^2. \tag{4.10}$$

In order to compute the BER, we have used the PDF derivation of a product of two random variables (RVs), which is generally given as [175]:

$$f(z) = \int_{-\infty}^{\infty} \frac{1}{|x|} f_X(x) f_Y\left(\frac{z}{x}\right) dx, \tag{4.11}$$

where z is the product of RVs x and y ($z = xy$). From (2.27), the PDF expressions for the channel gains of the S to $R1$ (h_{SR_1}) and $R1$ to $R2$ ($h_{R_1R_2}$) are given as:

$$f\left(h_{SR_1}\right) = \frac{2(\alpha\beta)^{\frac{\alpha+\beta}{2}}}{\Gamma(\alpha)\Gamma(\beta)} \left(h_{SR_1}\right)^{\frac{\alpha+\beta}{2}} K_{\alpha-\beta}\left(2\sqrt{\alpha\beta h_{SR_1}}\right), \tag{4.12}$$

$$f\left(h_{R_1R_2}\right) = \frac{2(\alpha\beta)^{\frac{\alpha+\beta}{2}}}{\Gamma(\alpha)\Gamma(\beta)} \left(h_{R_1R_2}\right)^{\frac{\alpha+\beta}{2}} K_{\alpha-\beta}\left(2\sqrt{\alpha\beta h_{R_1R_2}}\right). \tag{4.13}$$

Using the general PDF of (4.11), and considering $x = h_{SR_1}$, $y = h_{R_1R_2}$, and $h = h_{SR_1}h_{R_1R_2}$, the PDF of h can be computed as:

$$f(h) = \int_0^{\infty} f(h_{SR_1}) f\left(\frac{h}{h_{SR_1}}\right) \frac{1}{\left|h_{SR_1}\right|} dh_{SR_1} \tag{4.14}$$

Using the Meijer-G representation of the modified Bessel function of second type [[176], Eq.8.4.23.1] we can solve (4.14) as:

$$f(h)=\left(\frac{(\alpha\beta)^{\frac{\alpha+\beta}{2}}}{\Gamma(\alpha)\Gamma(\beta)}\right)^{2} h^{\frac{\alpha+\beta}{2}-1}\int_{0}^{\infty} h_{sR_1}^{-1} G_{0,2}^{2,0}\left(\alpha\beta h_{SR_1}\middle|\begin{matrix}-,-\\ \frac{\alpha-\beta}{2},\frac{\beta-\alpha}{2}\end{matrix}\right) \times G_{0,2}^{2,0}\left(\frac{\alpha\beta h}{h_{SR_1}}\middle|\begin{matrix}-,-\\ \frac{\alpha-\beta}{2},\frac{\beta-\alpha}{2}\end{matrix}\right) dh_{SR_1}. \tag{4.15}$$

Further, using the [[176], Eq. 8.24.1.1] and the property of Meijer-G function [[176], Eq. 8.2.2.15], we can simplify (4.15) and get the pdf of *h* as follows:

$$f(h)=\left(\frac{(\alpha\beta)^{\frac{\alpha+\beta}{2}}}{\Gamma(\alpha)\Gamma(\beta)}\right)^{2} \frac{h^{\frac{\alpha+\beta}{2}-1}}{\mathcal{g}_1^{\frac{\alpha+\beta}{2}}}\, G_{0,4}^{4,0}\left(\frac{(\alpha\beta)^2 h}{\mathcal{g}_1}\middle|\begin{matrix}-\\ \frac{\alpha-\beta}{2},\frac{\beta-\alpha}{2},\frac{\alpha-\beta}{2},\frac{\beta-\alpha}{2}\end{matrix}\right). \tag{4.16}$$

Since the proposed system has three-hops, we will now include the PDF of the channel gain for R_2 to destination (h_{R_2D}), which is also Gamma-Gamma distributed and can be written similar to (4.12) and (4.13) as:

$$f\left(h_{R_2D}\right)=\frac{2(\alpha\beta)^{\frac{\alpha+\beta}{2}}}{\Gamma(\alpha)\Gamma(\beta)}\left(h_{R_2D}\right)^{\frac{\alpha+\beta}{2}} K_{\alpha-\beta}\left(2\sqrt{\alpha\beta h_{R_2D}}\right). \tag{4.17}$$

Now, let's consider a new random variable $h_{3e}=hh_{R_2D}$. Using (4.11) in the same way to derive $f(h)$, we obtain the PDF of the equivalent SNR at *D* as follow:

$$f(h_{3e})=\left(\frac{(\alpha\beta)^{\frac{\alpha+\beta}{2}}}{\Gamma(\alpha)\Gamma(\beta)}\right)^{3} \frac{h_{3e}^{\frac{\alpha+\beta}{2}-1}}{\mathcal{g}_1\mathcal{g}_2^{\frac{\alpha+\beta}{2}}} \times G_{0,6}^{6,0}\left(\frac{(\alpha\beta)^3 h_{3e}}{\mathcal{g}_1\mathcal{g}_2}\middle|\begin{matrix}-\\ \frac{\alpha-\beta}{2},\frac{\beta-\alpha}{2},\frac{\alpha-\beta}{2},\frac{\beta-\alpha}{2},\frac{\alpha-\beta}{2},\frac{\beta-\alpha}{2}\end{matrix}\right). \tag{4.18}$$

Last but not least, using (4.11) and the concept of transformation of RVs, we can derive the PDF of h_{eq} in Meijer-G function as:

$$f(h_{eq}) = \left(\frac{(\alpha\beta)^{\frac{\alpha+\beta}{2}}}{\Gamma(\alpha)\Gamma(\beta)}\right)^3 \frac{h_{eq}^{\frac{\alpha+\beta}{2}-1}}{(g_1 g_2 g_3)^{\frac{\alpha+\beta}{2}}} \times G_{0,6}^{6,0}\left(\frac{(\alpha\beta)^3 h_{eq}}{g_1 g_2 g_3}\middle| \begin{matrix} - , - \\ \frac{\alpha-\beta}{2}, \frac{\beta-\alpha}{2}, \frac{\alpha-\beta}{2}, \frac{\beta-\alpha}{2}, \frac{\alpha-\beta}{2}, \frac{\beta-\alpha}{2} \end{matrix}\right). \tag{4.19}$$

Following this PDF, the CDF of h_{eq} is evaluated as:

$$\begin{aligned} &F(h_{eq}) \\ &= \left(\frac{(\alpha\beta)^{\frac{\alpha+\beta}{2}}}{\Gamma(\alpha)\Gamma(\beta)}\right)^3 \left(\frac{h_{eq}}{g_1 g_2 g_3}\right)^{\frac{\alpha+\beta}{2}} \\ &\times G_{1,7}^{6,1}\left(\frac{(\alpha\beta)^3 h_{eq}}{g_1 g_2 g_3}\middle| \begin{matrix} \frac{2-\alpha-\beta}{2} \\ \frac{\alpha-\beta}{2}, \frac{\beta-\alpha}{2}, \frac{\alpha-\beta}{2}, \frac{\beta-\alpha}{2}, \frac{\alpha-\beta}{2}, \frac{\beta-\alpha}{2}, \frac{-\alpha-\beta}{2} \end{matrix}\right). \end{aligned} \tag{4.20}$$

Considering the non-return-to-zero on-off keying (NRZ-OOK) modulated signal format, the probability of error as a function of h_{eq} is given by:

$$P_e(h_{eq}) = \frac{1}{2} erfc\left(\frac{h_{eq}}{2\sqrt{2\sigma^2}}\right). \tag{4.21}$$

From (4.16) and CDF of h, the BER of the dual-hop system can be written as:

$$P_{e2} = \left(\frac{(\alpha\beta)^{\frac{\alpha+\beta}{2}}}{\Gamma(\alpha)\Gamma(\beta)}\right)^2 \frac{(8\sigma_2^2)^{\frac{\alpha+\beta+2}{4}}}{4\sqrt{2\pi\sigma_2^2}(g_1 g_2)^{\frac{\alpha+\beta}{2}} 2^2 (2\pi)^2} \times G_{3,10}^{8,3}\left(\frac{8\sigma_N^2(\alpha\beta)^4}{2^8 g_1^1 g_2^2}\middle| \begin{matrix}\frac{2-\alpha-\beta}{4}, \frac{2-\alpha-\beta}{4}, \frac{4-\alpha-\beta}{4} \\ \mathcal{G}^2, \frac{-\alpha-\beta}{4}, \frac{2-\alpha-\beta}{4}\end{matrix}\right), \tag{4.22}$$

where $\mathcal{G} = \frac{\alpha-\beta}{4}, \frac{\alpha-\beta+2}{4}, \frac{\beta-\alpha}{4}, \frac{\beta-\alpha+2}{4}$. Similarly, the BER for a triple-hop system is given as follows:

$$P_{e3} = \left(\frac{(\alpha\beta)^{\frac{\alpha+\beta}{2}}}{\Gamma(\alpha)\Gamma(\beta)}\right)^3 \frac{(8\sigma^2)^{\frac{\alpha+\beta+2}{4}}}{4\sqrt{2\pi\sigma^2}(g_1 g_2 g_3)^{\frac{\alpha+\beta}{2}} 8(2\pi)^3} \times G_{3,14}^{12,3}\left(\frac{8\sigma^2(\alpha\beta)^6}{2^{12}(g_1 g_2 g_3)^2}\middle| \begin{matrix}\frac{2-\alpha-\beta}{4}, \frac{2-\alpha-\beta}{4}, \frac{4-\alpha-\beta}{4} \\ \frac{\alpha-\beta}{4}, \frac{\alpha-\beta+2}{4}, \frac{\beta-\alpha}{4}, \frac{\beta-\alpha+2}{4}, \frac{\alpha-\beta}{4}, \frac{\alpha-\beta+2}{4}, \frac{\beta-\alpha}{4}, \frac{\beta-\alpha+2}{4}, \\ \frac{\alpha-\beta}{4}, \frac{\alpha-\beta+2}{4}, \frac{\beta-\alpha}{4}, \frac{\beta-\alpha+2}{4}, \frac{-\alpha-\beta}{4}, \frac{2-\alpha-\beta}{4}\end{matrix}\right). \tag{4.23}$$

By carefully observing (4.22) and (4.23), we can further generalize the BER expression for *N*-hop link as:

$$P_e = \left(\frac{(\alpha\beta)^{\frac{\alpha+\beta}{2}}}{\Gamma(\alpha)\Gamma(\beta)}\right)^N \frac{(8\sigma^2)^{\frac{\alpha+\beta+2}{4}}}{4\sqrt{2\pi\sigma_N^2}(g_N)^{\frac{\alpha+\beta}{2}} 2^N (2\pi)^N} \times G_{3,4N+2}^{4N,3}\left(\frac{8\sigma_N^2(\alpha\beta)^{2N}}{2^{4N}{\mathcal{F}_N}^2}\middle| \begin{matrix}\frac{2-\alpha-\beta}{4}, \frac{2-\alpha-\beta}{4}, \frac{4-\alpha-\beta}{4} \\ \mathcal{G}^N, \frac{-\alpha-\beta}{4}, \frac{2-\alpha-\beta}{4}\end{matrix}\right), \tag{4.24}$$

where $\mathcal{F}_N = g_1 g_2 \ldots g_N$, $\mathcal{G}^N$ implies that $\mathcal{G}$ is repeated *N*-times, and σ_N^2 denotes the equivalent variance for *N*-hop. Note that, if we consider the value of all gains to be equal as g then $\mathcal{F} = g^N$.

4.5 AOAF Numerical Analysis

This section presents numerical simulation using MATLAB and Optisystem software of the FSO relay-assisted system with no turbulence and the Gamma-Gamma turbulence. Throughout the analysis, we consider IM-DD based FSO system, where the information at the source *S* is transmitted to the destinations *D* via a number of all-optical relay R_i, where $i \in \{1,2, \ldots n\}$, as illustrated in Fig. 4.4. As shown in Fig. 4.4, there are no LoS paths between the *S* and *D*. We assume that, the channels between *S*, the i^{th} relay R_i and *D* are stationary, memoryless, and ergodic with independent but not necessarily identically distributed fading statistics.

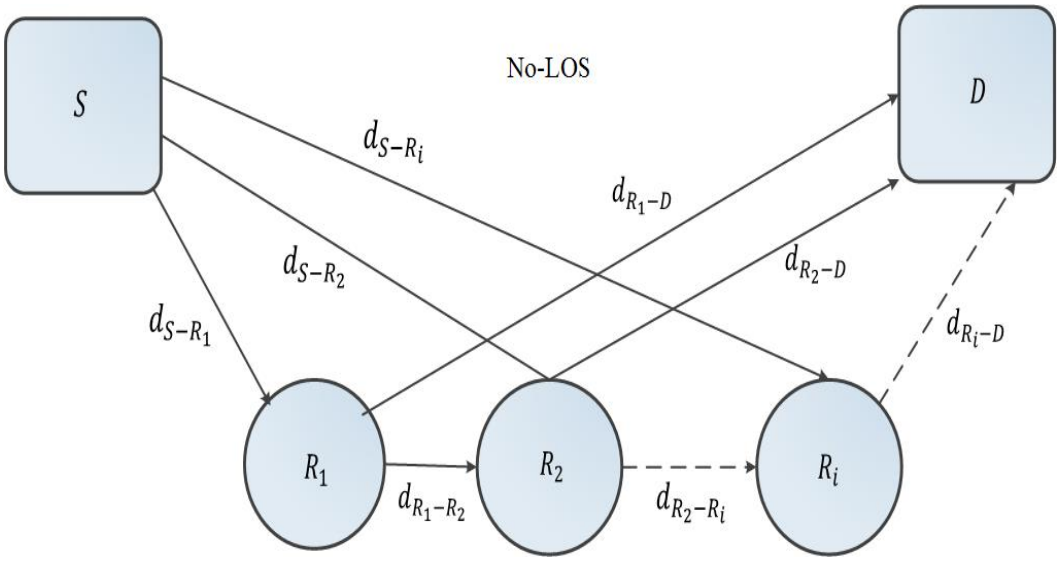

Fig. 4.4: FSO relay-assisted transmission systems.

4.5.1 Comparison of optical and electrical AF system

The numerical analysis starts by comparing the performance of a dual-hop relaying system in terms of the BER and SNR for signal amplification in optical and electrical domains under different turbulence regimes as shown in Fig. 4.5 (a) and (b),

respectively. Focusing particularly on an all-optical system using OA, we investigate the BER performance of the EDFA and the SOA, which are the most common OA used in relaying systems. Following that, we also consider the effect of aperture averaging as the additional way to combat turbulence.

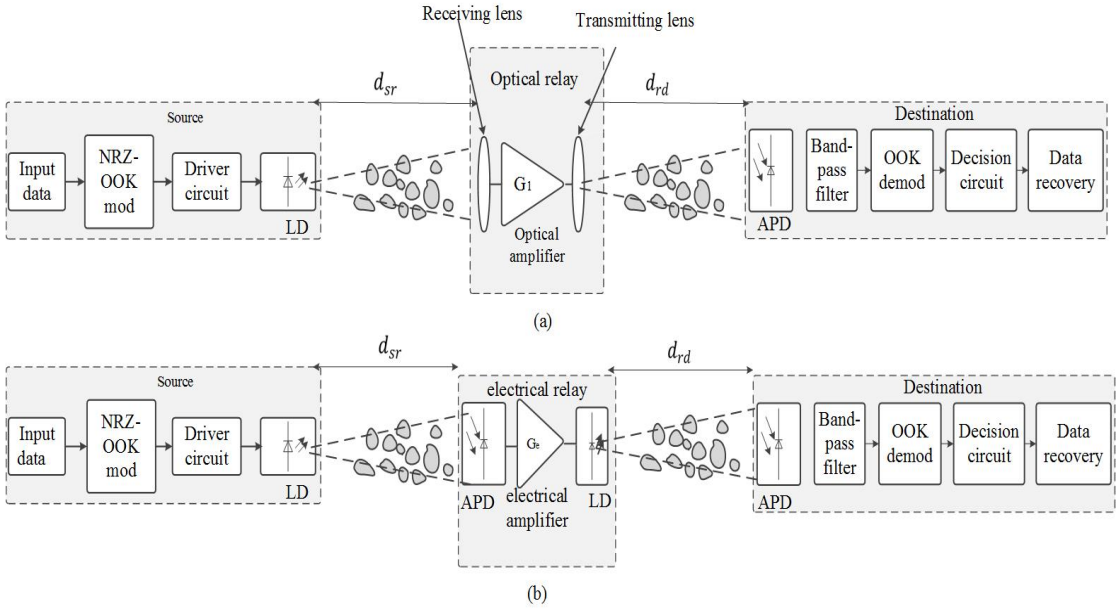

Fig. 4.5: Block diagram of AF dual-hop relay-assisted system: (a) all-optical relaying, and (b) electrical relaying.

At the Tx side, a pseudorandom bit sequence of 2^{16}–1 bit length in the NRZ-OOK signal format is generated for IM of a 1550 nm wavelength laser source at a data rate of 1 Gbps. Following propagation via the free space channel, the optical signal is amplified in the optical domain at the relay node for further transmission over the channel, see Fig. 4.5 (a). At the Rx the optical signal is then detected using an avalanche photodiode (APD). Following filtering and demodulation, a decision circuit is used to compare the detected signal with a threshold level to regenerate the original data stream. In the electrical based relay, we have used O/E and E/O conversion modules to regenerate the signal for further transmission over the free space channel, see Fig. 4.5 (b). In order to make a fair comparison, the output power levels of EDFA and SOA were kept at the same level of 2 dBm and their noise figures were set to 4.0 and 6.0 dBm, respectively as in [138]. In the

case of electrical amplifications, to compensate for channel fading variance the amplifier gain *G* to 10 dB in order to ensure that the output power of the amplifier is approximately 2 dBm. We also modelled the background radiation beat noise at the electrical relay as AWGN. The overall key system parameters are depicted in Table 4.1. The relay node is located at an equidistance between the *S* and the *D*. In order to vary the SNR, the optical transmit power P_{tx} was changed with an optical attenuator (placed after the laser diode) to sweep the input power P_{in} to the amplifier. We considered three turbulence levels of weak, moderate, and strong corresponding to σ_R^2 of 0.2, 1.6, and 3.5, respectively [7].

Table 4.1 : Dual-hop FSO system parameters

Parameter	**Value**	**Unit**
FSO Systems		
Bit rate	1×10^9	bit/s
Total link range	1000	m
Wavelength	1550	nm
Transmit power	5	dBm
Tx aperture	20	mm
Rx aperture	100	mm
Beam divergence	2	mrad
APD responsivity	1.0	A/W
EDFA		
Length	30	m
Gain shape	flat	
Noise figure	4.0	dB
SOA		
Injection current	300	mA
Length	50×10^{-6}	m
Confinement factor	0.35	
Noise figure	6.0	dB

The BER performance of a direct transmission link and the dual-hop FSO system with a fixed relay gain g_R for both optical (i.e., EDFA) and electrical amplifiers for two turbulence regimes σ_R^2 of 0.2 and 1.6 is shown in Fig. 4.6. As expected, for all link configurations, the BER performance degrades with the turbulence strength. The results also show the potential of the relaying system in combating turbulence induced fading

compared to the direct link with no relay. Furthermore, the results reveal that all-optical relaying outperforms the electrical relaying scheme, which also imposes additional complexity to the system and bandwidth restrictions [14]. For example, at a target BER of 10^{-5} there are SNR gains of ~3 dB and ~7.5 dB for the links with optical and electrical relaying, respectively, compared to the direct transmission link at $\sigma_R^2 = 0.2$. While at $\sigma_R^2 = 1.6$, the SNR gains of ~5.5 dB and ~9 dB are observed for the respective optical and electrical relaying systems when compared to the direct link. However, at higher BERs, we notice that the difference between the plots is much reduced for the two systems. This is due to the effect of the beat noise due to O/E and E/O conversions. Note that, the main noise sources are the shot noise and the electrical thermal noise, which are more dominant than the EDFA's ASE noise for the optical relaying case [177].

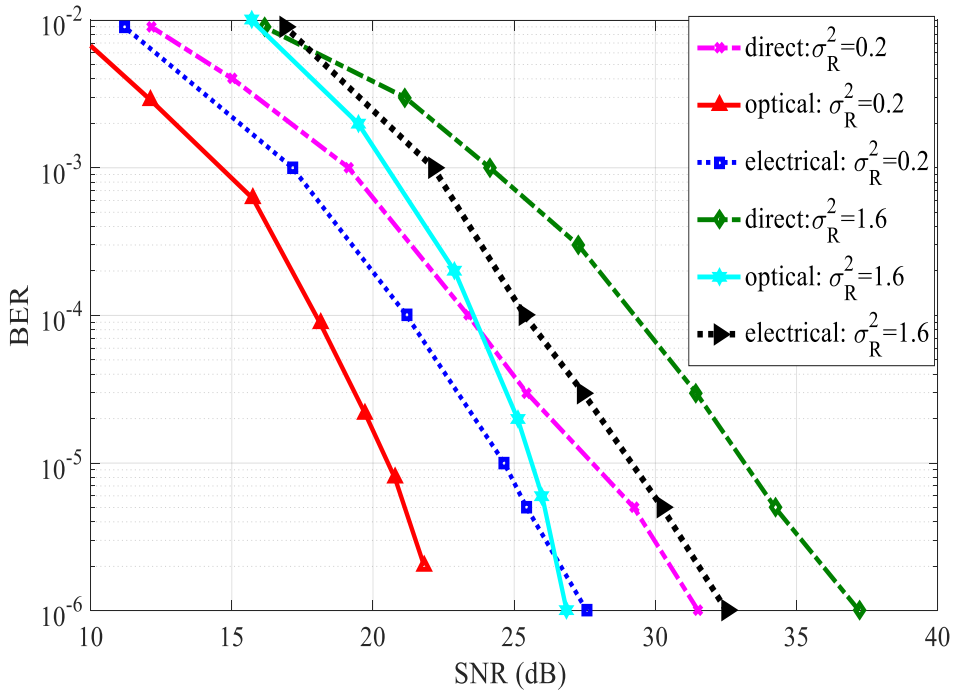

Fig. 4.6: BER versus SNR of direct transmission and dual-hop AF system for optical (EDFA-based) and electrical relaying systems for turbulence $\sigma_R^2 = 0.2$ and $\sigma_R^2 = 1.6$.

Next, we consider the simulated BER as a function of SNR for the dual-hop relaying system using EDFA and SOA for the three aforementioned turbulence regimes as depicted in Fig. 4.7. As illustrated, at a target BER of 10^{-5} the EDFA outperforms SOA

for turbulence regimes by ~2, ~3, and ~4.5 dB of SNR gains for σ_R^2 of 0.2, 1.6, and 3.5, respectively. The performance difference increases for stronger turbulence cases. This is because SOA typically has a higher noise figure and coupling loss, and suffers from increased levels of cross-talk. Note that, the coupling loss usually arises from turbulence distorted received phase of the optical signal [81]. This result also shows that the relayed transmission based on EDFA or SOA is an effective approach to improve the system performance (i.e., reduced BER or increased the transmission link span). Even though the EDFA offers improved performance compared to SOA, one may prefer to adopt the SOA due to its simpler implementation, more compact size and lower cost.

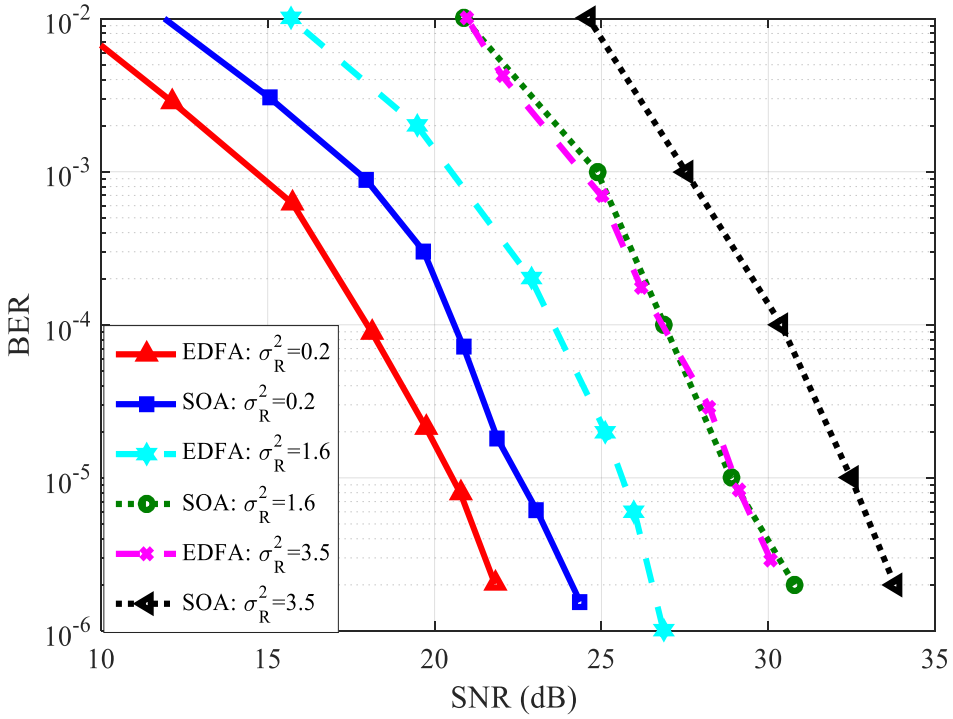

Fig. 4.7: BER versus SNR of dual-hop optical AF system using EDFA and SOA over different turbulence regimes.

Following that, we quantified the effect of Rx aperture size ∅ over the turbulence regime (i.e., $\sigma_R^2 = 1.6$) for the EDFA–based relaying system as illustrated in Fig. 4.8. The plots confirm the significant performance improvement obtained by increasing ∅. For instance, at a target BER of 10^{-5} the SNR gain and penalty of ~5.5 dB and ~ 10 dB

were achieved for ∅ increased from 100 mm to 300 mm and for ∅ reduced from 100 mm to 20 mm, respectively. Using a larger ∅, results in the Rx averaging out more fluctuations over the aperture and ultimately lower the BER. However, the trade-off by increasing ∅ is the system cost and the need for a PD with a larger active area. The larger area of Rxs can also result in collecting more background noise intrinsic to the wide aperture area.

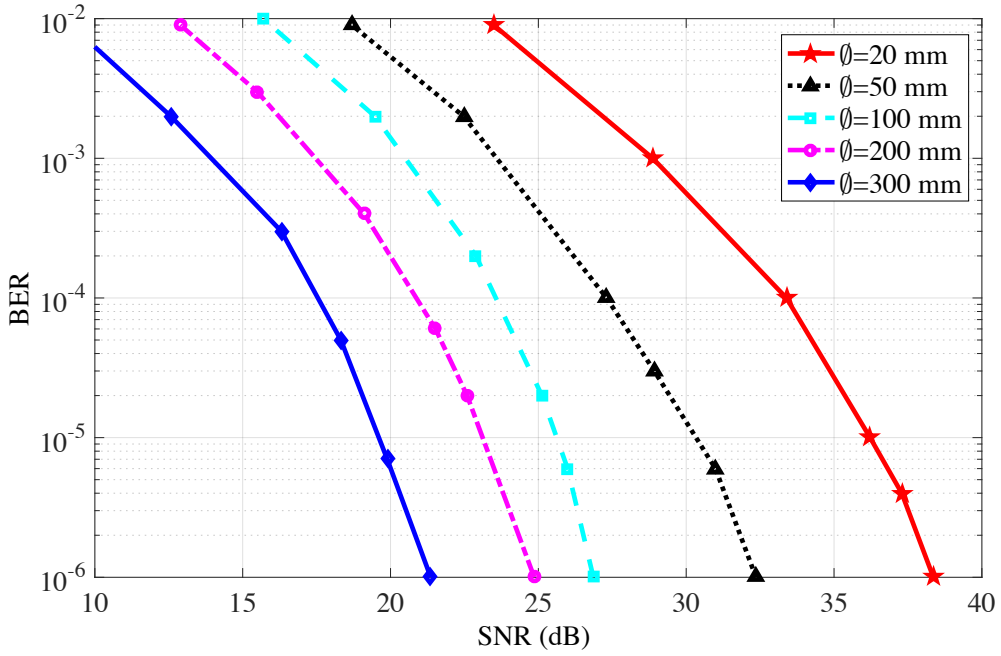

Fig. 4.8: BER versus SNR of EDFA-based optical relaying dual-hop AF system for different Rx aperture sizes ∅ over the moderate turbulence regime with $\sigma_R^2 = 1.6$.

4.5.2 Comparison of NRZ-OOK and RZ modulation format

This sub-section presents numerical BER analysis simulation of the triple-hop FSO relay-assisted system with no turbulence and with a strong turbulence regime σ_R^2 of 3.5 for NRZ-OOK and RZ-OOK formats. The bit rate, the signal amplitude, and the bandwidth were considered to be the same for both data formats in order to ensure a fair system performance comparison. We also set the consecutive nodes as equidistant along

the path (from the source to the destination) to ensure that the SNR is the same for each hop.

Fig. 4.9 shows the simulated BER as a function of SNR for NRZ-OOK and RZ-OOK for the triple-hop FSO link with no turbulence and with turbulence (i.e., $\sigma_R^2 = 3.5$). Also shown in insets are the eye diagrams and *Q*-factors for several values of SNR as an alternative indicator of the link performance. These results clearly illustrate the adverse effect of turbulence on the system under test, which significantly degrades the BER performance and the opening of eye-diagrams compare to the case with no turbulence. The plots also show that RZ-OOK offers improved BER performance and higher *Q*-factor compared to the NRZ-OOK. For example, at a target BER of 10^{-6} there is a SNR gain of ~1.3 dB for RZ-OOK compared to considering NRZ-OOK with no turbulence. However, with turbulence (of $\sigma_R^2 = 3.5$) there are ~3.5 dB and ~5.0 dB of SNR penalties for RZ-OOK and NRZ-OOK, respectively. Also, it is observed from the figure that for a BER of 10^{-7} the *Q*-factors are 4.86 and 5.06 for NRZ-OOK and RZ-OOK, respectively over the turbulence regime. This performance improvement is achieved at the cost of doubling the transmission bandwidth [19].

Fig. 4.10 presents the numerically simulated BER as a function of SNR for single, dual-hop, and triple-hop FSO links for NRZ-OOK and RZ-OOK over a strong turbulence regime $\sigma_R^2 = 3.5$. As predicted, the BER performance improves as the number of the hops increases from single-to-triple hop links regardless of the modulation scheme. Likewise, the plots confirm once again the advantage of RZ over NRZ. As it can be seen from the figure, RZ-OOK outperforms NRZ-OOK by ~1.9, ~1.7 , and ~1.5 dB in terms of the SNR gain for single, dual, and triple-hop links, respectively. Furthermore, at a target BER of 10^{-6} and by considering RZ-OOK, dual-hop and triple-hop links provide SNR gains of ~5.0 dB and ~6.2 dB, respectively compared to direct transmission. These

substantial improvements show the potential of multi-hop FSO transmission in combating the turbulence effect.

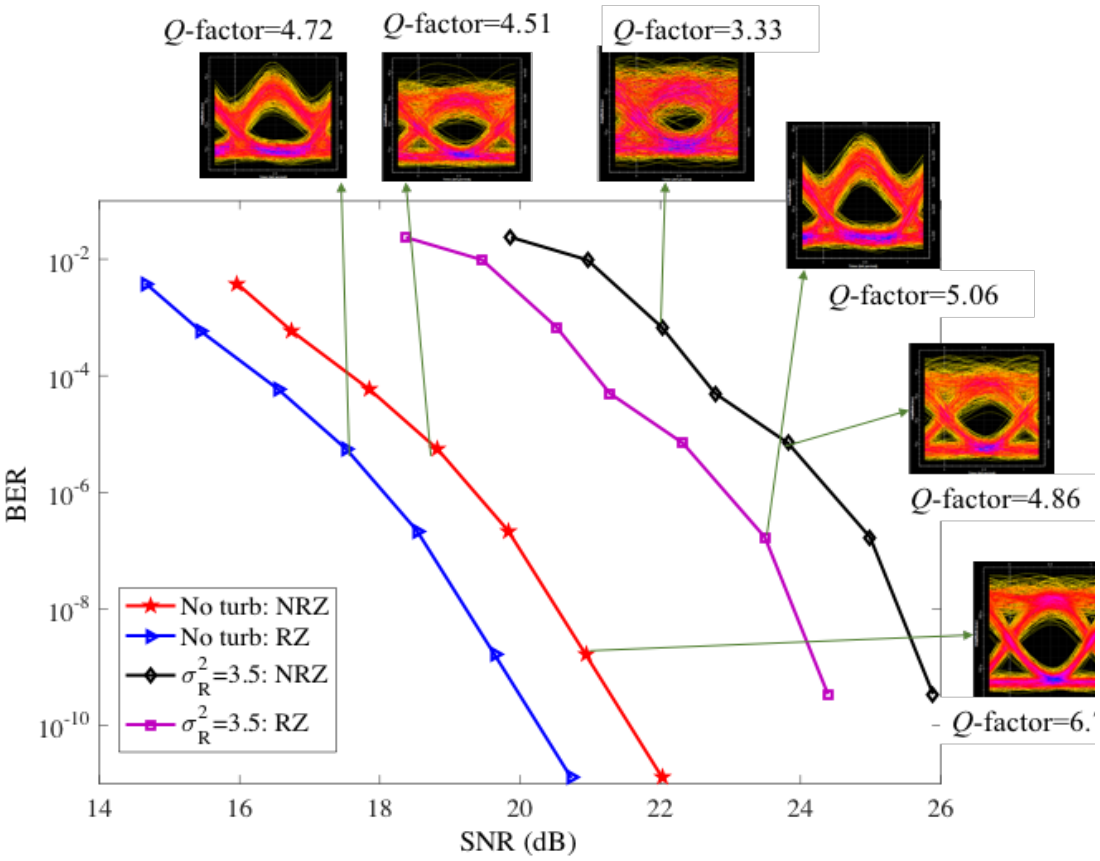

Fig. 4.9: Numerical simulation of BER vs SNR for NRZ and RZ triple-hop FSO links over no turbulence and turbulence $\sigma_R^2 = 3.5$.

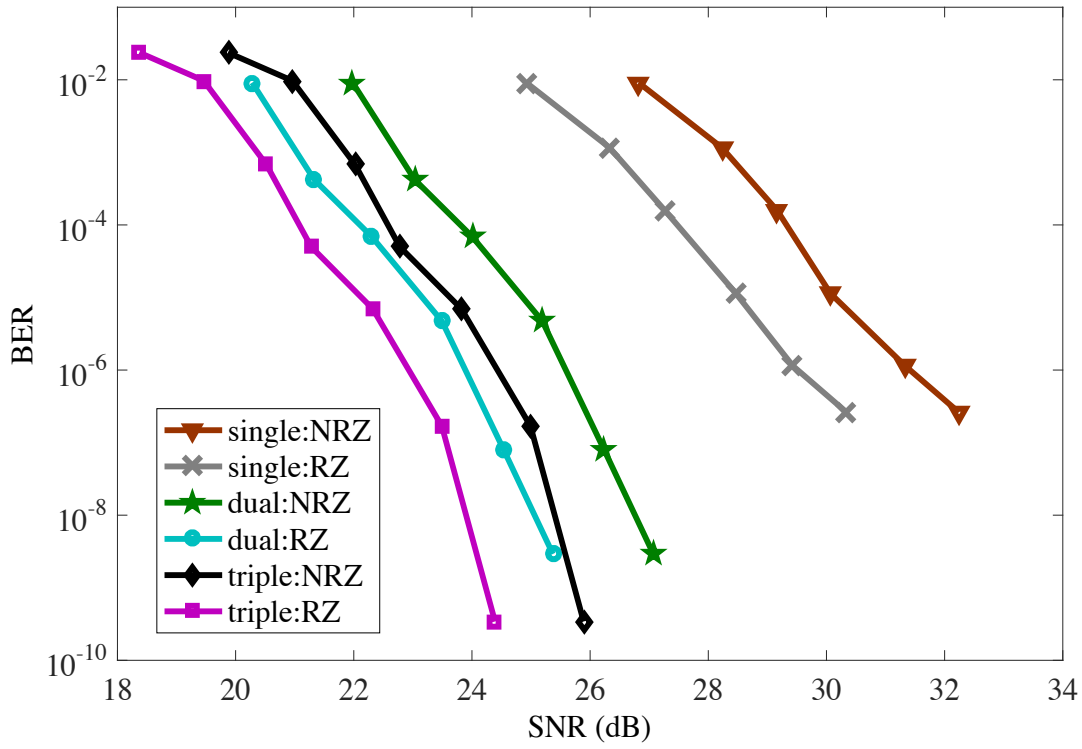

Fig. 4.10: Numerical simulation of BER vs SNR for single, dual, and triple-hop FSO links of NRZ-OOK and RZ-OOK with turbulence $\sigma_R^2 = 3.5$.

4.6 Experimental Analysis for Single, Dual-Hop, and Triple-Hop AF Systems

Using the outdoor FSO measurement set-up it is challenging and time consuming to carry out full system performance evaluation under all weather conditions. However, using the purpose built indoor laboratory testbed we are able to carry out comprehensive measurement campagin for the proposed system under a controlled environment over a short time scale. In order to increase the reliability of measuring results, each measurement was taken three times over a 5-minute time interval between each measurement.

4.6.1 Triple-hop AF experimental setup

The schematic diagrams of proposed indoor experimental single, dual-hop, and triple-hop AF FSO relay assisted systems setup are illustrated in Fig. 4.11 (a), (b), and (c), respectively. The systems are composed of a combination of FSO links of a total span of 6.6 m, EDFA, single mode fibers (SMF), and optical components. As shown in Fig. 4.11(a), at the Tx, a signal source/BER tester (BERT-VeEX VEPAL TX300) is used to generate a pseudo-random binary sequence (PRBS) d_i in the NRZ-OOK format at R_{d} of 10 Gbps for IM of a 1550 nm distributed feedback (DFB) laser diode. An optical digital attenuator and a 50/50 coupler are used to control the level of transmit power P_s and split the signal into two, for both transmission and monitoring using an optical spectrum analyzer (OSA). The laser output is then launched into the free space channel via a gradient-index (GRIN) fiber collimator (Thorlabs 50-1550A-APC) with a clear aperture diameter lens of 0.18 cm. In order to focus the optical beam and minimize the divergence of the optical beam, two plano convex lenses Lens 1 and Lens 2 with a focal length f of 10 cm were placed after the Tx and before the Rx, respectively. At the Rx, a GRIN fiber collimator is used to couple the received optical beam into the SMF the output of which is amplified using an EDFA. The signal is then applied via a 50/50 coupler to an OSA and a BERT for the link assessment in terms of the BER and SNR. Both dual-hop and a triple-hop AF FSO relay system were implemented based on Fig. 4.11(a). Fig. 4.12 depicts the photo of an indoor experimental setup for the triple-hop AF FSO link.

In a controlled indoor environment using a dedicated atmospheric chamber, the strength of turbulence is controlled by blowing hot air from two 2 kW external heating fans in the direction perpendicular to the propagating optical beam along the transmission path. The heating sources were positioned near and/or away from the FSO Tx or Rx as shown in Fig. 4.13. In order to maintain a constant temperature gradient within the chamber well above the required 6° C along the propagation path the temperature were

kept at the room temperature of ~25° C and within the range of 25° C to 80° C, respectively with the wind speed of <10 m/s. The strength of turbulence was varied by means of controlling the output of the fan heaters and thus varying the temperature profile. Moreover, two plastic barriers were placed at the ends of optical table in order to maintain the temperature profile along the chamber. To continuously monitor the temperature profile along the channel and ultimately be able to determine C_n^2, we recorded the instantaneous temperatures every 4 seconds throughout the experiment using 20 temperature sensors positioned at 0.28 cm apart along the channel (i.e., between the Tx and the Rx) as shown in Fig. 4.12 (b). While carrying out the experimental measurement with no turbulence, we ensured that the temperature along the channel was kept at the room temperature. With turbulence, we continuously recorded the temperature at 20 different positions T_1-T_{20} along the channel. The close up shot of LoS FSO link 1, 2, and 3 are depicted in Fig. 4.13. All the main parameters adopted in the experimental setup are summarized in Table 4.2.

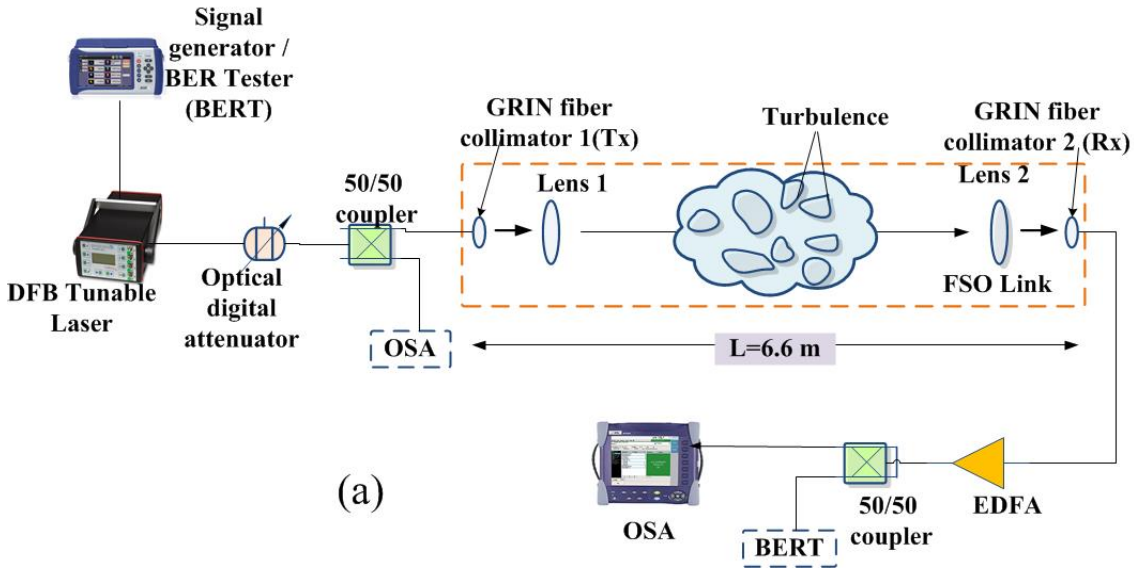

(a)

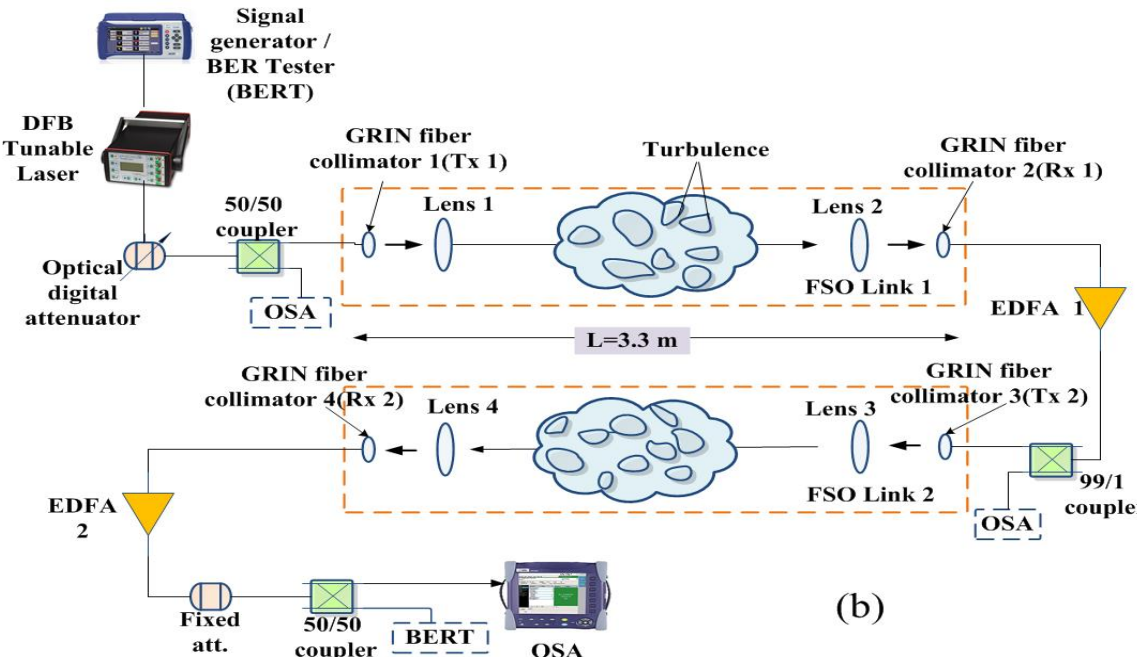

(b)

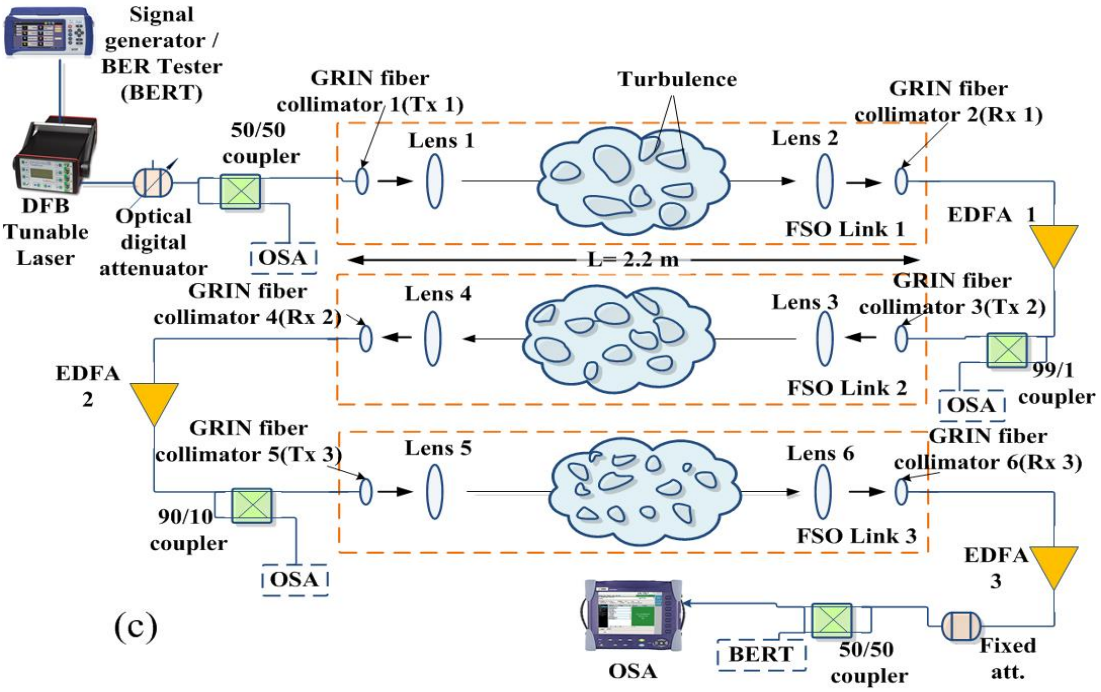

(c)

Fig. 4.11: Block diagram of the experimental setup of: (a) direct link, (b) dual-hop, and (c) triple-hop AF FSO relay-assisted systems.

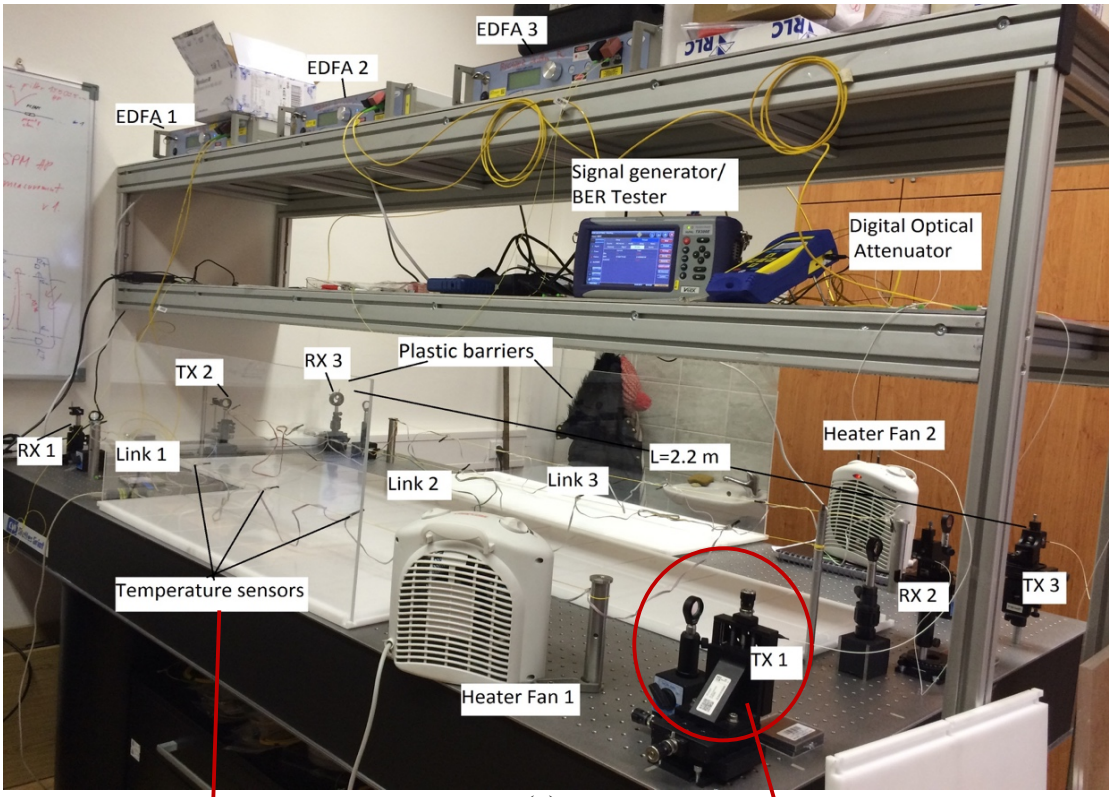

(a)

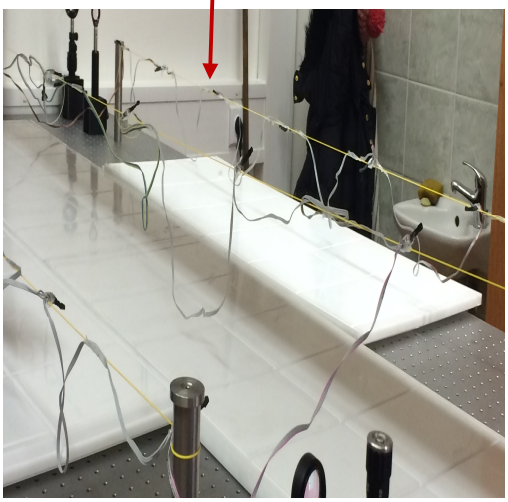

(b)

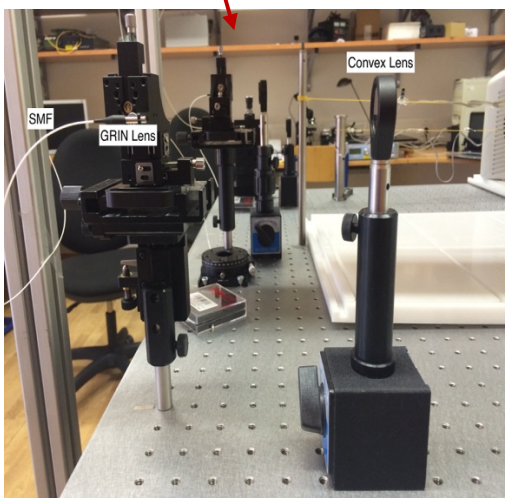

(c)

Fig. 4.12: Snapshot of the: (a) laboratory triple-hop FSO link setup, (b) temperature sensors, and (c) Tx 1 (GRIN and convex lenses).

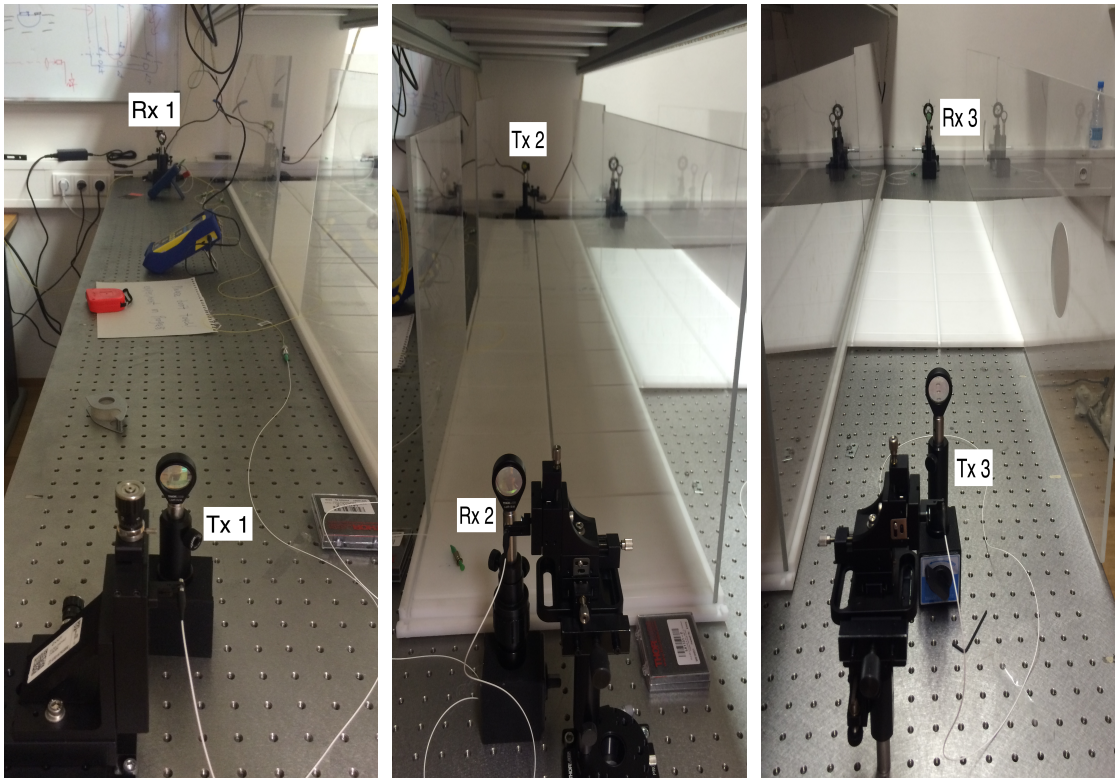

Link 1 Link 2 Link 3

Fig. 4.13: Line-of-sight of FSO link 1, link 2, and link 3.

Table 4.2 Main parameters used in experiment

	Parameter	Value
Transmitter	Data rate and signalling scheme	10 Gbps NRZ-OOK
	Laser type	DFB
	Wavelength	1550 nm
	Output power	0.91 dBm
	Grin-lens aperture	0.18 cm
	Beam divergence	0.25 mrad
Lens	Clear aperture	2.54 cm
	Focal distance	10 cm
EDFA	Max. ouput power	21 dBm
	Noise figure	< 7.5 dBm
Receiver	Clear aperture	0.18 cm
	Rx type	PIN
	Rx sensitivity	-16 to -1 dBm
	Responsivity	0.6 A/W
SMF-28	Mode-field diameter @1550 nm	10.4 ± 0.8 μm
	Attenuation @ 1550 nm	≤ 0.2 dB/km

4.6.2 Experimental results

4.6.2.1 Turbulence measurement

The scintillation effect due to atmospheric turbulence is simulated by exploiting the dependence of the channel index of refraction on the temperature variations. As aforementioned, the turbulence simulation process involves blowing hot air using two heaters fans at two different locations into the chamber. 20 temperature sensors were used to measure the instantaneous temperature every 4 seconds along the FSO propagation path. The variations of the temperature are shown in Fig. 4.14 below in terms of C_T^2 with respect to the temperature sensors gap along the propagation links, which proves the high variation of temperature obtained thus leading to higher C_n^2.

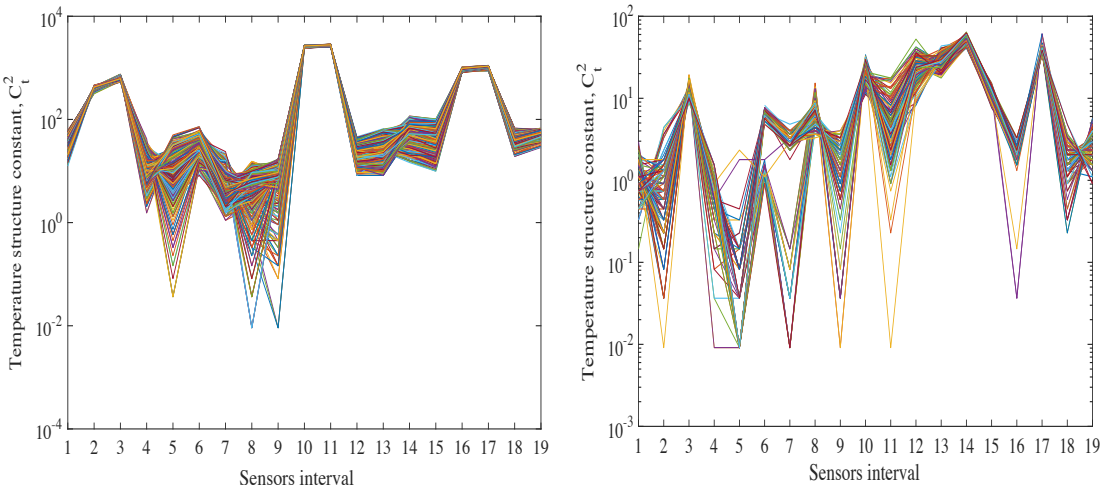

(a) (b)

Fig. 4.14: C_T^2 against temperature sensors gap for: (a) $C_n^2 = 3.8 \times 10^{-10}\ m^{-2/3}$, and (b) $C_n^2 = 5.4 \times 10^{-12}\ m^{-2/3}$

Fig. 4.15 shows the histograms of C_T^2, where the number of occurrence is normalized to the unity, which represents the occurrence PDF. By fitting the C_T^2 experimental data to the Gamma-Gamma distribution curve, we can see a good match between theoretical and measurement data. From the fit, we can confirm that the C_n^2 will be as accurate as possible.

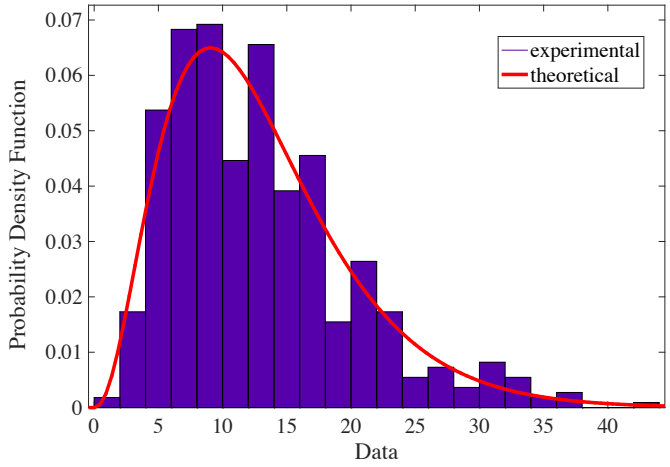

(a)

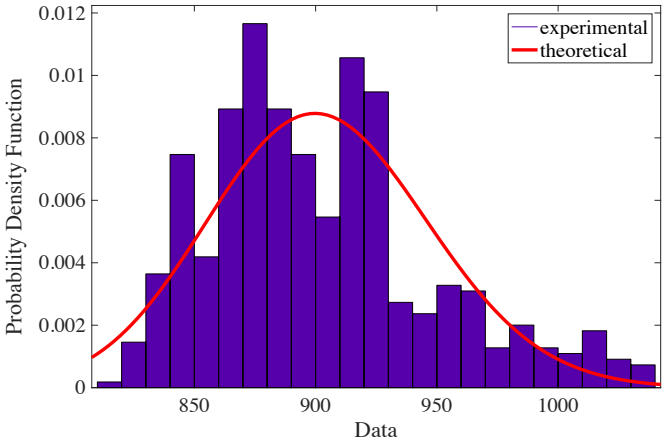

(b)

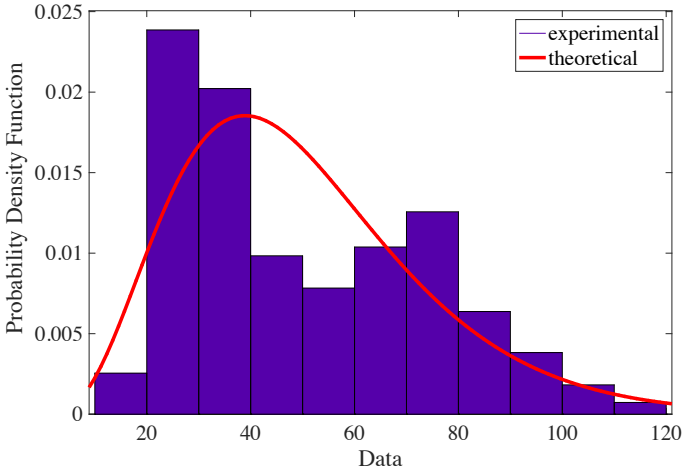

(c)

Fig. 4.15: (a), (b), and (c): Example of data sets for C_T^2 distribution; experimental and theoretical based on Gamma-Gamma distribution

4.6.2.2 Results and discussions

In this section, the experimental results for the single, dual-hop, and triple-hop all-optical FSO relay-assisted systems with and without turbulence are presented. The relays are located at equal distance between *S* and *D* in order to ensure that FSO links were balanced and the SNR was the same for each hop. Based on the measured temperature profile and calculations using 2.13, 2.14, and 2.16, we have determined three average values for C_n^2 of 3.8×10^{-10} m$^{-2/3}$, 5.5×10^{-11} m$^{-2/3}$, and 5.4×10^{-12} m$^{-2/3}$, which correspond to σ_R^2 of 0.77, 0.11, and 0.01, respectively for a total link span of 6.6 m. Results are validated theoretically by means of numerical evaluation of the BER using (4.23).

Fig. 4.16 presents comparison of measured and theoretical BER performance for single, dual, and triple-hop FSO links under a clear channel with no turbulence. We can observe from the figure that with the serial relay-assisted technique there is a remarkable improvement in the BER performance compared to the link with no relays. For example, for the measured data, at a BER of 10^{-5} there are ~3.0 dB and ~6.0 dB of SNR gains for dual and triple-hops, respectively compared to the single FSO link. Note that, by splitting the overall link span into smaller sections more energy (or power) is conserved. Notice the perfect match between theoretical and measured plots for all cases, particularly for the BER values below 10^{-4}. The slight mismatch between predicted and measured plots at higher values of BER (i.e., $>10^{-4}$) is due to losses associated with the optical components and ASE noise of EDFA in experimental case.

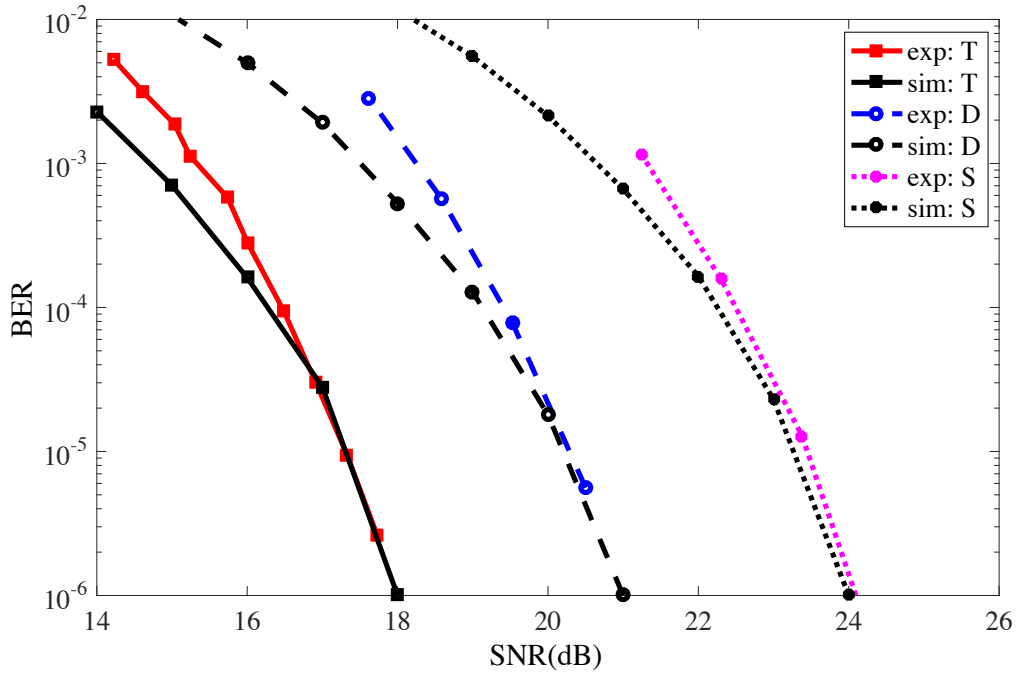

Fig. 4.16: Experimental (exp) and theoretical (theo) results for BER vs. SNR for single (*S*), dual-hop (*D*), and triple-hop (*T*) with no turbulence

Fig. 4.17 then illustrates the measured and predicted BER performance against the SNR for single, dual, and triple-hop FSO links under a turbulence regime (i.e., $C_n^2 = 3.8 \times 10^{-10}$ m$^{-2/3}$) compared with the experimental result for the triple-hop link with no turbulence. As expected, under a stronger turbulence regime the propagating optical wave front will experience much higher degree of intensity and phase fluctuations [21]. Similar to Fig. 4.16, we observe that the relay-assisted schemes offer much improved BER performance compared to the direct FSO link. For example, at a target BER of 10^{-5}, (well below the forward error correction standard of 10^{-3}) the SNR gains are ~1.5 dB and ~4.2 dB for dual-hop and triple-hop links, respectively for the measured data when compared to the direct FSO link experiencing the same level of turbulence. These higher performance gains are because of the ability of multi-hop transmissions to exploit the distance-dependent turbulence induces fading variance. Comparing the predicted with experimental results confirms the validity of the BER analysis outlined in Section 4.4. Note that, at a BER of 10^{-5} the SNR penalty for the triple-hop link with turbulence is ~4

dB when compare to the same link without turbulence. This additional SNR is required to compensate for the turbulence induced power fades.

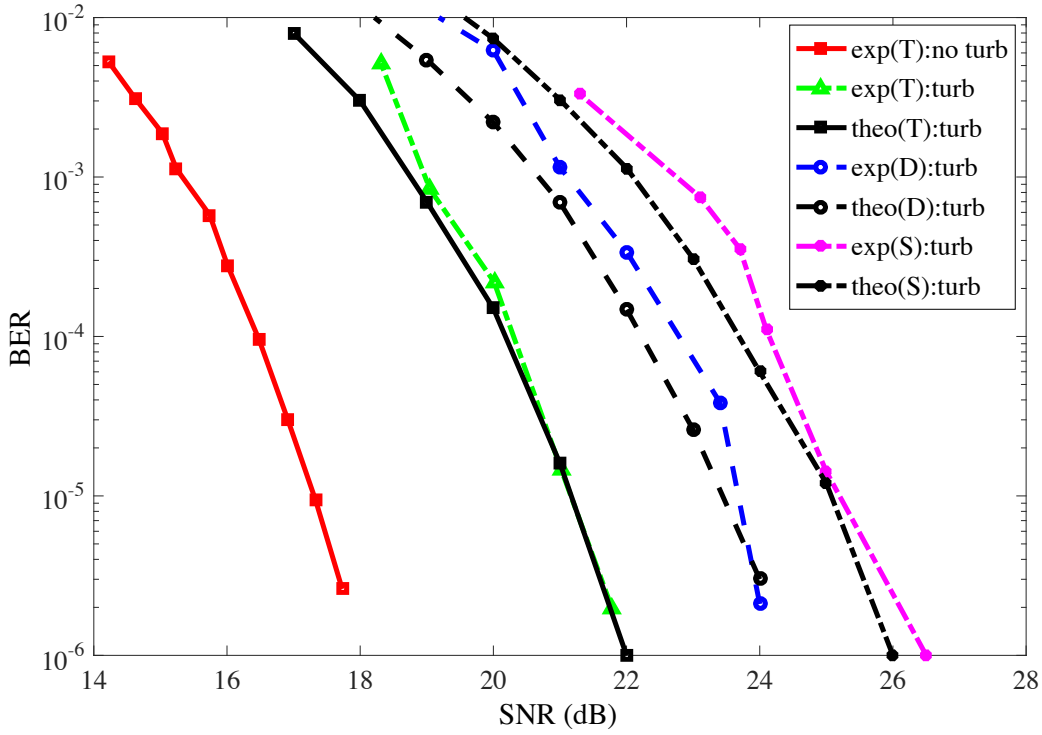

Fig. 4.17: Experimental (exp) and theoretical (theo) results for BER vs. SNR for *S*, *D*, and *T* for $C_n^2 = 3.8\times10^{-10}$ m$^{-2/3}$, and exp. T with no turbulence

Furthermore, Fig. 4.18 depicts the experimental and theoretical results for the BER performance against the SNR for single, dual-hop, and triple-hop FSO links for $C_n^2 = 5.4\times10^{-12}$ m$^{-2/3}$. As a benchmark, the measured BER of a triple-hop link with no turbulence is also shown in the figure. By increasing the number of hops/relays, there is an improvement in the SNR requirement. The results confirm the potential of the relaying system in combating the turbulence induced fading compared to the direct single link. As observed, there is a trade-off between the number of relays and the average P_s to achieve a particular BER. For example, for measured plots at a BER of 10^{-5} the SNR gains are ~2.8 dB and ~4.8 dB for dual-hop and triple-hop, respectively compared to the single FSO link. As mentioned before, these SNR gains are because of reduced effects of the

turbulence as the link span is shortened in relayed based systems. The marginal differences between the theoretical and measured plots in terms of SNR less than 0.5 dB at higher values of BER stem from the fact that no ideal theoretical turbulence flow can be experienced in real practical environment. Furthermore, at a BER of 10^{-5} and $C_n^2 = 5.4 \times 10^{-12}$ $m^{-2/3}$, the SNR penalty for the triple-hop link is ~2.0 dB compare to link with no turbulence. The SNR penalty is approximately 2.0 dB less compared to the link with $C_n^2 = 3.8 \times 10^{-10}$ $m^{-2/3}$ as in Fig. 4.17.

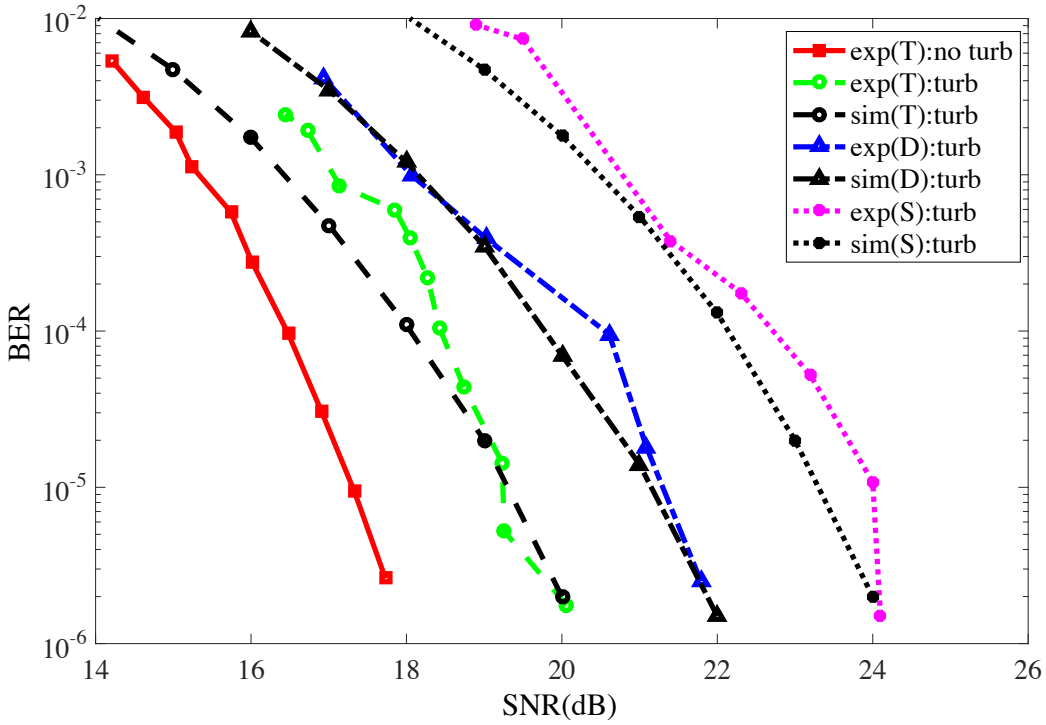

Fig. 4.18: Experimental (exp) and theoretical (theo) results for BER vs. SNR for *S*, *D*, and *T* links for $C_n^2 = 5.4 \times 10^{-12}$ $m^{-2/3}$, and an exp. T link with no turbulence

Moreover, Fig. 4.19 illustrates the measured and theoretical BER performance against the SNR for the case of triple-hop FSO link for different turbulence levels. We can observe reasonable match between the analytically simulated and measured plots. However, for lower values of SNR, the analytical results slightly differ from the measured data owing to the OA noise. The BER performance degrades with the turbulence strength. For example, at a BER of 10^{-5} the SNR penalties are ~ 2.0 dB, 3.7 dB, and ~4.0 dB for

C_n^2 of 5.4×10^{-12} $m^{-2/3}$, 5.5×10^{-11} $m^{-2/3}$, and 3.8×10^{-10} $m^{-2/3}$, respectively compared to the link with no turbulence. Note, at higher levels of turbulence the beam front of propagating optical wave experiences higher level of intensity and phase fluctuations, which ultimately leads to much wider, scattered and random optical beam patters at the Rx as discussed in [29]. This characteristic is best described by Kolmogrov's theory of turbulence where the refractive index changes in the order of several parts per million in every 1°K variation in the atmospheric temperature [32].

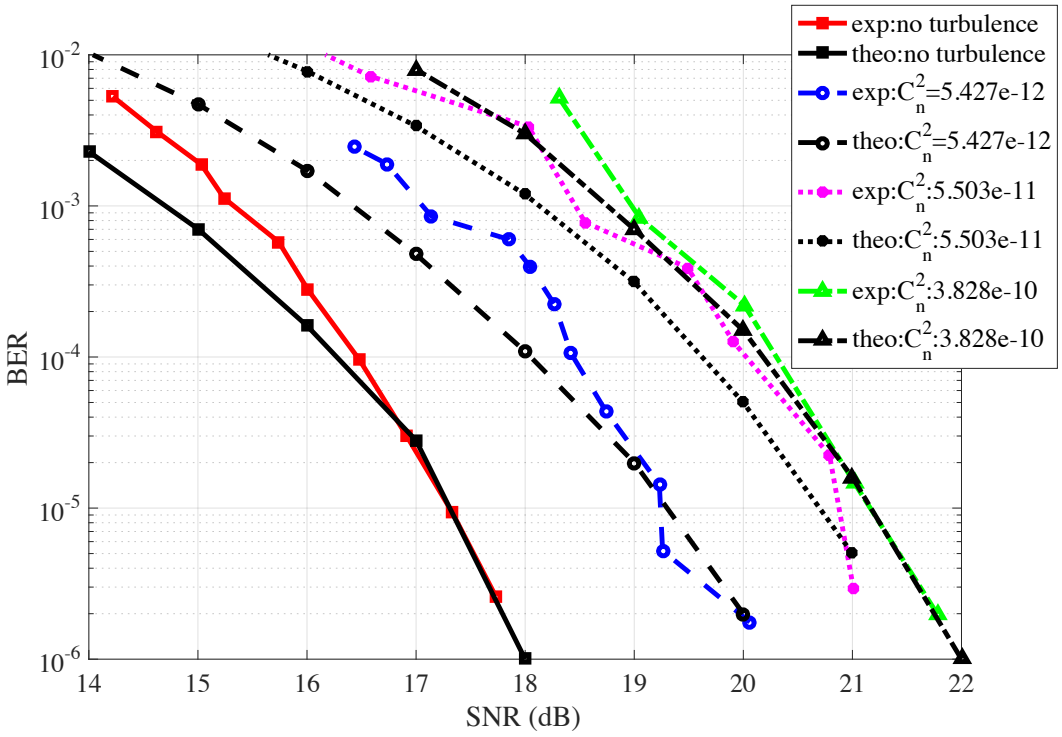

Fig. 4.19: Experimental (exp) and theoretical (theo) results for BER vs SNR for *T*-hop link with and without turbulence.

Finally, in order to provide more insight into the practical application of the system, we further consider the extension of the link span to 500 m, which is compatible with the last mile network access typical requirements in urban areas [7]. Fig. 4.20 shows the simulated BER performance for single, dual-hop, and triple-hop all-optical relay-assisted FSO links for C_n^2 of 10^{-12} and 10^{-16} $m^{-2/3}$, representing typical strong and weak

turbulence regimes in an outdoor environment [178]. The plots confirm that the proposed scheme can successfully be adopted in a real practical environment, to ensure link availability and quality performance under turbulence conditions. For example, at a target BER of 10^{-3} the triple-hop link offers SNR gains of ~4 dB and ~5 dB for $C_n^2 = 10^{-16}$ and 10^{-12} $m^{-2/3}$, respectively, compared to the single link transmission case.

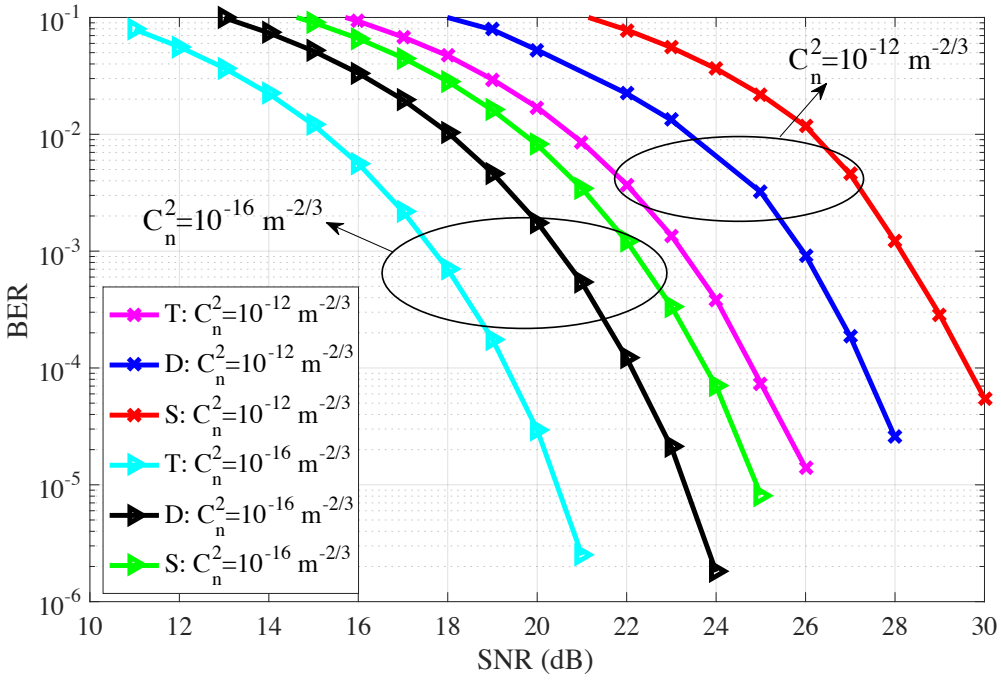

Fig. 4.20: Simulated BER performance for all-optical *S*, *D*, and *T*-hops FSO links for C_n^2 of 10^{-12} $m^{-2/3}$ and 10^{-16} $m^{-2/3}$ and a total link span of 500 m

Using the oscilloscope, we captured the eye diagrams for the single, dual-hop, and triple-hop FSO link over $C_n^2 = 5.4 \times 10^{-12}$ $m^{-2/3}$ for BER values of 10^{-6}, 10^{-4}, and 10^{-2} respectively as shown in Fig. 4.21. From the eye diagrams, we obtained the *Q*-factor values of 7.68, 4.86, 3.21 for triple-hop, 6.87, 3.92, and 2.8 for dual hop, and 5.06, 3.11, and 1.31 for single link and each value corresponding to BER values of 10^{-6}, 10^{-4}, and 10^{-2}, accordingly. Note that, for BER of 10^{-6}, the widest eye opening is observed using the triple-hop link, and reduces substantially by reducing the number of hops. Consequently, the height and width of the eye openings keep decreasing with higher attenuation levels, thus leading to deterioration of the link performance and increased in timing jitter. The

worst case scenario was experienced for the single link at a BER of 10^{-2} with the eye opening almost closed and a Q-factor of 1.31. The similar pattern of eye diagrams were captured for the case of $C_n^2 = 3.8 \times 10^{-10}$ $m^{-2/3}$ for single, dual-hop, and triple-hop for BER values of 10^{-6}, 10^{-4}, and 10^{-2} as depicted in Fig. 4.22. For a higher turbulence level, the Q-factor decreases as BER increases. For example, for the triple-hop system, at BER values of 10^{-6}, 10^{-4}, and 10^{-2} the Q-factors are 6.05, 3.91, and 2.12, respectively. While for the single-hop system, the eye diagrams were completely shut and cannot be captured at a BER of 10^{-2}. This can be explained as follow. When the optical beam propagates through the turbulence channel, the beam experiences scattering (phase fluctuation) and power losses. The longer the link, more light beams are lost. By shortening the distance, the fading variances along the link decrease, and ultimately improves the performance of the relay-assisted system. This improvement is due to the fact that fading variance is distance-dependent in a FSO channel and relay-assisted transmission takes advantage of the resulting shorter hops.

	(a) Triple-hop	(b) Dual-hop	(c) Single link
BER=10^{-6}	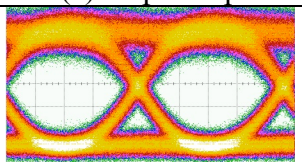 Q=7.68	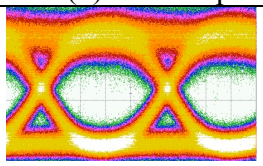 Q=6.87	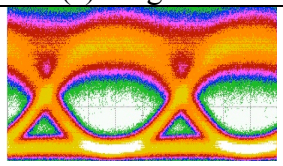 Q=5.06
BER=10^{-4}	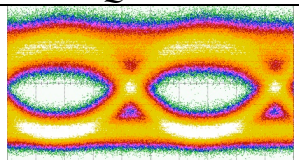 Q=4.86	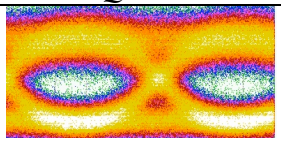 Q=3.92	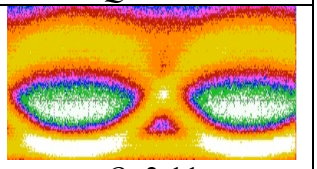 Q=3.11
BER=10^{-2}	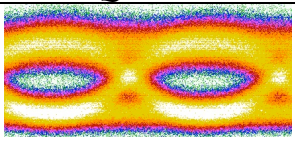 Q=3.21	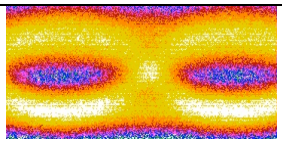 Q=2.8	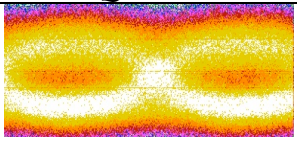 Q=1.31

Fig. 4.21: Measured eye-diagrams of received FSO system for: (a) triple-hop, (b) dual-hop, and (c) single link for BER values of 10^{-6}, 10^{-4}, and 10^{-2}, respectively over $C_n^2 = 5.4 \times 10^{-12}$ $m^{-2/3}$.

	(a) Triple-hop	(b) Dual-hop	(c) Single link
BER=10^{-6}	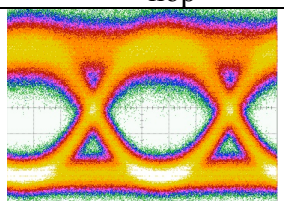 Q=6.05	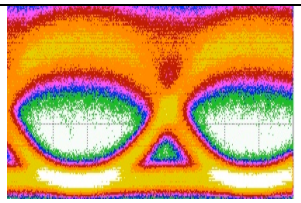 Q=4.83	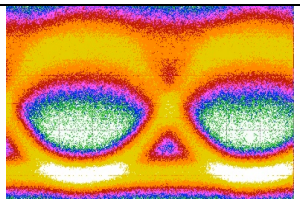 Q=4.06
BER=10^{-4}	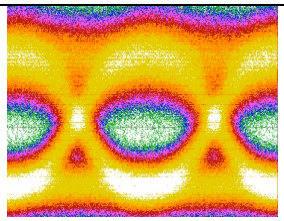 Q=3.91	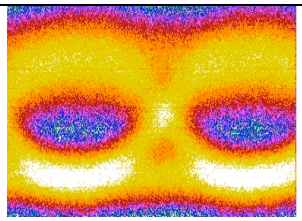 Q=3.1	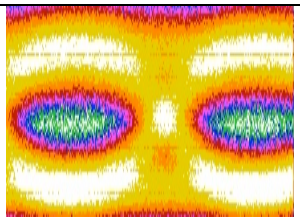 Q=2.62
BER=10^{-2}	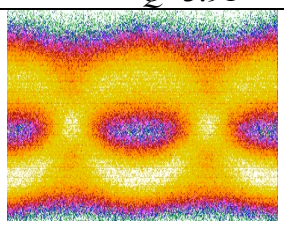 Q= 2.12	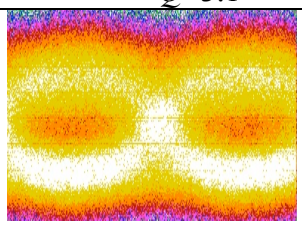 Q=0.95	Eye diagram could not be captured

Fig. 4.22: Measured eye-diagrams of received FSO system for: (a) triple-hop, (b) dual-hop, and (c) single link for BER values of 10^{-6}, 10^{-4}, and10^{-2}, respectively over $C_n^2 = 3.8 \times 10^{-10}$ $m^{-2/3}$.

4.7 Performance Analysis of a Triple-Hop FSO System with Turbulence

In Section 4.6, we considered identical turbulence conditions over the entire hops. However in real scenarios, each hop can experience different turbulence regimes. This is because turbulence can be localized to a small area due to the different thermal flows in close vicinity of buildings, in open and semi-open urban and suburban areas, heating from air conditioning units etc. Therefore, in this section, we extend our previous investigations by considering each hop experiencing different turbulence regimes and consequently evaluate the link's performance via experimental and numerical simulations.

4.7.1 Experimental setup

The triple-hop all-optical FSO setup and system parameters are similar as discussed in Section 4.6.2. For the purpose of investigating the effect of turbulence occurrence for the individual hop, we considered seven different turbulent scenarios, as illustrated in Fig. 4.23, and the no turbulence case (used as benchmark). Note that, with no turbulence the temperature was kept constant at the room temperature along the propagation path. We organized the investigation into three main categories: (i) a single hop with turbulence, see Fig. 4.23 (a, b, and c) with $C_n^2 = 6.6 \times 10^{-10}$ m$^{-2/3}$; (ii) two hops with turbulence, where $C_n^2 = 2.1 \times 10^{-10}$ m$^{-2/3}$ for links 1 and 2 (link 3 with no turbulence) and $C_n^2 = 2.2 \times 10^{-10}$ m$^{-2/3}$ for links 2 and 3 (link 1 with no turbulence), see Fig. 4.23 (d) and (e); and (iii) three hops with turbulence with $C_n^2 = 3.8 \times 10^{-10}$ m$^{-2/3}$ as shown in Fig. 4.23 (f) and with $C_n^2 = 1.2 \times 10^{-9}$ m$^{-2/3}$ for link 1 and $C_n^2 = 2.3 \times 10^{-10}$ m$^{-2/3}$ for links 2 and 3, see Fig. 4.23 (g). In order to isolate each section and ensure a specific temperature gradient within the chambers we used plastic dividers that were placed between them.

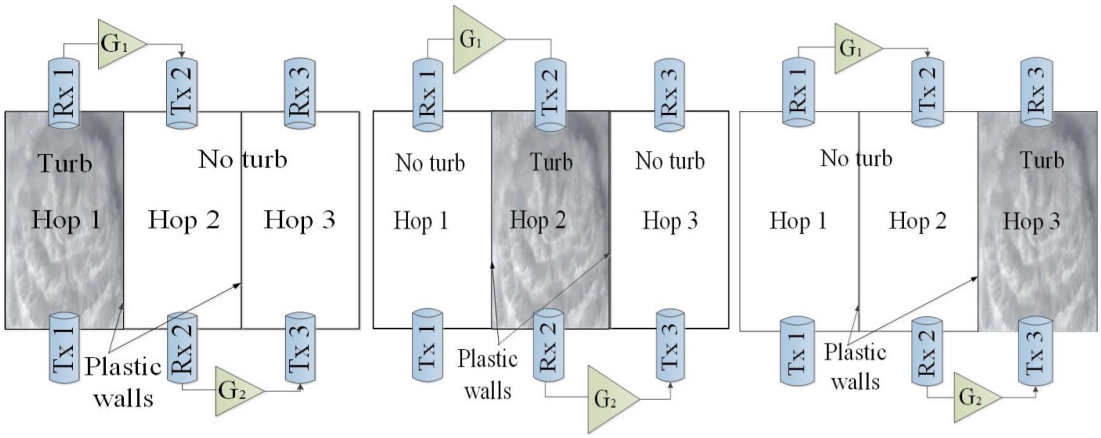

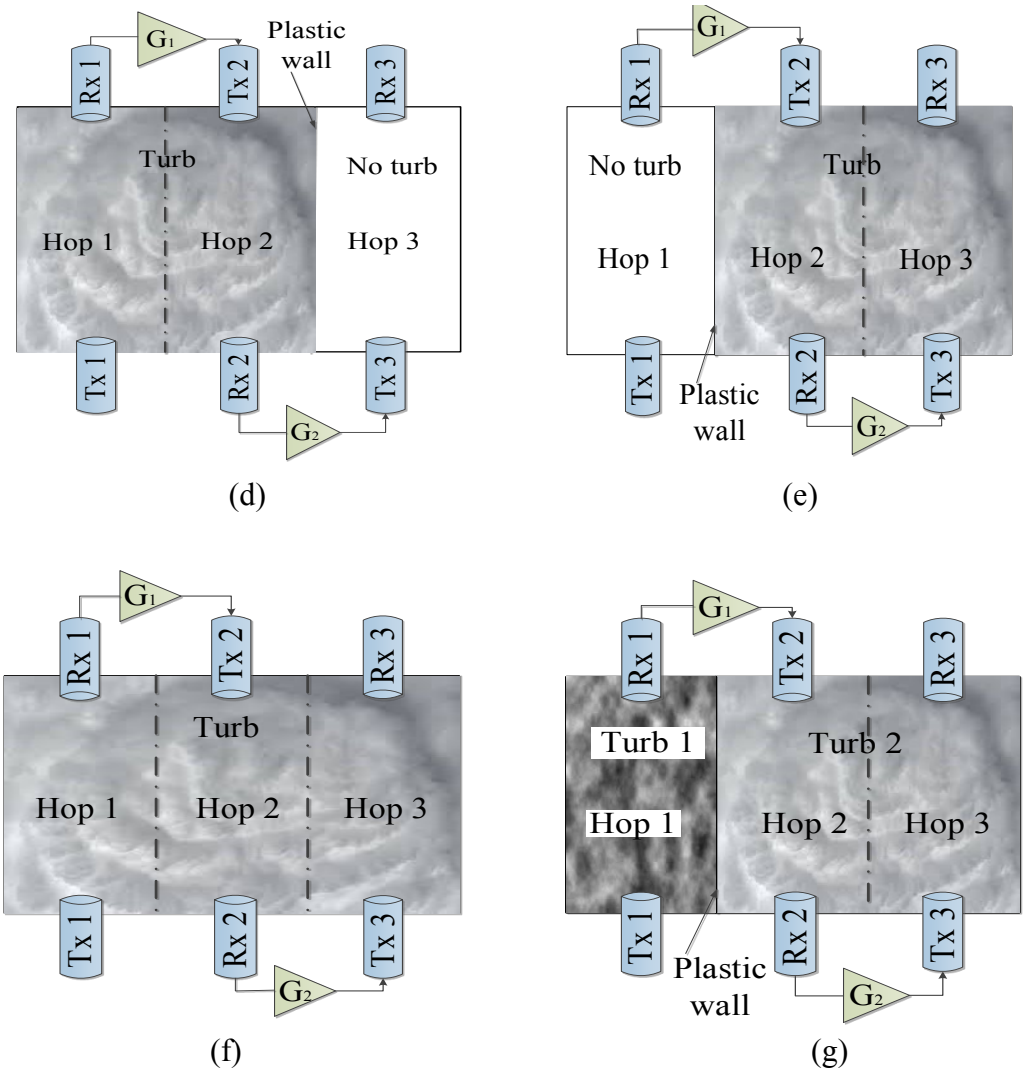

Fig. 4.23: Different test cases with turbulence (turb): (a), (b), (c) links 1, 2, and 3 are affected by turbulence; (d) links 1 and 2 with the turbulence and link 3 is with no turbulence, (e): links 2 and 3 with the same turbulence level and link 1 with no turbulence; (f) all links with the same turbulence regime; and (g) link 1 with different turbulence strength and links 2 and 3 with the same turbulence level.

4.7.2 Results and analysis

This section presents the measured BER results for the triple-hop AOAF FSO system for the seven aforementioned turbulence conditions. The experimental results are also validated by means of numerical simulations. We furthermore evaluate the worst case scenario with each hop of 500 m long, as a typical practical case study e.g., as in the last mile network access.

A. One hop with turbulence

We begin with the case where only a single link is experiencing turbulence, see Fig. 4.23(a)-(c). Fig. 4.24 depicts the measured and simulated BER as a function of optical SNR. Also shown for reference is the measured BER for the case with no turbulence. As we can see, the plot (c) displays the worst performance compared to plots (a) and (b). For example, at a target BER of 10^{-4} the SNR penalties are approximately 2.3, 3.5, and 4.5 dB for plots (a), (b), and (c), respectively, compared with no turbulence case. Note that, there is a good match between the measured and predicted plots. The slight mismatch between the plots could be due to the losses from optical components as well as the ASE noise of EDFA in the experiments. These results reveal that in multi-hop FSO links the location of turbulence have impact on the entire link performance. The multi-hop link performance is significantly affected when the turbulence occurs close to the Rx end.

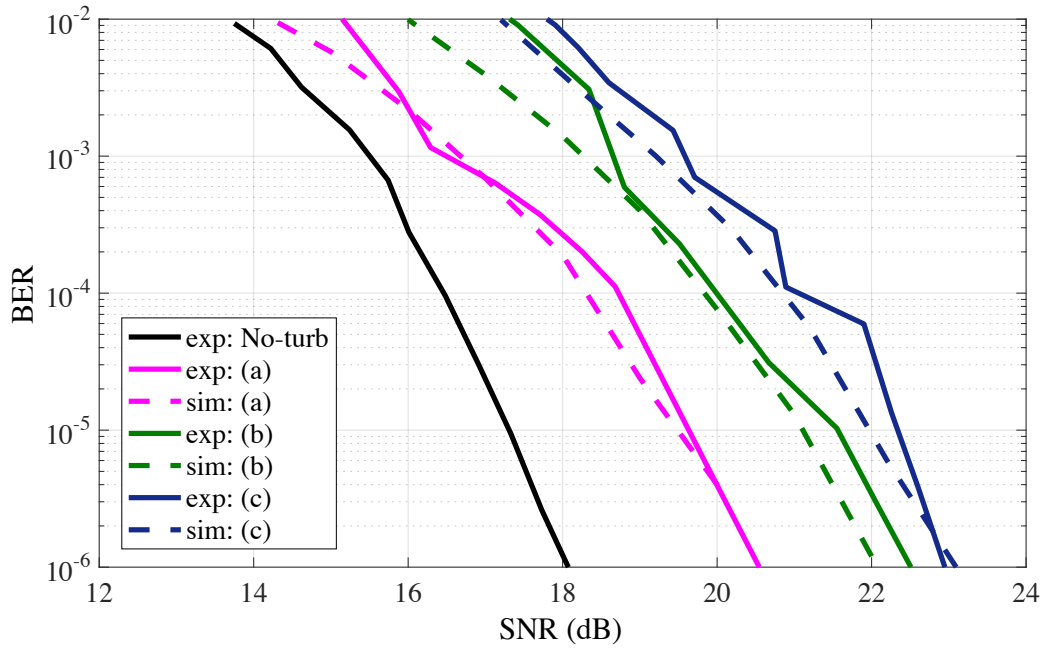

Fig. 4.24: Experimental (exp) and simulated (sim) BER vs. the optical SNR for NRZ-OOK triple-hop FSO relay-assisted system for: (a) no turbulence (No-turb) and links shown in Fig. 4.23 (a), (b), and (c),

B. Two hops with turbulence

Now let's consider the case where two out of the links (i.e., hops) are impaired by the same turbulence conditions. Fig. 4.25 depicts the BER as a function of SNR for the uncoded NRZ-OOK FSO system with the configurations shown in Fig. 4.23 (d) and (e), where there is a good match between the experimental and simulated results. Here, we notice that the plot (e) show the worst case, where turbulence is near the Rx end. This is in consistence with the conclusions of the previous subsection. E.g., for a target BER of 10^{-4} the SNR penalties are about 3.7 and 5.3 dB for plots (d) and (e), respectively compared with the no turbulence case.

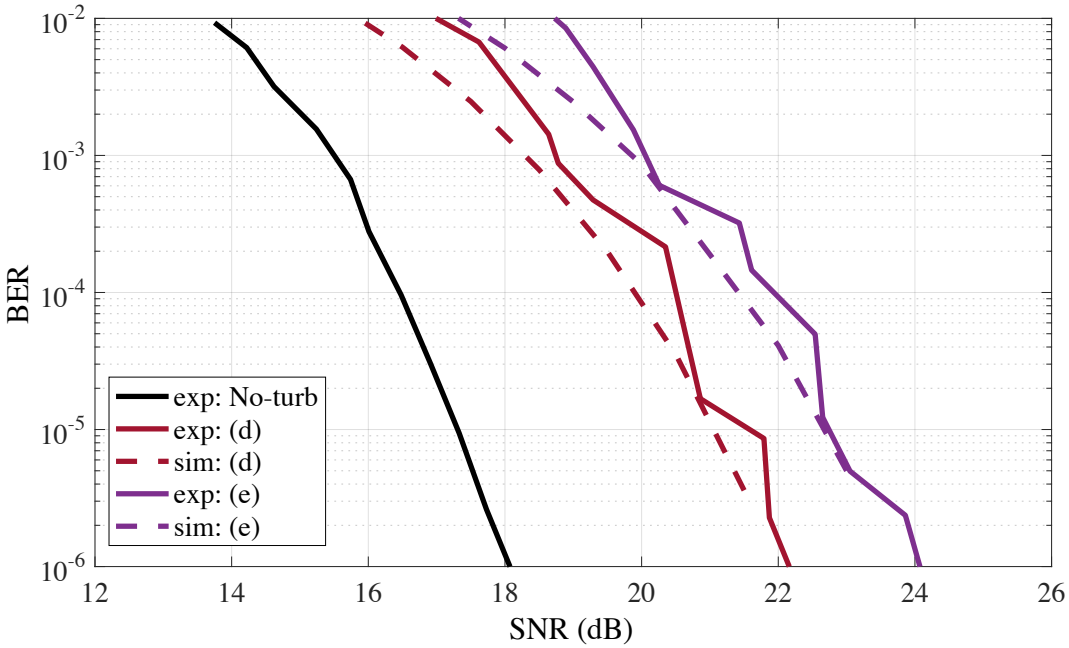

Fig. 4.25: Experimental (exp) and simulated (sim) BER vs. the optical SNR for NRZ-OOK triple-hop FSO relay-assisted system for no turbulence (No-turb) and links shown in Fig. 4.23 (d) and (e).

C. All hops with turbulence

Finally, we consider the most common case where all hops are experiencing some scale of turbulence, see Fig. 4.23 (f) and (g), where the BER results are shown in Fig. 4.26. For fair comparison, we have also included a simulated plot (denoted as h), which

is the inverse turbulence condition of (g) with $C_n^2 = 2.3\times10^{-10}$ m$^{-2/3}$ for the link 1 and $C_n^2 = 1.2\times10^{-9}$ m$^{-2/3}$ for links 2 and 3. As expected, the plot (h) with the most significant turbulence effect around the Rx end has the worst performance. Compared to the no turbulence case and for a BER of 10^{-4} we have SNR penalties of about 3.5, 6.3, and 7.4 dB for plots (f), (g), and (h), respectively.

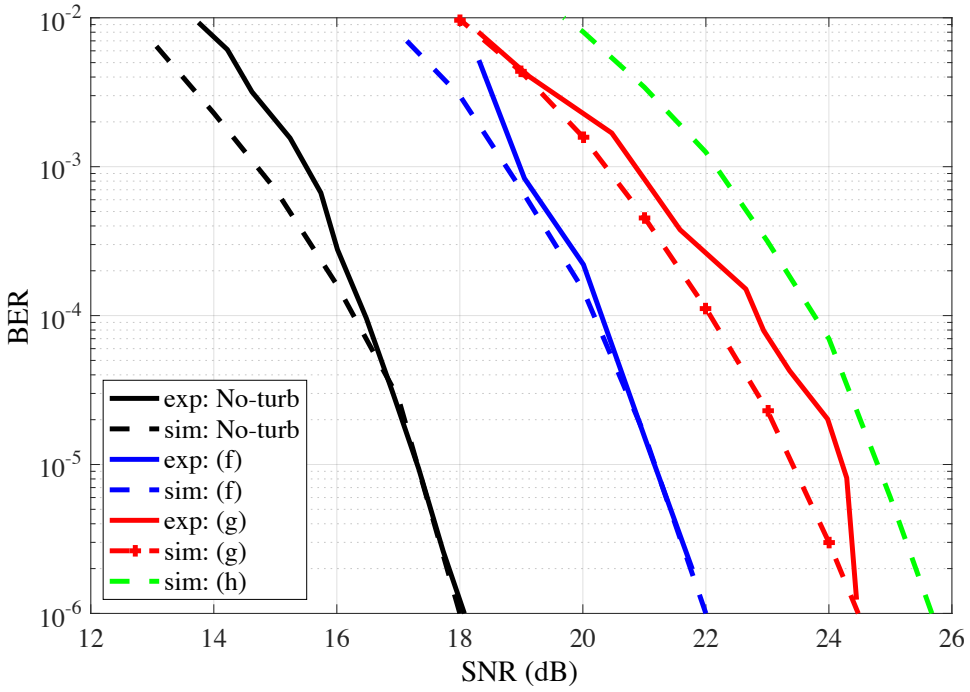

Fig. 4.26: Experimental (exp) and simulated (sim) BER vs. the optical SNR for NRZ-OOK triple-hop FSO relay-assisted system for no turbulence (No-turb) and links shown in Fig. 4.23 (f) and (g), and sim (h).

D. Extensions for the case of longer link span

In order to get an insight to the effect of turbulence in a practical outdoor link, we have extended our investigations of the worst case plots from Fig. 4.24, Fig. 4.25, and Fig. 4.26 by scaling the total link span to 1500 m with plots shown as (cR), (eR), and (hR) in Fig. 4.27. This is a fair example of the last mile network access in urban areas [7], where in order to consider typical outdoor conditions, we assume the weak-to-moderate turbulence regime with $C_n^2 \sim 10^{-14}$ m$^{-2/3}$ [9]. Fig. 4.27 shows the simulated BER

performance against the SNR for uncoded NRZ-OOK FSO for three scenarios: (i) plot (cR) only for the link 3 with $C_n^2 = 10^{-14}$ m$^{-2/3}$; (ii) plot (eR) for links 2 and 3 with C_n^2 =10^{-14} m$^{-2/3}$; (iii) and plot (hR) corresponds to the link 1 with $C_n^2 = 10^{-15}$ m$^{-2/3}$ and links 2 and 3 with $C_n^2 = 10^{-14}$ m$^{-2/3}$. As expected, the BER plots follow the same trend as in Fig. 4.24, Fig. 4.25, and Fig. 4.26 but in case of an outdoor link, with increased SNR penalties between different cases. E.g., at a BER of 10^{-4} we notice SNR penalties of about 4, 5.8, and 9.1 dB for scenarios (cR), (eR), and (hR), respectively compared to the no turbulence case.

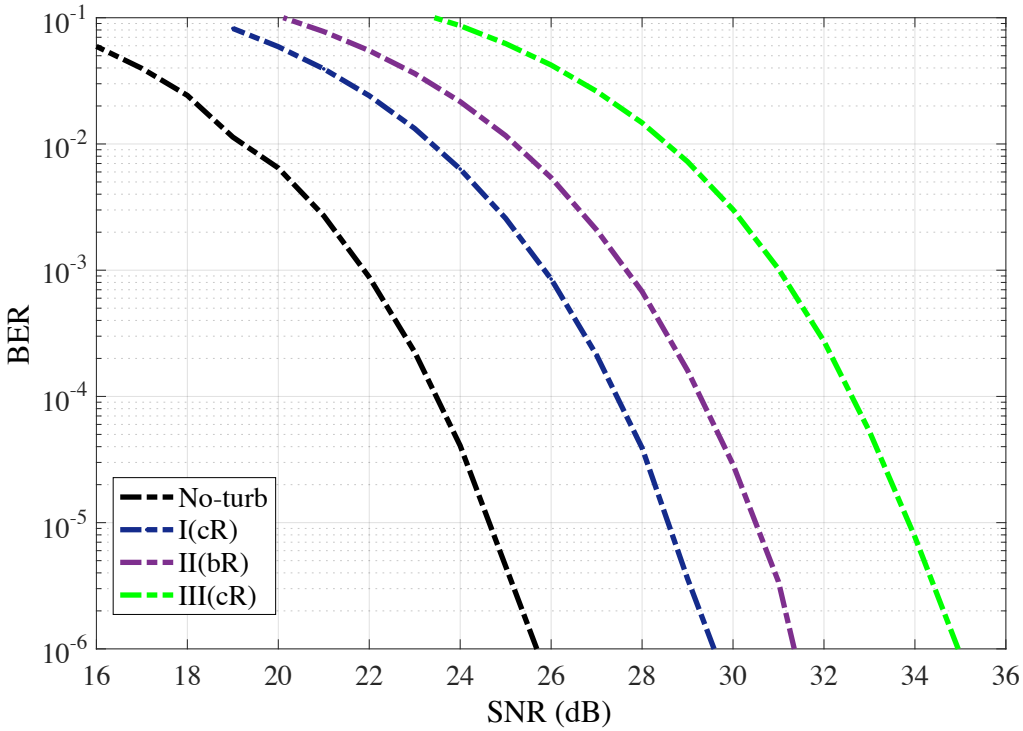

Fig. 4.27: Simulated BER vs. the optical SNR uncoded NRZ-OOK for all-optical triple-hop FSO relay assisted link with a total link span of 1500 m for no turbulence (No-turb), and turbulence cases of (cR), (eR), and (hR).

4.8 Summary

In this chapter, we investigated the performance of all-optical FSO links using the AF relaying technique over turbulence channels. AF is the simplest technique of relay-

assisted system by simply amplify and forward the received signal to the next relay/destination. With the help of OA, AF scheme becomes a prominent method to improve the overall system performance while reducing the distance-dependent turbulence effect. We carried out the numerical analysis and provided a mathematical framework for the end-to-end SNR and BER performances for the general multi-hop relay-assisted FSO link considering the Gamma-Gamma turbulence model. We validated the analysis through the experimental and we showed that good agreements were obtained between the analytical and measurements. The experimental analyses were divided into two parts, where in first part the performances of single, dual-hop, and triple-hop FSO system were investigated through identical turbulence channel. It means that we considered that all the hop experienced the same turbulence induced fading variance with the same C_n^2. In the analysis, we confirmed that there is an improvement in the SNR when the number of hops/relays increase. Thus, the results proved the potential of relaying turbulence induced fading compared to the direct single link.

On the other hand, we considered each hop of the triple-hop AOAF FSO system experiencing different turbulence regimes in the second part of analysis. The performances were evaluated experimentally and analytically. The results showed that the most significant turbulence effect around the Rx end has the worst performance. The notable and highlighted findings in this chapter have motivated the development of another technique of all-optical relaying to further optimize the performance of the relay-assisted system, which will be presented in Chapter 5.

Chapter 5

ALL- OPTICAL REGENERATE-AND-FORWARD RELAYING TECHNIQUE

5.1 Introduction

FSO communications are severely affected by the atmospheric turbulence fading. In Chapter 4, an AOAF relaying technique was thoroughly discussed via theoretical and experimental validations. Even though AOAF is the simplest technique that can be implemented, OAs amplify the signal and noise together. Thus, there is a limited number of relay that can be implemented, since after the saturation point, the performance of the system will start to degrade, as more noise will be amplified than the signal itself. Therefore, AORF is introduced in this chapter as means to overcome this particular problem by eliminating the background noise at each relay and consequently regenerating the signal for longer transmission link distance. The ability to regenerate signals also ensures maximum flexibility in network design and architecture, by providing greater tolerance in adding or dropping channels [2].

The all optical regeneration technique is likely to be an important block within future optical communication systems for high-speed operations, as well as to increase

scalability, capability, and flexibility. Several regeneration architectures that rely on optical nonlinear effects have been proposed to replace the widespread optoelectronic regenerators that are currently used for long haul systems. Although all-optical 3R (re-amplification, reshaping, and retiming) regenerators have demonstrated great performance and versatility, 2R (re-amplification and reshaping) regenerators can be used beneficially in medium distance transmission systems [179].

All-optical 2R regeneration has attracted considerable interest due to its simpler and cheaper implementation compared to the 3R regeneration technique. The 2R regeneration technique is important especially for transmitting high data rates signal, which has been realized through a number of nonlinear phenomena such as SPM, four-wave mixing (FWM), cross-phase modulation (XPM), and stimulated Raman Scattering. Among these phenomena, SPM is most often utilised effect due to its simplicity, since neither a pump source nor a probe source are required. In general, 2R regenerators lead to an extinction ratio improvement and an amplitude noise reduction [180].

The next generation of AORF techniques, which will strongly depend on nonlinear effects, has already attracted significant research and development efforts. However, the technology is still considered to be in its infancy, and as such, more research is required before the technology is ready for wide scale commercial deployment. In this chapter, an AORF relaying technique is introduced for a relay-assisted FSO communication link to enhance the capability of FSO networks. An SPM based 2R regenerator, also known as a Mamyshev regenerator, was implemented in our AORF system, where the basic components consist of an EDFA, a HNLF, and an OBPF. The EDFA is used to boost the power to broaden the spectrum in the HNLF, while the OBPF is utilised to reshape the signal by selecting the desired portion of the signal only. Compared to the AOAF, which only requires an EDFA at the relay, this new AORF system provides better performances by removing all of the accumulated noise prior to

re-transmitting the signal to the next destination. The contribution of this chapter is to analyse the performance of AORF FSO dual-hop systems under the effects of turbulence channels. The performance of the aforementioned systems is tested experimentally in terms of BER, SNR, and *Q*-factor, in a controlled laboratory environment.

The rest of the chapter is organized as follow: Section 5.2 introduces the background and associated literatures pertaining to the investigation studies and performance analysis of optical regeneration in optical communication systems. Section 5.3 outlines the mathematical concepts behind the SPM-based AORF FSO system. An experimental analysis of the aforementioned system is presented in Section 5.4, where the experimental setup is thoroughly discussed in Section 5.4.1. Section 5.4.2 presents our findings, where the laser spectrum is shown in Section 5.4.2.1, while the pulse measurements, obtained using an auto-correlator, are depicted in Section 5.4.2.2. Sections 5.4.2.3 investigates the BER and SNR performance of the dual-hop AORF FSO system and compare the system with the dual-hop AOAF FSO system. A *Q*-factor analysis is presented in Section 5.4.2.4 using the captured eye-diagrams. Finally, concluding remarks are highlighted in Section 5.5.

5.2 Background and Motivation

Optical regeneration is at the forefront of current research interests in optical communications systems, due to the higher demand of migrating traditional electronic processes to the optical domain. Optical amplification has already been utilised for a number of applications in current optical networks, as the use of EDFAs, SOAs, and Raman amplifiers is now commonplace. With the development of long haul optical telecommunication systems working at high repetition rates (40 Gbit/s and beyond) [181], performing all-optical regeneration has become of great importance in combating cumulative noise, further improving the signal quality, and increasing the transmission

link distance. As previously mentioned in Chapter 3, three basic signal processing functions which are (*i*) Re-amplification, (*ii*) Re-shaping, and (*iii*) Re-timing, are required to form either a 1R, 2R, or 3R regenerator, based on these nomenclatures. Furthermore, different all-optical regenerators based on nonlinear effects such as SPM [182]–[185], XPM [149], [186] and FWM [187]–[189], have also been studied before. Among them, the SPM-based 2R regenerator proposed by P.V. Mamyshev in 1998 [151] presents an attractive regeneration choice due to its experimental setup simplicity and robustness, where its function is based on spectral broadening followed by an offset spectral filtering. This method has drawn much attention because it reduces sensitivity to polarization and environmental instabilities compared to other regenerating schemes. Unlike other technologies that exhibit longer response times, such as SOAs, this scheme is capable of high-bit rate operation due to the quasi-instantaneous response time of the Kerr nonlinearities in optical fibers [190]. Since it first demonstration, numerous research works have extensively studied the possibilities of the device theoretically [141], [181], [191] and experimentally [182], [192]–[194].

General theoretical guidelines have been proposed in [190] to design a high-performance 2R optical regenerators based on SPM in normally dispersive fibers, with a transfer function exhibiting a high extinction ratio improvement. Since this work was derived for idealized lossless fibers and also neglected the effect of ASE, a set of generalised scaling rules of the SPM optical 2R regenerators has been reported in [195]. In [195], the authors extended the derivation by taking into account the effect of fiber attenuation, and experimentally validated the scaling rules using a 1 km length of HNLF. The guidelines were further analysed by [191] and [196] to optimize the system performance of all-optical 2R regenerators of the Mamyshev type. In [191], the characterisation of the regenerator was theoretically investigated by considering noise and amplitude jitter suppression, as well as the impact of a trade-off between these two

effects on the overall system performance. Further investigations were carried out in [196] by studying the effect of residual dispersion and ASE noise on the *Q*-factor performance, while the research in [197] focused on the importance of filtering on the performance of SPM-based regenerators. The authors of the latter study experimentally demonstrated that the center wavelength offset of the spectral slicing filter should be set to be moderate, based on an inherent trade-off between the signal extinction ratios and the output OSNR. By increasing the offset, the suppression of the logical zero levels is enhanced gradually, but the signal energy after filter also starts to deplete. Consequently, the amplitude fluctuations of the pulse become severe, thus leading to degrading the OSNR.

In 2002, M. Rochette et al. showed that, the all-fiber optical 2R regenerator integrated with a tunable, low dispersion fiber Bragg grating filter can significantly improve the sensitivity and OSNR [198]. This research is considered a breakthrough in the context of optical regeneration. However, the mechanisms underlying this BER improvement were not understood. M. Rochette et al. further performed extensive theoretical [142], [155], [199] and experimental [150] studies on the operation of the Mamyshev 2R regenerator that has different transfer functions for the logical ones and logical zeros, which can effectively lead to removing the noise from the degraded noisy signal, thereby improving the BER performances. The effectiveness of this type of regenerator in reducing the noise was also demonstrated by [200], showing the *Q*-factor improvement that can be obtained by selecting suitable input and output power levels of the filter. However, in [141], it was demonstrated that the transfer function itself is not sufficient to give the best performance for the regenerator. The authors experimentally proposed a pulse compressor to be added to the SPM based Mamyshev regenerator to reduce the effect of intra-channel interactions and Brilloiun scattering at 42.6 Gbit/s RZ-33% transmission systems, which can improve the eye-opening of the eye

diagram by 2.3 dB in a back-to-back configuration. In addition, in [201], the dispersion and nonlinear effects that occurs simultaneously inside HNLFs were also shown to play an important role, and therefore need to be properly optimized. Despite the numerous theoretical and experimental demonstrations, the design optimization of such regenerators is not straightforward, due to the wide variety of input signal parameters (pulse width, duty cycle, input power), and the numerous physical properties of the fibers (chromatic dispersion $\mathfrak{D}$, nonlinearity coefficient γ, and fiber length L_f).

In addition to the aforementioned demonstrations, in 2002, the studies reported in [157], [202] demonstrated an impressive in-line 40 Gbit/s highly-dispersed-pulse transmission over one million kilometres by cascading 4 × 100 km over 2500 times, and implementing a spectrum broadening based regenerator in a normal dispersion fiber and subsequently narrow-band filtering. The results showed that the 2R regenerator enabled up to 5000 km transmission with Q-values higher than 15.6 dB, whereas using a 3R regenerator, the Q-value dramatically increased, enabling up to one million kilometres transmission by removing the accumulated timing jitter. However, a higher number of regenerators were needed to compensate the ~100000 dB fiber loss. Other long haul transmission experiments using optical regeneration have been demonstrated theoretically or experimentally by cascading either 2R [139], [187], [203], [204] or 3R [139], [205], [206] optical regenerators. Similarly to [157], [202], such studies found that BER degradations were observed when 2R optical regenerators were cascaded due to accumulating the timing jitter, which occurs due to transmission impairments (i.e. non-linear effects and ASE) and the properties of the regenerator itself [139].

Note that, all of the aforementioned investigations were based on optical fiber communications. To the best of the author's knowledge, only the study reported in [35] implemented an all-optical 2R Mamyshev-based regenerator for a FSO communication link, acting as the relaying system. The authors in that study theoretically analysed the

improvement that the regenerator offers in mitigating the accumulation of background noise. Furthermore, they transmitted 500 mW of signal power with a 10 Gbps bit rate at λ of 1550 nm, using a 80 GHz BPF and a 36 m length of HNLF with a nonlinear parameter of 1100 W/km. The results showed that for the dual-hop FSO system, the maximum accessible transmission distance increased from 0.8 km to 1.9 km for the all-optical AF system and the 2R regenerator relaying-based system respectively, compared to the direct transmission system. Furthermore, the results also showed that when the relay was increased from single to triple-hop, the regenerator was able to eliminate the background noise at each relay by offering a power gain improvement of 1.4 dB, 2.9 dB, and 5.3 dB respectively, compared to the all-optical AF system at a BER of 10^{-5}. However, the authors only considered the background noise as the limiting factor and neglected the effect of the atmospheric turbulence on the system performances. Moreover, details of the analysis were not sufficient and the investigation was purely analytical with no experimental work. Until now, there have been no further investigations conducted to implement an all-optical 2R regenerator in FSO systems. Therefore, in this research, we have carried out an in-depth experimental analysis of all-optical 2R Mamyshev-based regenerators, by considering the impact of the turbulence-induced effects on the overall system performance. The theoretical background and experimental analysis will be discussed in detail in next sections.

5.3 Theoretical Background

This section intends to provide an overview of the SPM-based AORF relaying technique and the associated mathematical models. Particular attention is paid to the SPM principle in HNLFs, as it is a core element of the AORF system.

5.3.1 SPM-based AORF relay structure

Fig. 5.1 presents the typical structure of an SPM-based AORF relay-assisted system, commonly referred to as a Mamyshev regenerator. The system consists of three main components, which are an EDFA, HNLF, and a BPF with a centre wavelength that is offset from the signal wavelength. The principle of the regenerator can be explained as follows. After propagating over a dispersive channel, the degraded optical signal is first fed into an EDFA, which is used to boost the power to a suitably high level at the input of the HNLF. Note that, an additional filter is often inserted after the EDFA to reject the out-of-band ASE noise. When passing through the HNLF, high peak-power pulses experience SPM, which broadens the spectrum, while low peak power noise remains unaffected when passing through the HNLF. The BPF acts as a reshaping function, where the central wavelength of the BPF accounts for the pulse duration and the operating wavelength of the optical subsystem. Furthermore, the BPF properties determine some regenerator characteristics, such as the power transfer function, and most importantly, the shape of the regenerated pulse and the signal to noise ratio. The power transfer function of regenerator consists of a step-like function which suppresses low level noise and stabilizes the peak pulse power [207]. Thus, undesired ghost pulses can be suppressed at the output of the regenerator. As a result, the signal quality at the system output improves, and the extinction ratio can consequently be improved when this type of OR is used along the communication link. The BPF must be adjustable in bandwidth, tunable in wavelength, dispersion-less to avoid pulse broadening, and with a Gaussian transmission spectrum to enable Gaussian pulse shaping in the time domain [207].

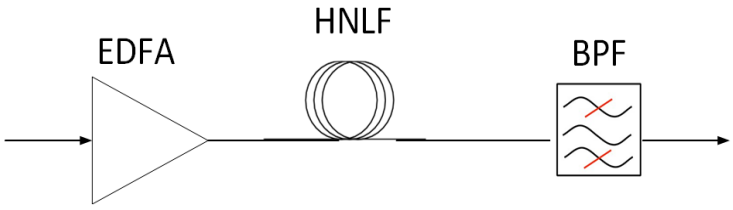

Fig. 5.1 The typical structure of an SPM-based ORF relay.

Recall that SPM refers to the self-induced phase shift experienced by an optical field during its propagation in optical fibers. It can be understood as a modulation, where the intensity of the signal modulates its own phase. The propagation of an optical pulse through an optical fiber is governed by the nonlinear Schrödinger equation given as [156]:

$$i\frac{\partial A}{\partial z} = -\frac{i\alpha_{att}}{2}A + \frac{\beta_2}{2}\frac{\partial^2 A}{\partial \mathcal{T}^2} - k_{nl}|A|^2 A, \tag{5.1}$$

where A is the slowly varying amplitude of the pulse envelope, and $\mathcal{T}$ is measured in a frame of reference moving with the pulse at the group velocity v_g, where $\mathcal{T} = t - \frac{z}{v_g}$. The three terms on the right-hand side of the equation govern the effects of fiber losses α_{att}, dispersion β_2, and nonlinearity k_{nl} on a pulse propagating inside an optical fiber, respectively. All three parameters become functions of z when loss- and dispersion-management schemes are employed for long-haul lightwave systems.

Then, let us introduce a normalized time scale, τ as [156]:

$$\tau = \frac{\mathcal{T}}{\mathcal{T}_0} = \frac{t - z/v_g}{\mathcal{T}_0}, \tag{5.2}$$

where $\mathcal{T}_0$ is the pulse width. A normalized amplitude U can also be introduced as follows [156]:

$$A(z,\tau) = \sqrt{P_0}\exp\left(-\frac{\alpha_{att}z}{2}\right)U(z,\tau), \tag{5.3}$$

where P_0 is the peak power of the incident pulse. By using Eqns. (5.1), (5.2), and (5.3), $U(z,\tau)$ is found to satisfy [156]:

$$i\frac{\partial U}{\partial z} = \frac{\beta_2}{2L_D}\frac{\partial^2 U}{\partial \tau^2} - \frac{\exp(-\alpha_{att} z)}{L_{NL}}|U|^2 U, \tag{5.4}$$

where L_D is the dispersion length and L_{NL} is the nonlinear length, which are given by [156]:

$$L_D = \frac{\mathcal{T}_0^2}{|\beta_2|}, \tag{5.5}$$

and

$$L_{NL} = \frac{1}{k_{nl} P_0}. \tag{5.6}$$

These two characteristic distances provide the length scales over which dispersive and nonlinear effects become important for pulse evolution [208]. To analyze the effect of fiber nonlinearity on the SPM, the fiber dispersion is ignored, and the dispersion coefficient β_2 in Eq. (5.4) is set to zero. Therefore, Eq. (5.4) reduces to:

$$\frac{\partial U}{\partial z} = \frac{i\exp(-\alpha_{att} z)}{L_{NL}}|U|^2 U. \tag{5.7}$$

Eq. (5.7) has the following general solution for the field amplitude at the output of a fiber of length L_f given as [156]:

$$U(L_f, \mathcal{T}) = U(0, \mathcal{T}) \exp\left[i\emptyset_{NL}(L_f, \mathcal{T})\right], \tag{5.8}$$

where $U(0, \mathcal{T})$ is the field amplitude at $z = 0$, and $\emptyset_{NL}(L_f, \mathcal{T})$ is the nonlinearity-induced phase change given by [156]:

$$\emptyset_{NL}(L_f, \mathcal{T}) = |U(0, \mathcal{T})|^2 (L_{eff}/L_{NL}). \tag{5.9}$$

The effective length L_{eff} for a fiber of length L_f is defined as [156]:

$$L_{eff} = \frac{[1-\exp(-\alpha_{att} L_f)]}{\alpha_{att}}. \tag{5.10}$$

Eq. (5.8) shows that SPM modifies the nonlinear phase shift $\emptyset_{NL}$ across the pulse, but the intensity envelope (i.e., the pulse shape) remains unaffected. Furthermore, in Eq. (5.9), $\emptyset_{NL}$ increases with fiber length L_f. In the absence of fiber losses, $\alpha_{att} = 0$, and

$L_{eff} = L_f$. The maximum phase shift $\emptyset_{max}$ occurs at the pulse center (i.e., located at $\mathcal{T} = 0$). By normalizing U such that $|U(0,T)| = 1$, $\emptyset_{max}$ can be expressed by [156]:

$$\emptyset_{max} = L_{eff}/L_{NL} = k_{nl}P_0L_{eff}. \tag{5.11}$$

In general, the temporally varying phase shift induces a temporally varying frequency shift, and thus the amount of spectral broadening in a nonlinear medium differs across the pulse from its central frequency w_0. By taking the derivative of nonlinear phase shift, the difference Δw_{SPM} is given as [156]:

$$\Delta w_{SPM}(T) = \left|\frac{\partial \emptyset_{NL}(L_f, \mathcal{T})}{\partial \mathcal{T}}\right| = \left|\frac{\partial}{\partial \mathcal{T}}(|U(0,\mathcal{T})|^2)\right|\frac{L_{eff}}{L_{NL}}. \tag{5.12}$$

The time dependence of Δw_{SPM} is referred to as frequency chirping. The chirp induced by SPM increases in magnitude with the propagated distance L_f. In other words, new frequency components are continuously generated as the pulse propagates across the fiber. These SPM-induced frequency components broaden the spectrum of an initially un-chirped pulse over its initial width at $z = 0$. By solving (5.12), the SPM-induced chirp $\Delta w_{SPM}(\mathcal{T})$, given the incident field $U(0,\mathcal{T})$, is given by [156]:

$$\Delta w_{SPM}(\mathcal{T}) = \frac{2m_g}{\mathcal{T}_0}\frac{L_{eff}}{L_{NL}}\left(\frac{\mathcal{T}}{T_0}\right)^{2m_g-1}\exp\left[-\left(\frac{\mathcal{T}}{\mathcal{T}_0}\right)^{2m_g}\right], \tag{5.13}$$

where m_g determines the shape of the incident pulse. For larger values of m_g, the incident pulse becomes nearly rectangular with increasingly steeper leading and trailing edges, known as a super-Gaussian pulse. Fig. 5.2 illustrates the variation of (a) the nonlinear phase shift $\emptyset_{NL}$, and (b) frequency chirp Δw_{SPM} across the pulse at $L_{eff} = L_{NL}$ for a Gaussian pulse ($m_g = 1$) and a super-Gaussian pulse ($m_g = 3$). For the case of $m_g = 1$ (i.e., for a Gaussian pulse), Eq. (5.13) can be simplified to:

$$\Delta w_{SPM}(\mathcal{T}) = \frac{2\mathcal{T}}{\mathcal{T}_0{}^2}\frac{L_{eff}}{L_{NL}}\exp\left[-\left(\frac{\mathcal{T}}{\mathcal{T}_0}\right)^2\right], \tag{5.14}$$

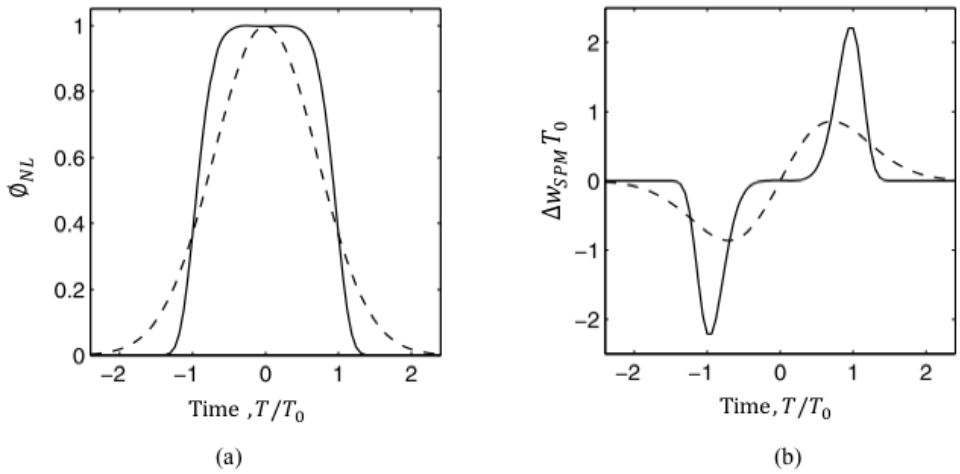

Fig. 5.2: Temporal variation of the SPM-induced (a) phase shift $\emptyset_{NL}$ and (b) frequency chirp Δw_{SPM}, for Gaussian (dashed curve) and super-Gaussian (solid curve) pulses.

However, in our case, we are focusing on the spectral broadening itself. In the case of unchirped input pulses, SPM always leads to spectral broadening. An estimate of the magnitude of the SPM-induced spectral broadening can be obtained from the peak value of Δw_{SPM} in Fig. 5.2. Alternatively, by plugging the value of L_{NL} from (5.6) into (5.12), and taking the time average over a one bit interval T_b, the average spectrum broadening for a Gaussian pulse can be calculated via [151]:

$$\overline{\Delta w_{SPM}} = \Delta w_0 \, n_2 I_p L_f, \tag{5.15}$$

where $\Delta w_0 \sim 1/T_0$ is the initial spectral bandwidth of the pulse, and $I_p = P_t/A_{eff}$ is the pulse intensity, which varies for different pulses. It is clear from the equation that the spectrum broadening increases by the initial bandwidth Δw_0, the nonlinear refractive index n_2, the average pulse intensity I_p, and the propagated distance L_f.

After propagating through the nonlinear medium, which in our case is an HNLF, the pulses pass through a BPF, whose center frequency w_f, is shifted with respect to the input signal carrier frequency w_0, by a certain value Δw_{shift} given as:

$$w_f = w_0 + \Delta w_{shift}. \tag{5.16}$$

When the pulse spectral broadening in (5.15) is small enough, which occurs when [151]:

$$\frac{\overline{\Delta w_{SPM}}}{2} < \Delta w_{shift}, \tag{5.17}$$

the pulse is rejected by the filter. In the regenerator, this occurs when I_p is too small (e.g., noise in logical zeros level). If the pulse intensity is high, (e.g. at logical ones level), the new spectral bandwidth satisfies [151]:

$$\frac{\overline{\Delta w_{SPM}}}{2} \geq \Delta w_{shift}. \tag{5.18}$$

In such a case, depending on the amount of spectral broadening, the filter center frequency, and the filter bandwidth Δw_f, part of the SPM-broadened spectrum passes through the filter and the rest is rejected. The spectral width of the filtered pulse is determined by the spectral bandwidth. By changing the filter spectral bandwidth Δw_f, the bandwidth of the SPM-broadened spectrum changes. Note that, if $\Delta w_f \sim \Delta w_0$, the output pulse width is the same as the input pulse width.

In the case where I_p is very high compared to the critical pulse intensity I_{cr} ($I_p \gg I_{cr}$), the pulse spectrum broadens extensively, where $w_{SPM} \geq \Delta w_{shift}$, and the intensity of the output pulse I_{out} is independent of the input pulse intensity I_p. This results in a nonlinear transfer function for the regenerator, and consequently, suppressing the noise in the signal. Therefore, a pulse transfer function for the regenerator can be defined in terms of output pulse intensity versus input pulse intensity as follows [151]:

$$I_{out} = \begin{cases} 0 & \text{if} \quad I_p < I_{cr} \\ I_c & \text{if} \quad I_p > I_{cr}, \end{cases} \tag{5.19}$$

where I_c is the constant output pulse intensity. I_{cr} can be adjusted to compromise a trade-off between removing the noise at logical zeros and suppressing the amplitude fluctuations at logical ones level, and can be determined from [151]:

$$I_{cr} = \frac{2\Delta w_{shift}}{\Delta w_0 (2\pi/\lambda) n_2 L_f}. \tag{5.20}$$

The transfer function portrays the ability of the regenerator to offer both an extinction ratio improvement and amplitude equalization. The slope of the power transfer function at the logical "0" and "1" bit power levels defines the regenerative properties of the device [190]. Fig. 5.3 shows the concept of a typical nonlinear transfer function of an ideal 2R regenerator and its application in removing noise at logical zero levels and suppressing the amplitude fluctuations at logical ones levels.

It is worth noting that the regeneration process imposes a considerable power loss to the signal by rejecting a major portion of the pulse spectrum. Therefore, an OA is required after the regenerator to boost up the signal and increase its average power to the average transmit power at the source P_t. Section 5.4 provides the details of an experimental demonstration of the AORF relaying technique, together with the results obtained. The performance of AORF is then compared with that of the AOAF technique.

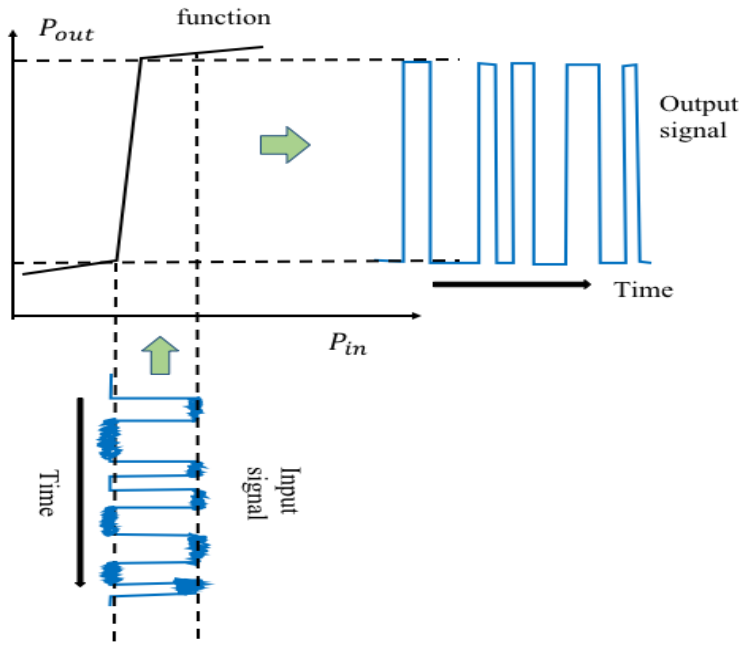

Fig. 5.3: The concept of the nonlinear transfer function of the 2R regenerator.

5.4 Experimental Analysis of FSO AORF Relay-based System

In this section, the performance of the novel dual-hop FSO AORF SPM-based 2R regenerator relay-assisted system is discussed under turbulence and no turbulence conditions. Experimental demonstrations were conducted in a controlled indoor laboratory environment, and the setup as well as the outcomes of the experiments are discussed thoroughly in this section. The comprehensive measurements were carried out several times in order to mimic the real outdoor environment and ensure that the analysis is valid for the real-world scenarios. In addition, the turbulence generation using a dedicated chamber was used in analysing the FSO AOAF system performance, as discussed in Chapter 4 and demonstrated by several research studies before [18], [86], [93], [209]. To the best of the author's knowledge, this is the first experimental demonstration employing an all-optical 2R regenerator in an FSO relaying system.

5.4.1 Experimental setup

Fig. 5.4 illustrates the experimental block diagram of the proposed all-optical dual-hop regenerate-and-forward FSO relay-assisted communication system, based on a 2R (or a Mamyshev) regenerator, under the influence of atmospheric channel turbulence effects. The system contained four main stages, namely signal transmission by a Tx, signal degradation by turbulence effects, signal regeneration by means of an SPM-based 2R regenerator, and a Rx. The total link span was 4.4 m. At the Tx, a wavelength tunable (U2t TMLL 1550) photonics pulse source was used, which has a continuous wavelength tuning range from 1480-1580 nm. The tunable mode locked laser was operated such as to emit pulses at the operating wavelength of 1547 nm and at a repetition rate of 10 GHz.

The pulses had a Gaussian profile, with a full-width at half-maximum (FWHM) pulse width of 2.2 ps, and emulated an RZ-OOK signal. The pulsed signal was then fed into a 99/1 fiber coupler, with 1% of the signal sent to an OSA for continuous monitoring during the wavelength characterisation. The remaining 99% of the signal was passed through a pre-amp EDFA, and a variable digital attenuator for varying the input power to enable the adjustment of the SNR. The output signal was then launched into the free space channel via a pigtail GRIN fiber collimator (Thorlabs 50-1550A-APC) with a clear aperture diameter lens of 0.18 cm. Two plano convex lenses (CL 1 and CL 2) with a focal length *f* of 10 cm were placed after the Tx and before the Rx respectively, in order to focus the optical beam and minimize its divergence. The degraded signal was injected into the following regenerator for signal reshaping.

The regenerator consisted of an EDFA and an HNLF, followed by a OBPF. Since the received power after the FSO turbulence channel was too small (~-15 dBm) for a booster EDFA to operate at (as it requires more -10 dBm of input power to operate), a pre-amp EDFA was placed beforehand. The launch output power of the booster EDFA was then adjusted to a power level sufficient to induce SPM spectral broadening in the HNLF. The signal was then fed into a 500-m long HNLF. The HNLF had a chromatic dispersion of -2.5 ps/nm/km, a dispersion slope of 0.019 ps/nm^2/km, an attenuation loss of 0.88 dB/km, and the nonlinearity coefficient of 11.5 W^{-1}km^{-1} at 1550 nm. At the output of the HNLF, a wavelength and bandwidth tunable OBPF OTF-950 filter (bandwidth adjustable range of 0.2-6.0 nm) was detuned with respect to the input signal wavelength in order to transmit the SPM-generated optical frequencies and reject the original spectrum, thus providing an excellent optical control and a flat-top passband shape. After regeneration, the signal was passed through a 99/1 fiber coupler prior to another free space channel transmission. A similar setup to that used in Link 1 above was used for the Link 2 transmission (see Fig. 5.4).

At the Rx, another GRIN fiber collimator was used to couple the received optical beam into an SMF, and feed it into a pre-amp EDFA for further amplification. The signal was then passed into a 90/10 coupler, in which 90% of the signal went to an OSC, and the remaining 10% was fed to an OSA for link assessment. A 10-dB fixed attenuator was placed after the EDFA to protect the OSA and OSC. The turbulence channel was implemented in the controlled indoor environment using a dedicated atmospheric chamber by blowing hot air from two 2 kW fan heaters in the direction perpendicular to the propagating optical beam along the transmission path. The strength of turbulence was varied by means of controlling the output and position of the fan heaters, thereby varying the temperature profile. Furthermore, the temperature profiles were maintained by concealing the air of the free space channel with two plastic barriers. To continuously monitor the temperature profile along the channel and ultimately determine the value of c_n^2, the instantaneous temperatures were recorded every 4 seconds throughout the experiment using 20 temperature sensors positioned at 0.22 cm apart along the channel, as illustrated in Fig. 5.4. While carrying out the experimental measurement with no turbulence, we ensured that the temperature along the channel was kept at the room temperature. With turbulence, the temperature at 20 different positions (T_1-T_{20}) was continuously recorded along the channel. A snapshot of the indoor laboratory in which experimental setup of the all-optical dual-hop 2R regenerative FSO relay-based system was implemented is depicted in Fig. 5.5. Furthermore, the main parameters used in the experiment are summarized in Table 1.

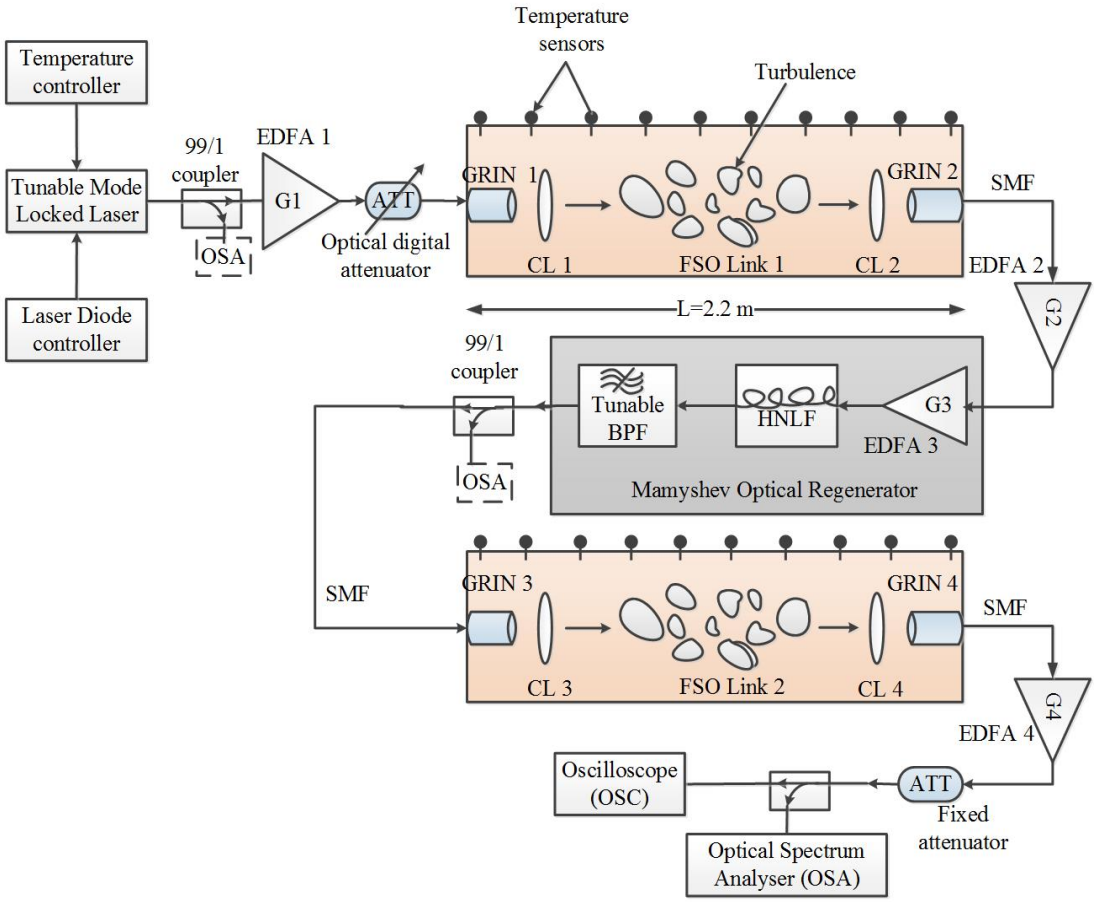

Fig. 5.4: Block diagram of the experimental setup of the all-optical 2R regenerative FSO relay-based system. CL: Convex lens.

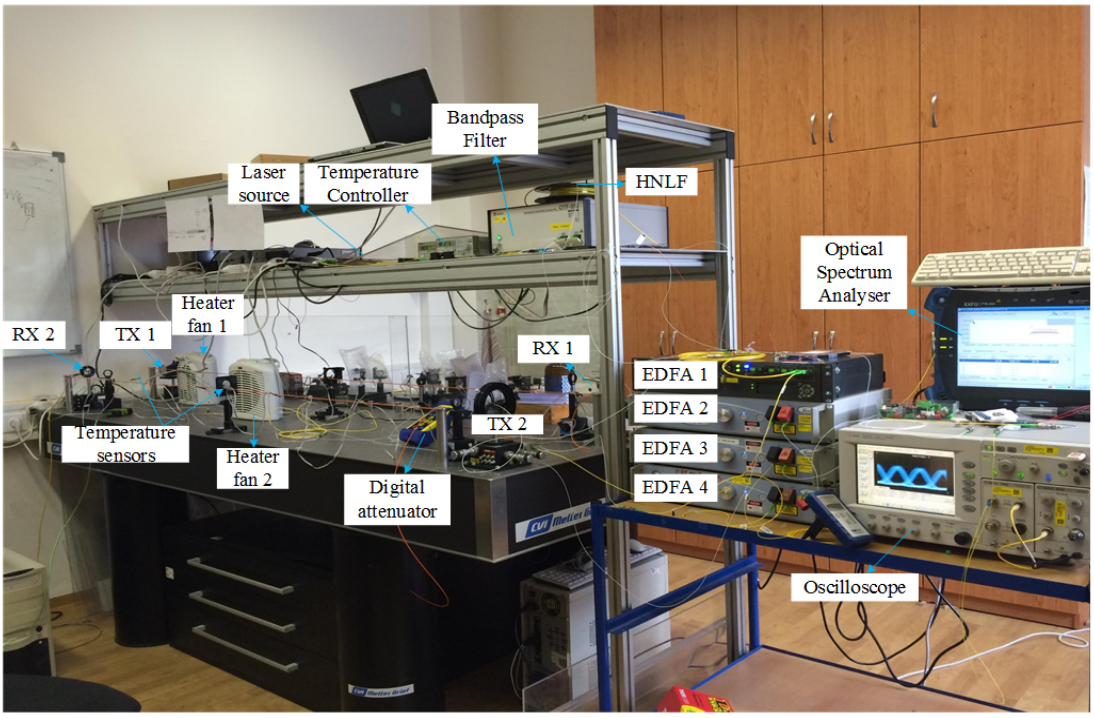

Fig. 5.5: Snapshot of the indoor laboratory in which the all-optical 2R regenerative FSO relay-based system was implemented.

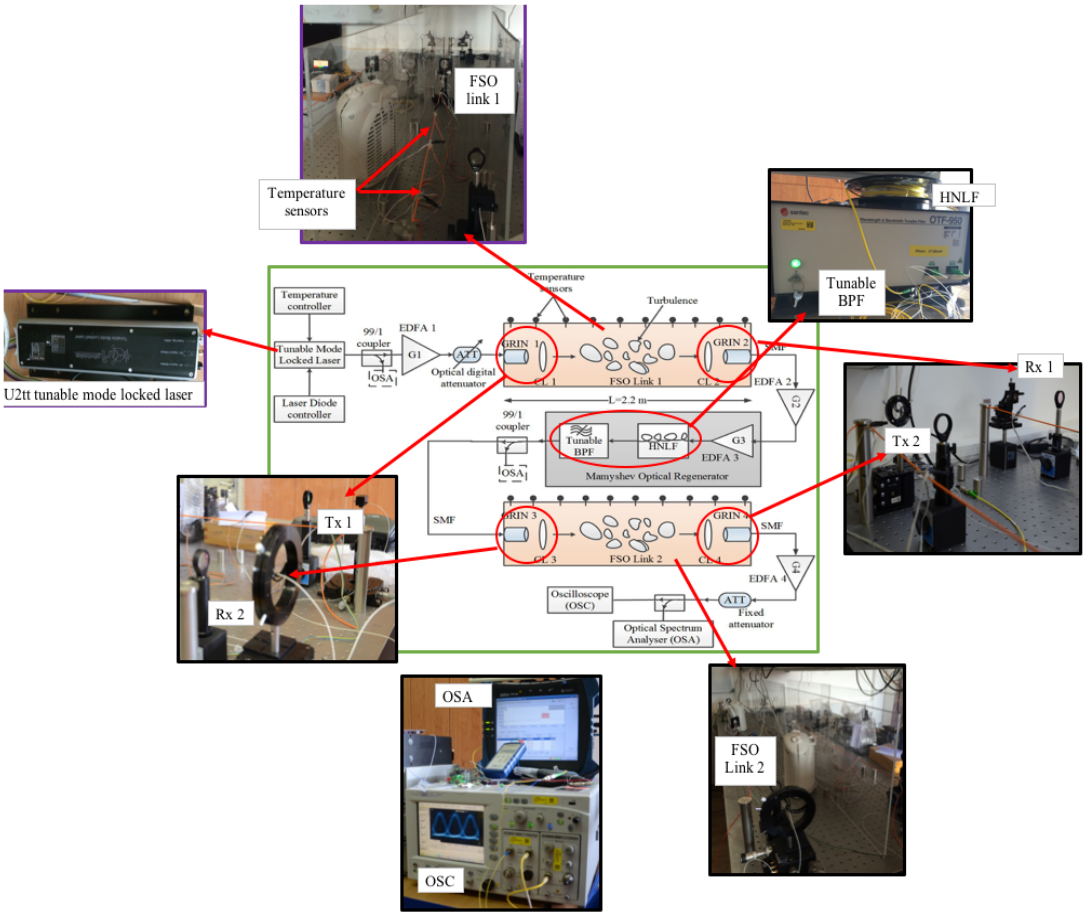

Fig. 5.6: Snapshot of the devices used in the experimental setup.

Table 5.1: The main parameters used in the AORF FSO relay-assisted system experiment

	Parameter	**Value**
Transmitter	Repetition rate and signalling scheme	10 GHz , RZ-OOK
	Laser pulse width	2 ps
	Wavelength	1547 nm
	Laser output power	-17.2 dBm
	Temperature controller current	110.8 mA
	Grin-lens aperture	0.18 cm
	Beam divergence	0.25 mrad
Convex lens	Clear aperture	2.54 cm
	Focal distance	10 cm
EDFA	Max. output power	21 dBm
	Noise figure	<7.5 dBm
	EDFA 1 output power	9 dBm
	EDFA 2 output power	6.6 dBm
	EDFA 3 output power	16 dBm
	EDFA 4 output power	0 dBm

HNLF	Length	500 m
	Attenuation	0.88 dB/km
	Nonlinearity coefficient	11.5 $W^{-1}km^{-1}$
	Dispersion	-2.5 to 2.0 ps/nm/km
	Dispersion slope	0.019 ± 0.004 $ps/nm^2/km$
	Zero dispersion wavelength	1556 nm
	Effective mode area	11.6 μm^2
	Numerical aperture	0.16
Tunable OBPF	Wavelength	1550 nm
	Bandwidth @ 3 dB	4 nm
	Accuracy	≤0.05 nm
	Chromatic dispersion	≤ 10 pm/nm
	Maximum input power	+27 dBm
	Insertion loss uniformity	≤0.3 dB
	Return loss	≥45 dB
	Crosstalk	≥50 dB
	Operating temperature	15 to 35 °C

5.4.2 Results and discussions

In this section, the performance of the dual-hop AORF FSO relay-based system with and without turbulence is investigated. In addition, the BER performance of AORF is compared with that of the AOAF dual-hop system.

5.4.2.1 Laser spectrum

In this section, an analysis of the shape and spectrum of the 350 Gbps RZ pulse signal transmitted by the tunable mode-locked fiber laser is provided. The FWHM of the pulse train was measured to be 2.2 ps using an auto-correlator. Fig. 5.7 and Fig. 5.8 show an example of U2t photonics mode-locked laser signal spectrum captured using the OSA, and the laser spectrum at a central wavelength of 1547 nm and a bandwidth of 6 nm captured using the auto-correlator, respectively. The central wavelength was chosen to be a few nanometres below the zero dispersion wavelength λ_{ZD} of the HNLF (1556 nm) in order to have as a uniform a gain as possible over a broad bandwidth. Moreover, the dispersion effect only played a minor role during the SPM-induced spectral broadening.

Note that, it is not always practical to match the operating wavelength with λ_{ZD} due to the devices suitability.

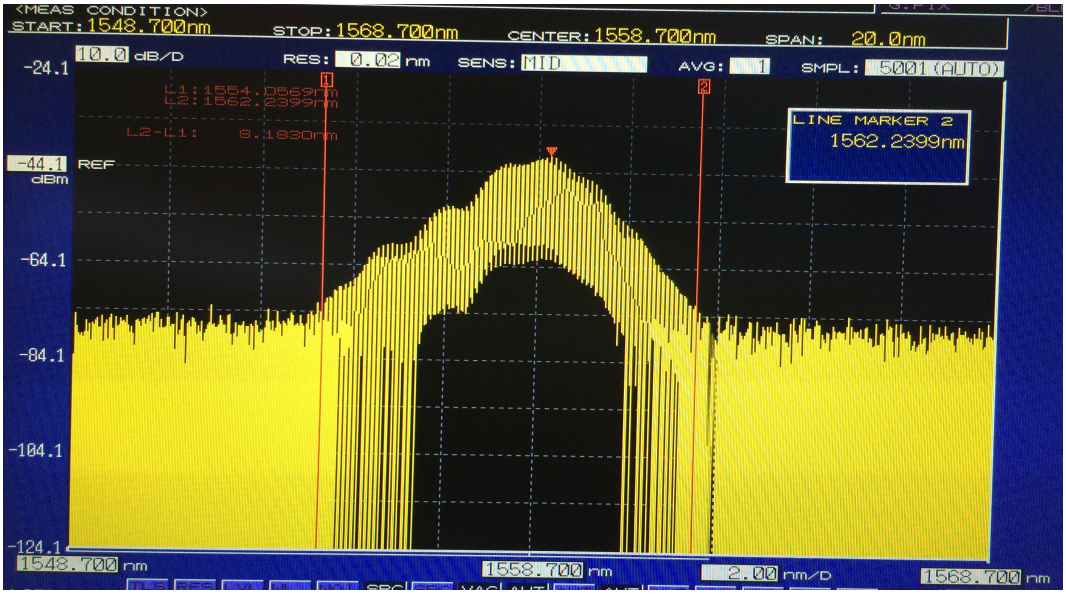

Fig. 5.7: Example of the U2t photonics mode-locked laser spectrum.

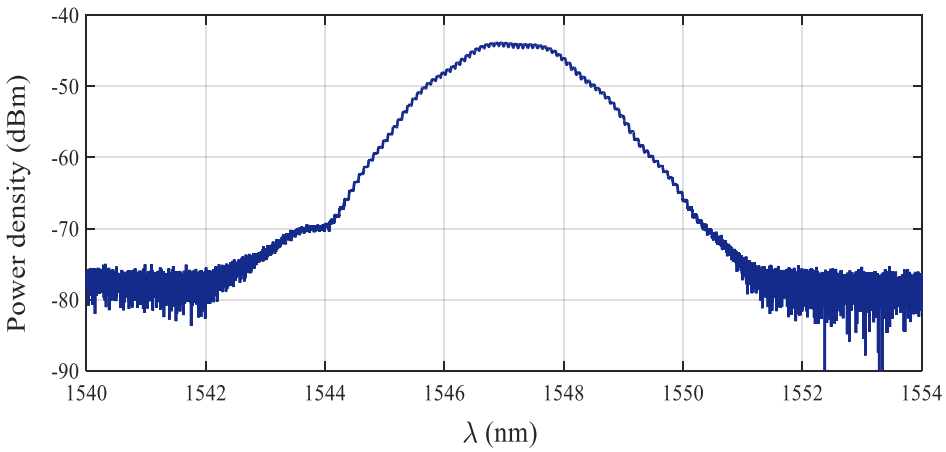

Fig. 5.8: Laser spectrum at a central wavelength of 1547 nm, P_t of -20 dB, and bandwidth of 6 nm.

In the first stage, a number of input power levels were tested by launching each level into the EDFA to observe the corresponding spectral broadening inside the HNLF. Pulse broadening was observed using the OSA at 13 dBm, 16 dBm, and 19 dBm of EDFA output power, and compared with the laser spectrum, as shown in Fig. 5.9. Simultaneously, the tunable OBPF was tuned at a bandwidth of 4 nm, and the central

wavelengths were varied to ensure the injected light entered the laser cavity during the build-up of the regenerated pulse. Four central wavelengths were chosen, which are 1547 nm, 1550 nm, 1552 nm, and 1555 nm, at each of aforesaid EDFA output power. Based on the measurement, the EDFA output power of 16 dBm was found to be the most suitable power level, as the broadening was sufficient enough to fill the entire bit slot of the 3 nm OBPF offset, without the need for excessive EDFA average power. Fig. 5.10 illustrates the filter spectrum at the four aforementioned wavelength with EDFA output power of 16 dBm fed into the HNLF. The result was confirmed by the pulse measurement using the auto-correlator, as discussed in the next subsection. Note that the slight asymmetry in the spectra is due to the dispersion slope of the HNLF. Furthermore, the cleanly broadened spectra indicate that there was no serious nonlinear crosstalk between the signals propagating in the HNLF [144]. In the experiment, the filter wavelength was set at 1550 nm with a bandwidth of 4 nm to reject the out-of-band portion of the unwanted signal. Fig. 5.11 depicts a spectrum comparison of the laser pulse at a central wavelength of 1547 nm, and the broadened pulse after the HNLF at an EDFA output power of 16 dBm, and an OBPF central wavelength and bandwidth of 1550 nm and 4 nm respectively.

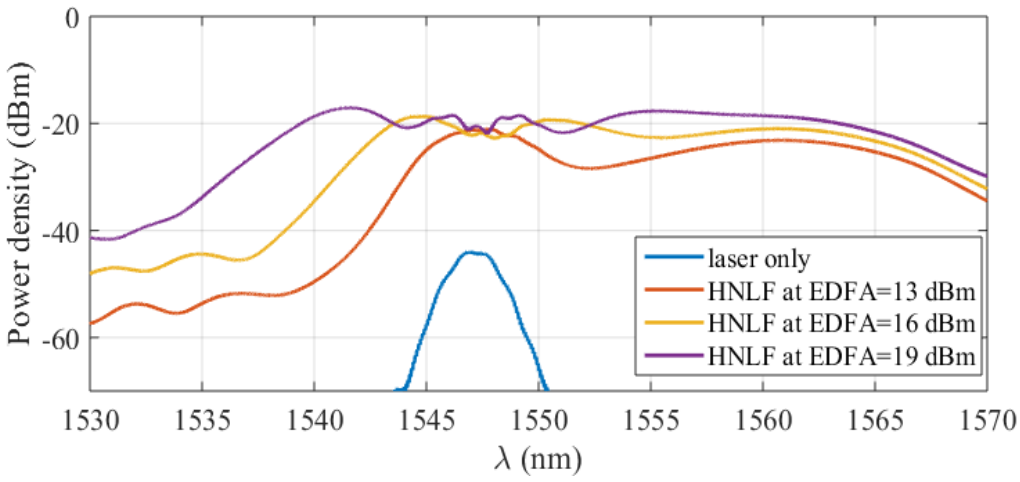

Fig. 5.9: Spectral broadening of the laser after the HNLF at different EDFA pumping power levels of 13 dBm, 16 dBm, and 19 dBm, at a central wavelength 1547 nm. The spectra were captured using a Yokogawa spectrum analyzer.

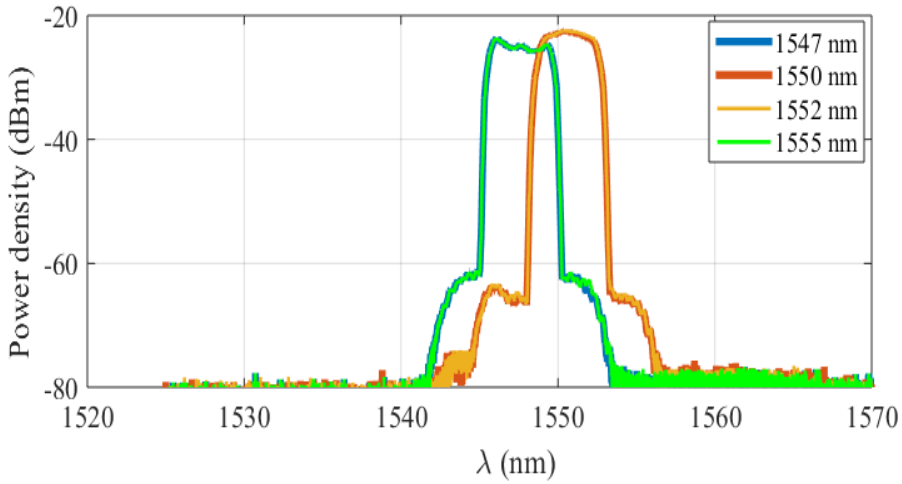

Fig. 5.10: The spectrum of the filter at different central wavelengths (1547 nm, 1550 nm, 1552 nm, and 1555 nm) at filter bandwidth of 4 nm with 16 dBm of EDFA output power.

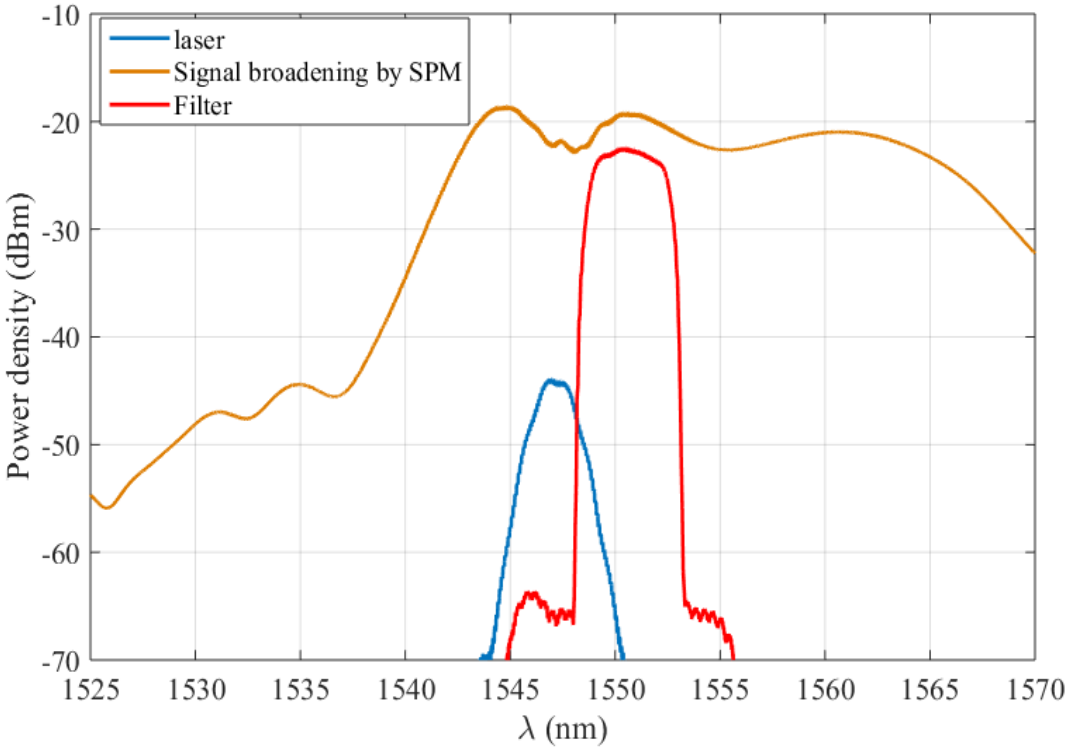

Fig. 5.11: Spectra of the laser pulse, the SPM-broadened pulse for EDFA output power of 16 dBm, and the filter at 1550 nm.

5.4.2.2 Pulse measurements using auto-correlator

One of the methods used to characterise an ultrafast short pulse is to measure the temporal pulse-width using an auto-correlator capable of measuring small pulse widths. In our case, an APE pulseCheck auto-correlator was used for such purpose, which can measure pulse widths as small as <10 ps, all the way up to 400 ps. The pulse width, measured at the FWHM, is a critical factor for the adjustment of any laser system. In this subsection, the behaviour of the pulses is experimentally investigated when they propagate through the FSO turbulence channel and regenerated by the Mamyshev regenerator. The time domain auto-correlation traces of the obtained pulses were captured at several places, including after the FSO link 1, after the Mamyshev regenerator, and after the FSO link 2. As previously mentioned, the output power of EDFA that needed to be fed into the HNLF was verified by measuring the pulsed signal. Four different EDFA output power levels were chosen, which are 16 dBm, 17 dBm, 18 dBm, and 19 dBm, as shown in Fig. 5.12. The results show that, the pulse width at FWHM increases with the pump power (i.e., increasing gain). Having a narrower pulse width indicates that lower dispersion effects were experienced by the pulse, as was the case the 16 dBm EDFA pumping power [210]. Hence, the 16 dBm power level was chosen, as the pulse displayed the most compression level at this power. Since the SPM-induced broadening effect is linear only over the central part of the pulse, only the central part is compressed. However, the energy in the pulse wings remains uncompressed and appears as a broad pedestal.

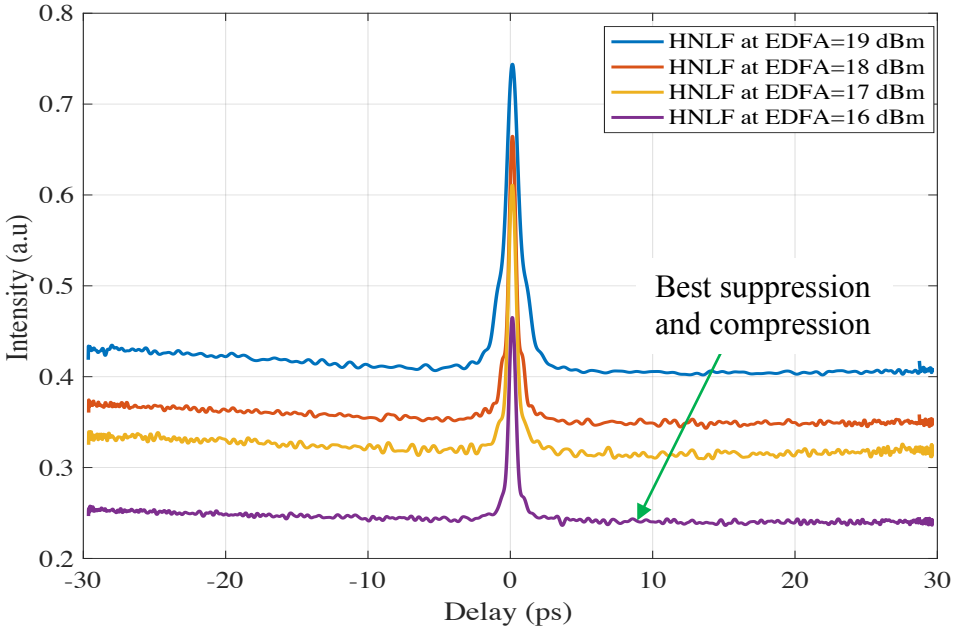

Fig. 5.12: FWHM pulses after the HNLF at different EDFA pumping power levels.

Experiments were performed using 2.2 ps pulses over the entire experiment, which were obtained from the mode-locked laser, show that the pulse energy varied when passes mentioned three stages (i.e., after FSO link 1, after Mamshev regenerator, and after FSO link 2). The laser pulse is shown in Fig. 5.13. After propagating through the first FSO link with turbulence of $C_n^2 = 6.8 \times 10^{-10}$ $\mathrm{m}^{-2/3}$, the amplitude of the pulse reduced and the noise in the pedestal increased due to the losses experienced in the turbulence channel. The pulse after the first FSO link is shown in Fig. 5.14. The pulse was then fed into the Mamyshev regenerator and the signal was regenerated, as shown in Fig. 5.15, where we can see that the pulse was compressed from an FWHM of 3.73 ps to 2.0 ps. This effect is understood by bearing in mind that spectrally filtering the SPM-induced chirp on one of pulse edges results in carving the pulse edge in the time domain, thus compressing the pulse. After that, the signal was re-transmitted to the FSO link 2 with the same turbulence strength, and was captured as shown in Fig. 5.16. Note that, since there was no regenerator applied after FSO link 2, the result of Fig. 5.16 represents the final outcome of the system.

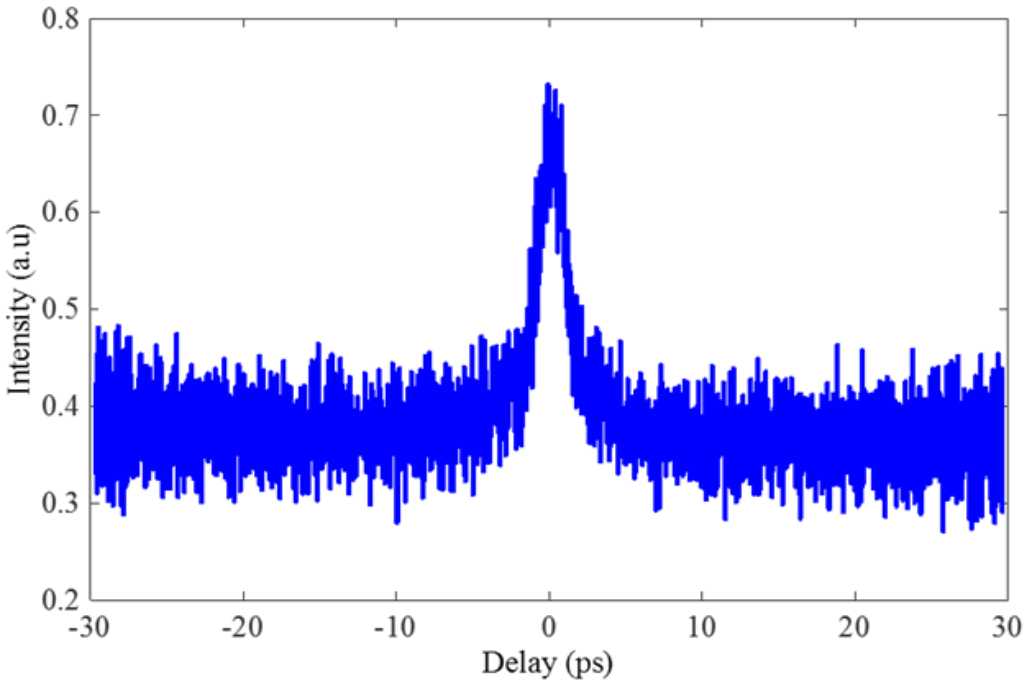

Fig. 5.13: The laser pulse at 1547 nm.

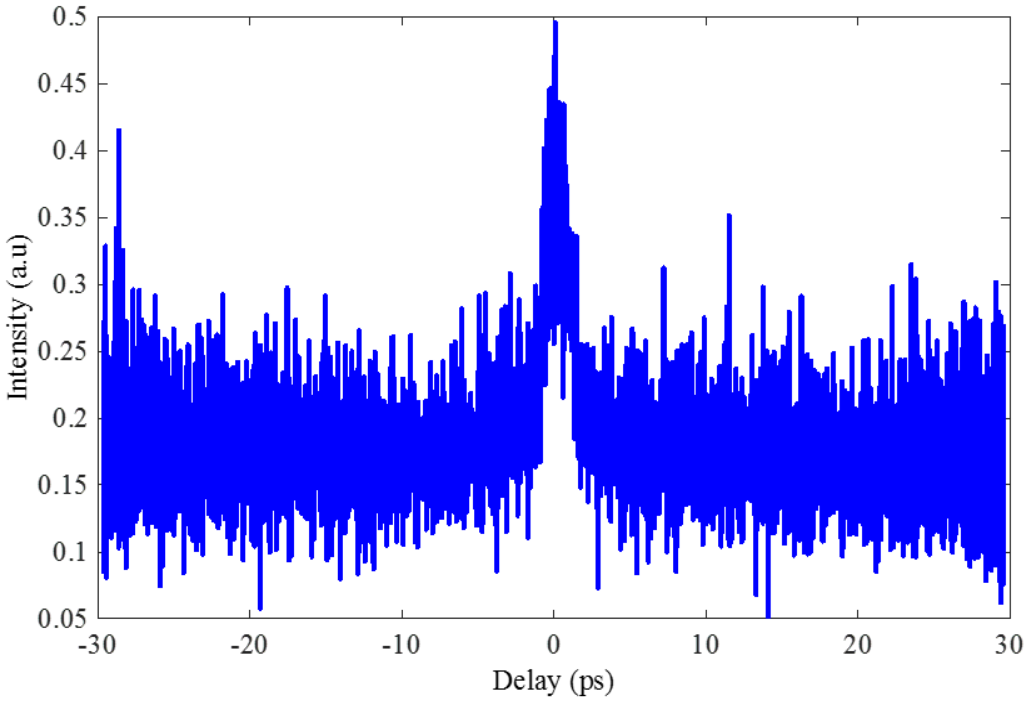

Fig. 5.14: The laser pulse after FSO link 1.

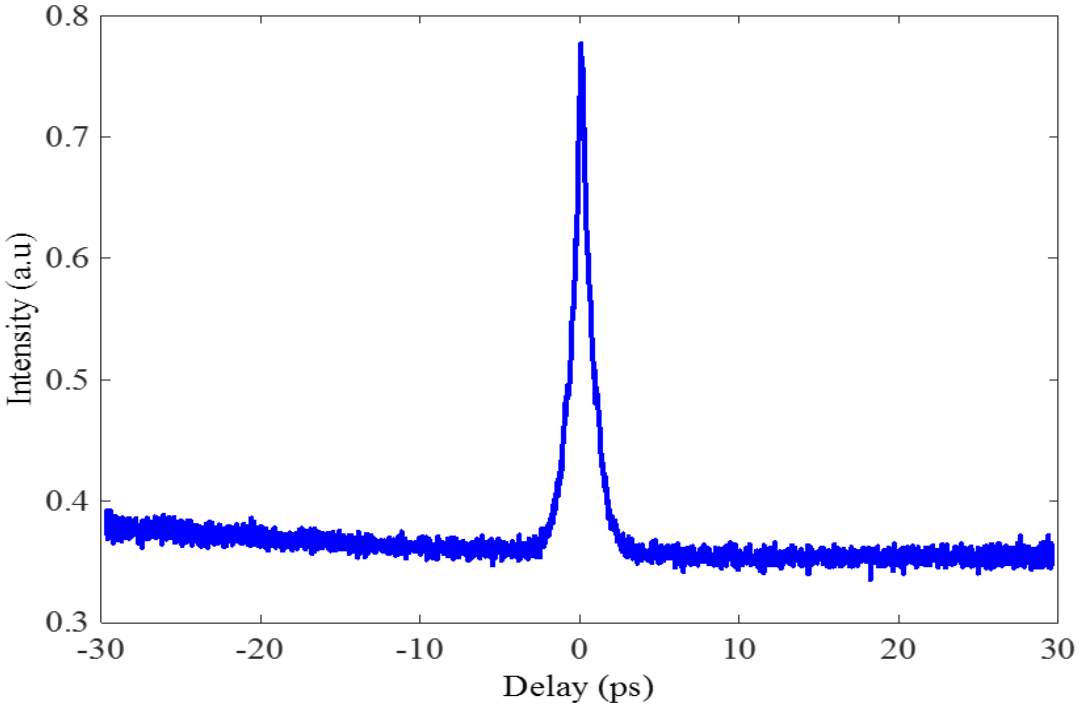

Fig. 5.15: The laser pulse after the Mamyshev regenerator.

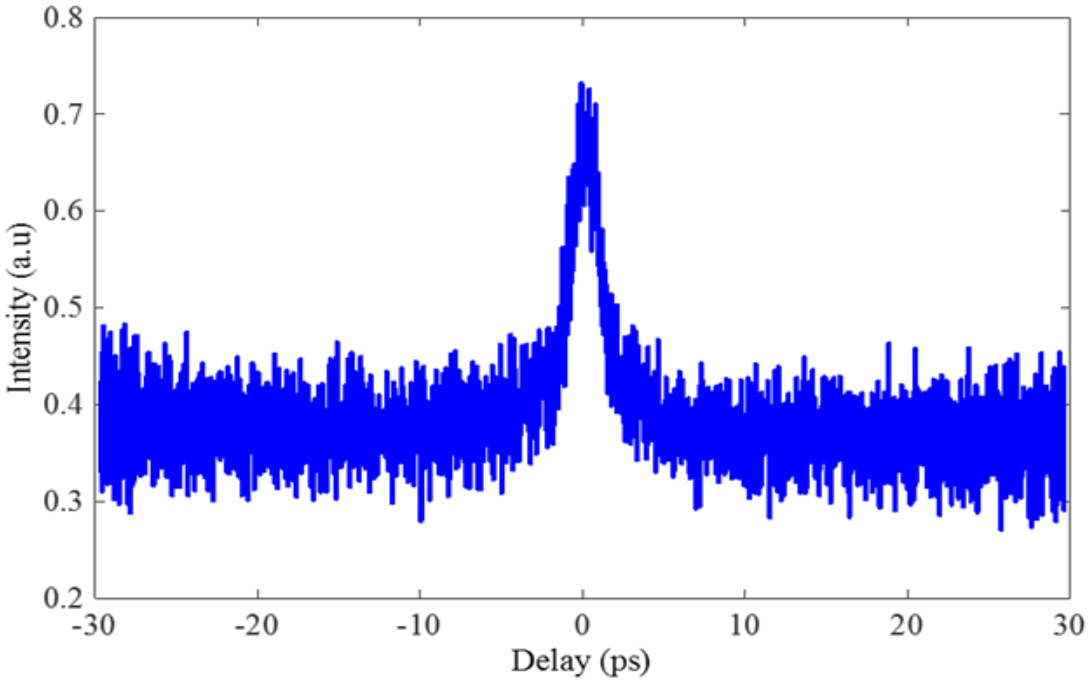

Fig. 5.16: The laser pulse after FSO link 2.

5.4.2.3 BER analysis

In this subsection, the experimental BER results of the AOAF and AORF FSO relay-assisted systems with and without turbulence are presented. The relays were located at equal distance between the Tx and the Rx in order to ensure that the FSO links were balanced and the SNR was the same for each hop. Based on the measured temperature profile and calculations using Eqns. 2.13, 2.14, and 2.16, we determined three average values of turbulence regimes, which were $C_n^2 = 1.6 \times 10^{-11}$ m$^{-2/3}$, $C_n^2 = 6.8 \times 10^{-10}$ m$^{-2/3}$, and $C_n^2 = 1.9 \times 10^{-9}$ m$^{-2/3}$. Note that, the total link span was 4.4 m for both relaying systems.

At the beginning, the BER performance of AORF and AOAF was examined experimentally for a single FSO link with a transmission span of 2.2 m, where both of the schemes were placed at the end of the link in order to reduce the effects of turbulence. The purpose of this investigation was to clarify the capability of AORF compared to AOAF as a noise mitigation technique. Fig. 5.17 presents the measured BER performance for AOAF and AORF for a single FSO link with no turbulence and two turbulence regimes of $C_n^2 = 1.06 \times 10^{-9} m^{-2/3}$ and $C_n^2 = 9.28 \times 10^{-10} m^{-2/3}$. One can observe from the figure that by applying the AORF scheme, there was a remarkable improvement in the BER performance compared to the AOAF technique. For example, at a BER of 10^{-3}, ~2.6 dB, ~2.2 dB, and ~2.1 dB SNR penalties were recorded for the AOAF scheme compared to the AORF scheme for the no turbulence, $C_n^2 = 9.28 \times 10^{-10} m^{-2/3}$, and $C_n^2 = 1.06 \times 10^{-9} m^{-2/3}$ cases, respectively. These performance gains are due to the ability of the AORF technique to reduce the turbulence-induced power fading at the end of the link.

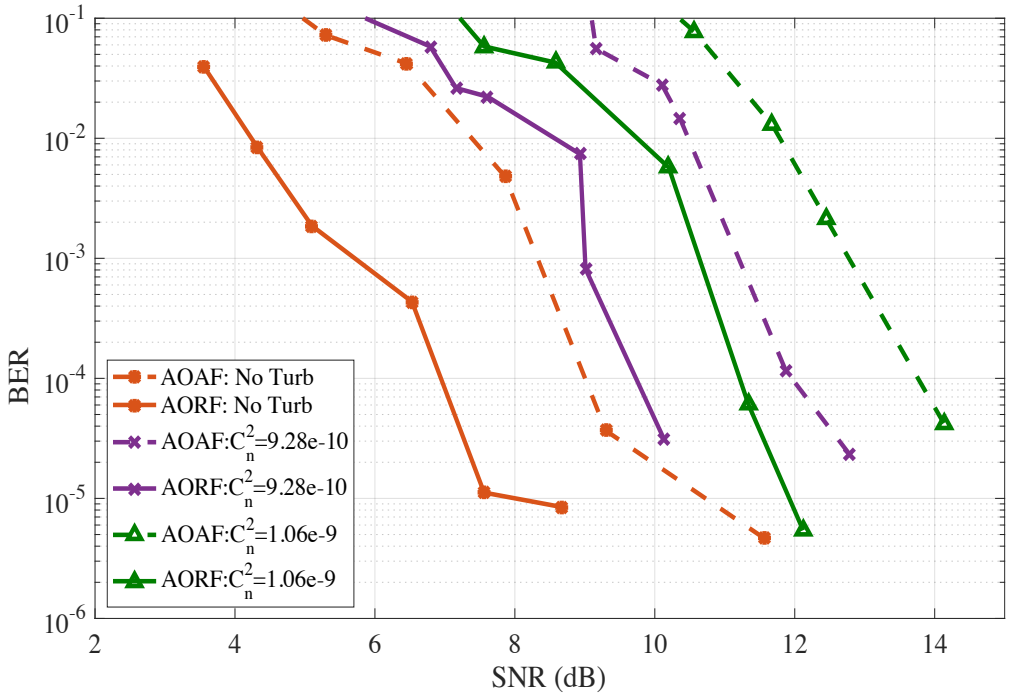

Fig. 5.17: Experimental BER vs. SNR of the AORF and AOAF FSO relay-assisted systems for a single link, with and without turbulence.

The dual-hop FSO link was then investigated both theoretically and experimentally by placing either the AOAF or AORF relaying scheme at the centre of the link. Note that, by splitting the overall link span into smaller sections, more energy (or power) is conserved. Fig. 5.18 depicts the comparison of measured and theoretical BER against SNR for the AORF dual-hop FSO relaying scheme without turbulence and with turbulence regimes of $C_n^2 = 1.9 \times 10^{-9} m^{-2/3}$, $C_n^2 = 6.8 \times 10^{-10} m^{-2/3}$, and $C_n^2 = 1.6 \times 10^{-11} m^{-2/3}$. The figure demonstrates that under stronger turbulence regimes, the propagating optical wave front experiences much higher levels of intensity and phase fluctuations, which lead to higher SNR penalties compared to the no turbulence case. For example, for the measured data, at a target BER of 10^{-3}, the SNR penalties were ~4.8 dB, ~8.0 dB, and ~10.0 dB for the system under turbulence of $C_n^2 = 1.6 \times 10^{-11} m^{-2/3}$, $C_n^2 = 6.8 \times 10^{-10} m^{-2/3}$, and $C_n^2 = 1.9 \times 10^{-9} m^{-2/3}$, respectively, when compared to the system with no turbulence. Notice the perfect match between theoretical and

measured plots for all cases. The slight mismatch between the predicted and measured plots at some points are due to losses associated with the optical components and ASE noise of EDFA in experimental case.

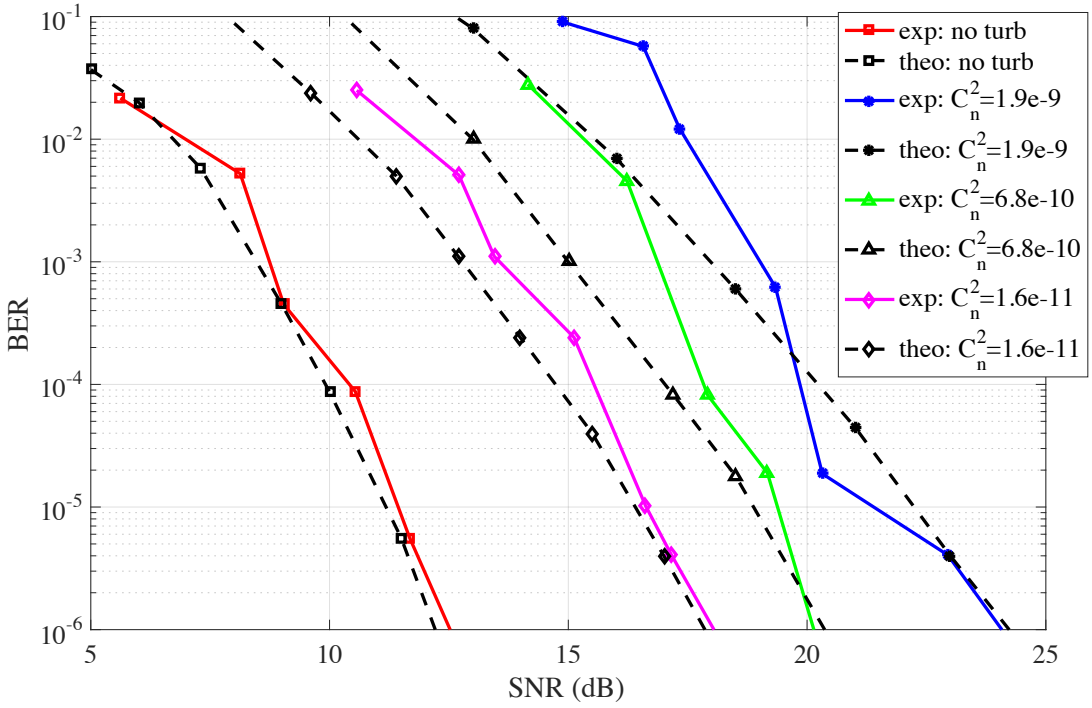

Fig. 5.18: Experimental (exp) and theoretical (theo) BER vs. SNR for the AORF dual-hop FSO link with and without turbulence.

A similar measurement was then performed for the AOAF dual-hop FSO relay-assisted scheme under the three aforementioned turbulence regimes. Fig. 5.19 then presents the measured and predicted BER performance against SNR for the AOAF dual-hop FSO relay-assisted system without turbulence and with turbulence regimes of $C_n^2 = 1.9 \times 10^{-9} m^{-2/3}$, $C_n^2 = 6.8 \times 10^{-10} m^{-2/3}$, and $C_n^2 = 1.6 \times 10^{-11} m^{-2/3}$. As expected, similar patterns as those depicted by Fig. 5.18 were observed, where stronger turbulence regime resulted in higher SNR penalties. For instance, at a target BER of 10^{-3}, the SNR penalties recorded were ~3.1 dB, ~8.2 dB, and ~9.4 dB for the turbulence levels of $C_n^2 = 1.6 \times 10^{-11} m^{-2/3}$, $C_n^2 = 6.8 \times 10^{-10} m^{-2/3}$, and $C_n^2 = 1.9 \times 10^{-9} m^{-2/3}$,

respectively, for the measured data when compared to the system with no turbulence. These results show a good agreement with the data presented in Chapter 4, where under a stronger turbulence regime the propagating optical wave front will experience higher degree of intensity and phase fluctuations.

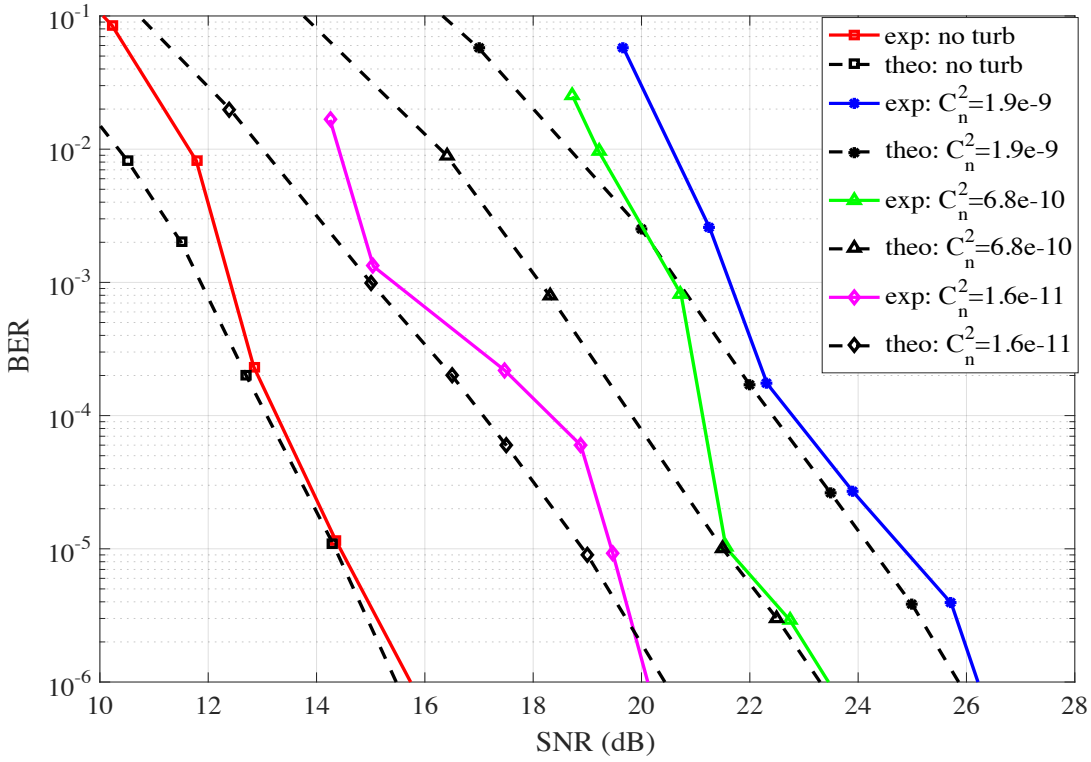

Fig. 5.19: Experimental (exp) and theoretical (theo) BER vs SNR for the AOAF dual-hop FSO link with and without turbulence.

Fig. 5.20 depicts a clear comparison of the measured BER performance against the SNR for the AORF (Fig. 5.18) and AOAF (Fig. 5.19) dual-hop FSO relay-assisted systems without turbulence and under the three aforementioned turbulence regimes. In this figure, one can clearly observe that the AORF system outperformed the AOAF systems for all the cases. For example, at a target BER of 10^{-3}, the AORF system recorded SNR gains of ~3.5 dB, ~1.8 dB, ~3.7 dB, ~3.0 dB compared to AOAF system for no turbulence, $C_n^2 = 1.6 \times 10^{-11}\ \mathrm{m}^{-2/3}$, $C_n^2 = 6.8 \times 10^{-10}\ \mathrm{m}^{-2/3}$, and $C_n^2 = 1.9 \times 10^{-9}\ \mathrm{m}^{-2/3}$, respectively. This outstanding BER performance of the AORF relaying

scheme is a result of the capability of the Mamyshev system in removing unwanted signal noise, and boosting the signal again by using the OA. The plots confirm that the AORF relaying scheme can be adopted successfully in a real practical environment to guarantee link availability and higher quality performance under turbulence conditions, with increased complexity and higher cost trade-offs compared to the AOAF scheme. The principle behind the superior AORF performance can be explained as follows. The regenerator, which is based on SPM broadening followed by spectral filtering, displays different transfer functions for the logical ones and logical zeros of RZ signal. Such discrimination arises from the intrinsically different temporal profile of the coherent pulsed signal and random noise [150]. The transfer function is engineered so that the pdfs of the logical ones and logical zeros entering the regenerator are compressed to produce noise-flattened bits, thereby improving the SNR [142].

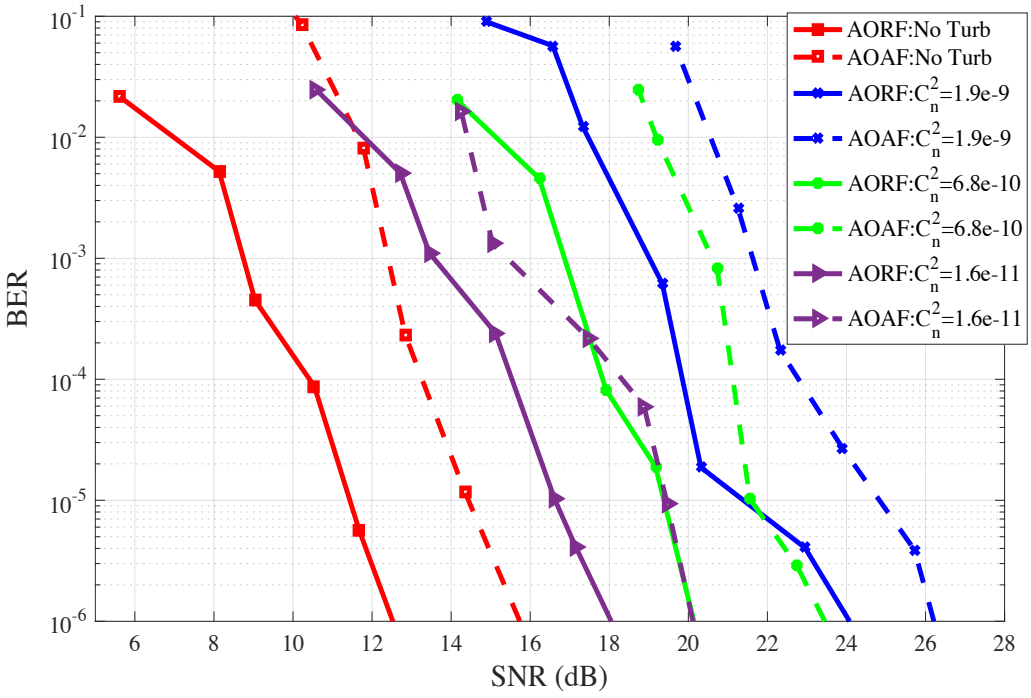

Fig. 5.20: Experimental BER vs. SNR for the AORF and AOAF dual-hop FSO links with and without turbulence.

In order to provide further insight into the capability of the AORF scheme over the AOAF scheme, a different turbulence configuration was set-up for the FSO dual-hop link. The first configuration, denoted here as Scenario 1, was such that link 1 had no turbulence and link 2 had a turbulence of $C_n^2 = 7.5 \times 10^{-10}$ m$^{-2/3}$. The configuration was then alternated by having a turbulence of $C_n^2 = 7.5 \times 10^{-10}$ m$^{-2/3}$ at link 1, and making link 2 turbulence-free (Scenario 2). The experimental results are also validated by means of numerical simulations. Fig. 5.21 depicts the BER performance against SNR for Scenario 1 and Scenario 2 for both AORF and AOAF schemes. The figure shows that for both theoretical and experimental, Scenario 1 imposed higher SNR penalties compared to Scenario 2. For example, for measured data, when comparing Scenario 1 and Scenario 2 at a target BER of 10^{-3}, Scenario 2 resulted in SNR penalties of ~3.3 dB and ~2.4 dB for the AORF and AOAF systems, respectively, compared to Scenario 1. Likewise, when comparing the AORF and AOAF systems in each scenario, there was a ~2.0 dB and ~2.9 dB SNR difference in Scenario 1 and Scenario 2, respectively at the target BER of 10^{-3}. These results prove the capability of the AORF system in reducing the turbulence induced fading prior to re-transmission, which results in a better BER performance. Note that, there is a good match between the measured and predicted plots. The slight mismatch between the plots could be due the losses from optical components.

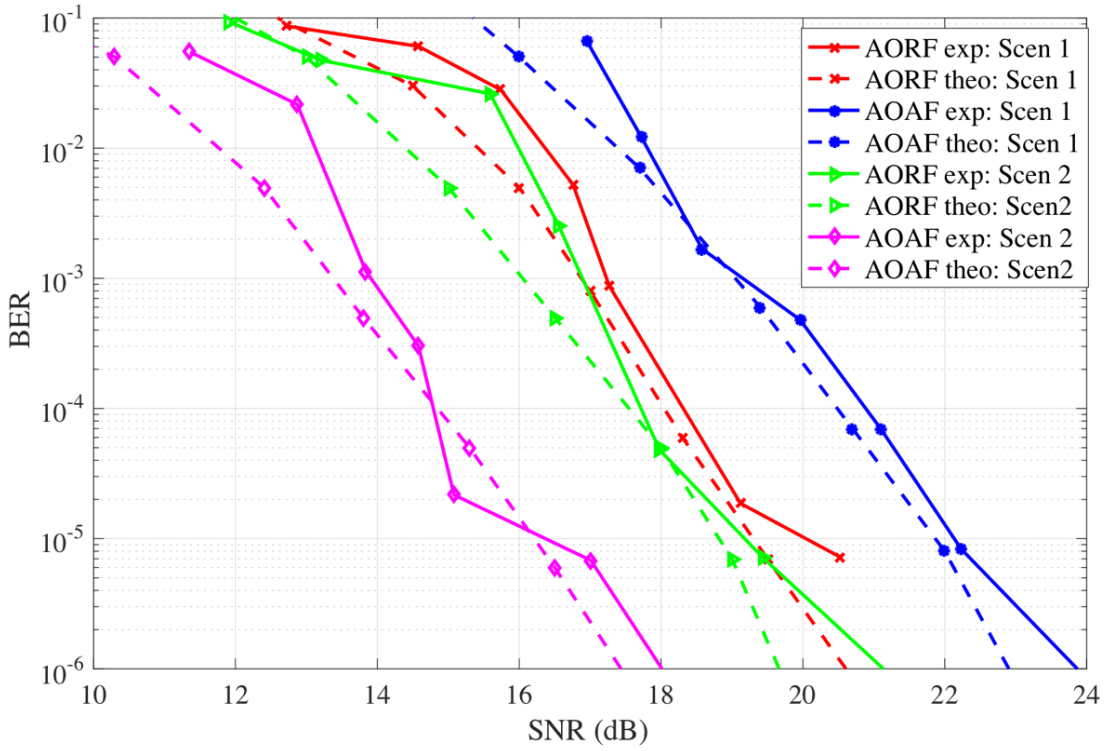

Fig. 5.21: Experimental (exp) and theoretical (theo) BER vs SNR for the AORF and AOAF dual-hop FSO links with different turbulence configurations.

In order to have clearer view of all turbulence conditions of the AORF and AOAF dual-hop FSO relay-assisted systems, all experimental results of each system were combined in Fig. 5.22 and Fig. 5.23, respectively. As such, Fig. 5.22 and Fig. 5.23 present the BER performance against the SNR for the AORF and AOAF dual-hop FSO links, respectively, without turbulence and under five different turbulence regimes. From the figures, we can affirm that the presence of turbulence induced fading plays a significant role in determining the overall BER system performance. This is due to the fact that atmospheric turbulence induces time-varying changes in the refractive index, which in turn affect the amplitude, phase and propagation direction of the optical signal. These changes result in time-varying power fluctuations of the received signal and ultimately affect to the overall system performance. By shortening the link into several hops and

introducing the AORF relaying scheme at the relay, the distance-dependent turbulence induced effects can be reduced, thus resulting in a better BER performance.

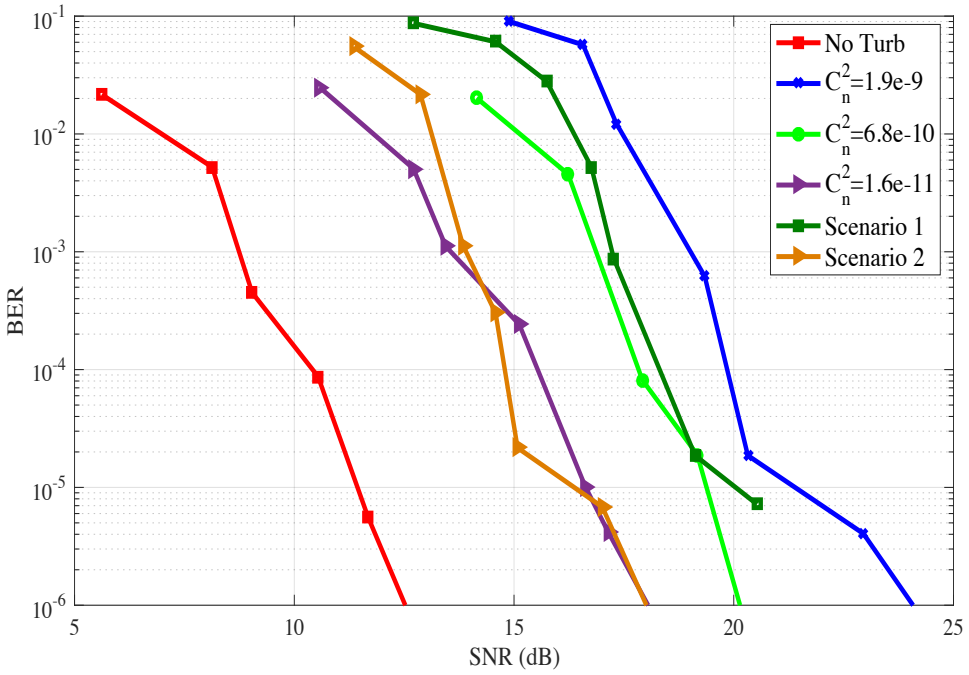

Fig. 5.22: Experimental BER vs SNR for the AORF dual-hop FSO links for all different turbulence configurations considered in the study.

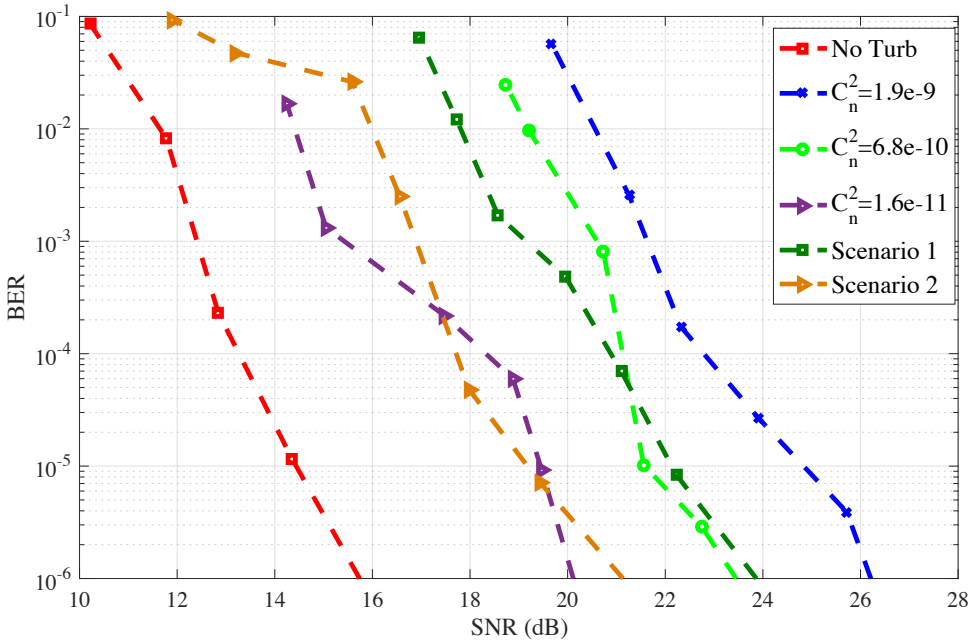

Fig. 5.23: Experimental BER vs SNR for the AOAF dual-hop FSO links for all different turbulence configurations considered in the study.

5.4.2.4 Eye diagrams

Using an oscilloscope, the eye diagrams of the received RZ signal were captured for the AORF and AOAF dual-hop FSO links without turbulence and under turbulence regimes of $C_n^2 = 1.6 \times 10^{-11}$ m$^{-2/3}$, $C_n^2 = 6.8 \times 10^{-10}$ m$^{-2/3}$, and $C_n^2 = 1.9 \times 10^{-9}$ m$^{-2/3}$, for BER values of 10^{-3} and 10^{-6}, as presented in Fig. 5.24 and Fig. 5.25, respectively. From the eye diagrams in Fig. 5.24, at a target BER of 10^{-3}, the *Q*-factor values of 4.81, 3.51, 2.8, and 1.4 were obtained for the AOAF dual-hop FSO link, and 6.62, 5.63, 4.32, and 3.6 for AORF dual-hop FSO link, for the no turbulence case and under turbulence regimes of $C_n^2 = 1.6 \times 10^{-11}$ m$^{-2/3}$, $C_n^2 = 6.8 \times 10^{-10}$ m$^{-2/3}$, and $C_n^2 = 1.9 \times 10^{-9}$ m$^{-2/3}$, respectively. As predicted, the *Q*-factor progressively decreased due to the turbulence induced fading, where the worst case scenario was experienced by the link under the turbulence regime of $C_n^2 = 1.9 \times 10^{-9}$ m$^{-2/3}$. Note that, AORF outperformed AOAF in terms of having larger eye openings and higher *Q*-factors for all conditions. A similar pattern of eye diagrams was observed for a BER of 10^{-6}, as depicted in Fig. 5.25. The height and width of the eye openings decreased with higher levels of turbulence for both AOAF and AORF systems. The *Q*-factor values of 6.32, 5.63, 4.29, and 3.02 were recorded for the AOAF dual-hop FSO link, and 8.32, 7.69, 6.73, and 4.16 for the AORF dual-hop FSO link, corresponding to no turbulence, $C_n^2 = 1.6 \times 10^{-11}$ m$^{-2/3}$, $C_n^2 = 6.8 \times 10^{-10}$ m$^{-2/3}$, and $C_n^2 = 1.9 \times 10^{-9}$ m$^{-2/3}$, respectively.

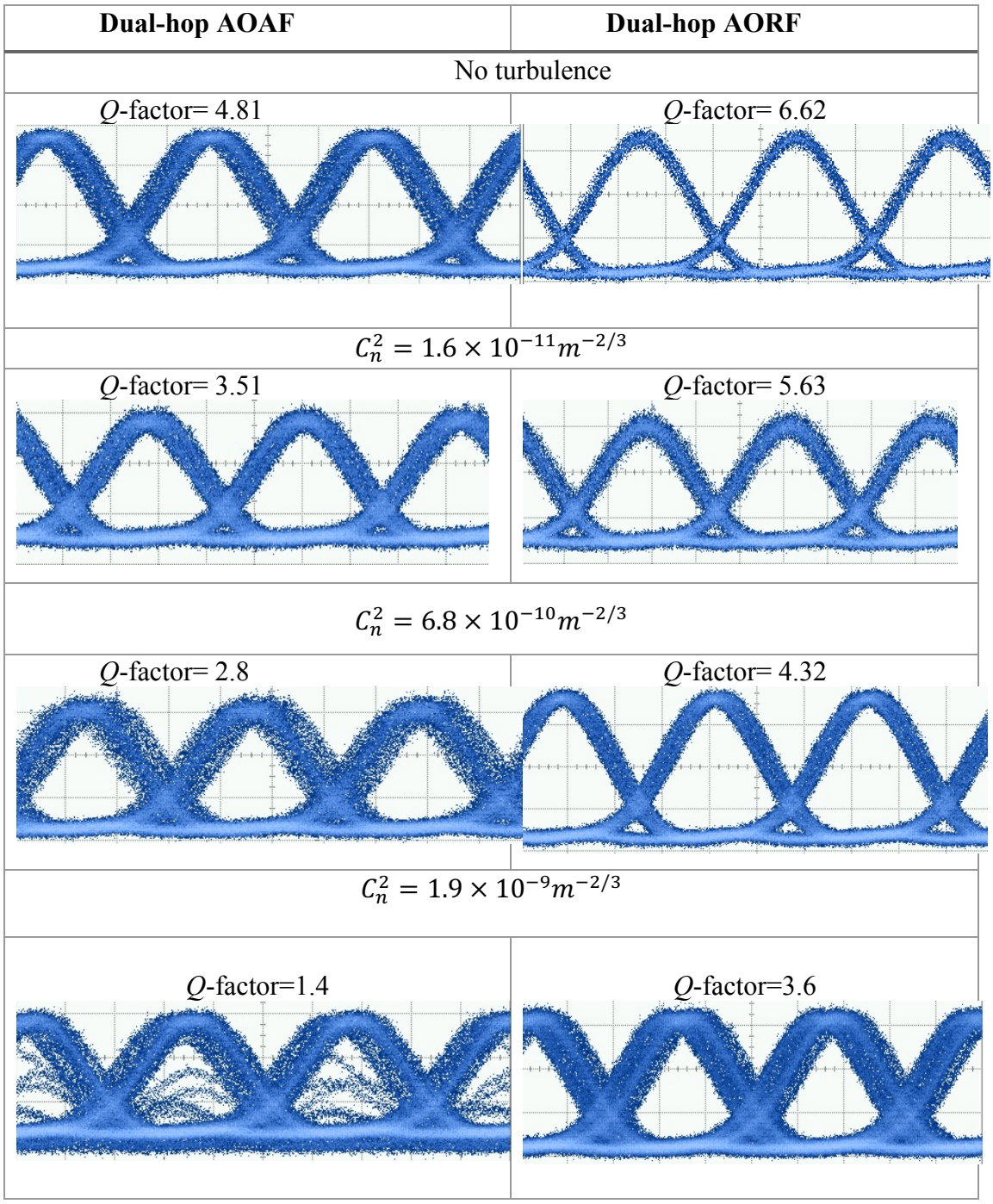

Fig. 5.24: Captured eye-diagrams of the RZ signal for dual-hop AOAF and AORF with and without turbulence, at a BER value of 10^{-3}.

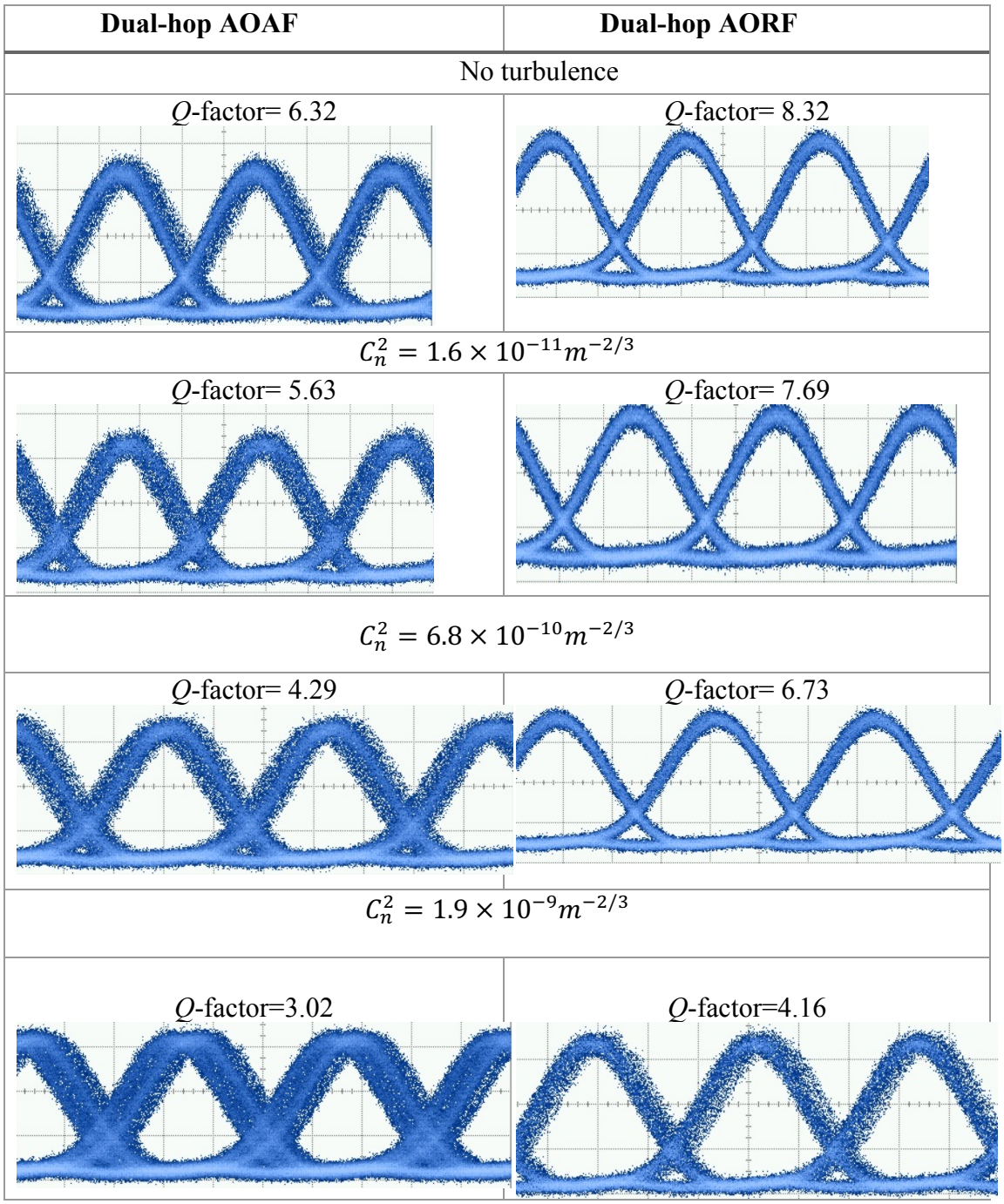

Fig. 5.25: Captured eye-diagrams of the RZ signal for dual-hop AOAF and AORF with and without turbulence, at a BER value of 10^{-6}.

5.5 Summary

In this chapter, the performance of all optical FSO links utilising the all-optical regenerate-and-forward technique over turbulence channels was investigated theoretically and practically. Since the AOAF relaying technique has the drawback of accumulating noise at every relay, there is a limit on the number of relays that can be employed in the system. Hence, the AORF technique was introduced in the context of FSO links to overcome the limitation imposed by the AF relaying technique and simultaneously increase the transmission link span. The AORF FSO link can remove all noise and regenerate the signal prior to re-transmission to the next relay/destination. To the best of the author's knowledge, this was the first experimental demonstration employing an all-optical 2R regenerator in FSO relaying systems.

The experimental investigation was carried out in an indoor laboratory setup, and the atmospheric turbulence channel was simulated under a controlled condition, mimicking the real-world turbulence scenario. The experimental analysis was conducted for both AORF and AOAF dual-hop FSO links, with and without turbulence, to ensure a fair comparison. The performance was evaluated by obtaining BER and SNR measurements, as well as retrieving *Q*-factor values from the eye-diagrams of the received RZ signal. The experimental investigation was carried out for two turbulence scenarios, where in the first scenario, the turbulence induced fading variance C_n^2 was the same for both links, while in second scenario, the value of C_n^2 for link 1 and link 2 was distinctive. In both scenarios, the AORF technique was shown to outperform the AOAF scheme in all tested turbulence regimes. Thus, the results proved the capability of the AORF relaying scheme in enhancing the performance of FSO links in terms of availability and reliability. This technique could be a key function in future optical

networks, since it could constitute a generic compensation for all signal degradations such as noise and timing jitter.

Chapter 6

CONCLUSIONS AND FUTURE WORKS

6.1 Conclusions

In this research project, extensive studies were carried out to investigate the effect of turbulence induced channel fading on all-optical FSO relay-assisted communications links. Through the acquisition of in-depth knowledge pertaining to the effect of turbulence on the FSO links and the capability of relaying technique in enhancing the overall system performances through the relevant literatures, new optimization and evaluation regarding to the design of the FSO relay-based system were proposed and presented in this thesis. In addition, a novel state of the art laboratory test-bed was demonstrated translucently for comprehensive test and measurement, and measured results were compared with the predicted data.

Relay-assisted FSO communication is one of the alternative mitigation solutions that offers diversity within the networks, which can be adopted to combat link failure thus substantially improve the link availability and distance. Albeit its tremendous performances, the turbulence fading variance still becomes the main challenges for the overall system performances since the FSO transmission is using the air as the transmission channel. To mitigate the degrading effect of the turbulence-induced fading, all-optical relay-assisted system were chosen as the potential solution as this technique

elegantly exploit the distance-dependent of the turbulence effect, while maintaining the high data rate communication.

This thesis commenced from the brief overview on the FSO communications networks in Chapter 2. The key fundamental regarding FSO communication systems as well as the application and features of FSO technology that makes it more viable compared with the existing RF technologies were explained. Following that, the diverse atmospheric channel conditions, which become the main challenges to the FSO technologies such as absorption, attenuation, and atmospheric turbulence were highlighted. Chapter 2 also discussed the relevant performance metrics to quantify the FSO communication systems, which include SNR, BER, and eye diagrams. In Chapter 3, few mitigation techniques in FSO systems were discussed. Among them aperture averaging and spatial diversity techniques are the most popular mitigation techniques due to its simplicity and effectiveness. Recently, relay-assisted or multi-hop transmission systems have been introduced as a powerful fading mitigation tool as an alternate option in realizing the spatial diversity advantages. Hence, this chapter elaborated the principle and configurations of this relay-assisted FSO communication as well as the concept of all-optical FSO relay-based systems. Then, two proposed AOAF and AORF FSO relay-based systems were explained. Also discussed were the fundamental theory of optical amplifier and the regenerator.

Chapter 4 presented the main finding of this research work regarding to the AOAF FSO relay-assisted for utilizing the FSO network capabilities. This is done by using an optical amplifier at the relay, to boost the received signal and forward it the next relay/destination. The performance analysis of single, dual-hop, and triple-hop AOAF FSO were comprehensively discussed theoretically and experimentally under the effects of turbulence channels. A mathematical framework for the end-to-end SNR and BER performance for the general multi-hop relay assisted FSO link was also outlined,

considering the Gamma-Gamma distribution model. The novel experimental demonstration were discussed and results presented a good agreement between the analytical calculations and measurements, particularly at relatively high SNRs. For the analysis of triple-hop AOAF system, two turbulence configurations were demonstrated using the same experimental setup discussed in Section 4.6.1. In the first configuration, we assumed the turbulence were identical for all-hops, which means that all-hops have the same C_n^2. Then, in second configuration, the occurrences of turbulence were differed, where seven turbulence scenarios were considered. Based on the results, it was proven that the triple-hop FSO link substantially improves the overall link performance under atmospheric turbulence. As it was analytically shown, these significant performance gains are due to the ability of multi-hop transmissions to exploit distance-dependent turbulence induced fading variance by implicitly shortening the transmission span.

Even though AOAF is simple and straightforward to be implemented, OA amplified the signal and noise together, which limit the transmission span. Therefore, in Chapter 5, AORF was proposed to overcome this particular issue by eliminating the background noise and regenerate the signal at each relay, before re-transmit to the next relay or destination. This technique significantly increase the total transmission distance and ensures the maximum flexibility in network design by providing greater tolerance in adding or dropping the channel. Also discussed in this particular chapter is the design of the regenerator, which is based on the SPM nonlinear concept or also known as Mamyshev regenerator. The experimental setup for dual-hop AORF FSO relay-assisted system was carried out in the dedicated indoor laboratory test-bed where the basic components consists of an EDFA, HNLF, and OBPF. Then, the performance analysis of the AORF FSO dual-hop system was evaluated using the standard metrics of BER, SNR, eye-diagrams, and *Q*-factor values under several turbulence regimes, and compared with dual-hop AOAF FSO systems. The results proved that by applying AORF scheme there

was remarkable improvement in the BER and *Q*-factor performance compared to the AOAF technique, by removing the unwanted signal noise at the relay before re-transmission to the next relay or destination.

Last but not least, this research had experimentally verified the capability of all-optical FSO relay-assisted system to guarantee link availability and higher quality performance under turbulence induced fading, simultaneously increase the transmission link distance. To the best of our knowledge, this was the first experimental demonstration based on all-optical multiple-hop relay-assisted system for both aforementioned systems. By implementing an all-optical system, the overall system complexity is reduced (compared to electrical relaying) making it an attractive solution for future ad-hoc optical wireless systems.

6.2 Recommendations for Future Works

This thesis has contributed to the analysis and optimization of the all-optical FSO relay-assisted system that employing either AOAF or AORF at the intermediate node under the effect of turbulence-induced fading, which have progressively uncovered more research opportunities and areas of improvement pertaining to the system study.

- As a straight forward progression of the proposed all-optical FSO relaying system presented here, the study and experimental demonstration in real practical field with typical terrestrial FSO link distance, i.e., 500 m for last mile access network, for both proposed system can prove very significant. This, potentially will provide interesting findings regarding the implementation of FSO system in real field environment, thus prove the suitability of relaying system as a tool for increasing communication systems throughput.

- A comprehensive design benchmark of AOAF FSO relay-assisted systems was presented in Chapter 4, taking into account the effect of turbulence induced fading. However, another mitigation approaches, namely, aperture averaging, can be incorporated to the existing system, Furthermore, since we only used NRZ-OOK in the investigation of AOAF scheme, higher order modulation can also be integrated such as *M*-order pulse amplitude modulation (*M*-PAM), in order to obtain the best BER performance. In addition, the influences of other atmospheric effects such as absorption and attenuation (i.e. rain, snow, and fog) as well as the effect of pointing error on the particular system can also be investigated to attain better performance accuracy. Thereafter, more extensive simulation and experimental studies are required to observe and validate the aforementioned suggested system.
- In the proposed system of AORF FSO relay-assisted system presented in Chapter 5, practical demonstration without analytical investigation was presented. Better enhancement of the system can be achieved by varying the output power of the EDFA that fed to the HNLF, HNLF length, and the OBPF bandwidth and wavelength, which can be done through analytical and simulation studies. There will be a trade-off between the length of the HNLF and the cost, which can be exploited depends on the application. Similar suggestion as previously mentioned for AOAF can be adopted in here.
- Another future work is the design of the cooperative communication based on the proposed relaying system for future ad-hoc networking system. Multi-directional links which include the transceiver system can be consolidated for better functional system. Also can be included is the selective relaying where better path will be chosen to make sure the signal arrived at the destination if the desired path is temporary blocked or broken.

References

[1] "Internet growth statistics," 2016. [Online]. Available: http://www.internetworldstats.com/emarketing.htm. [Accessed: 04-Sep-2016].

[2] S. Wabnitz and B. J. Eggleton, *All-optical signal processing: Data communication and storage*. Springer Series in Optical Sciences, 2015.

[3] K.-L. Du and M.N.S.Swamy, *Wireless communication systems from RF subsystems to 4G enabling technologies*. United Kindom: Cambridge University Press, 2010.

[4] A. Osseiran *et al.*, "Scenarios for the 5G mobile and wireless communications : the vision of the METIS project," *IEEE Commun. Mag.*, vol. 52, no. 5, pp. 26–35, 2014.

[5] A. K. Majumdar, *Advanced free space optics (FSO): A system approach*, vol. 140. USA: Springer, 2015.

[6] S. Arnon, J. R. Barry, G. K. Karagiannidis, R. Schober, and M. Uysal, *Advanced optical wireless communication systems*. New York, USA: Cambridge University Press, 2012.

[7] Z. Ghassemlooy, W. Popoola, and S. Rajbhandari, *Optical wireless communications: System and channel modelling with MATLAB*. United Kingdom: CRC Press Taylor and Francis Group, 2013.

[8] G. Parca, "Optical wireless transmission at 1.6-Tbit/s (16×100 Gbit/s) for next-generation convergent urban infrastructures," *Opt. Eng.*, vol. 52, no. 11, p. 116102, Nov. 2013.

[9] M. Uysal, C. Capsoni, Z. Ghassemlooy, and A. Bousouvalas, *Optical wireless communications : An emerging technology*, no. March. Switzerland: Springer International Publishing, 2016.

[10] E. Ciaramella *et al.*, "1.28 Terabit/s (32x40 Gbit/s) WDM transmission system for free space optical communications," *IEEE J. Sel. Areas Commun.*, vol. 27, no. 9, pp. 1639–1645, 2009.

[11] L. C. Andrews and R. L. Phillips, *Laser beam propagation through random media*, 2nd Ed. Washington, USA: SPIE Press, 2005.

[12] M. H. Mahdieh and M. Pournoury, "Atmospheric turbulence and numerical evaluation of bit error rate (BER) in free-space communication," *Opt. Laser Technol.*, vol. 42, no. 1, pp. 55–60, Feb. 2010.

[13] J. Vitásek *et al.*, "Atmospheric Turbulences in Free Space Optics Channel," pp. 104–107, 2011.

[14] K. Prabu, D. S. Kumar, and T. Srinivas, "Performance analysis of FSO links under Strong atmospheric turbulence conditions using various modulation schemes," *Optik (Stuttg).*, vol. 125, no. 19, 2014.

[15] A. García-Zambrana, C. Castillo-Vázquez, and B. Castillo-Vázquez, "On the capacity of FSO links over gamma-gamma atmospheric turbulence channels using OOK signaling," *Eurasip J. Wirel. Commun. Netw.*, 2010.

[16] R. Pernice, A. Andò, A. Parisi, A. C. Cino, and A. C. Busacca, "Moderate-to-Strong Turbulence Generation in a Laboratory Indoor Free Space Optics Link and Error Mitigation via RaptorQ Codes," in *ICTON*, 2016, pp. 1–4.

[17] I. E. Lee, Z. Ghassemlooy, W. P. Ng, and M. Uysal, "Performance analysis of free space optical links over turbulence and misalignment induced fading channels,"

2012 8th Int. Symp. Commun. Syst. Networks Digit. Signal Process., pp. 1–6, Jul. 2012.

[18] J. Perez, S. Zvanovec, Z. Ghassemlooy, and W. O. Popoola, "Experimental characterization and mitigation of turbulence induced signal fades within an ad hoc FSO network.," *Opt. Express*, vol. 22, no. 3, pp. 3208–18, Mar. 2014.

[19] M. Ijaz *et al.*, "Experimental Investigation of the Performance of OOK-NRZ and RZ Modulation Techniques under Controlled Turbulence Channel in FSO Systems," in *5th International Symposium on Telecommunications (IST)*, 2010, pp. 59–64.

[20] M. Ahmad and O. Awwad, "Synergies of Radio Frequency and Free Space Optics Communication : New Hybrid Solutions for Next Generation Wireless Mesh Networks," *Int. J. Comput. Networks*, vol. 4, no. 4, pp. 135–155, 2012.

[21] I. E. Lee, Z. Ghassemlooy, W. P. Ng, and S. Rajbhandari, "Fundamental analysis of hybrid free space optical and radio frequency communication systems," in *Proc. 12th Annual Post Graduate Symposium on the Convergence of Telecommunication, Networking, and Broadcasting (PGNet 2011)*, pp. 281-285, 2011.

[22] M. M. Abadi, Z. Ghassemlooy, S. Zvanovec, D. Smith, M. R. Bhatnagar, and Y. Wu, "Dual purpose antenna for hybrid free space optics/RF communication systems," *J. Light. Technol.*, vol. 34, no. 14, pp. 3432–3439, 2016.

[23] W. O. Popoola and Z. Ghassemlooy, "BPSK subcarrier intensity modulated free-space optical communications in atmospheric turbulence," *J. Light. Technol.*, vol. 27, no. 8, pp. 967–973, 2009.

[24] A. T. Pham, T. C. Thang, S. Guo, and Z. Cheng, "Performance bounds for turbo-coded SC-PSK/FSO communications over strong turbulence channels," in *International Conference on Advanced Technologies for Communications*, 2011, pp. 161–164.

[25] M. Uysal, J. Li, and M. Yu, "Error rate performance analysis of coded free-space optical links over gamma-gamma atmospheric turbulence channels," *IEEE Trans. Wirel. Commun.*, vol. 5, no. 6, pp. 1229–1233, 2006.

[26] Z. Zhao, S. D. Lyke, and M. C. Roggemann, "Adaptive optical communication through turbulent atmospheric channels," in *IEEE International Conference on Communications*, 2008, pp. 5432–5436.

[27] F. E. Zocchi, "A simple analytical model of adaptive optics for direct detection free-space optical communication," *Opt. Commun.*, vol. 248, no. 4–6, pp. 359–374, 2005.

[28] G. Yang, M.-A. Khalighi, Z. Ghassemlooy, and S. Bourennane, "Performance evaluation of receive-diversity free-space optical communications over correlated Gamma-Gamma fading channels.," *Appl. Opt.*, vol. 52, no. 24, pp. 5903–11, Aug. 2013.

[29] M. Abaza, R. Mesleh, A. Mansour, and E. M. Aggoune, "Spatial diversity for FSO communication systems over correlated atmospheric turbulence channels," in *IEEE Wireless Communications and Networking Conference (WCNC)*, 2014, vol. 1, pp. 382–387.

[30] M.-A. Khalighi, N. Schwartz, N. Aitamer, and S. Bourennane, "Fading reduction by aperture averaging and spatial diversity in optical wireless systems," *J. Opt. Commun. Netw.*, vol. 1, no. 6, pp. 580–593, Oct. 2009.

[31] M. A. Khalighi, N. Aitamer, N. Schwartz, and S. Bourennane, "Turbulence Mitigation by Aperture Averaging in Wireless Optical Systems," in *10th International Conference on Telecommunications (ConTEL)*, 2009, pp. 59–66.

[32] I. E. Lee, Z. Ghassemlooy, W. P. Ng, M.-A. Khalighi, and S.-K. Liaw, "Effects of aperture averaging and beam width on a partially coherent Gaussian beam over free-space optical links with turbulence and pointing errors," *Appl. Opt.*, vol. 55,

no. 1, p. 1, 2016.
[33] F. S. Vetelino, C. Young, L. Andrews, and J. Recolons, “Aperture averaging effects on the probability density of irradiance fluctuations in moderate-to-strong turbulence,” *Appl. Opt.*, vol. 46, no. 11, pp. 2099–108, Apr. 2007.
[34] S. Navidpour, M. Uysal, and M. Kavehrad, “BER performance of free-space optical transmission with spatial diversity,” *IEEE Trans. Wirel. Commun.*, vol. 6, no. 8, pp. 2813–2819, Aug. 2007.
[35] S. Kazemlou, S. Hranilovic, and S. Kumar, “All-optical multihop free-space optical communication systems,” *J. Light. Technol.*, vol. 29, no. 18, pp. 2663–2669, Sep. 2011.
[36] M. A. Khalighi and M. Uysal, “Survey on free space optical communication: A communication theory perspective,” *IEEE Commun. Surv. Tutorials*, vol. 16, no. 4, pp. 2231–2258, 2014.
[37] A. Paraskevopoulos, J. Vucic, S. H. Voss, R. Swoboda, and K.-D. Langer, “Optical wireless communication systems in the Mb/s to Gb/s range , suitable for industrial applications,” *IEEE/ASME Trans. Mechatronics*, vol. 15, no. 4, pp. 541–547, 2010.
[38] A. Vavoulas, H. G. Sandalidis, and D. Varoutas, “Weather effects on FSO network connectivity,” *J. Opt. Commun. Netw.*, vol. 4, no. 10, p. 734, Sep. 2012.
[39] J. Zhuanhong, Z. Qinglin, and A. Faliang, “Atmospheric Attenuation Analysis in the FSO Link,” in *International Conference on Communication Technology, 2006 (ICCT ’06)*, 2006, pp. 1–4.
[40] X. Yi, Z. Liu, and P. Yue, “Optical scintillations and fade statistics for FSO communications through moderate-to-strong non-Kolmogorov turbulence,” *Opt. Laser Technol.*, vol. 47, 2013.
[41] S. V. Kartalopoulos, *Free Space Optical Networks for Ultra-Broad Band Services*. 2011.
[42] Z. Ghassemlooy, H. Le-Minh, and M. Ijaz, “Free Space Optical Communications,” in *Optical And Microwave Technologies for Telecommunication Networks*, vol. Chapter 10, no. 2, UK: J Wiley, 2016, pp. 349–377.
[43] H. Willebrand and B. Ghuman, *Free Space Optics: Enabling Optical Connectivity in Today’s Networks*, 1st ed. US: Sams Publishing, 2001.
[44] H. Hemmati, *Deep Space Optical Communications*. John Wiley & Sons, 2006.
[45] P. C. Gurumohan and J. Hui, “Topology design for free space optical networks,” in *IEEE International Conference on Computer Communications and Networks*, 2003, pp. 576–579.
[46] R. Sabella and P.Lugli, *High speed optical communications*. UK: Springer, 2002.
[47] G. P. Agrawal, *Lightwave technology: Telecommuniction systems*. New Jersey: Wiley-Interscience, 2005.
[48] A. Majumdar and J. C. Ricklin, *Free-space laser communications: Principles and advances*. New York, USA: Springer, 2008.
[49] R. R. Iniguez, S. M. Idrus, and Z. Sun, *Optical Wireless Communications: IR for Wireless Connectivity*. USA: CRC Press Taylor and Francis Group, 2008.
[50] M. Ijaz, “Experimental characterisation and modelling of atmospheric fog and turbulence in FSO,” University of Northumbria at Newcastle, 2013.
[51] D. Rockwell and S. Mecherle, “Wavelength selection for optical wireless communications systems.” fSona Communication Corporation, 2001.
[52] A. K. Majumdar, “Free space laser communication performance in the atmospheric channel,” in *Free space laser communications: Principles and advances*, vol. 2, 2005, pp. 57–108.
[53] Z. Ghassemlooy and W. O. Popoola, “Terrestrial Free-Space Optical Communications,” in *Mobile and Wireless Communications: Network layer and*

circuit level design, S. A. Fares and F. Adachi, Eds. InTech, 2010, pp. 355–392.
[54] L. Ibbotson, "The Fundamentals of Signal Transmission," 1999.
[55] Z. Ghassemlooy, S. Arnon, M. Uysal, Z. Xu, and J. Cheng, "Emerging optical wireless communications-Advances and challenges," *IEEE J. Sel. Areas Commun.*, vol. 33, no. 9, pp. 1738–1749, 2015.
[56] K. Tsukamoto, A. Hashimoto, Y. Aburakawa, and M. Matsumoto, "The case for free space," *IEEE Microw. Mag.*, vol. 10, no. 5, pp. 84–92, 2009.
[57] M. Matsumoto *et al.*, "An alternative access technology for Next Generation Networks based on full-optical wireless communication links," *Proc. First Itu-T Kaleidosc. Acad. Conf. Innov. Ngn Futur. Netw. Serv.*, p. 221–228\n443, 2008.
[58] D. K. Borah, A. C. Boucouvalas, C. C. Davis, S. Hranilovic, and K. Yiannopoulos, "A review of communication-oriented optical wireless systems," *EURASIP J. Wirel. Commun. Netw.*, vol. 1, pp. 1–28, 2012.
[59] V. W. S. Chan, "Optical Satellite Networks," *J. Light. Technol.*, vol. 21, no. 11, pp. 2811–2827, 2003.
[60] H. Hemmati and B. J. Thompson, *Near-Earth Laser Communications*. Taylor & Francis Group, 2008.
[61] H. Kaushal, V. K. Jain, and S. Kar, "Improvement of ground to satellite FSO link performance using transmit diversity in weak atmospheric turbulence," in *International Conference on Intelligent and Advanced Systems (ICIAS) 2010* , 2010, pp. 1–6.
[62] M. Toyoshima *et al.*, "Ground-to-Satellite Laser Communication Experiments," *IEEE Aerosp. Electron. Syst. Mag.*, vol. 23, no. 8, pp. 10–18, 2008.
[63] D. Kedar, S. Arnon, and Ben-Gurion, "Urban optical wireless communication networks: The main challenges and possible solutions," *IEEE Opt. Commun.*, vol. 42, no. 5, pp. 2-S7, 2004.
[64] S. Bloom, E. Korevaar, and J. Schuster, "Understanding the performance of free-space optics [Invited]," *J. Opt. Netw.*, vol. 2, no. 6, pp. 178–200, 2003.
[65] T. Plank, E. Leitgeb, and M. Loeschnigg, "Recent developments on free space optical links and wavelength analysis," in *International Conference on Space Optical Systems and Applications (ICSOS)*, 2011, pp. 14–20.
[66] M. Uysal and M. M. Fareed, "Cooperative diversity systems for wireless communication," in *Selected Topics in Information and Coding Theory*, World Scientific, 2010, pp. 623–662.
[67] J. C. Ricklin, S. M. Hammel, F. D. Eaton, and S. L. Lachinova, "Atmospheric channel effects on free-space laser communication," *J. Opt. Fiber Commun. Reports*, vol. 3, no. 2, pp. 111–158, 2006.
[68] ITU-R, "RECOMMENDATION ITU-R P.1814, Prediction methods required for the design of terrestrial free-space optical links ." 2007.
[69] L. B. Stotts, P. Kolodzy, A. Pike, B. Graves, D. Dougherty, and J. Douglass, "Free-space optical communications link budget estimation.," *Appl. Opt.*, vol. 49, no. 28, pp. 5333–5343, 2010.
[70] O. Bouchet, H. Sizun, C. Boisrobert, F. de Fornel, and P.-N. Favennec, *Free-space optics Propagation and Communication*, vol. 2. London: ISTE Ltd, 2006.
[71] W. Popoola, Z. Ghassemlooy, M. S. Awan, and E. Leitgeb, "Atmospheric channel effects on terrestrial free space optical communication links," in *International Conference on Electronics, Computers abd Artificial Intelligence (ECAI 2009)*, 2009, vol. 3, pp. 17–23.
[72] M. S. Awan, L. C. Horwath, S. S. Muhammad, E. Leitgeb, F. Nadeem, and M. S. Khan, "Characterization of Fog and Snow Attenuations for Free-Space Optical Propagation," *J. Commun.*, vol. 4, no. 8, pp. 533–545, 2009.
[73] I. I. Kim, B. McArthur, and E. Korevaar, "Comparison of laser beam propagation

at 785nm and 1550nm in fog and haze for optical wireless communications," *Proc. SPIE Opt. Wirel. Commun. III*, vol. 4214, no. 26, 2000.
[74] H. Weichel, *Laser beam propagation in the atmosphere*. Bellingham, Washington: SPIE, 1990.
[75] M. Achour, "Simulating Atmospheric Free-Space Optical Propgation, Part II: Haze, Fog, and Low Clouds Attenuations," *Proceeding SPIE*, vol. 4873, no. 1, 2002.
[76] L. C. Andrews, R. L. Phillips, and C. Y. Hopen, *Laser Beam Scintillation with Applications*. Washington, USA: SPIE Press, 2001.
[77] Z. Ghassemlooy, H. Le Minh, S. Rajbhandari, J. Perez, and M. Ijaz, "Performance analysis of ethernet / fast-ethernet free space optical communications in a controlled weak turbulence conditions," *J. Light. Technol.*, vol. 30, no. 13, pp. 2188–2194, 2012.
[78] M. Hulea, Z. Ghassemlooy, S. Rajbhandari, and X. Tang, "Compensating for optical beam scattering and wandering in FSO communications," *J. Light. Technol.*, vol. 37, no. 7, pp. 1323–1328, 2014.
[79] R. Esposito, "Power scintillations due to the wandering of the laser beam," *Proc. IEEE*, vol. 55, pp. 1533–1534, 1967.
[80] W. O. Popoola, "Subcarrier Intensity Modulated free-Space Optical Communication Systems," University of Northumbria at Newcastle, 2009.
[81] A. O. Aladeloba, A. J. Phillips, and M. S. Woolfson, "Improved bit error rate evaluation for optically pre-amplified free-space optical communication systems in turbulent atmosphere," *IET Optoelectron.*, vol. 6, no. July 2011, pp. 26–33, 2012.
[82] M. R. Bhatnagar, "Performance analysis of decode-and-forward relaying in gamma-gamma fading channels," *IEEE Photonics Technol. Lett.*, vol. 24, no. 7, pp. 545–547, 2012.
[83] M. A. Al-Habash, L. C. Andrews, and R. L. Phillips, "Mathematical model for the irradiance probability density function of a laser beam propagating through turbulent media," *Opt. Eng.*, vol. 40, no. 8, p. 1554, Aug. 2001.
[84] L. C. Andrews, R. L. Phillips, R. J. Sasiela, and R. Parenti, "Beam wander effects on the scintillation index of a focused beam," *Proc. SPIE 5793, Atmos. Propag. II*, vol. 28, 2005.
[85] A. Andò *et al.*, "Recovery capabilities of rateless codes on simulated turbulent terrestrial free space optics channel model," *Int. J. Antennas Propag.*, vol. 2013, no. Article ID 692915, 2013.
[86] R. Pernice *et al.*, "Indoor free space optics link under the weak turbulence regime: measurements and model validation," *IET Commun.*, vol. 9, no. April 2014, pp. 62–70, 2015.
[87] R. K. Tyson, "Bit-error rate for free-space adaptive optics laser communications," *J. Opt. Soc. Am.*, vol. 19, no. 4, pp. 753–758, 2002.
[88] H. G. Sandalidis, T. A. Tsiftsis, G. K. Karagiannidis, and M. Uysal, "BER performance of FSO links over strong atmospheric turbulence channels with pointing errors," *IEEE Commun. Lett.*, vol. 12, no. 1, pp. 44–46, 2008.
[89] S. V. Kartalopoulos, *Next generation intelligent optical networks: From Access to backbone*. USA: Springer, 2008.
[90] H. Yuksel, S. Milner, and C. C. Davis, "Aperture averaging for optimizing receiver design and system performance on free-space optical communication links," *J. Opt. Netw.*, vol. 4, no. 8, p. 462, 2005.
[91] A. A. Hashmi, A. Eftekhar, A. Yegnanarayanan, "Analysis of Optimal Adaptive Optics System for Hybrid RF-Wireless Optical Communication for Maximum Efficiency and Reliability," in *International Conference on Emerging*

Technologies, 2008.
[92] M. Uysal and J. Li, "BER performance of coded free-space optical links over strong turbulence channels," in *Vehicular Technology Conference. VTC 2004-Spring*, 2004, vol. 1, pp. 352–356.
[93] S. Rajbhandari, Z. Ghassemlooy, P. A. Haigh, T. Kanesan, and X. Tang, "Experimental error performance of modulation schemes under a controlled laboratory turbulence FSO channel," *J. Light. Technol.*, vol. 33, no. 1, pp. 244–250, 2015.
[94] X. Song and J. Cheng, "Subcarrier intensity modulated optical wireless communications using noncoherent and differentially coherent modulations," *J. Light. Technol.*, vol. 31, no. 12, 2013.
[95] A. Jaiswal, M. R. Bhatnagar, and V. K. Jain, "Performance evaluation of space shift keying in free-space optical communication," *J. Opt. Commun. Netw.*, vol. 9, no. 2, p. 149, 2017.
[96] S. Navidpour, M. Uysal, and M. Kavehrad, "BER Performance of Free-Space Optical Transmission with Spatial Diversity," *IEEE Trans. Wirel. Commun.*, vol. 6, no. 8, pp. 2813–2819, Aug. 2007.
[97] K. Kumar, D. K. Borah, and S. Member, "Quantize and encode relaying through FSO and hybrid FSO / RF links," *IEEE Trans. Veh. Technol.*, vol. 64, no. 6, pp. 2361–2374, 2015.
[98] W. Gappmair and M. Flohberger, "Error performance of coded FSO links in turbulent atmosphere modeled by gamma-gamma distributions," *IEEE Trans. Wirel. Commun.*, vol. 8, no. 5, pp. 2209–2213, 2009.
[99] T. Ohtsuki, "Turbo-coded atmospheric optical communication systems," in *EEE International Conference on Communications. Conference (ICC)*, 2002, vol. 5, pp. 2938–2942.
[100] I. B. Djordjevic, "LDPC-coded optical communication over the atmopsheric turbulence channel," in *Conference Record of the Forty-First Asilomar Conference on Signals, Systems and Computers*, 2007, pp. 1903–1909.
[101] M. Safari and M. Uysal, "Relay-assisted free-space optical communication," *IEEE Trans. Wirel. Commun.*, vol. 7, no. 12, pp. 5441–5449, 2008.
[102] L. C. Andrews, R. L. Phillips, and C. Y. Hopen, "Aperture averaging of optical scintillations: power fluctuations and the temporal spectrum," *Waves in Random Media*, vol. 10, no. 1, pp. 53–70, 2000.
[103] T. A. Tsiftsis, H. G. Sandalidis, G. K. Karagiannidis, and S. Member, "Optical wireless links with spatial diversity over strong atmospheric turbulence channels," *IEEE Trans. Wirel. Commun.*, vol. 8, no. 2, pp. 951–957, 2009.
[104] A. Sendonaris, E. Erkip, and B. Aazhang, "User cooperation diversity-Part I: System description," *IEEE Trans. Commun.*, vol. 51, no. 11, pp. 1927–1938, 2003.
[105] a. Sendonaris, E. Erkip, and B. Aazhang, "User cooperation diversity-Part II: Implementation aspects and performance analysis," *IEEE Trans. Commun.*, vol. 51, no. 11, pp. 1939–1948, 2003.
[106] J. N. Laneman, D. N. C. Tse, and G. W. Wornell, "Cooperative Diversity in Wireless Networks: Efficient Protocols and Outage Behavior," *IEEE Trans. Inf. Theory*, vol. 50, no. 12, pp. 3062–3080, Dec. 2004.
[107] G. Kramer, M. Gastpar, and P. Gupta, "Cooperative strategies and capacity theorems for relay networks," *IEEE Trans. Inf. Theory*, vol. 51, no. 9, pp. 3037–3063, 2005.
[108] A. Acompora and S. Krishnamurthy, "A broadband wireless access network based on mesh-connected free space optical links," *IEEE Pers. Commun.*, vol. 6, no. 10, pp. 62–65, 1999.
[109] H. Zhou, D. Hu, S. Mao, and P. Agrawal, "Joint relay selection and power

allocation in cooperative FSO networks," *GLOBECOM - IEEE Glob. Telecommun. Conf.*, pp. 2418–2423, 2013.
[110] C. Abou-rjeily and S. Haddad, "Inter-Relay Cooperation : A New Paradigm for Enhanced Relay-Assisted FSO Communications," *IEEE Trans. Commun.*, vol. 62, no. 6, pp. 1970–1982, 2014.
[111] C. Abou-Rjeily, "All-Active and Selective FSO Relaying: Do We Need Inter-Relay Cooperation?," *J. Light. Technol.*, vol. 32, no. 10, pp. 1899–1906, May 2014.
[112] E. Bayaki, D. S. Michalopoulos, and R. Schober, "EDFA-based all-optical relaying in free-space optical systems," *IEEE Trans. Commun.*, vol. 60, no. 12, pp. 3797–3807, Dec. 2012.
[113] X. Tang, Z. Wang, Z. Xu, and Z. Ghassemlooy, "Multihop free-space optical communications over turbulence channels with pointing errors using heterodyne detection," *J. Light. Technol.*, vol. 32, no. 15, pp. 2597–2604, 2014.
[114] C. K. Datsikas, K. P. Peppas, N. C. Sagias, and G. S. Tombras, "Serial Free-Space Optical Relaying Communications Over Gamma-Gamma Atmospheric Turbulence Channels," *J. Opt. Commun. Netw.*, vol. 2, no. 8, p. 576, Jul. 2010.
[115] S. M. Aghajanzadeh and M. Uysal, "Outage Performance and DMT Analysis of DF Parallel Relaying in FSO IM/DD Communications," in *IEEE Vehicular Technology Conference (VTC Fall)*, 2012, vol. 2, pp. 1–5.
[116] M. A. Kashani, M. Safari, and M. Uysal, "Optimal relay placement and diversity analysis of relay-assisted free-space optical communication systems," *Opt. Commun. Netw.*, vol. 5, no. 1, pp. 37–47, 2013.
[117] M. A. Kashani, M. Safari, and M. Uysal, "Optimal Relay Placement and Diversity Analysis of Relay-Assisted Free-Space Optical Communication Systems," *J. Opt. Commun. Netw.*, vol. 5, no. 1, pp. 37–47, Dec. 2013.
[118] M. Dohler and Y. Li, *Cooperative communications: Hardware, channel and PHY*. United Kindom: Wiley, 2010.
[119] A. Nasri, R. Schober, and I. F. Blake, "Performance and optimization of amplify-and-forward cooperative diversity systems in generic noise and interference," *IEEE Trans. Wirel. Commun.*, vol. 10, no. 4, pp. 1132–1143, 2011.
[120] L. Song, "Relay selection for two-way relaying with amplify-and-forward protocols," *IEEE Trans. Veh. Technol.*, vol. 60, no. 4, pp. 1954–1959, 2011.
[121] M. R. Bhatnagar, "Average BER analysis of relay selection based decode-and-forward cooperative communication over Gamma-Gamma fading FSO links," *2013 IEEE Int. Conf. Commun.*, pp. 3142–3147, Jun. 2013.
[122] C. Abou-Rjeily, "Achievable Diversity Orders of Decode-and-Forward Cooperative Protocols over Gamma-Gamma Fading FSO Links," *IEEE Trans. Commun.*, vol. 61, no. 9, pp. 3919–3930, 2013.
[123] S. Anees and M. R. Bhatnagar, "Performance evaluation of decode-and-forward dual-hop asymmetric radio frequency-free space optical communication system," *IET Optoelectron.*, vol. 9, no. 5, pp. 232–240, 2015.
[124] J. N. Laneman and G. W. Wornell, "Distributed space–time-coded protocols for exploiting cooperative diversity in wireless networks," *IEEE Trans. Inf. Theory*, vol. 49, no. 10, pp. 2415–2425, 2003.
[125] G. P. Agrawal, *Fiber-optic communications systems*, 3rd Editio. New York, USA: John Wiley & Sons, 2002.
[126] U. Adar, T. Kuzniz, I. D. Haber, and N. Budin, "An all-optical multi-hop (cascaded) high bit rate wireless communication field trial," in *Optical Fiber Communication Conference and Exhibit (OFC)*, 2002, no. 2001, pp. 446–448.
[127] P. C. Becker, N. A. Olsson, and J. R. Simpson, *Erbium-doped fiber amplifiers: Fundamentals and technology*. Academic Press, 1999.

[128] T. Mukai, Y. Yamamoto, and T. Kimura, “Optical amplification by semiconductor lasers,” in *Semiconductors and Semimetals*, vol. 22, Academic Press, 1985, pp. 265–319.
[129] H. Ghafouri-Shiraz, *The principles of semiconductor laser diodes and amplifiers: Analysis and transmission line laser modeling*. London: Imperial College Press, 2004.
[130] A. Abisayo, “Optically Amplified Free-space Optical Communication Systems,” University of Nottingham, 2013.
[131] D. N. Payne, I. M. Jauncey, L. Reekie, and R. J. Mears, “High-gain rare-earth-doped fiber amplifier at 1.54 μm,” in *International Conference on Integrated Optics and Optical Fiber Communication*, 1987, vol. 3, p. 167.
[132] R. Ramaswami, K. N. Sivarajan, and G. H. Sasaki, *Optical networks: A practical perspective*, 3rd Editio., vol. 12, no. 6. USA: Morgan Kaufmann-Elsevier, 2010.
[133] S. Betti, G. De Marchis, and E. Iannone, *Coherent optical communications systems*. United State: John Wiley & Sons, 1995.
[134] M. YÜCEL, “Increase of transmission distance using EDFA and module design for free space optics applications,” *Gazi Univ. J. Sci.*, vol. 25, no. 1, pp. 119–125, 2012.
[135] C. Barnard, S. Member, P. Myslinski, J. Chrostowski, S. Member, and M. Kavehrad, “Analytical Model for Rare-Earth-Doped Fiber Amplifiers and Lasers,” vol. 30, no. 8, pp. 1817–1830, 1994.
[136] M. Premaratne and G. P. Agrawal, *Light propagation gain media: Optical amplifiers*. United States of America: Cambridge University Press, 2011.
[137] P. Urquhart, *Advances in Optical Amplifiers*. 2011.
[138] C. Lin, *Optical components for communications: Principles and applications*. Kluwer Academic Publishers, 2004.
[139] Z. Zhu, M. Funabashi, Z. Pan, B. Xiang, L. Paraschis, and S. J. B. Yoo, “Jitter and amplitude noise accumulations in cascaded all-optical regenerators,” *J. Light. Technol.*, vol. 26, no. 12, pp. 1640–1652, 2008.
[140] T. I. Lakoba, J. R. Williams, and M. Vasilyev, “Low-power, phase-preserving 2R amplitude regenerator,” *Opt. Commun.*, vol. 285, no. 3, pp. 331–337, 2012.
[141] T. N. Nguyen *et al.*, “Self-phase-modulation-based 2R regenerator including pulse compression and offset filtering for 42.6 Gbit/s RZ-33% transmission systems,” *Opt. Express*, vol. 17, no. 20, pp. 2900–2902, 2009.
[142] M. Rochette, J. N. Kutz, J. L. Blows, D. Moss, J. T. Mok, and B. J. Eggleton, “Bit-error-ratio improvement with 2R optical regenerators,” *IEEE Photonics Technol. Lett.*, vol. 17, no. 4, pp. 908–910, 2005.
[143] V. B. Heidelberg, *Nonlinear optics in telecommunications*. New York, USA: Springer, 2004.
[144] G. P. Agrawal, *Nonlinear Fiber Optics*, 5th Editio. United Kingdom: Academic Press, 2013.
[145] S. P. Singh and N. Singh, “Nonlinear effects in optical fibers: Origin, management and applications,” *Prog. Electromagn. Res.*, vol. 73, pp. 249–275, 2007.
[146] G. P. Agrawal, *Nonlinear Fiber Optics*, 4th Ed. London: Academic Press, 2007.
[147] H. Padda, “Noise modelling for 2R optical regenerator systems,” University of Nottingham, 2009.
[148] L. Provost, F. Parmigiani, P. Petropoulos, and D. J. Richardson, “Investigation of simultaneous 2R regeneration of two 40-Gb/s channels in a single optical fiber,” *IEEE Photonics Technol. Lett.*, vol. 20, no. 4, pp. 270–272, 2008.
[149] C. Ito and J. C. Cartledge, “Polarization independent all-optical 3R regeneration based on the Kerr effect in highly nonlinear fiber and offset spectral slicing,” *IEEE J. Sel. Top. Quantum Electron.*, vol. 14, no. 3, pp. 616–624, 2008.

[150] M. Rochette, L. Fu, V. Ta'eed, D. J. Moss, and B. J. Eggleton, "2R optical regeneration: An all-optical solution for BER improvement," *IEEE J. Sel. Top. Quantum Electron.*, vol. 12, no. 4, pp. 736–743, 2006.
[151] P. V Mamyshev, "All-optical data regeneration based on self-phase modulation effect," in *European Conference on Optical Communications*, 1998, vol. 1, no. September, pp. 475–476.
[152] T.-H. Her, G. Raybon, and C. Headley, "Optimization of pulse regeneration at 40 Gb/s based on spectral filtering of self-phase modulation in fiber," *IEEE Photonics Technol. Lett.*, vol. 16, no. 1, pp. 200–202, 2004.
[153] N. Yoshikane, I. Morita, T. Tsuritani, A. Agata, N. Edagawa, and S. Akiba, "Benefit of SPM-based all-optical reshaper in receiver for long-haul DWDM transmission systems," *IEEE J. Sel. Top. Quantum Electron.*, vol. 10, no. 2, pp. 412–420, 2004.
[154] M. Matsumoto, "Performance analysis and comparison of optical 3R regenerators utilizing self-phase modulation in fibers," *J. Light. Technol.*, vol. 22, no. 6, pp. 108–109, 2004.
[155] L. B. Fu, M. Rochette, V. G. Ta, D. J. Moss, and B. J. Eggleton, "Investigation of self-phase modulation based optical regeneration in single mode As2Se3 chalcogenide glass fiber," *Opt. Express*, vol. 13, no. 19, pp. 7637–7644, 2005.
[156] G. P. Agrawal, *Applications of nonlinear fiber optics*, 2nd Editio., vol. 1. Academic Press, 2015.
[157] G. Raybon *et al.*, "40 Gbit/s Pseudo-linear transmission over one million kilometers," in *Optical Fiber Communication Conference*, 2002.
[158] J. A. P. Cetina, "Passively mode-locked semiconductor lasers for all-optical applications," Dublin City University, 2014.
[159] R. G. M. P. Koumans and R. Van Roijen, "Theory for passive mode-locking in semiconductor laser structures including the effects of self-phase modulation, dispersion, and pulse collisions," *IEEE J. Quantum Electron.*, vol. 32, no. 3, pp. 478–492, 1996.
[160] R. Paschotta, *Field guide to laser pulse generation*. Bellingham, Washington USA: SPIE Press, 2008.
[161] W. O. Popoola, Z. Ghassemlooy, C. G. Lee, and a. C. Boucouvalas, "Scintillation effect on intensity modulated laser communication systems—a laboratory demonstration," *Opt. Laser Technol.*, vol. 42, no. 4, pp. 682–692, Jun. 2010.
[162] J. Akella, M. Yuksel, and S. Kalyanaraman, "Error analysis of multi-hop free-space optical communication," in *IEEE International Conference on Communications ICC*, 2005, vol. 0, no. C, pp. 1777–1781.
[163] T. A. Tsiftsis, H. G. Sandalidis, G. K. Karagiannidis, and N. C. Sagias, "Multihop free-space optical communications over strong turbulence channels," in *IEEE International Conference on Communications*, 2006, vol. 0, no. c, pp. 2755–2759.
[164] M. Karimi and M. Nasiri-kenari, "Free space optical communications via optical amplify-and-forward relaying," *J. Light. Technol.*, vol. 29, no. 2, pp. 242–248, 2011.
[165] M. A. Kashani, M. M. Rad, M. Safari, and M. Uysal, "All-optical amplify-and-forward relaying system for atmospheric channels," *IEEE Commun. Lett.*, vol. 16, no. 10, pp. 1684–1687, Oct. 2012.
[166] P. V Trinh, N. T. Dang, and A. T. Pham, "All-optical AF relaying FSO systems using EDFA combined with OHL over gamma-gamma channels," in *IEEE International Conference on Communications*, 2015, no. 1, pp. 5098–5103.
[167] P. V Trinh, S. Member, N. T. Dang, A. T. Pham, and S. Member, "All-Optical relaying FSO systems using EDFA combined with optical hard-limiter over atmospheric turbulence channels," *J. Light. Technol.*, vol. 33, no. 19, pp. 4132–

4144, 2015.
[168] J. Y. Wang *et al.*, "Free-space optical communications using all-optical relays over weak turbulence channels with pointing errors," in *International Conference on Wireless Communications & Signal Processing (WCSP)*, 2013, pp. 1–6.
[169] P. V. Trinh, A. T. Pham, H. T. T. Pham, and N. T. Dang, "BER analysis of all-optical AF dual-hop FSO systems over gamma-gamma channels," *IEEE 4th Int. Conf. Photonics*, no. 1, pp. 175–177, Oct. 2013.
[170] L. Yang, X. Gao, and M. Alouini, "Performance analysis of relay-assisted all-optical FSO networks over strong atmospheric turbulence," *J. Light. Technol.*, vol. 32, no. 23, pp. 4011–4018, 2014.
[171] J. Libich, M. Komanec, S. Zvanovec, P. Pesek, W. O. Popoola, and Z. Ghassemlooy, "Experimental verification of all-optical dual hop 10 Gbit/s FSO link under turbulence regimes," *Opt. Lett.*, vol. 40, no. 3, pp. 391–394, 2015.
[172] J. Zhang, L. Dai, Y. Zhang, and Z. Wang, "Unified performance analysis of mixed radio frequency/free space optical dual-hop transmission systems," *J. Light. Technol.*, vol. 33, no. 11, pp. 2286–2293, 2015.
[173] G. T. Djordjevic, M. I. Petkovic, A. M. Cvetkovic, and G. K. Karagiannidis, "Mixed RF/FSO relaying with outdated channel state information," *J. Sel. Areas Commun.*, vol. 33, no. 9, pp. 1935–1948, 2015.
[174] I. S. Ansari, F. Yilmaz, and M. S. Alouini, "Impact of pointing errors on the performance of mixed RF/FSO dual-hop transmission systems," *IEEE Wirel. Commun. Lett.*, vol. 2, no. 3, 2013.
[175] A. Papoulis and S. U. Pillai, *Probability, Random Variables, and Stochastic Processes*. New York: McGraw-Hill, 2002.
[176] A. P. Prudnikov, I. A. Brychkov, and O. I. Marichev, *Integrals and series: More special functions*, Vol 3. New York, USA: Gordon and Breach Science Publishers, 1990.
[177] Le Nguyen Binh, *Optical fiber communications systems:Theory and practice with MATLAB and simulink models*. CRC Press Taylor and Francis Group, 2010.
[178] M. A. Kallistratova and D. F. Timanovskiy, "The distribution of the structure constant of refractive index fluctuations in the atmospheric surface layer," *Repr. from Izv. Atmos. Ocean Phys.*, vol. 7, no. 1, pp. 73–75, 1990.
[179] S. S. Hnaung, "Design and Implementation of 10Gbps All-optical 2R Regenerator," vol. 4, no. 6, pp. 3–7, 2014.
[180] J.-C. Simon *et al.*, "Long distance transmission using optical regeneration," in *Optical Fiber Communication Conference*, 2008, pp. 8–10.
[181] C. Finot *et al.*, "Numerical study of an optical regenerator exploiting self-phase modulation and spectral offset filtering at 40 Gbit/s," *Opt. Commun.*, vol. 281, no. 8, pp. 2252–2264, 2008.
[182] P. P. Baveja, D. N. Maywar, A. M. Kaplan, and G. P. Agrawal, "Self-phase modulation in semiconductor optical amplifiers: Impact of amplified spontaneous emission," *IEEE J. Quantum Electron.*, vol. 46, no. 9, pp. 1396–1403, 2010.
[183] M. Matsumoto, "Analysis of a 2R optical regenerator utilizing self-phase modulation in a highly nonlinear fiber," pp. 613–614, 2002.
[184] M. Matsumoto and O. Leclerc, "Analysis of 2R optical regenerator utilising self-phase modulation in highly nonlinear fibre," *Electron. Lett.*, vol. 38, no. 12, pp. 576–577, 2002.
[185] Govind P. Agrawal, "Self-phase modulation and spectral broadening of optical pulses in SLA," *IEEE J. Quantum Electron.*, vol. 25, no. 11, pp. 2297–2306, 1989.
[186] I. Tomkos, C. Kouloumentas, and S. Tsolakidis, "Performance studies of multi-wavelength all-optical 2R regeneration subsystems based on highly non-linear fibers," *Proc. 2007 9th Int. Conf. Transparent Opt. Networks, Ict. 2007*, vol. 1, pp.

132–135, 2007.
[187] G. Xu, Z. Li, T. Yang, and C. Huang, “Analysis of a 2R all-optical regenerator utilizing cascaded four-wave mixing in a highly nonlinear fiber,” *Optik (Stuttg).*, vol. 124, no. 21, pp. 4758–4761, 2013.
[188] J. Wang *et al.*, “Simultaneous 3r regeneration of 4 × 40-Gbit/s WDM signals in a single fiber,” *IEEE Photonics J.*, vol. 4, no. 5, pp. 1816–1822, 2012.
[189] G. Hesketh and P. Horak, “All-optical phase regeneration of multi-level amplitude and phase shift keyed signals,” in *Conference on Lasers and Electro-Optics Europe and International Quantum Electronics Conference*, 2013, vol. 748, no. 2011, pp. 1–1.
[190] L. A. Provost, C. Finot, P. Petropoulos, K. Mukasa, and D. J. Richardson, “Design scaling rules for 2R-optical self-phase modulation-based regenerators,” *Opt. Express*, vol. 15, no. 8, pp. 5100–5113, 2007.
[191] P. Johannisson and M. Karlsson, “Characterization of a self-phase-modulation-based all-optical regeneration system,” *IEEE Photonics Technol. Lett.*, vol. 17, no. 12, pp. 2667–2669, 2005.
[192] L. Provost, F. Parmigiani, P. Petropoulos, and D. J. Richardson, “Investigation of timing jitter reduction in a bidirectional 2R all-optical Mamyshev regenerator,” in *OFC/NFOEC 2008 - 2008 Conference on Optical Fiber Communication/National Fiber Optic Engineers Conference*, 2008.
[193] M. Matsumoto, “Efficient all-optical 2R regeneration using self-phase modulation in bidirectional fiber configuration.,” *Opt. Express*, vol. 14, no. 23, pp. 11018–11023, 2006.
[194] M. Matsumoto, “Fiber-based all-optical signal regeneration,” *IEEE J. Sel. Top. Quantum Electron.*, vol. 18, no. 2, pp. 738–752, 2012.
[195] L. Provost, C. Finot, K. Mukasa, P. Petropoulos, and D. J. Richardson, “Generalisation and experimental validation of design rules for self-phase modulation-based 2R-regenerators,” in *Conference on Optical Fiber Communication and the National Fiber Optic Engineers*, 2007, pp. 6–8.
[196] M. Aoudeh and J. C. Cartledge, “Impact of residual dispersion and ASE noise on the performance optimization of all-optical regenerators utilizing self-phase modulation in a highly nonlinear fiber,” *IEEE J. Sel. Top. Quantum Electron.*, vol. 12, no. 4, pp. 717–725, 2006.
[197] Y. Yang and C. Lou, “Experimental investigation of the influence of filters on regeneration performance in self-phase modulation based regenerator,” *Microw. Opt. Technol. Lett.*, vol. 49, no. 1, pp. 192–195, 2007.
[198] T. Her *et al.*, “Enhanced 40-Gbit/s receiver sensitivity with all-fiber optical 2R regenerator,” in *Technical Digest Conference Lasers and Electro-Optics Society*, 2002, pp. 534–535.
[199] M. Rochette, J. L. Blows, and B. J. Eggleton, “An all-optical regenerator that discriminates noise from signal,” in *European Conference on Optical Communication*, 2005, vol. 3, pp. 403–404 vol.3.
[200] T. Nguyen, M. Gay, L. Bramerie, T. Chartier, J.-C. Simon, and M. Joindot, “Noise reduction in 2R-regeneration technique utilizing self-phase modulation and filtering.,” *Opt. Express*, vol. 14, no. 5, pp. 1737–47, 2006.
[201] P. P. Baveja, D. N. Maywar, and G. P. Agrawal, “Optimization of all-optical 2R regenerators operating at 40 Gb/s: Role of dispersion,” *J. Light. Technol.*, vol. 27, no. 17, pp. 3831–3836, 2009.
[202] J. Leuthold *et al.*, “40 Gbit/s transmission and cascaded all-optical wavelength conversion over 1 000 000 km,” *Electron. Lett.*, vol. 38, no. 16, pp. 890–892, 2002.
[203] J. Mørk, F. Öhman, and S. Bischoff, “Analytical expression for the bit error rate of cascaded all-optical regenerators,” *IEEE Photonics Technol. Lett.*, vol. 15, no.

10, pp. 1479–1481, 2003.
[204] Z. Huang, A. Gray, I. Khrushchev, and I. Bennion, “10-Gb/s transmission over 100 Mm of standard fiber using 2R regeneration in an optical loop mirror,” *IEEE Photonics Technol. Lett.*, vol. 16, no. 11, pp. 2526–2528, 2004.
[205] G. Gavioli, V. Mikhailov, B. Thomsen, and P. Bayvel, “Investigation of transmission with cascaded all-optical 3R regenerators and variable inter-regenerator spacing,” *Electron. Lett.*, vol. 41, no. 3, p. 146, 2005.
[206] M. Sorokina, A. Perentos, A. D. Ellis, S. K. Turitsyn, and S. Sygletos, “A 3R Regeneration Scheme for Highly Spectral Efficient Signal Waveforms,” in *International Conference on Transparent Optical Networks*, 2015, vol. 3, pp. 1–4.
[207] M. Rochette, I. C. M. Littler, R. W. McKerracher, and B. J. Eggleton, “A dispersionless and bandwidth-adjustable FBG filter for reconfigurable 2R-regeneration,” *IEEE Photonics Technol. Lett.*, vol. 17, no. 8, pp. 1680–1682, 2005.
[208] M. F. Ferreira, *Nonlinear Effects in Optical Fibers*. New Jersey: John Wiley & Sons, 2011.
[209] S. Zvanovec, J. Perez, Z. Ghassemlooy, S. Rajbhandari, and J. Libich, “Route diversity analyses for free-space optical wireless links within turbulent scenarios.,” *Opt. Express*, vol. 21, no. 6, pp. 7641–50, Mar. 2013.
[210] V. Cristofori, “Short-pulse propagation in fiber optical parametric amplifiers,” Technical University of Denmark, 2013.